

# **Light-Matter Interactions: Plasmon & Phonon Polaritons in Refractory Nitrides for Nanophotonics**

A thesis submitted for the degree of

Doctor of Philosophy

by

**Krishna Chand Maurya**

Supervisor: Dr. Bivas Saha



Chemistry and Physics of Materials Unit

Jawaharlal Nehru Centre for Advanced Scientific Research

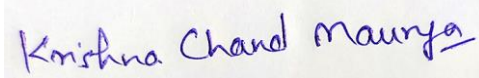
Bangalore - 560064, India

December 2022

## DECLARATION

I hereby declare that the matter embodied in the thesis entitled “**Light-Matter Interactions: Plasmon & Phonon Polaritons in Refractory Nitrides for Nanophotonics**” is the result of investigations carried out by me at the Chemistry and Physics of Materials Unit, Jawaharlal Nehru Centre for Advanced Scientific Research, Bangalore, India, under the supervision of **Dr. Bivas Saha** and that it has not been submitted elsewhere for the award of any degree or diploma.

In keeping with the general practice of reporting scientific observations, due acknowledgement has been made whenever the work described is based on the findings of other investigators. Any omission that might have occurred by oversight or error of judgement is regretted.



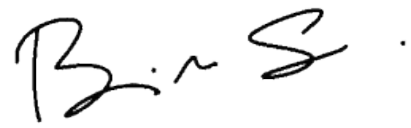
Krishna Chand Maurya

Date: 28<sup>th</sup> December 2022

Place: Bangalore, India

## CERTIFICATE

I hereby certify that the matter embodied in this thesis entitled "**Light-Matter Interactions: Plasmon & Phonon Polaritons in Refractory Nitrides for Nanophotonics**" has been carried out by **Mr. Krishna Chand Maurya** at the Chemistry and Physics of Materials Unit, Jawaharlal Nehru Centre for Advanced Scientific Research, Bangalore, India, under my supervision and that it has not been submitted elsewhere for the award of any degree or diploma.



---

Dr. Bivas Saha  
(Research Supervisor)

Date: 28<sup>th</sup> December 2022

Place: Bangalore, India

*Dedicated to my loving family.*

# Table of Contents

---

|  |     |
|--|-----|
| Table of Contents .....  | v   |
| Acknowledgements .....   | vii |
| List of Publications .....   | ix  |
| Abstract .....   | 1   |
| Introduction .....   | 5   |
| 1.1 Polaritons: half-light-half-matter quasiparticle .....   | 7   |
| 1.2 Light propagation in matter .....  | 9   |
| 1.3 Plasmon polariton: light & free electron interaction.....                                      | 11  |
| 1.4 Phonon polariton: light & optical phonon interaction .....                                     | 16  |
| 1.5 Nitride materials.....   | 17  |
| 1.6 Refractory nitrides for nanophotonics: .....   | 18  |
| Plasmon Polariton in Refractory Transition Metals (Ta, W, Mo) and Nitrides (TiN, HfN, ZrN).....    | 20  |
| 2.1 Introduction.....  | 21  |
| 2.2 Growth of refractory transition metals.....  | 22  |
| 2.3 Plasmon polariton in refractory transition metals .....  | 23  |
| 2.4 Plasmon polariton in refractory transition metal nitrides .....                                | 28  |
| 2.5 Surface plasmon polariton in metals.....   | 32  |
| 2.6 Conclusion .....   | 32  |
| Infrared Plasmon and Phonon-Polaritons in Polar Semiconducting Scandium Nitride (ScN).....         | 34  |
| 3.1 Introduction.....  | 35  |
| 3.2 Growth of scandium nitride (ScN) film.....   | 37  |
| 3.3 Plasmon polariton in ScN .....   | 39  |
| 3.4 Phonon polariton in ScN.....   | 44  |
| 3.5 Transmission electron microscopy of ScN .....  | 46  |
| 3.6 Conclusion .....   | 48  |
| Morphology-Controlled Reststrahlen Band and Infrared Plasmon-Polariton in GaN Nanostructures ..... | 49  |
| 4.1 Introduction.....  | 50  |
| 4.2 Growth of GaN nanostructures .....   | 52  |
| 4.3 Reststrahlen band of GaN nanostructures.....   | 53  |

|  |     |
|--|-----|
| 4.4 Infrared plasmon polariton in GaN nanostructures.....  | 59  |
| 4.5 Plasmonic response of various mid-IR nanostructured plasmonic material.....                                  | 61  |
| 4.6 Conclusion .....   | 62  |
| TiN/Al <sub>0.72</sub> Sc <sub>0.28</sub> N Metal/Dielectric Multilayers-based Bi-functional Optical Cavity..... | 63  |
| 5.1 Introduction.....  | 64  |
| 5.2 Growth of TiN/Al <sub>0.72</sub> Sc <sub>0.28</sub> N/TiN MDM structures .....                               | 66  |
| 5.3 Optical characterization of TiN/Al <sub>0.72</sub> Sc <sub>0.28</sub> N/TiN MDM structures.....              | 67  |
| 5.4 Optical characterization of TiN/Al <sub>0.72</sub> Sc <sub>0.28</sub> N based double cavity .....            | 70  |
| 5.5 Optical phonon modes in MDM structures.....  | 72  |
| 5.6 Conclusion .....   | 76  |
| TiN/Al <sub>0.72</sub> Sc <sub>0.28</sub> N Superlattice-based Anisotropic Optical Medium for Spin Photonics ... | 77  |
| 6.1 Introduction.....  | 78  |
| 6.2 Growth of TiN/Al <sub>0.72</sub> Sc <sub>0.28</sub> N Superlattice .....                                     | 79  |
| 6.3 Optical characterization .....   | 79  |
| 6.4 Hyperbolic photonic dispersion in uniaxial medium:.....  | 81  |
| 6.5 Photon spin Hall effect.....   | 82  |
| 6.6 Conclusion .....   | 83  |
| Conclusion and Outlook .....   | 84  |
| 7.1 Future perspective:.....   | 90  |
| 7.2 Conclusion: .....  | 91  |
| Appendix A- Experimental Techniques.....   | 92  |
| A1 Magnetron Sputtering.....   | 92  |
| A2 Spectroscopic ellipsometry measurements.....  | 93  |
| A3 Fourier-transform infrared spectroscopy (FTIR) .....  | 95  |
| Appendix B - Supplementary data .....  | 97  |
| B1 Supplementary data of chapter 2.....  | 97  |
| B2 Supplementary data of chapter 3.....  | 102 |
| B3 Supplementary data of chapter 4.....  | 113 |
| B4 Supplementary data of chapter 5.....  | 122 |
| List of Figures .....  | 130 |
| References.....  | 137 |

## Acknowledgements

---

The last several years at JNCASR have been the most rewarding years of my life. Certainly, PhD is a daunting task. However, I am incredibly lucky to have met so many wonderful people during my time here, who helped me to make this journey possible. None of the achievements would have been possible without them. Here I would like to thank them all for their help and support.

First and foremost, I would like to thank my supervisor, Dr. Bivas Saha, for selecting me as his first PhD student and for continuously passing me his wisdom. For his effort to keep me focused, at the same time his encouragement, to keep pushing me to solve challenging problems. I am grateful to him for cherishing me as a researcher.

I thank Prof. C. N. R. Rao for making such a beautiful campus and being a source of immense inspiration. I thank our CPMU Chairman Prof. A. Sundaresan for conducting the unit nicely. I would like to thank all my JNC seniors and especially want to thank Dr. Abhijit Chatterjee, Dr. Shashidhara Acharya, Dr. Bharath B for helping me whenever I struggled with my experiments.

I would like to thank my collaborators Dr. Magnus Garbrecht, Ms. A. I. K. Pillai for the beautiful TEM images. I must thank Dr. Abhijit Chatterjee, Prof. S. M. Shivaprasad; Animesh Bhui, and Prof. Kanishka Biswas for their fruitful collaborations.

I acknowledge the Chemistry and Physics of Materials Unit (CPMU) and the International Center for Materials Science (ICMS), JNCASR for providing the facilities. I thank CSIR for the fellowship.

I thank Mr. Jeremy Van Derslice and Dr Neha Singh from J.A. Woollam Co.; Dr Ty Newhouse-Illige from PVD Products; Mr Hameed Basha and Dr Vijay Veer from Bruker for giving me training on ellipsometer, sputtering system, and FTIR respectively.

I want to thank all my lab mates from both the HIRG and MBE labs: Dr. Sanjay Nayak, Dr. Shashidhara, Dr. Saraswati, Dr. Abhijit, Dr. Rajendra, Shivaram, Bidesh, Dheemahi, Sourjyadeep, Krithika, Sneha, Prasanna, Sourav, Deeksha, Rahul, Dr. Nidhi, Mehak, Debmalya, Ankit for all the wonderful time we spend together.

I thank all my teachers from my previous school and college for inspiring me to pursue a career in science. Especially, I thank Acharya Vidyadhar from my high school for making science and mathematics interesting and enjoyable subjects to learn. I thank Prof. T. V. Ramakrishnan, Prof. B. P. Mondal, Prof. R. D. S. Yadav, and Prof. R. P. Malik from Banaras Hindu University (BHU) for making my strong foundation in Physics. I would like to thank Prof. Anshuman Kumar Srivastava from IIT Bombay for introducing me plasmonic and nanophononics for the first time. The course ‘Physics of Nanoscale Devices’ taught by Prof. Anshuman, inspired me to pursue a research career in Photonics.

I thank all my JNC friends- Debendra, Bidhan, Sinay, Prasenjit, Arpan, Anshuman, Bitan, Debattam, Supriti, Soumik, Anjana, and all my batchmates for all the fun we had.

I thank all my school and college friends- Saurabh, Pushpendra, Himanshu, Piyush, Sushovan, Vikram, Manu, Pankaj, Kiran, Durgesh, Prashant, Ritesh, Ramji and ...more for the wonderful memories.

Finally, I thank my family for their love and support.



## List of Publications

---

1. **K. C. Maurya**, D. Rao, S. Acharya, P. Rao, A. I. K. Pillai, S. K. Selvaraja, M. Garbrecht and B. Saha, "Polar Semiconducting Scandium Nitride as an Infrared Plasmon and Phonon-Polaritonic Material" *Nano Letters*, **22**, *13*, 5182-5190 (2022). <https://doi.org/10.1021/acs.nanolett.2c00912>.
2. **K. C. Maurya**, A. I. K. Pillai, M. Garbrecht and B. Saha, "Simultaneous Optical Resonances at Visible and Mid-Infrared Frequencies with Epitaxial TiN/Al<sub>0.72</sub>Sc<sub>0.28</sub>N/TiN Metal/Polar-Dielectric/Metal Multilayers." *Materials Today Physics*, **27**, 100797 (2022). <https://doi.org/10.1016/j.mtphys.2022.100797>.
3. **K. C. Maurya\***, A. Chatterjee\*, S. M. Shivaprasad, and B. Saha, " Morphology-Controlled Reststrahlen Band and Infrared Plasmon-Polariton in GaN Nanostructures" *Nano Letters*, **22**, 9606–9613 (2022). <https://pubs.acs.org/doi/10.1021/acs.nanolett.2c03748>.
4. P. Das, **K. C. Maurya**, J. L. Schroeder, M. Garbrecht and B. Saha, "Near-UV-to-near-IR Hyperbolic Photonic Dispersion in Epitaxial (Hf,Zr)N/ScN Metal/Dielectric Superlattices " *ACS Appl. Energy Mater.*, **5**, *4*, 3898–3904, (2022). <https://pubs.acs.org/doi/10.1021/acsaem.1c03467>
5. P. Das, B. Biswas, **K. C. Maurya**, M. Garbrecht & B. Saha. Refractory Plasmonic Hafnium Nitride and Zirconium Nitride Thin Films as Alternatives to Silver for Solar Mirror Applications. *ACS Appl. Mater. Interfaces*, **14**, *41*, 46708–46715 (2022) [doi.org/10.1021/acsaem.1c03467](https://doi.org/10.1021/acsaem.1c03467)
6. **K. C. Maurya**, A. Bhui, K. Biswas, and B. Saha, "Anisotropic Epsilon-near-pole (ENP) Resonance Leads to Hyperbolic Photonic Dispersion in Homologous (Bi<sub>2</sub>)<sub>m</sub>(Bi<sub>2</sub>Se<sub>3</sub>)<sub>n</sub> Topological Quantum Materials" *Appl. Phys. Lett.* **119**, 011902 (2021). (*Editor's Pick*). <https://doi.org/10.1063/5.0053587>.
7. **K. C. Maurya**, B. Biswas, D. Rao and B. Saha, "Giant Enhancement of Plasmonic Response and Epsilon-Near-Zero Signature in Refractory Transition Metals (Ta, W

and Mo) Deposited at High-Temperature" *Appl. Phys. Lett.* **118**, 041902 (2021).  
<https://doi.org/10.1063/5.0027497>.

8. **K. C. Maurya**, V. M. Shalaev, A. Boltasseva and B. Saha, "Reduced Optical Losses in Refractory Plasmonic Titanium Nitride (TiN) Thin Films Deposited with Molecular Beam Epitaxy" *Opt. Mater. Express.* **10**, 2679 (2020).  
<https://doi.org/10.1364/ome.405259>.

9. **K. C. Maurya**, B. Biswas, M. Garbrecht and B. Saha, "Wave-vector Dependent Raman Scattering from Coupled Plasmon- Longitudinal Optical Phonon Modes and Fano Resonance in n-type ScN." *Phys. Status Solidi RRL*, 1900196 (2019).  
<https://doi.org/10.1002/pssr.201900196>.

10. **K. C. Maurya**, A. I. K. Pillai, M. Garbrecht and B. Saha, "Ferrell and Berreman Modes in Epitaxial TiN/Al<sub>0.72</sub>Sc<sub>0.28</sub>N Superlattice." (*Under preparation 2023*).

## BOOK CHAPTER

1. **K. C. Maurya** and B. Saha, Chapter Title: "Plasmon and Phonon-Polaritons in Refractory Transition Metal Nitrides" *World Scientific. (In-press 2023)*

## Abstract

---

The subject of light-matter interactions is of importance from fundamental science to technological aspects covering physics, chemistry, materials, electrical and optical engineering. Classically, light-matter interactions are the result of an oscillating electromagnetic (EM) field resonantly interacting with charged particles. Quantum mechanically, quantized light fields (or photon) couple to quantum states of matter. When light enters a medium, unlike propagation in a vacuum, its propagation is affected by the interaction with the material. An EM wave can cause excitation of material if it resonates with an electronic oscillator (or electric dipole) in the medium. Polaritons are hybrid quasiparticles formed by the strong coupling of electromagnetic waves to an electric dipole. Polaritons have the unique property of having a high wavenumber, which allows them to confine light to subwavelength scales, enabling the imaging and manipulation of nanoscale objects beyond the diffraction limit of light. They can also enhance absorption and emission processes in materials, leading to more efficient energy conversion and optoelectronic devices. Polaritons have been used to achieve room temperature condensation, a phenomenon in which a macroscopic fraction of particles occupies the same quantum state, leading to novel quantum fluid behavior. In addition, polaritons can exhibit strong nonlinear behavior, making them attractive for nonlinear optics applications such as all-optical switching and signal processing.

In materials, different types of electronic oscillators (or electric dipoles), such as collectively oscillating free electrons (or plasmons) in metals, electron-hole pairs (or excitons) in semiconductors, lattice vibrations (phonons) in polar dielectrics, magnons in magnetic materials, Cooper pair plasmons in superconductors, etc., can interact with light to form different types of polaritons. The nomenclature of the quasiparticles becomes 'dipole + polariton', such as plasmon-polariton, phonon-polariton, exciton-polariton, etc. The energy range of these polaritons depends on the number and mass of the carriers involved. Depending on the spectral range required, the type of polariton or material can be chosen. For example, metals (plasmon polaritons) are generally used for visible applications, polar dielectric materials (phonon polaritons) can be chosen for mid-infrared applications, and magnetic materials (magnon polaritons) can be chosen for terahertz applications, etc. In this thesis, we have mainly focused on plasmon and phonon polaritons.

Among these polaritons, the plasmon polariton (or simply plasmon) is the most popular. Noble metals such as Ag and Au are the best plasmonic materials due to their low optical losses. However, there are several limitations with noble metals, such as complementary metal-oxide-semiconductor (CMOS) incompatibility, difficulty in fabrication and integration, softness and high cost. In addition, metals typically exhibit high optical losses in the infrared regime, which includes longer wavelengths beyond the visible range. This is primarily due to the increased damping caused by various factors such as electron scattering, electron-electron interactions, and electron-phonon interactions, which result in the dissipation of energy and reduced plasmonic performance. As a result, noble metals are not very efficient for several practical applications, especially for high-temperature applications and infrared nanophotonics. To address these challenges, we have studied plasmon and phonon polaritons in several refractory transition metals and metal nitrides from the visible to the infrared. Refractory materials are a class of materials with high melting temperatures and high hardness. In this thesis, we have also explored the refractory metal-dielectric metamaterial structures for photonic applications such as bifunctional optical cavity, extreme anisotropic optical medium (hyperbolic medium), selective and tunable absorber, etc. This thesis is divided into seven chapters as described below:

Chapter 1 of the thesis provides an overview of polaritons and the fundamental concept of light-matter interaction. It introduces the basic principles of how light interacts with matter to produce phenomena such as polaritons. Polaritons are hybrid particles that arise from the strong coupling between electromagnetic waves and oscillating charges in a material, such as electrons or lattice vibrations. The chapter highlights the importance of understanding the properties of polaritons and their interactions with matter in various applications such as optoelectronic devices, sensing and energy conversion.

Chapter 2 focuses on the plasmonic response of refractory transition metals and metal nitrides, in particular tantalum (Ta), tungsten (W), molybdenum (Mo), titanium nitride (TiN), hafnium nitride (HfN) and zirconium nitride (ZrN) thin films. These films are deposited by magnetron sputtering, a common technique for thin film deposition. Spectroscopic ellipsometry is used, a powerful optical characterization technique, to investigate the optical properties of these films and assess their plasmonic response. The results reported in this chapter show that the transition metal films, and metal nitrides studied exhibit high quality plasmonic response. Among them, TiN stands out with the lowest optical loss compared to previously reported films.

In general, metals exhibit high optical losses in the infrared due to intraband transitions, making them inefficient for infrared plasmonics. Chapter 3 of the thesis introduces scandium nitride (ScN), a degenerate semiconductor, as an infrared polaritonic material and demonstrates its ability to exhibit both plasmonic and phonon polariton resonances through carrier concentration modulation via n-type (oxygen) and p-type (magnesium) doping. Ellipsometry (for the 0.21  $\mu\text{m}$  to 2.5  $\mu\text{m}$  spectral range) and Fourier transform infrared spectroscopy (FTIR for the 1.1  $\mu\text{m}$  to 100  $\mu\text{m}$  spectral range) are used for optical characterisation, revealing the potential of ScN for various infrared photonic applications such as sensing, imaging and energy conversion. This chapter highlights the importance of carrier concentration engineering in shaping the optical properties of ScN and presents new opportunities for designing efficient infrared photonic devices on this platform.

Chapter 4 of the thesis explores the infrared polaritonic response of gallium nitride (GaN) nanostructures. GaN, a well-known III-V semiconductor, has gained significant attention for its remarkable properties, including blue light emission in LEDs. In addition, GaN nanostructures, such as nanorods, nanocolumns, and nanowall-networks, offer advantages over thin films due to their reduced dislocation density, confinement effects, and large surface-to-volume ratio. These features enable enhanced light emission, sensing, catalysis, and other applications. We investigate honeycomb-shaped GaN nanowall networks and vertically standing nanorods, revealing that morphology plays a crucial role in modifying the Reststrahlen band and inducing plasmon resonance. Overall, Chapter 4 sheds light on the influence of morphology on the polaritonic behaviour of GaN nanostructures and highlights the importance of considering nanostructuring as a means to tailor the optical properties of materials for infrared photonics.

The next two chapters of the thesis focus on the combined effect of refractory metal and dielectric based artificial structures, also known as metamaterials, for nanophotonic applications. In chapter 5, TiN/ $\text{Al}_x\text{Sc}_{1-x}\text{N}$  metal-dielectric-metal (MDM) optical cavities are investigated and several functionalities are demonstrated. These functionalities include mimicking orbital coupling in photonic structures, where the cavity modes exhibit behaviour similar to that of electron orbitals in atoms or molecules. In addition, the TiN/ $\text{Al}_x\text{Sc}_{1-x}\text{N}$  MDM cavities are shown to achieve simultaneous light absorption in the visible and mid-infrared (IR) regions. This can be used for efficient light harvesting and thermal sensing applications, where the metamaterial can absorb and utilize energy from a broad spectral range.

In Chapter 6, TiN/Al<sub>x</sub>Sc<sub>1-x</sub>N superlattices are used to design an extremely anisotropic optical medium, known as a hyperbolic medium, with highly contrasting dielectric permittivity along different directions, resulting in unique optical properties. These hyperbolic metamaterials can be used to control and manipulate the spin states of light, offering potential for novel spin-based information processing devices such as spin filters, spin waveguides and spin modulators.

In Chapter 7, the thesis provides a summary of the research and presents future avenues for work on refractory photonic materials and metamaterials. The research has covered a wide range of electromagnetic regimes, from visible to long wavelength infrared, and has explored various functionalities including plasmonics, phononics, optical cavity and extreme anisotropic hyperbolic medium. The results of the research represent a significant advance in the development of a nitride materials platform for nanophotonic applications. Potential applications include solar energy conversion, optical computing, quantum information processing, bio-photonics and more.

## Introduction

Light as a renewable energy source has immense potential for various applications such as power generation, telecommunications, healthcare, defense, mobile and computer displays, among others. It covers a wide range of the electromagnetic spectrum, including visible light as well as gamma rays, X-rays, microwaves and radio waves. Advanced techniques are used to precisely manipulate light using specialized materials, often at the nanoscale, thousands of times smaller than a human hair. Materials research has always been crucial in enabling new scientific concepts in next-generation technologies and the development of industries, including the Industrial Revolution.

The World Economic Forum divides the evolution of industry into four major milestones. The first industrial revolution took place in the late 18<sup>th</sup> century with the invention of steam engines and water turbines, which marked the transition from hand production methods to machines. The second industrial revolution, also known as the technological revolution, occurred in the 19<sup>th</sup> century with the invention of electricity and the establishment of extensive railway and telegraph networks, enabling faster transport and communication. The third industrial revolution, known as the digital revolution, began in the late 20<sup>th</sup> century with the widespread use of computers and the advent of fiber-optic communications. We are currently experiencing the fourth generation of the industrial revolution, known as the information technology era. This revolution is characterized by advances in cloud computing, artificial intelligence, social networking, and other technological innovations. Information technology has played a significant role in making the global pandemic more manageable through virtual meetings, cloud conferencing, distance learning, online entertainment, and other digital solutions. The impact of information technology has been far-reaching, transforming various aspects of society and industries. It has revolutionized communications, business operations, education, healthcare, entertainment and much more. The ability to connect globally in real time, access vast amounts of data and harness artificial intelligence has reshaped the way we live and work.

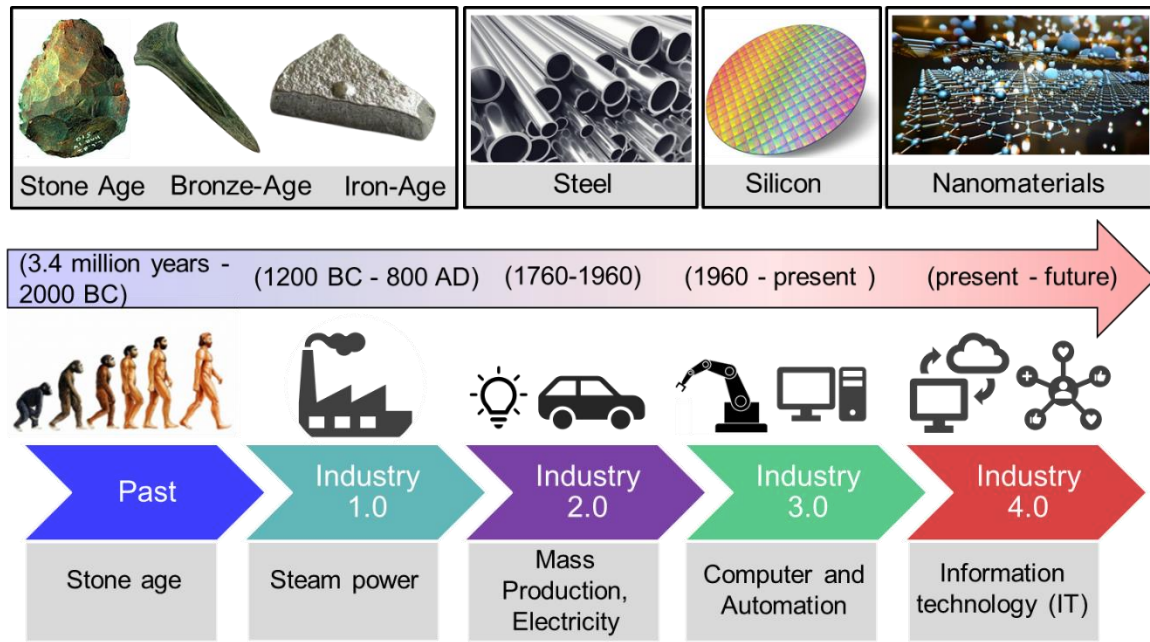


**Figure 1.1 Schematic diagram of the evolution of industry along with the materials.** New materials enable the new scientific concept and further into next-generation technology and the industrial revolution. Conventionally, the industry revolution can be divided into four major leaps. The first industrial revolution: steam. The second industrial revolution: electricity. The third industrial revolution: digital / computing. The fourth industrial revolution: connectivity / artificial intelligence.

From the iron age to the silicone age, industry evolved from 1<sup>st</sup> generation to 4<sup>th</sup> generation (see Figure 1.1). However, each generation of technology has a certain saturation level of performance. To outperform the existing technology, a novel concept or methodology is required. In the industrial revolution, material research plays an important role by enabling new scientific concepts into next-generation technology. For example, if we look at our present technology, semiconductor technologies and optical communication are ubiquitous and have revolutionized our information technology-based society. The volume of information processing and data storage have risen exponentially, mainly because of the scaling down of the size of semiconductor electronic components, and transistor counts have increased generally following Moore's law<sup>1</sup>. In semiconductor manufacturing, scaling of the electronic component from 10  $\mu\text{m}$  (in 1971) to 3 nm (in 2022) semiconductor process technology is commercially reached to increase volume density. For continuous demand for more energy- efficient and faster devices, further scaling will face many substantial difficulties such as increased process variability, lower yield, increasing costs, high heat dissipation and power consumption.



In photonic devices, on the other hand, the carrier is an electromagnetic (EM) wave (or light), and it is well known that nothing can travel faster than light. But the size of optical devices, including optical fibers, is typically larger than electronic devices because of the nature of light and the physical properties of materials used in optics. The wavelength of light used in optical communication is typically in the range of 1300-1550 nanometers, which is much larger than the size of electronic components such as transistors and integrated circuits. As a result, the components used in optical devices, including fibers, lenses, and detectors, need to be physically larger than their electronic counterparts to interact with the light. So, for the next generation of technology, we need a carrier that can have the speed of light and the dimension of electrons. Polaritons are half-light half-matter quasiparticles, that have the potential to overcome the limitations of existing technology.

### **1.1 Polaritons: half-light-half-matter quasiparticle**

Polaritons are hybrid quasiparticles formed by the strong coupling of electromagnetic waves to an electric dipole. Polaritons are essential for subwavelength light confinement, enhancing absorption and emission; enabling room temperature condensation and strong nonlinearity.<sup>2</sup> In materials, different types of dipoles (see Figure 1.2) such as the collectively oscillating free electron (or plasmon) in metals, electron–hole pair (or exciton) in a semiconductor, lattice vibration (phonon) in polar dielectric materials, magnon in antiferromagnetic and ferromagnetic resonances, Cooper pair plasmon in superconductors, etc.; can interact with light to form different types of polaritons.<sup>3</sup> The nomenclature of the quasiparticles become ‘dipole + polariton’ such as plasmon polariton, phonon polariton, etc. The energy of these polaritons depends on the number and mass of the carriers involved. For example, an electron has a lower mass than the atom, consequently, plasmons are found in a higher energy range than the phonon-polariton ( $\omega \propto 1/m$ ) as shown in Figure 1.3. In ‘Polariton panorama’<sup>3</sup>, 70 types of polaritons are discussed. In my thesis, I have focused mainly on plasmon and phonon polaritons.

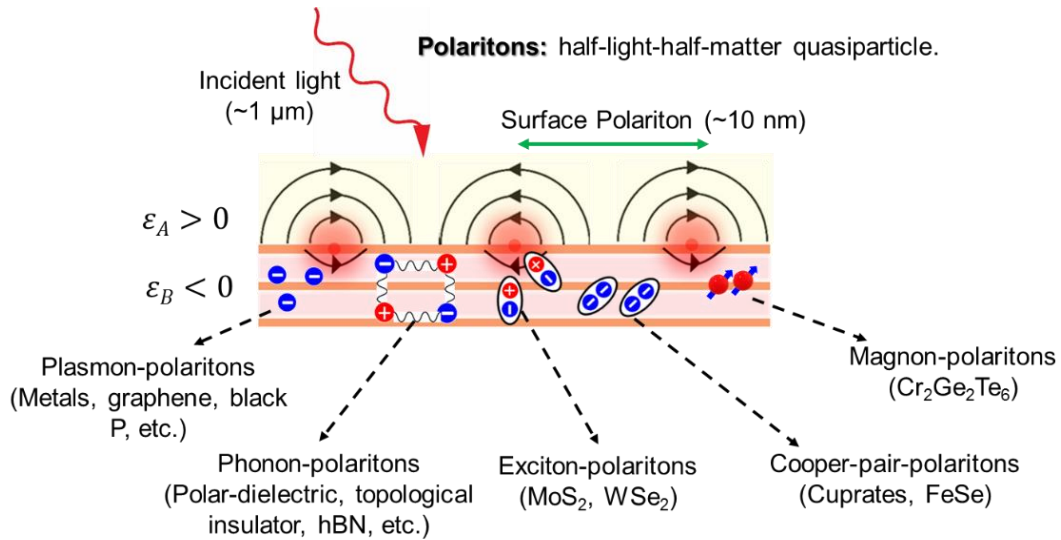


**Figure 1.2 Types of polaritons.** In material, several types of electronic oscillators or dipoles can interact with light to form polaritons. For example- plasmon in metals, phonon in dielectrics, exciton in semiconductors, cooper pair in superconductors, magnon in magnetic materials and more (there are 70 types of polaritons are discussed in ‘Polariton Panorama’<sup>3</sup>), can interact with light to form various types of polaritons.

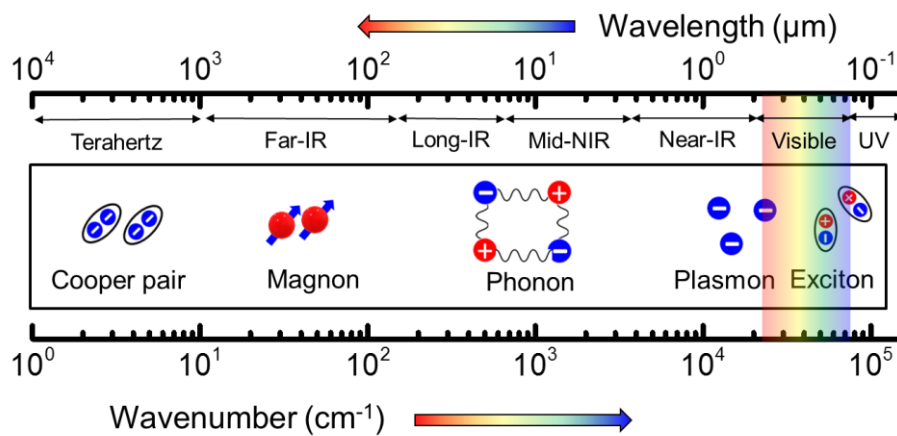


**Figure 1.3 The energy scale of various types of polaritons.** In general, exciton and plasmon polaritons lie in the ultraviolet to the near-infrared electromagnetic spectrum, depending on the materials. Phonon polaritons lie in the mid-to-long wavelength infrared region, while spin-wave-polaritons lie in the far infrared. Cooper-pair-polariton lies in the terahertz range. One can choose the material for various polaritons according to the requirement.

The field of polaritonics has received significant attention recently, although some of the polaritons have been known for decades. For example, in the ancient Roman era, the Lycurgus cup showed vibrant colors due to optical plasmonic resonances induced in the metal nanoparticles embedded in glass (see Figure 1.4). In the 19<sup>th</sup> century, Michael

Faraday systematically studied the synthesis and optical response of colloidal gold. But researchers could not identify their underlying color-controlling surface plasmonic principles until the 1950s. Research on plasmonics was boosted in the mid-1970s when surface-enhanced Raman scattering was discovered.<sup>4</sup> When light interacts with free electrons in metals, consequently, a surface wave of charge density propagates on the metal's surface. This surface wave is named as surface plasmon wave that enabled light confinement below the diffraction limit. Light can strongly couple with the metals via surface plasmon, and it has two important consequences: first, light can be confined below the diffraction limit, and second, the local electromagnetic field enhances by many orders of magnitudes due to the presence of plasmon excitation. However, in recent years, plasmonic materials have become essential<sup>5,6</sup> for subwavelength imaging, plasmon-induced hot carrier<sup>7</sup>, electro-thermo-plasmonic nanotweezers<sup>8</sup>, efficient absorbers<sup>9</sup>, hot-electron generation<sup>10</sup>, nanoparticle trapping<sup>11,12</sup>, photocatalysis<sup>13</sup>, and solar-thermophotovoltaics<sup>14,15</sup>.



**Figure 1.4 Ancient Roman Lycurgus cup.** It appears green in reflected light while red in transmitted light. These glasses are mixed with gold nanoparticles (typically 10–100 nm in size).<sup>16</sup>

## 1.2 Light propagation in matter

From a classical point of view, light is an electromagnetic wave. Inside a homogeneous and linear medium, the propagation of light can be described by the Maxwell equations (for the regions where there is no free charge or free current)<sup>17</sup>

$$\begin{aligned} \nabla \cdot \mathbf{E} &= 0, & \nabla \times \mathbf{E} &= -\frac{\partial \mathbf{B}}{\partial t}, \\ \nabla \cdot \mathbf{B} &= 0, & \nabla \times \mathbf{B} &= \varepsilon\mu \frac{\partial \mathbf{E}}{\partial t}, \end{aligned} \quad (1.1)$$

where  $\mathbf{E}$  and  $\mathbf{B}$  are electric and magnetic field, respectively. Light propagates through the medium with a speed  $v$ , which depends on the medium's dielectric permittivity ( $\epsilon$ ) and permeability ( $\mu$ ) as follow:

$$v = \frac{1}{\sqrt{\epsilon\mu}} = \frac{c}{n} \quad (1.2)$$

Where  $n$  is the refractive index

$$n = \sqrt{\frac{\epsilon\mu}{\epsilon_0\mu_0}} \quad (1.3)$$

Here  $\epsilon_0$  and  $\mu_0$  are the permittivity and permeability for free space. For most materials,  $\mu$  is very close to  $\mu_0$ , so  $n = \sqrt{\epsilon_r}$ ;  $\epsilon_r$  is the relative permittivity. Practically, when light passes through any medium, some part of it will always be absorbed. It is also referred as optical loss of medium and defined as complex refractive index ( $\tilde{n}$ ).

$$\tilde{n} = n + i \kappa \quad (1.4)$$

Here  $n$  is related to the phase velocity ( $c/v$ ) and  $\kappa$  is the extinction coefficient related to the absorption coefficient. The complex refractive index can be inserted in the complex wavenumber ( $k = \tilde{n}\omega/c$ ), consequently, the expression of the wave becomes

$$E = E_0 e^{ik \cdot r} = E_0 e^{i(n+i\kappa)\frac{\omega}{c}r} = E_0 e^{in\frac{\omega}{c}r} \times e^{-\kappa\frac{\omega}{c}r} \quad (1.5)$$

This expression is oscillatory along with a damping term which arise from the imaginary part of the refractive index. The real,  $n$ , and imaginary,  $\kappa$ , parts of the complex refractive index are not independent to each other while related through the Kramers–Kronig relations. Since the complex refractive index ( $\tilde{n}$ ) is also related to the complex dielectric permittivity ( $\tilde{\epsilon}_r = \epsilon_1 + i\epsilon_2$ ), the imaginary part is related to the optical loss of the medium.

When light passes from one medium, a, to another medium, b, its reflection and transmission depend on the following boundary conditions

$$\begin{aligned} \epsilon_a E_a^\perp &= \epsilon_b E_b^\perp & E_a^\parallel &= E_b^\parallel \\ B_a^\perp &= B_b^\perp & \frac{1}{\mu_a} B_a^\parallel &= \frac{1}{\mu_b} B_b^\parallel \end{aligned} \quad (1.6)$$

By solving these boundary conditions, one can find the relation for the reflection and transmission of light, also known as the Fresnel's equations.

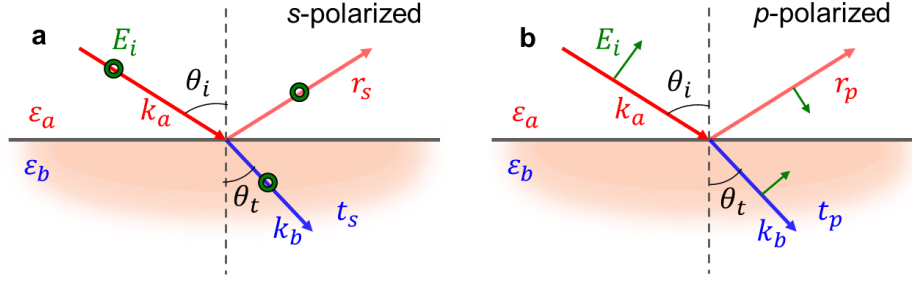


**Figure 1.5 Fresnel coefficients for  $s$  and  $p$  polarized light.** Schematic representation of the incident, reflected, and transmitted light at the boundary between two materials with permittivity  $\epsilon_a$  and  $\epsilon_b$  for both the  $s$  and  $p$ -polarizations, in terms of their corresponding Fresnel coefficients.

The Fresnel coefficients ( $r_s, r_p, t_s, t_p$ ) describe reflection ( $R$ ) and transmission ( $T$ ) intensity of polarized light ( $s$  or  $p$ ) (see Figure 1.5) as the following equation

$$r_s = \frac{n_a \cos\theta_i - n_b \cos\theta_t}{n_a \cos\theta_i + n_b \cos\theta_t} \quad (1.7)$$

$$r_p = \frac{n_a \cos\theta_t - n_b \cos\theta_i}{n_a \cos\theta_t + n_b \cos\theta_i} \quad (1.8)$$

$$t_s = \frac{2 n_a \cos\theta_i}{n_a \cos\theta_i + n_b \cos\theta_t} \quad (1.9)$$

$$t_p = \frac{2 n_a \cos\theta_i}{n_a \cos\theta_t + n_b \cos\theta_i} \quad (1.10)$$

Since the reflected and incident light propagate in the same medium. So, reflection intensity can be written as  $R = |r|^2$ , while transmission intensity  $T = \frac{n_b \cos\theta_t}{n_a \cos\theta_i} |t|^2$ . The complex refractive indices of the incident material ( $n_a$ ) and the reflective material ( $n_b$ ) together with the incident angle  $\theta_i$  are used to calculate the reflectance for both  $p$ - and  $s$ -polarized light.

### 1.3 Plasmon polariton: light & free electron interaction

When light incidents on a metal, its free electrons oscillate collectively to oppose the external field. The collective oscillation of the free electrons is called plasmon. The electromagnetic response of metals is governed by the Drude model<sup>18</sup>

$$\epsilon = \epsilon_1 + i\epsilon_2 = \epsilon_\infty \left( 1 - \frac{\omega_p^2}{\omega^2 + i\gamma\omega} \right) \quad (1.11)$$

Here  $\epsilon_\infty$  is the high-frequency dielectric constant,  $\omega_p$  and  $\gamma$  are the plasma frequency ( $\omega_p = \sqrt{\frac{ne^2}{m^*\epsilon_0}}$ ,  $n$  is carrier concentration,  $m^*$  is effective mass) and damping factor (describing the scattering and ohmic losses), respectively. Below the plasma frequency (or above the corresponding wavelength), metals exhibit a negative real permittivity ( $\epsilon_1$ ) and the optical losses ( $\epsilon_2$ ) that arise from the electronic transitions. Optical loss is a critical factor that limits the performance of optical devices.

The plasma frequency  $\omega_p$  (or corresponding wavelength  $\lambda_p$ ) is a crucial parameter in light-metal interaction (see Figure 1.6):

- For frequencies above  $\omega_p$ , metals behave like dielectrics and allow the propagation of light ( $\epsilon_1 > 0$ ).
- For frequencies below  $\omega_p$ , electrons can screen the radiation. Therefore, metals do not allow the penetration of light and display a highly reflective behavior ( $\epsilon_1 < 0$ ).

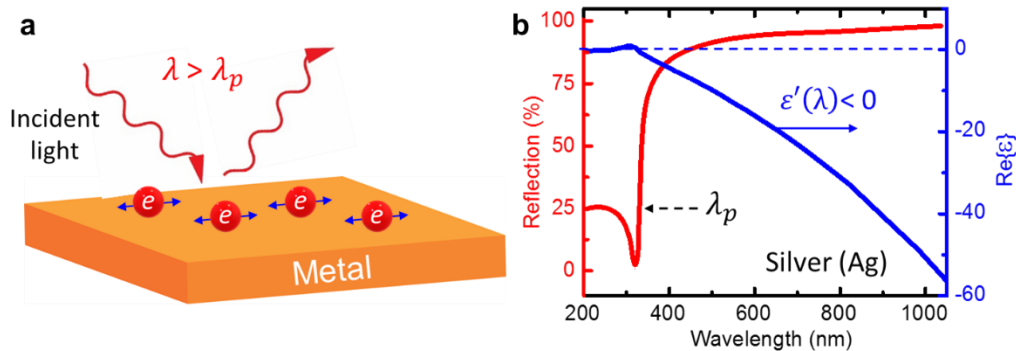


**Figure 1.6. Interaction of light with a metal.** (a) Schematics for the interaction of light with free electrons in metal (bulk plasmon). (b) Reflection curve of silver along with its real part of dielectric permittivity. Beyond 330 nm, Ag is highly reflective, and the real part of permittivity turns from positive-to-negative, this crossover wavelength is known as plasma wavelength ( $\lambda_p$ ) and the corresponding frequency is plasma frequency.

Once the plasmonic regime ( $\epsilon_1 < 0$ ) is identified, one can excite the surface plasmon polariton (SPP) modes. Surface plasmon polaritons are evanescent electromagnetic wave excitations, propagating at the interface between a dielectric and a metal. These surface modes arise due to the coupling of the electric field to the metal's oscillating electron plasma. However, the surface modes cannot be excited directly on metal surfaces with light due to the momentum mismatch between free-space light and polaritons. Surface polariton

modes can be achieved by coupling light to the conducting medium through a high-index prism (Kretschmann configuration is very common), or by introducing higher momentum through grating coupling, or through the fabrication of the nanostructure of the polaritonic medium (see Figure 1.7). In general, two types of surface waves are observed, first, propagating surface polariton wave at metal/dielectric interface, and second, localized surface wave in nanostructures. By exciting these surface modes, one can manipulate the light in a very small dimension (below the diffraction limit).

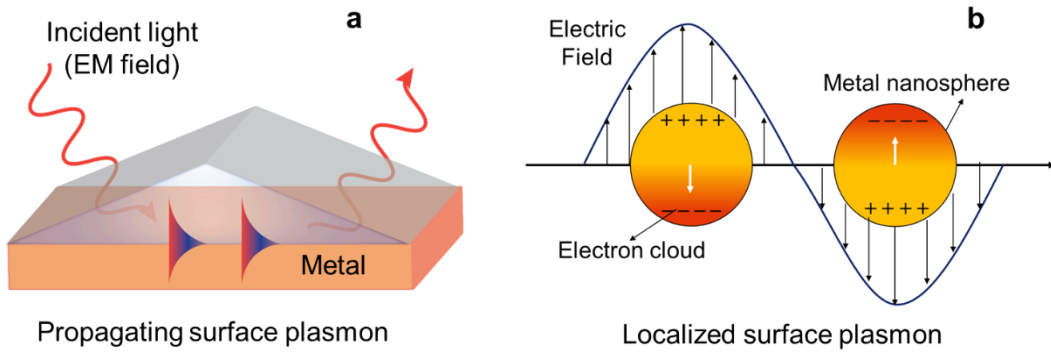


**Figure 1.7 Schematics for the two types of surface-plasmon-resonances.** (a) propagating surface plasmon polaritons along the dielectric-metal interface; (b) localized surface plasmons on the surface of a metal nanoparticles.

The surface plasmon polaritons (SPP) are the  $p$ -polarized waves. By solving the Maxwell equations, one can find the dispersion for the SPP along the surface in terms of the permittivity of the metal and of the dielectric as<sup>19</sup>

$$k_{SPP} = \frac{\omega}{c} \sqrt{\frac{\epsilon_M \epsilon_D}{\epsilon_M + \epsilon_D}} \quad (1.12)$$

where  $\epsilon_M = \epsilon_1 + i \epsilon_2$  is the dielectric permittivity of metal while  $\epsilon_D$  for dielectric medium. For SPP mode, it must satisfy  $\epsilon_M \epsilon_D < 0$  or  $\epsilon_M + \epsilon_D < 0$ . In metals, below plasma frequency,  $\omega_p$  (or above  $\lambda_p$ ), this condition can be satisfied.

The confinement of plasmon-polaritons can be achieved through various methods depending on the system and geometry involved.

One common approach is the use of metal-dielectric waveguides to support propagating surface plasmon-polaritons. Surface plasmon-polaritons (SPPs) are waves that propagate along the interface between a metal and a dielectric material. The resonance condition  $\epsilon_M +$

$\varepsilon_D \rightarrow 0$  (the Fröhlich condition), where  $\varepsilon_M$  and  $\varepsilon_D$  are the permittivities of the metal and dielectric, respectively, indicates that the real parts of the permittivities have equal magnitudes but opposite signs at the interface.<sup>19</sup> This condition allows for the strong coupling of electromagnetic waves with the collective oscillations of electrons in the metal, leading to the formation of SPPs that propagate along the metal-dielectric interface in the subwavelength dimensions.

Another way to confine plasmon-polaritons is to use nanostructures, such as metallic nanoparticles, nanowires, or nanocavities. These nanostructures can support localized surface plasmon resonances (LSPRs), which are collective oscillations of electrons confined to the surface of the nanostructure. LSPRs can trap and confine plasmon-polaritons, allowing for strong field localization and enhancement in dimensions much smaller than the wavelength of the incident light. In the case of metal nanoparticles or spheres, the Fröhlich condition is modified to  $\varepsilon_M + 2\varepsilon_D \rightarrow 0$ , which can be obtained from the Mie scattering theory.<sup>19</sup> By controlling the size, shape, and material properties of these nanostructures, the confinement and enhancement of plasmon-polaritons can be tailored.

Figure 1.8 shows the dispersion relation for a silver-vacuum interface as given by Eq. (1.12). Silver's dielectric function is described by the Drude model [see Eq. (1.11)] with the following parameters  $\varepsilon_\infty = 1.5$ ,  $\omega_p = 9.0$  eV and  $\gamma = 70$  meV.<sup>20</sup> In the figure, there are two different modes of distinct nature. Above the  $\omega_{sp} = \omega_p / \sqrt{\varepsilon_\infty + 1}$ , also called surface plasmon frequency, it is Brewster mode, which is not bounded at the interface, therefore, not a surface mode. While below the  $\omega_{sp}$ , it is propagating wave along the interface. Since the SPP lies below the light cone ( $k = \omega/c$ ), light cannot directly excite the surface modes without special phase-matching techniques. To achieve the phase-matching condition, light can be allowed to pass through a dielectric ( $k = n\omega/c$ ) and excite the surface plasmon polariton modes.



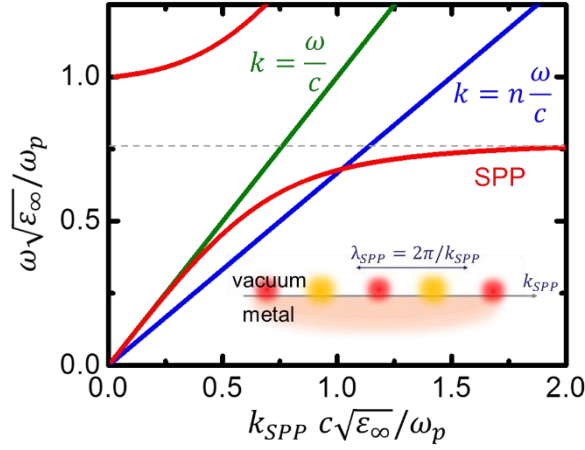


**Figure 1.8 Dispersion relation of surface plasmon-polaritons in an air-silver interface.** We represent the real and imaginary parts of the dispersion relation of surface plasmons in an air-silver interface, given by equation 1.8. We use the Drude model to describe the metal, with parameters  $\epsilon_\infty = 1.5$ ,  $\omega_p = 9.0$  eV and  $\gamma = 70$  meV.<sup>20</sup>

SPPs are the propagating evanescent wave where the propagation distance and skin depth are the important parameters for a metal. The propagation length ( $L$ ) is defined as the distance for the SPP intensity to decay by a factor of  $1/e$ .

$$L = \frac{1}{2 \operatorname{Im}(k_x)} \quad (1.13)$$

The plasmon decay length ( $\delta$ ) (or skin depth) (where the electric field falls off evanescently perpendicular to the metal surface) can be calculated as

$$\delta = \frac{2\pi}{\lambda} \sqrt{\frac{|\epsilon_1| + \epsilon_D}{|\epsilon_M|^2}} \quad (1.14)$$

These parameters are essential for nanophotonic devices. Optical losses limit both the propagation distance of SPPs and their decay length to the interface. Typically, at optical frequencies, the propagation length of SPPs is around the order of 10 micrometers and the decay length is around 25 nm – 50 nm into the metallic region. Apart from that, localized surface plasmon polariton is another way to confine light in a very small dimension can be seen in reference <sup>21</sup> in detail.

### 1.4 Phonon polariton: light & optical phonon interaction

Typically, metals exhibit a plasma frequency in the UV-visible range, but doping can extend it to the near and mid-infrared regions. However, metals and doped semiconductors are not efficient for mid-to-long infrared applications due to high optical losses. Therefore, for nanophotonic applications in the mid-to-long wavelength infrared range, the phonon polariton is employed as an alternative to the plasmon-polariton. Phonon polariton arises from the hybridization of light with lattice vibrations (or optical phonon) in polar dielectric materials like AlN, SiC, GaN, 2D van der Waals materials, etc.<sup>18,22</sup> In these materials, the polar lattice behaves collectively like a dipole, opposing incident light within a certain wavelength range, resulting in a spectral region of high reflectivity known as the Reststrahlen band, between the longitudinal optical (LO) and transverse optical (TO) phonon modes. The permittivity contributions of optical phonons (LO and TO) can be expressed as<sup>23</sup>

$$\epsilon_{PhP} = \epsilon_{\infty} \left( 1 + \frac{\omega_{LO}^2 - \omega_{TO}^2}{\omega_{TO}^2 - \omega^2 - i\omega\gamma} \right) \quad (1.15)$$

Here  $\omega_{LO}$  and  $\omega_{TO}$  are the LO and TO phonon frequencies, respectively, and  $\gamma$  is the damping of the phonons,  $\epsilon_{\infty}$  is the background permittivity due to bound charges.

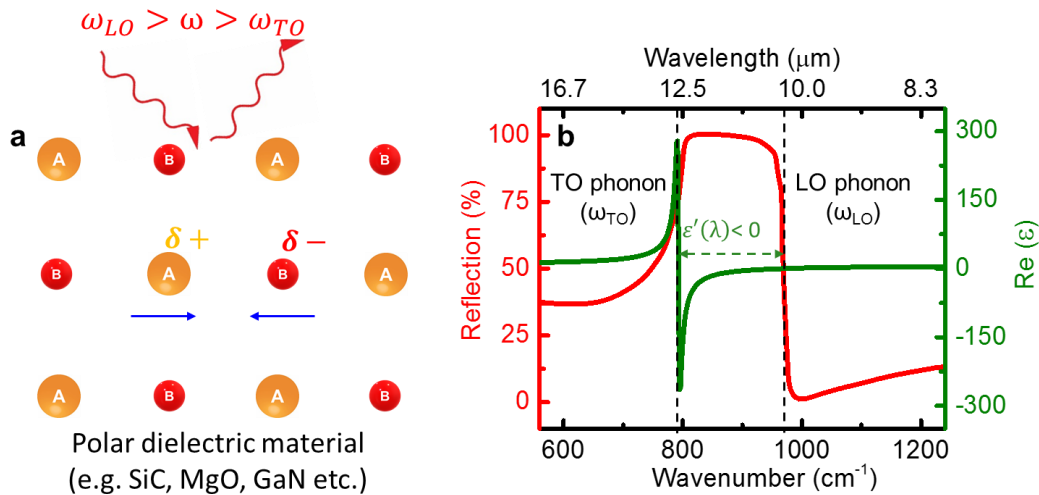


**Figure 1.9 Interaction of light with a polar dielectric.** (a) Schematics for interaction of light with ionic lattice of polar dielectric material. (b) Reflection curve of a polar dielectric material (SiC) along with its real part of the dielectric permittivity. Polar dielectric material shows high reflectivity between the longitudinal optical (LO) and transverse optical (TO) phonon frequency, which is referred to as the Reststrahlen band.

Similar to metals, where light can be confined in subwavelength dimensions by exciting the surface plasmon polaritons. Polar dielectrics can support the surface phonon polariton within the residual radiation band. In addition, polar-dielectric materials are often more efficient in the mid to long IR region because they offer several advantages over metals.

1. One advantage of using polar dielectric materials is that they have lower optical losses in the infrared compared to metals. Metals often have higher optical losses in the IR due to their intrinsic properties, which can limit the efficiency and performance of devices that rely on surface plasmon polaritons (SPPs) for applications such as sensing, imaging or energy conversion.
2. In general, optical phonons in polar dielectrics have longer lifetimes ( $\sim 1-100$  picoseconds) than free carriers in a metal ( $\sim 10$  femtoseconds). Consequently, SPhPs have a longer lifetime than SPPs. This longer lifetime of SPhPs can result in longer propagation lengths and better confinement of light, leading to improved performance in certain devices.

## 1.5 Nitride materials

Nanophotonic devices are the artificial heterostructures of metals and dielectrics or semiconductors that enable various light-matter interaction mechanisms to manipulate electromagnetic waves. To produce high quality photonic structures (low loss, defect-free, easy to tune their electronic or optical properties), epitaxial integration of metal and dielectric or semiconductor is essential. Epitaxial integration of different materials (i.e., metal, dielectric and semiconductor) from the same family is easier from a practical point of view.

The nitride family contains various classes of important materials including metals (TiN, ZrN, TaN), semiconductors (GaN, InN, ScN), dielectrics (AlN, AlScN), magnetic materials (Mn<sub>4</sub>N, GdN, EuN), etc. In addition, most of the nitrides are chemically stable, corrosion-resistant, mechanically hard, have high melting temperatures, and are refractory in nature. However, not all the metals in the periodic table form stable nitrides. In figure 1.10, the list of important metals which form stable nitride is presented along with their important properties.<sup>24</sup>

|    |    |                 |    |    |    |                   |    |    |    |               |    |    |    |    |    |    |    |    |    |
|----|----|-----------------|----|----|----|-------------------|----|----|----|---------------|----|----|----|----|----|----|----|----|----|
| H  |    |                 |    |    |    |                   |    |    |    |               |    |    |    |    |    |    | He |    |    |
| Li | Be | III-V Nitrides  |    |    |    | Refractory metals |    |    |    | Piezoelectric |    |    |    | B  | C  | N  | O  | F  | Ne |
| Na | Mg | Acceptor/ Donor |    |    |    | Layered           |    |    |    | Magnetic      |    |    |    | Al | Si | P  | S  | Cl | Ar |
| K  | Ca | Sc              | Ti | V  | Cr | Mn                | Fe | Co | Ni | Cu            | Zn | Ga | Ge | As | Se | Br | Kr |    |    |
| Rb | Sr | Y               | Zr | Nb | Mo | Tc                | Ru | Rh | Pd | Ag            | Cd | In | Sn | Sb | Te | I  | Xe |    |    |
| Cs | Ba | *               | Hf | Ta | W  | Re                | Os | Ir | Pt | Au            | Hg | Tl | Pb | Bi | Po | At | Rn |    |    |
| Fr | Ra | **              | Rf | Db | Sg | Bh                | Hs | Mt | Ds | Rg            | Cn | Nh | Fl | Mc | Lv | Ts | Og |    |    |
|    |    | *               | La | Ce | Pr | Nd                | Pm | Sm | Eu | Gd            | Tb | Dy | Ho | Er | Tm | Yb | Lu |    |    |
|    |    | **              | Ac | Th | Pa | U                 | Np | Pu | Am | Cm            | Bk | Cf | Es | Fm | Md | No | Lr |    |    |

**Figure 1.10** The elements which form stable nitrides are shown in the periodic table. Color codes indicate the physical properties or use of elements in the nitride family.

Epitaxial integration of nitride-based metal/dielectric (or semiconductor) heterostructures enables additional functionalities for various applications such as light-emitting diodes (LEDs), laser diodes (LDs), thermionic emission-based thermoelectric devices, optical anisotropic (hyperbolic) medium, solar-energy converters, and photodetectors. So, the nitride family provide a wide range of different material and give the flexibility to integrate them. Also, unintentional impurities in nitrides play an important role in their electrical and optical properties. In this thesis, we have explored the strong light-matter interaction via plasmon and phonon polariton in nitride-based metals (i.e., transition metal nitrides TiN, ZrN, HfN), semiconductors (GaN, ScN), dielectrics (AlN,  $Al_xSc_{1-x}N$ ), and their heterostructures. The detailed experimental and simulation work are discussed in later chapters.

### 1.6 Refractory nitrides for nanophotonics:

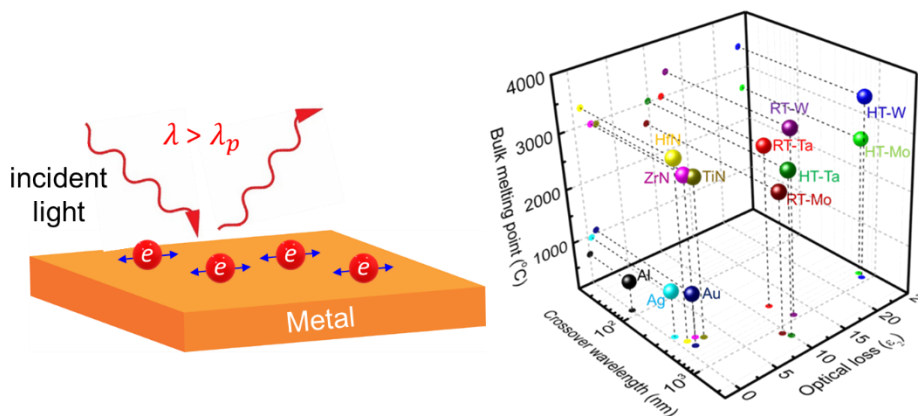
Nanophotonics is the study and manipulation of light at the nanoscale, involving the interaction of light with nanostructures such as nanoparticles, nanowires and nanoantennas. Nanophotonics has revolutionized several fields, including telecommunications, imaging, sensing and energy harvesting, by enabling novel functionalities previously unattainable with conventional optics. With the advent of polariton-based nanophotonics, the field has seen significant advances such as enhanced light-matter interactions, strong confinement of light, and the ability to tune and manipulate polariton states, leading to new opportunities in next-generation technologies. Recent research in polariton-based nanophotonics has witnessed the demonstration of strong coupling in high-Q (quality factor) resonant

nanostructures, such as microcavities and metasurfaces. These structures allow light to be confined to subwavelength volumes, leading to the generation of highly localised and enhanced fields that can be exploited for ultrasensitive sensing, nonlinear optics and quantum information processing. In addition, the ability to manipulate polariton states by external stimuli, such as electric and magnetic fields, has opened up new possibilities for the development of reconfigurable and tunable nanophotonic devices.

Many nanophotonic applications require integration with electronic components for signal processing, control, and data communication. Refractory nitrides have shown promise for compatibility with complementary metal-oxide-semiconductor (CMOS) technology, which is a widely used fabrication process for integrated circuits and semiconductor devices. CMOS compatibility refers to the ability of a material or process to be integrated into standard CMOS fabrication processes without significant modifications or adverse effects on device performance. CMOS-compatible refractory nitrides allow seamless integration of nanophotonic and electronic components on the same chip, enabling efficient interfacing and communication between photonic and electronic circuits. This can enable the development of advanced integrated photonic systems for various applications such as optical communication networks, sensing systems and quantum photonics. The combination of CMOS compatibility and desirable optical properties makes refractory nitrides promising materials for nanophotonic applications, offering the potential for integration with existing CMOS technology to enable the development of advanced photonic devices for various applications.

## Plasmon Polariton in Refractory Transition Metals (Ta, W, Mo) and Nitrides (TiN, HfN, ZrN)

Noble metals such as Ag and Au are the most popular plasmonic materials due to their low optical losses. But these metals exhibit many limitations such as complementary metal-oxide-semiconductor (CMOS) incompatibility, difficulty in fabrication and integration, softness, high cost, etc. There are other metals, such as transition metals and transition-metal-nitrides, that can provide advantages in stability, design flexibility, integration, and tunability over noble metals. The plasmonic response of the metals strongly depends on the growth conditions and crystal quality. In this chapter, we demonstrate epitaxial, highly crystalline refractory transition metals (Ta, W, and Mo) and nitrides (TiN, HfN, and ZrN), which exhibit strong plasmonic response. We have grown these metals at several growth conditions to improve and optimize their plasmonic properties. Even in one of the TiN films, the optical losses are found lower than the Au in most of the visible-to-near-IR spectral range. Materials with better crystal qualities showed a better plasmonic response.



K. C. Maurya, V. M. Shalaev, A. Boltasseva, B. Saha, *Opt. Mater. Express* 10 (2020) 2679.

K. C. Maurya, B. Biswas, D. Rao, B. Saha, *Appl. Phys. Lett.* 118 (2021) 041902.

## 2.1 Introduction

Noble metals (Au and Ag) are the excellent plasmonic material<sup>25</sup> in the visible to the near-UV spectral range due to low optical loss. But due to softness<sup>26</sup>, low melting temperature of nanostructures, and CMOS incompatibility, noble metals are not suitable for practical refractory applications.<sup>27,28</sup> Refractory transition metals (RTMs) such as Ta, W, and Mo are corrosion resistant, mechanically hard, and are actively used for a range of industrial applications such as in incandescent light bulb filaments, X-ray tubes, gas turbine, capacitors in electronic industry, and radiation shielding<sup>29</sup>. In addition, RTMs also exhibit some of the largest melting temperature in materials, Ta (3017°C), W (3422°C), and Mo (2633°C) and are stable against creep deformation at high temperatures<sup>29</sup>. Due to the metallic nature, RTMs exhibit very low electrical resistivity Ta (135 nΩ-m), W (50 nΩ-m), and Mo (53 nΩ-m) at room temperature<sup>29</sup>. Low diffusivities in silicon (Si), also make RTMs useful for Si-technology, for example, Ta has been used as a diffusion barrier in VLSI (Very Large Scale Integration) technology for preventing Cu from penetrating into Si<sup>30</sup>. Smooth patterned nanostructures of RTMs have been shown for a various photonic applications like absorber<sup>31</sup>, thermal emitter<sup>32</sup>, photonic crystal<sup>33</sup>, thermophotovoltaics<sup>15</sup> etc., albeit with not so good material and optical properties.

Traditionally the plasmonic materials that exhibit negative real component of the dielectric permittivity ( $\epsilon_1$ ) and very small imaginary component of the dielectric permittivity ( $\epsilon_2$ ) or optical losses were regarded as ideal candidates for the demonstration of interesting and exotic optical phenomena as well as for the practical device implementations<sup>19</sup>. However, in recent years, it is realized that higher  $\epsilon_2$  in plasmonic materials are essential<sup>5,6</sup> for the confinement and impedance effects<sup>34</sup> such as loss-induced heating<sup>35</sup>, plasmon-induced hot carrier<sup>7</sup>, and electro-thermo-plasmonic nanotweezer<sup>8</sup>. At the same time, epsilon-near-zero (ENZ) materials that exhibit  $\epsilon_1$  close to zero<sup>36</sup> at certain wavelength ranges are developed, which has brought many possibilities in nano-photonic devices.<sup>37-39</sup> ENZ materials with large optical losses can be useful for efficient absorbers<sup>9</sup>, hot-electron generation<sup>10</sup>, nanoparticle trapping<sup>11,12</sup>, photo-catalysis<sup>13</sup>, and solar-thermophotovoltaics<sup>14,15</sup>.

Unfortunately, there are only a handful of reports on the optical properties of RTMs<sup>40,41</sup> that do not show promising plasmonic and ENZ characteristics. Though there are some scattered reports on the epitaxial growth of RTMs (Ta<sup>42</sup>, W<sup>43</sup>, and Mo<sup>44</sup>) at high substrate

temperature, almost all the optical characterization of RTMs rely on room-temperature deposited films that are polycrystalline in nature and exhibit little-to-no plasmonic response. Therefore, with the motivation to develop RTMs as the plasmonic and ENZ materials, in this chapter, we demonstrate high-temperature deposited Ta, W, and Mo thin films that exhibit broadband ENZ behaviour accompanied with high-quality plasmonic characteristics in the visible-to-near-IR spectral range. The high substrate temperature during depositions increases adatom mobility necessary to overcome the Ehrlich–Schwoebel, surface diffusion, and grain boundary activation barriers and result in impurity free smooth films with high crystalline quality<sup>45,46</sup> that increase intrinsic carrier concentration and carrier mobility while decreasing the carrier scattering that results in optical losses.

## 2.2 Growth of refractory transition metals

RTMs (Ta, W, and Mo) thin films were deposited on (001) MgO and (0001) Al<sub>2</sub>O<sub>3</sub> substrates with reactive rf-magnetron sputtering (PVD Products Inc.) (see Appendix A for details). Two sets of samples with substrate held at (a) room temperature (30°C) denoted as RT and (b) 700°C denoted as HT were deposited. The growth parameters, such as substrate temperature, gas flow, base pressure play a significant role in determining the crystal quality of thin films during deposition. For example, at higher substrate temperatures, the atoms or molecules of the deposited material have higher kinetic energy, leading to increased diffusion on the substrate surface. This can result in improved atomic mobility and rearrangement of atoms or molecules, leading to the formation of larger and more well-ordered crystals with improved crystal quality. In our case, we have grown RTMs at high temperature at 700 °C which is the maximum capability of the instrument.

All films under investigation are ~ 100 nm thick. To ensure a fair comparison, all RTMs used in the study are sufficiently thick to prevent light transmission. The skin depth of metals in the ultraviolet (UV) to visible range is typically around 40-60 nm. In this study, all metals are 100 nm thick to ensure that light cannot pass through them and that any differences observed are not due to variations in thickness. As films deposited on MgO and Al<sub>2</sub>O<sub>3</sub> substrates show similar results, most of the results presented in this chapter are from films deposited on MgO substrates. The ambient temperature optical characterization was performed with a variable angle spectroscopic ellipsometer and the experimental ( $\psi$ ,  $\Delta$ )



spectra were fitted with a combination of the Drude-Lorentz model (see Appendix B1 supplementary data (SD) B1) for details).

### 2.3 Plasmon polariton in refractory transition metals

Results show that all RTMs films (see Fig. 2.1) exhibit plasmonic behaviour ( $\epsilon_1 < 0$ ) in the near IR spectral ranges that are accompanied with ENZ regions. Spectral position and the nature of ENZ, however, not only depend on the metals under investigation but also on the growth conditions. RT-deposited films are found to exhibit double ENZ characteristics i.e., the sign of  $\epsilon_1$  changing from negative-to-positive and vice-versa in the UV and near-IR spectral ranges, respectively. For example, in RT-Ta, the double ENZ regions are found to be at 210 nm and 1410 nm, while for RT-Mo and for RT-W, the ENZ points are located at 210 nm and 1200 nm, and at 254 nm and 880 nm respectively. Optical losses ( $\epsilon_2$ ) corresponding to such ENZ points are found to be 4.14 and 9.94 for RT-Ta, 3.17 and 9.48 for RT-Mo, and 4.79 and 12.7 for RT-W. After the ENZ region in the near-IR (when  $\epsilon_1$  changed from positive-to-negative, all three RTMs exhibit negative  $\epsilon_1$  characteristic of their plasmonic nature. RT-W is found to exhibit the largest negative  $\epsilon_1$  among the three metals primarily due to its larger carrier concentrations that were verified with its larger Drude plasma frequency ( $\omega_p$ ) (see supplementary data table B1.1). Optical losses of the RT-W, however, are larger compared to the other two films.

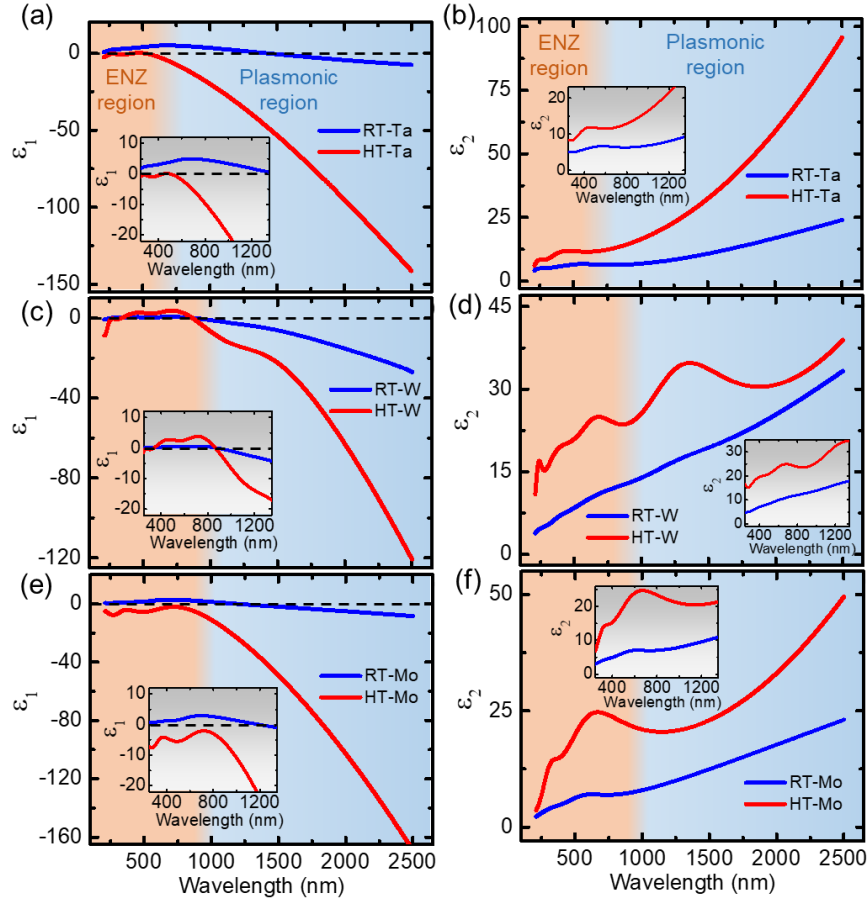


**Figure 2.1 The optical property of refractory transition metals (RTMs).** (a,c,e) The real ( $\epsilon_1$ ) and (b,d,f) imaginary ( $\epsilon_2$ ) part of the dielectric permittivity of sputter-deposited transition metals (Ta, W and Mo) thin film on MgO substrates at 25  $^{\circ}$ C (RT) and 700  $^{\circ}$ C (HT) substrate temperature. The insets show ENZ regions and double-ENZ behaviour of the films. Optical response ( $\epsilon_1$ ) of HT-RTMs films is significantly larger in comparison to RT-RTMs, consequently, optical loss ( $\epsilon_2$ ) is also large. Note: Color gradient in the figures is according to the HT-RTMs.

Compared to the RT-RTMs, high-temperature deposited metals exhibit significantly larger negative  $\epsilon_1$  in the near-IR spectral range and relatively higher optical losses ( $\epsilon_2$ ). For example, at 2500 nm, the  $\epsilon_1$  in RT-Ta was measured to be -7, while the same HT-Ta is -140 (see Fig. 2.1(a)). In addition, with their larger  $\epsilon_1$ , optical losses or  $\epsilon_2$  of the HT-RTMs films are also much higher (see Fig. 2.1(b)). Larger  $\epsilon_1$  and  $\epsilon_2$  in HT films can be explained by the Drude model in eq. 2.1 that represents the free-electron response, where

$$\epsilon = \epsilon_1 + i\epsilon_2 = 1 - \frac{\omega_p^2}{\omega^2 + i\Gamma_D\omega} \quad (2.1)$$

$$\epsilon_1 = 1 - \frac{\omega_p^2}{\omega^2 + \Gamma_D^2} \quad (2.2)$$

$$\varepsilon_2 = \frac{\omega_p^2 \Gamma_D}{\omega^3 + \Gamma_D^2 \omega} \quad (2.3)$$

Fitting of the experimental results show (see supplementary data table B1.1) that  $\omega_p$  is significantly larger in HT-RTMs compared to the RT-RTMs due to their larger number of free carriers and leads to larger  $\varepsilon_1$  and  $\varepsilon_2$ . For example, compared to a  $\omega_p$  of 3.41 eV in RT-Ta, HT-Ta exhibit about two times larger  $\omega_p$  of 6.85 eV. Similarly, the flat  $\varepsilon_1$  in HT-RTMs results from the total contribution of inter-band transitions, intra-band transitions or additional scattering losses due to defects in RTMs in the 210 nm -1200 nm spectral range that leads to large Lorentz damping constant (see supplementary data table B1.1) and does not allow a monotonic decrease in  $\varepsilon_1$  with the increase in wavelength. Flatter  $\varepsilon_1$  and its value close to zero make HT-RTMs better suited for several ENZ applications with a broader spectral operation range. For example, in HT-Ta ENZ wavelength ranged (corresponding to  $-2 < \varepsilon_1 < 2$ ) from 230 nm - 600 nm, while for HT-W ENZ wavelengths encompassed 340 nm to 865 nm spectral region. Though the ENZ regions of the HT-RTMs are broad, the corresponding optical losses are found to be large at 7.6 to 11 for HT-Ta (see Fig. 2.1(a)) and 5.9 to 12.4 for HT-W (see Fig. 2.1(c)), respectively. While such large optical losses prevent the HT-RTMs to achieve NZI, but it should be conducive for a range of confinement and impedance effects in ENZ regions.

To understand the origin of superior metallic (plasmonic) and ENZ behaviour in HT-RTMs, reflectivity measurements and detailed materials characterization with high-resolution X-ray diffraction (HRXRD) and atomic force microscopy (AFM) are performed (see Fig. 2.2 for Ta that is representative for other metals). Symmetric  $2\theta$ - $\omega$  HRXRD diffractogram of the HT-Ta showed a peak at  $38.26^\circ$  representing its (110) oriented growth on (002) MgO substrates (see fig. 2.2(a)). The full-width-at-the-half-maxima (FWHM) of the rocking curve is found  $2.4^\circ$  in the HT-Ta/MgO film that represents its nominal single crystalline nature. From the HRXRD analysis, it appears that HT-Ta crystallizes in body-centered cubic  $\alpha$ -Ta phase with a space group  $Im\bar{3}m$  (229) and a lattice constant of 3.32 Å. XRD analysis on the RT-Ta exhibit a peak at  $37.2^\circ$  that corresponds to the (111) oriented growth of  $\beta$ -Ta phase and represents a lattice constant of 3.41 Å (see supplementary data figure B1.2). Bulk Ta crystallizes in the  $\alpha$ -Ta phase, while the  $\beta$ -Ta is usually obtained in physical vapor deposited films at low temperatures. Increasing the temperature of  $\beta$ -Ta to more than  $700^\circ\text{C}$  converts it to  $\alpha$ -phase that was observed<sup>47</sup> previously. Therefore, the high-temperature

growth at 700°C in this work directly results in the  $\alpha$ -Ta phase. The XRD peak intensity is significantly larger and peak width is much smaller for HT-Ta than RT-Ta that represents its excellent crystal quality. Therefore, the superior optical properties of HT-Ta are not only due to its better crystalline quality but also due to its different crystal structure. HT-Ta exhibits  $\sim 80\%$  reflectivity in the near-IR spectral range and a sharp dip in reflection below 1000 nm representing its plasmonic characteristics. In comparison, RT-Ta exhibits much smaller reflection (40%) and a less pronounced dip that correlates well with its significantly smaller  $\epsilon_1$  (see Fig. 2.2(b)) compared to HT-Ta. Atomic force micrographs showed that HT-RTMs surfaces are much smoother, with the RMS-surface roughness 0.5 nm, while the same for RT-Ta found to be 1.6 nm (see Fig. 2.2 (c, d)).

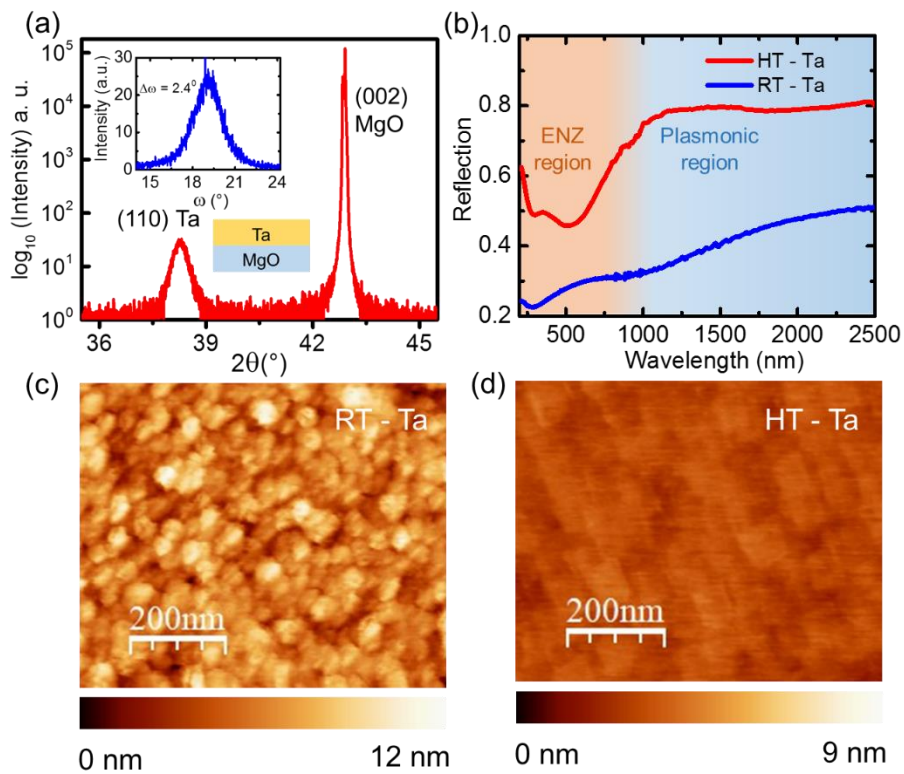


**Figure 2.2** Symmetric  $2\theta - \omega$  X-ray diffractogram of HT-Ta/MgO thin film along with its rocking curve ( $\omega$ -scan) in the inset. Ta was found to grow with (110) orientations on (002) MgO substrate. The FWHM ( $\Delta\omega$ ) of the rocking curve was found  $2.4^{\circ}$  in the HT-Ta/MgO film (b) HT-Ta film exhibits much higher reflectivity and a sharp dip close to ENZ regions compared to RT-Ta. Atomic force micrographs (AFM) of exhibit rms. surface roughness of (c) 1.6 nm in RT - Ta film and (d) 0.5 nm in HT - Ta film, respectively.

In Fig. 2.3 (a), the dielectric permittivity of sputter grown HT-RTMs (Ta, W, Mo) is shown along with noble metals (Ag and Au). Compared to the noble metals, where  $\epsilon_1$  decreased monotonically and sharply at the plasma frequency, HT-RTMs exhibit comparatively flat

$\epsilon_1$  in the UV-to-visible spectral range, and a subsequent monotonic and sharp decrease in the near-IR regions. However, compared to the Au and Ag,  $\epsilon_1$  of RTMs is smaller than is expected due to their lower carrier densities, and  $\epsilon_2$  is relatively larger. Traditionally, the plasmonic materials with negative real component of the permittivity ( $\epsilon_1$ ) and very small optical losses ( $\epsilon_2$ ) were regarded as a good plasmonic material. However, in recent years, it is realized that higher  $\epsilon_2$  in plasmonic materials are essential<sup>5,6</sup> for the confinement and impedance effects<sup>34</sup> such as loss-induced heating<sup>35</sup>, plasmon-induced hot carrier<sup>7</sup>, and electro-thermo-plasmonic nanotweezer<sup>8</sup>.

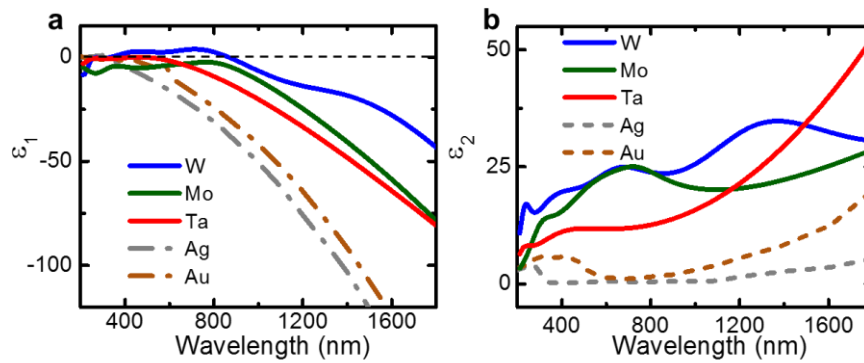


**Figure 2.3** (a) The real ( $\epsilon_1$ ) and imaginary ( $\epsilon_2$ ) component of the dielectric permittivity sputter-deposited HT-Ta, HT-W, and HT-Mo thin film are compared with the optical parameters of noble metals (such as Au<sup>25</sup> and Ag<sup>25</sup>).

The permittivity ( $\epsilon_1$  and  $\epsilon_2$ ) depends on the  $\omega_p$  and  $\Gamma_D$ . Since noble metals, Ag and Au, have a higher charge carrier density than transition metals. However, the losses in noble metals are low compared to transition metals such as tungsten or tantalum due to their low  $\Gamma_D$  (damping factor). This property is due to the fact that noble metals have a very low electron scattering rate, which means that electrons can move freely through the material without colliding with impurities or defects in the crystal lattice. As a result, the resistivity and damping factor of noble metals are very low (see table 7.1), which means that optical losses are also low. On the other hand, transition metals such as tungsten or tantalum have a higher electron scattering rate due to their more complex electronic structures, which means that the electrons in these materials are more likely to collide with impurities or defects in the crystal lattice. This results in relatively higher electrical resistance and higher optical losses due to high damping factor in these materials. However, it's important to note that the

electronic properties of metals are influenced by various factors, including crystal structure, temperature, and impurities, and can be tailored through doping, alloying, and other means. However, there is room for reducing optical losses in refractory transition metals through various strategies. One approach is to minimize the defects and impurities in the material by improving the synthesis and processing methods. For instance, using high-purity starting materials, optimizing the growth conditions, and employing post-processing techniques like annealing can reduce the defect density and improve the optical quality of the material. Another promising strategy is to tailor the electronic band structure of the material to minimize the interband transitions that cause absorption. This can be achieved by doping the material with impurities or creating heterostructures with other materials, which can modify the energy levels of the material and reduce the absorption. However, there may be fundamental reasons that limit the reduction of optical losses in refractory transition metals. The inherent electronic structure and energy levels of these materials may result in certain absorption bands that cannot be eliminated. Additionally, the presence of impurities, defects, or grain boundaries in the films can also contribute to losses and may be challenging to eliminate completely.

Sputter-deposited highly crystalline refractory transition metals (Ta, W, and Mo) show plasmonic nature in the visible-to-near-IR spectral applications. The development of refractory transition metals (Ta, W, and Mo) marked a significant step in the research on alternative plasmonic and nano-photonics materials and will be useful for efficient absorbers, hot-electron generation, photo-catalysis, local heating, nanoparticle trapping, and other solar energy conversion devices.

## **2.4 Plasmon polariton in refractory transition metal nitrides**

In the previous section, we saw the plasmonic property of transition metals (Ta, Mo, and W), which have a relatively high optical loss. But for many applications such as optical nano-circuits<sup>48</sup>, photon tunneling<sup>49,50</sup>, super-coupling<sup>51</sup>, extreme nonlinear interactions<sup>52</sup>, and ultrafast switching<sup>53</sup>, plasmonic materials with low optical loss are required. Transition metal nitrides such as titanium nitride (TiN), hafnium nitride (HfN), and zirconium nitride (ZrN) are excellent plasmonic materials for visible spectral range and their optical properties are very close to Au and Ag.<sup>54-58</sup> We have deposited these metals at various

conditions and various growth techniques, such as magnetron-sputtering and molecular-beam-epitaxy (MBE), to improve the plasmonic properties.<sup>59,60</sup> Since these nitrides have similar plasmonic properties, so only TiN properties are discussed further. TiN is hard (hardness of  $\sim 30$  GPa), chemically stable, and exhibits a very high melting temperature of  $2930^\circ\text{C}$  which makes it suitable for refractory plasmonic material.<sup>61,62</sup> In addition, due to its ceramic nature, TiN exhibits low surface energies of  $24\text{-}39\text{ mJ/m}^2$ <sup>63</sup> which is much smaller than the surface energies of noble metals ( $\sim 1\text{-}2\text{ J/m}^2$ )<sup>64</sup>. Such lower surface energies allow for uniform TiN ultra-thin film depositions with smooth surfaces. Also, TiN is CMOS compatible and already has been used as a buffer layer in the integrated circuit (IC) fabrication process.

In this section, the plasmonic property of epitaxial single-crystalline TiN thin films grown with ultra-high vacuum (UHV) plasma-assisted MBE is discussed. In Fig. 2.4, the dielectric permittivity of MBE grown TiN film deposited on MgO and  $\text{Al}_2\text{O}_3$  substrates exhibits a crossover wavelength (transition from positive-to-negative  $\epsilon_1$  representative of the metallic nature) near  $470\text{ nm}$ . The optical properties depend on the growth parameters, growth conditions, and substrate as well. Films deposited on MgO substrate have higher  $\epsilon_1$  (magnitude) compared to the films deposited on  $\text{Al}_2\text{O}_3$  substrate due to the higher carrier concentrations of TiN on MgO substrate. Optical loss ( $\epsilon_2$ ) of the films was also found to increase with an increase in the wavelength (see Fig. 2.4(b)) due to intraband transitions. The  $\epsilon_2$  of TiN/ $\text{Al}_2\text{O}_3$  exhibited significantly smaller losses compared to the TiN/MgO due to the smaller Drude damping constants in TiN films deposited on (0001)  $\text{Al}_2\text{O}_3$  substrates compared to the ones deposited on (111) MgO substrates. Better crystal quality leads to smaller damping constant in TiN/ $\text{Al}_2\text{O}_3$ , the lower FWHM of the rocking curve in HRXRD is the evidence (see Fig. 2.5). The optical loss in TiN in most parts of the visible ( $300\text{ nm} - 580\text{ nm}$ ) and near-IR spectral ranges ( $1000\text{ nm} - 2000\text{ nm}$ ) is lower than Au.

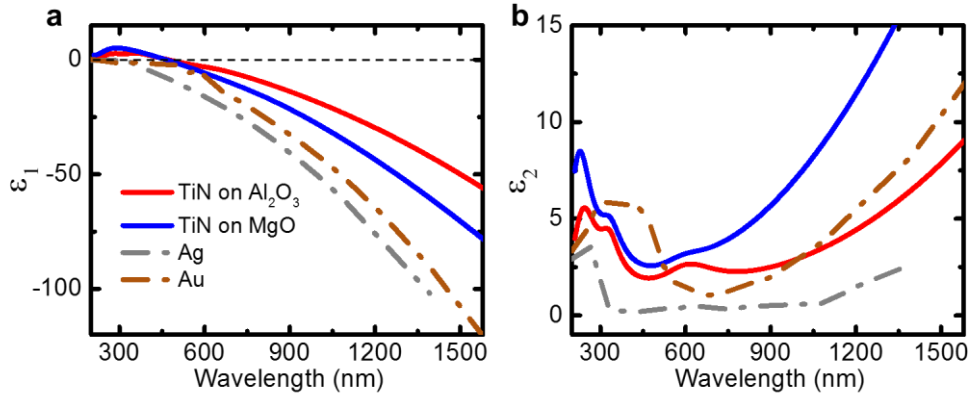


**Figure 2.4** (a) The real ( $\epsilon_1$ ) and (b) imaginary ( $\epsilon_2$ ) part of the dielectric permittivity of TiN thin film on MgO and Al<sub>2</sub>O<sub>3</sub> substrates are presented.

HRXRD spectra of TiN films are shown in figure 2.5, MBE deposited TiN thin films grow with 002 orientations on the (001) MgO substrates (TiN/MgO) and with 111 orientations on the (0001) Al<sub>2</sub>O<sub>3</sub> substrates (TiN/Al<sub>2</sub>O<sub>3</sub>) respectively. The FWHM of the rocking curve was found 0.19° for TiN/MgO and 0.03° for TiN/Al<sub>2</sub>O<sub>3</sub> sample. That indicates that TiN/Al<sub>2</sub>O<sub>3</sub> has superior crystal quality than TiN/MgO. The lattice parameter (*c*-axis) was found 4.25 Å and 4.24 Å for TiN/MgO and TiN/Al<sub>2</sub>O<sub>3</sub>, respectively. Plan-view atomic force microscopy (AFM) image of TiN/MgO film exhibits (see Fig. 2.5 (c)) square-shaped densely packed features with an average feature size of ~ 60 nm. While TiN/Al<sub>2</sub>O<sub>3</sub> film showed pyramidal features with an average pyramid size of ~ 20 nm. The surface RMS-roughness was 1.2 nm and 3.8 nm for TiN/MgO film and TiN/Al<sub>2</sub>O<sub>3</sub> film, respectively.



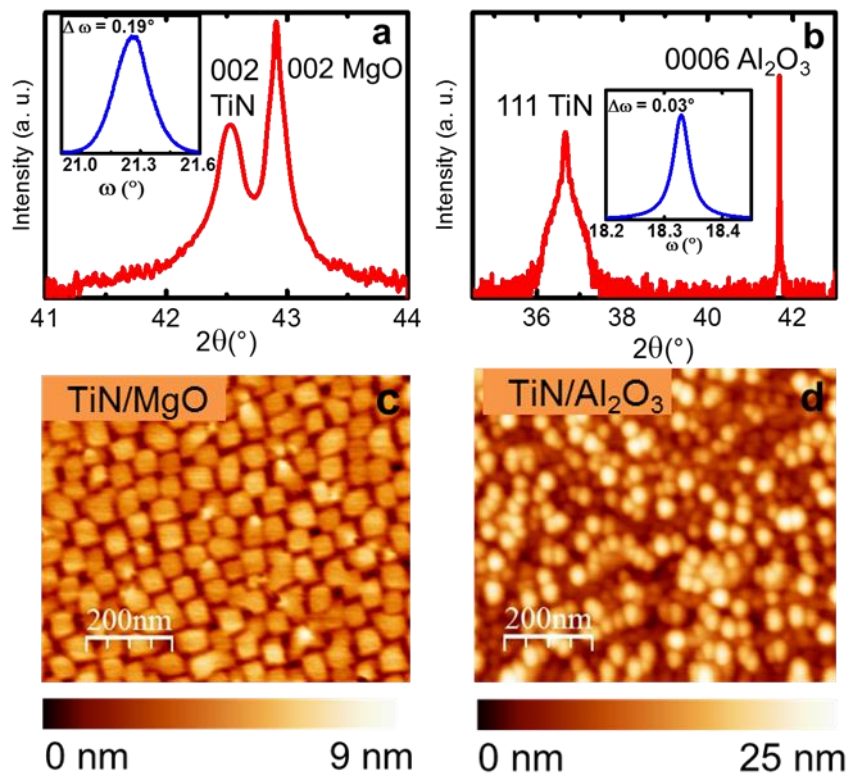


**Figure 2.5** XRD spectra of TiN/MgO (a) and TiN/Al<sub>2</sub>O<sub>3</sub> (b) thin films along with their rocking curve ( $\omega$ -scan) in the insets. Atomic force micrographs of TiN/MgO (c) and TiN/Al<sub>2</sub>O<sub>3</sub> (d).

Reflection (R) and transmission (T), as a function of the angle of incidence, are shown in figure 2.6. TiN showed a clear and distinct peak at  $\sim 430$  nm near its crossover wavelength (where  $\epsilon_1$  turn positive-to-negative). TiN is highly reflective in most of the visible to near-IR spectral range.

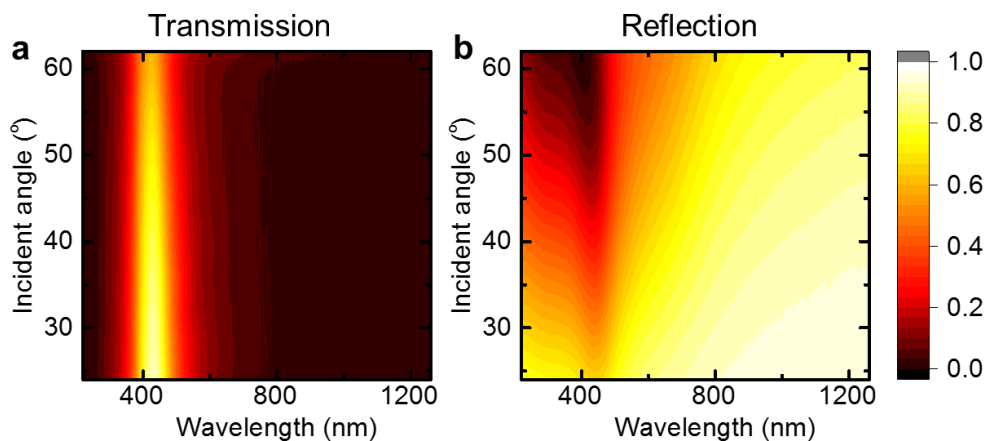


**Figure 2.6** (a) Transmission and (b) reflection spectra of TiN/Al<sub>2</sub>O<sub>3</sub> are presented as a function of wavelength and the angle of incidence.

## 2.5 Surface plasmon polariton in metals

Further, the surface-plasmon-polariton (SPP) propagation length ( $L$ ) at metal-air interfaces and plasmon-decay length ( $\delta$ ) in the metal (or penetration depth) were also calculated from the experimental dielectric permittivity. Results show that SPP propagation length is about 10-100  $\mu\text{m}$  for RTMs (W, Ta and Mo) and nitrides (TiN and ZrN). The plasmon decay length in RTMs is around 30 nm - 40 nm in the NIR region that is similar to TiN and ZrN, while at the visible regime.

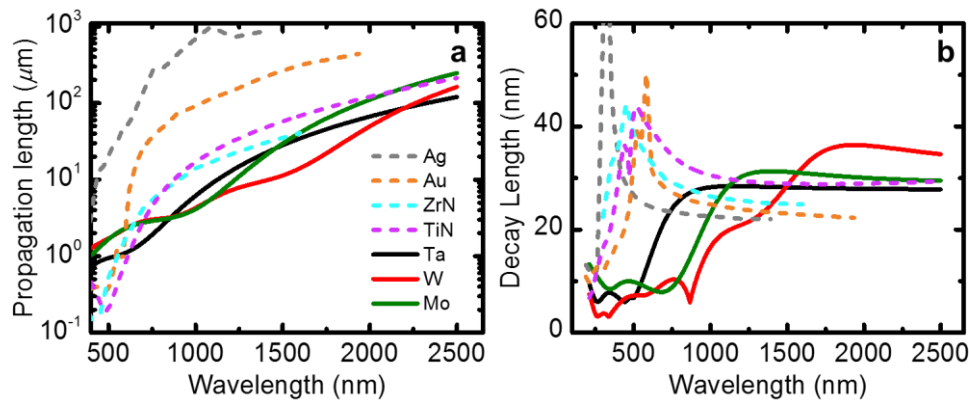


**Figure 2.7 Surface plasmon polariton in metals.** (a) SPP propagation length ( $L$ ) and (b) plasmon decay length ( $\delta$ ) in transition metal (Ta, W and Mo) and transition metal nitrides (such as TiN and ZrN) are compared with noble metals (such as Au<sup>25</sup> and Ag<sup>25</sup>).

## 2.6 Conclusion

Figure 2.8 summarizes the plasmonic property of transition metals (W, Ta, and Mo), transition metal nitrides (TiN, ZrN, and HfN), and noble metals (Ag, Au, and Al). Optical loss at their crossover wavelength is compared. The optical property strongly depends on the growth parameters. For example, RTMs grown at room temperature (RT-RTMs) exhibit lower optical loss but their optical response (real part of permittivity or  $\epsilon_1$ ) is not very strong. While RTMs grown at high temperature (700  $^{\circ}\text{C}$ ) (HT-RTMs) have strong optical response (large negative  $\epsilon_1$ ) and their optical loss is also high. So, there is a trade-off between  $\epsilon_1$  and  $\epsilon_2$  that can be easily controlled by the growth condition according to the required application.

Also, epitaxial single-crystalline TiN thin films are deposited with ultra-high vacuum plasma-assisted molecular beam epitaxy (UHV-PEMBE) that exhibit reduced optical

losses compared to the previously reported MBE and sputter-deposited TiN thin films. The lower optical loss in TiN/Al<sub>2</sub>O<sub>3</sub> compared to Au in most of the visible-to-near-IR spectral range would enable low-loss SPP propagation in improved plasmonic devices. The development of MBE-deposited TiN thin film with reduced optical losses could enable its integration with III-V semiconductors such as GaN, InN, etc. and leads to TiN-based photonic/plasmonic on-chip devices, broad-band light absorbers and emitters for solar-thermophotovoltaics, and hot-carrier-assisted devices with improved efficiencies.

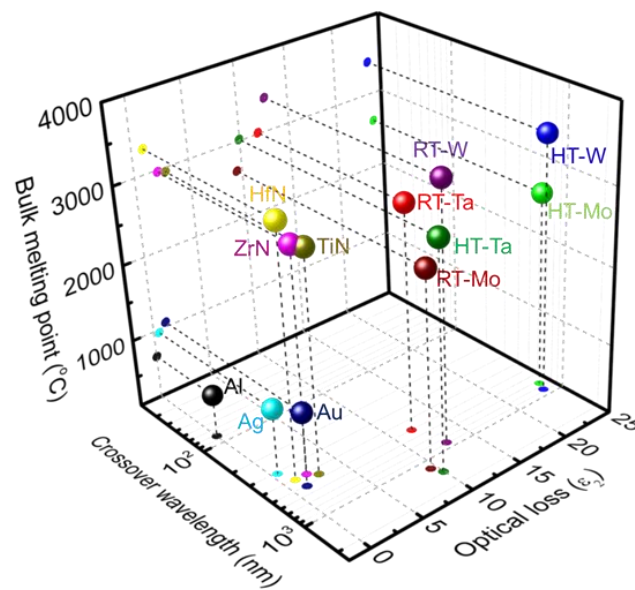
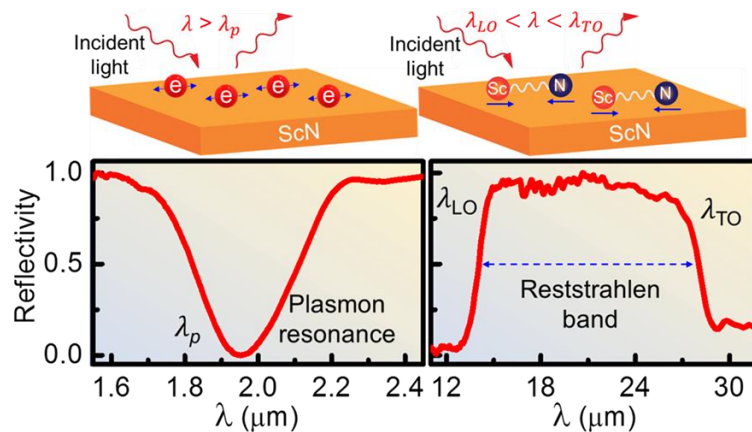


**Figure 2.8** Comparison of metals with their optical loss at crossover wavelength (where  $\epsilon_1$  turn positive-to-negative) and their bulk melting point.

## Infrared Plasmon and Phonon-Polaritons in Polar Semiconducting Scandium Nitride (ScN)

Traditionally doped-semiconductors and conducting metal oxides (CMO) are used to achieve plasmon-polaritons in the near-to-mid infrared (IR), while polar dielectrics are utilized for realizing phonon-polaritons in the long-wavelength IR (LWIR) spectral regions. However, demonstrating low-loss plasmon- and phonon-polaritons in one host material will make it attractive for practical applications. In this chapter, we demonstrate high-quality tunable short-wavelength IR (SWIR) plasmon-polariton and LWIR phonon-polariton in complementary metal-oxide-semiconductor compatible group III-V polar semiconducting scandium nitride (ScN) thin films. We achieve both resonances by utilizing n-type (oxygen) and p-type (magnesium) doping in ScN that allows modulation of carrier concentration from  $5 \times 10^{18}$  to  $1.6 \times 10^{21} \text{ cm}^{-3}$ . Our work enables infrared nanophotonics with an epitaxial group-III semiconducting nitride, opening the possibility for practical applications.



K. C. Maurya, D. Rao, S. Acharya, P. Rao, A. I. K. Pillai, S. K. Selvaraja, M. Garbrecht and B. Saha.

*Nano Letters*, 22, 13, 5182-5190 (2022).

### 3.1 Introduction

Polaritons, the hybrid quasiparticles of photons and electric dipoles<sup>65-67</sup> (collective free electron oscillations, optical lattice vibrations or excitons) have attracted significant interest for numerous infrared nano-photonic applications<sup>2</sup> including nano-laser<sup>68,69</sup>, non-linear optics<sup>52,70,71</sup>, heat-harvesting<sup>72-74</sup>, etc. Due to their sub-diffraction mode confinement and field enhancement, plasmon- and phonon-polaritons are also researched extensively for overcoming the fundamental resistance-capacitance (RC) delay in electronics and the diffraction limit in photonic devices<sup>75,76</sup>. However, applications of polaritons in practical devices so far are limited primarily due to the significant optical losses arising from the scattering of the free electrons and optical phonon modes. Therefore, materials exhibiting low-loss and high-quality plasmon-polariton in the near-to-mid IR and phonon-polaritons in the LWIR are in great demand<sup>77</sup>. Practical applications also require that such materials should exhibit structural and high-temperature stability, CMOS compatibility, ease-of-fabrication, ease-of-integration with existing optoelectronic devices, and abundance.

Achieving plasmon resonance in the IR region of the electromagnetic spectrum requires materials to exhibit carrier concentration in the  $10^{19}$ - $10^{21}$   $\text{cm}^{-3}$  range with high carrier mobilities. Further, to accomplish low-losses, such materials should not exhibit interband/intraband transitions in the wavelength range of interest and should comprise a low defect density. As a result, heavily doped semiconductors such as *n*-type InAs<sup>78</sup>, *n*-type and *p*-type Si<sup>79</sup>, conducting metal oxides (CMOs)<sup>80</sup> such as indium tin oxide (ITO), aluminum-doped zinc oxide (AZO), gallium-doped zinc (GZO) oxide, cadmium oxide (CdO)<sup>81,82</sup>, patterned graphene structures<sup>83,84</sup>, and semiconductor meta-surfaces<sup>85</sup> are used as plasmonic materials in the near (0.8-1.4  $\mu\text{m}$ ) and mid (3-15  $\mu\text{m}$ )-IR spectral ranges. However, achieving low-loss high-quality plasmon resonance in the SWIR (1.4-3  $\mu\text{m}$ ) spectral region with high-mobility materials has been challenging. SWIR is an important spectral window for long-distance telecommunication (1.260-1.675  $\mu\text{m}$ ), hyperspectral imaging, solar cell, electronic board and produce inspection, anti-counterfeiting, surveillance, and a host of other applications<sup>18,76</sup>.

Achieving phonon-polaritons, on the other hand, requires polar dielectric materials, where macroscopic electric field stiffens the force constant of the longitudinal-optical (LO) phonons and splits the LO and transverse-optical (TO) phonon modes at the zone center<sup>23</sup>.

Within the frequency range bounded by the LO and TO, termed as the *Reststrahlen* band<sup>86</sup>, the real component of the dielectric permittivity ( $\epsilon_1$ ) becomes negative, and electromagnetic modes couple to the TO phonon giving rise to its evanescent character and confinement at the surface. Such confined surface-phonon-polariton (SPhP) has emerged as a promising light-matter coupling mechanism in the LWIR range and several other applications such as passive radiative cooling, bio-molecular fingerprinting, diagnosis tools for cancer and dentistry detection are proposed<sup>18,87</sup>. So far, excitation and engineering of SPhP are performed with well-established dielectric materials such as 4H-SiC<sup>88</sup>, h-BN<sup>89,90</sup>, or AlN<sup>91</sup> with large bandgap and low carrier densities. Active tuning of the SPhP mode frequency is also demonstrated with carrier injection in polar dielectrics such as in InP, 4H-SiC, etc.<sup>92,93</sup>

Demonstration of low-loss and high-quality plasmon- and phonon-polaritons in one host material will make it attractive for practical device implementations. Conceptually, achieving plasmon and phonon-polariton in one host material is possible if the electronic and phonon resonances are spectrally separated from each other (see Eq. 3.1 for the total dielectric permittivity), and the carrier concentration can be tuned from as low as  $10^{18}$  to  $10^{21}$   $\text{cm}^{-3}$  while retaining a moderately high mobility at the same time. To achieve this, dopants should not introduce defect states inside the bandgap of semiconductors that otherwise could pin the Fermi level. Additionally, dopant states should not alter the valence and/or conduction band edges, which could drastically change carrier effective mass and mobility. Satisfying all of the conditions could be quite challenging for many well-established semiconductors.

$$\epsilon_{total}(\omega) = \epsilon_1 + i\epsilon_2 = \epsilon_\infty \left( 1 - \frac{\omega_p^2}{\omega^2 + i\gamma\omega} + \frac{\omega_{LO}^2 - \omega_{TO}^2}{\omega_{TO}^2 - \omega^2 - i\omega\Gamma} \right) \quad (3.1)$$

$$\omega_p = \sqrt{\frac{ne^2}{m^*\epsilon_0}} \quad (3.2)$$

$$\epsilon_{plasmon}(\omega) = -\frac{\omega_p^2}{\omega^2 + i\gamma\omega} \quad (3.3)$$

Where,  $\epsilon_{total}(\omega)$  is the total dielectric permittivity<sup>18</sup> with contributions from the plasmon or Drude component (second term) and phonon (third term) resonances.  $\epsilon_\infty$ ,  $\omega_p$ ,

$\omega_{LO}$ ,  $\omega_{TO}$ ,  $\gamma$ ,  $\Gamma$ ,  $n$  and  $m^*$  are the high-frequency dielectric constant, plasma frequency, longitudinal optical and transverse optical phonon frequencies, plasmon and phonon damping constants, carrier concentration and effective mass respectively. As permittivity is a complex quantity, the real component ( $\epsilon_1$ ) signifies the strength of the polarization response, while the imaginary component ( $\epsilon_2$ ) describes the optical loss due to the interband and intraband transitions.

In this work, we demonstrate that *n*-type (oxygen) and *p*-type (magnesium)-doping in epitaxial ScN thin films lead to its tunable carrier concentration from  $5 \times 10^{18}$  to  $1.6 \times 10^{21}$   $\text{cm}^{-3}$  range, while retaining a moderately high mobility that gives rise to tunable high-quality low-loss SWIR plasmon- and LWIR high-quality phonon-polariton resonance.

### 3.2 Growth of scandium nitride (ScN) film

ScN is a rocksalt group-III (B) semiconducting transition-metal-nitride (TMN) and exhibits corrosion-resistant high hardness, high melting temperature ( $\sim 2600^\circ\text{C}$ ) and is stable at ambient temperature and pressure.<sup>94-98</sup> Due to the degenerate semiconducting nature with a direct bandgap of 2.2 eV and indirect gap of 0.9 eV<sup>99-101</sup>, ScN has attracted significant interest in recent years for thermoelectric energy conversion.<sup>102</sup> Lattice-matched (111) ScN seed-layers are also utilized to reduce the dislocation densities in (0002) GaN epilayers for light-emitting diodes<sup>103,104</sup>. As-deposited ScN thin films exhibit an *n*-type carrier concentration of  $(2-4) \times 10^{20}$   $\text{cm}^{-3}$  primarily due to the presence of oxygen impurities and exhibit a mobility in the 60-90  $\text{cm}^2/\text{Vs}$  range. Due to such high carrier concentrations, Fermi level in ScN resides inside the conduction band, about 0.2-0.3 eV inside the conduction band minima<sup>99</sup>. Recently, Mg-hole doping is used to reduce the high carrier concentration and *p*-type ScN is achieved with high mobility ( $\sim 25$   $\text{cm}^2/\text{Vs}$ )<sup>105</sup>. Photoemission measurement and first-principles calculation have demonstrated that both the oxygen and magnesium-doping in ScN do not introduce defect states within its bandgap, and they do not alter the valence and conduction band edges<sup>106</sup>. Due to such a rigid electronic band, the Fermi level moves freely from the conduction band to the valence band, giving rise to very high electron and hole-concentrations and large thermoelectric power factors<sup>102</sup>. Moreover, since optical phonons in ScN exhibit a maximum energy of  $\sim 84$   $\text{meV}$ <sup>107</sup>, plasmon-resonances in the SWIR region are well-separated from the phonon-polariton resonance. Therefore, high-mobility and tunable carrier concentration in ScN

provide a perfect testbed to achieve high-quality plasmon- and phonon-polariton in one host medium.

ScN thin films with carrier concentration ranging from  $1.6 \times 10^{21} \text{ cm}^{-3}$  to  $5 \times 10^{18} \text{ cm}^{-3}$  (see Table 3.1) are deposited inside an ultra-high vacuum (UHV) chamber at a base pressure of  $(2-4) \times 10^{-9}$  Torr (see Supplementary data (SD) section B2.1). Without any intentional doping, *n*-type ScN films exhibit a carrier concentration of  $3.6 \times 10^{20} \text{ cm}^{-3}$  with a mobility of  $43 \text{ cm}^2/\text{Vs}$ . Intentional oxygen-doping increase its *n*-type carrier concentration up to  $1.6 \times 10^{21} \text{ cm}^{-3}$ , while Mg-hole doping results in *p*-type films with carrier concentration as low as  $5 \times 10^{18} \text{ cm}^{-3}$ . Though the intentional doping reduces the mobility slightly, it remains sufficiently high (see Table 3.1) for achieving low-loss resonances. With increasing *n*-type doping concentration, the Fermi level in ScN moves higher up inside the conduction band ( $\sim 0.4 \text{ eV}$  from conduction band minima for the *n*-type doping concentration of  $1.6 \times 10^{21} \text{ cm}^{-3}$ ).<sup>101,108</sup> Similarly, hole-doping shifts the Fermi level close to the valence band. A detailed discussion about the band structure, electron and hole effective mass, average carrier scattering time and position of the Fermi level as a function of doping type and concentration are presented in the Appendix B section 2.

Table 3.1. Carrier concentration, mobility, and resistivity of ScN thin films are presented. The wavelength ( $\lambda_p$ ) corresponding to the plasmon- and phonon-polariton resonance frequency are listed.

| ScN films                               | Carrier concentration ( $\text{cm}^{-3}$ ) | Mobility ( $\text{cm}^2\text{V}^{-1}\text{s}^{-1}$ ) | Resistivity ( $\Omega\text{-cm}$ ) | Cross-over Wavelength $\lambda_p$ ( $\mu\text{m}$ ) | Carrier and doping type          |
|---|--|--|------------------------------------|---|----------------------------------|
| <b>SWIR Plasmon-polariton Resonance</b> |  |  |                                    |   |                                  |
| (a)                                     | $1.6 \times 10^{21}$                       | 29   | $1.4 \times 10^{-4}$               | 1.83  | <i>n</i> -type<br>(oxygen-doped) |
| (b)                                     | $1.4 \times 10^{21}$                       | 6  | $7.6 \times 10^{-4}$               | 2.08  |                                  |
| (c)                                     | $7.7 \times 10^{20}$                       | 22   | $3.8 \times 10^{-4}$               | 2.25  |                                  |



|                                 |                      |    |                      |                          |   |
|---------------------------------|----------------------|----|----------------------|--------------------------|---|
| (d)                             | $3.3 \times 10^{20}$ | 43 | $4.4 \times 10^{-4}$ | 2.35                     | <i>n</i> -type<br>(unintentionally<br>oxygen-doped) |
| LWIR Phonon-polariton Resonance |                      |    |                      |                          |   |
| (e)                             | $4.3 \times 10^{19}$ | 13 | $1.0 \times 10^{-2}$ | 14.58 (LO)<br>27.80 (TO) | <i>p</i> -type<br>(magnesium-<br>doped)             |
| (f)                             | $5.0 \times 10^{18}$ | 10 | $1.3 \times 10^{-1}$ | 14.58 (LO)<br>27.80 (TO) |   |

### 3.3 Plasmon polariton in ScN

The  $\epsilon_1$  of ScN (measured with a spectroscopic ellipsometer, see Fig. 3.1a, and Appendix B2 for detail) with the highest carrier concentration of  $1.6 \times 10^{21} \text{ cm}^{-3}$  exhibits epsilon near zero (ENZ) (a positive-to-negative cross-over) at  $1.83 \mu\text{m}$  (see Fig. 3.1b). At longer wavelengths,  $|\epsilon_1|$  increases monotonically due to the increasing metallic response. The optical loss, characterized by the imaginary component of the dielectric permittivity ( $\epsilon_2$ ) at  $\lambda_p$  is 1.2, which is smaller than the  $\epsilon_2$  of visible wavelength plasmonic materials such as Au<sup>25</sup>, TiN<sup>57</sup> etc. at their respective  $\lambda_p$ . Below  $1.83 \mu\text{m}$ , ScN acts as a dielectric medium with positive  $\epsilon_1$  and a peak in  $\epsilon_2$  near  $\sim 430 \text{ nm}$  (see Appendix B, SD Fig. B2.5) corresponds to the direct bandgap interband transition. Polarization-dependent reflectivity measurements (see Fig. 3.1b) show a clear dip near  $\lambda_p$  representative of the plasmonic nature. Angle-dependent reflectivity measurements (see Fig. 3.1c) clearly show the Brewster's angle in the *p*-polarized/*s*-polarized reflection curve. The calculated reflectance spectrum (see Fig. 3.1d) utilizing the permittivity of ScN in the Fresnel's equation matches well with the measured reflectivity which highlights consistency between the experiment and ellipsometry data fitting.

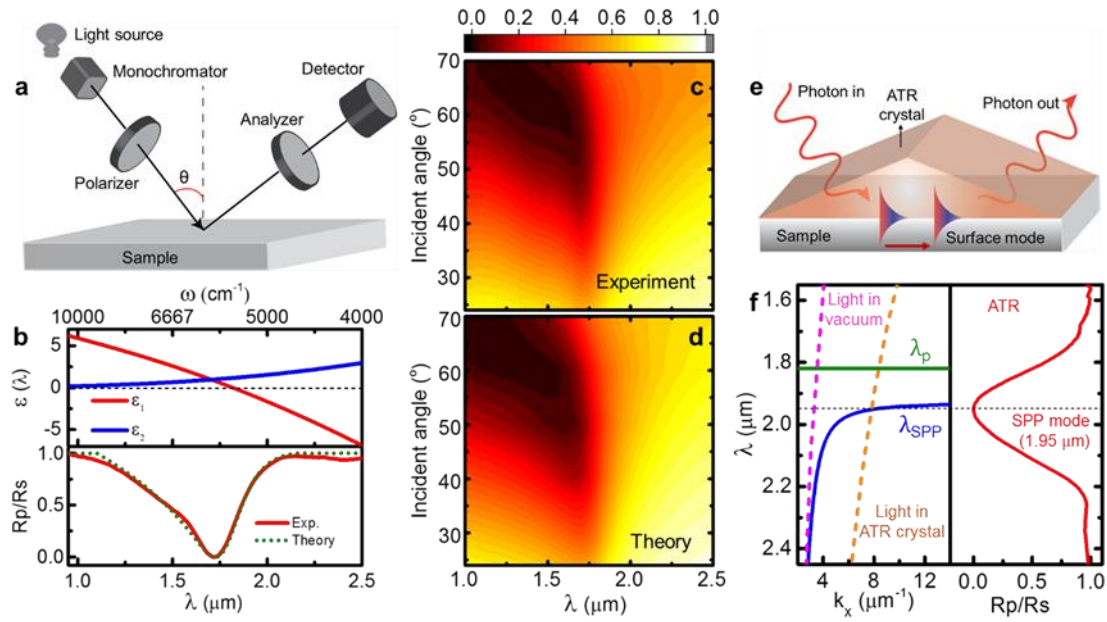


**Figure 3.1 Plasmon-polariton in ScN.** (a) Schematic diagram of a spectroscopic ellipsometer. (b) The real ( $\epsilon_1$ ) and imaginary ( $\epsilon_2$ ) component of the dielectric permittivity of ScN film with the highest carrier concentration of  $1.6 \times 10^{21} \text{ cm}^{-3}$  is presented. ScN becomes plasmonic after  $1.83 \mu\text{m}$ . ( $\epsilon_1 < 0$ ) with the optical loss of 1.2 at the wavelength ( $\lambda_p$ ) corresponding to its plasma frequency. Experimentally measured normalized reflectivity of ScN film is plotted as the ratio between the  $p$ -polarized to  $s$ -polarized light intensity which shows a dip near the  $\lambda_p$ . (c) Angle-dependent reflectivity curve of ScN film is presented. Brewster's angle is visible in the reflectivity curve. (d) Fresnel's equation-based theoretically calculated reflection curve matches well with the experimentally measured reflection curve. (e) A schematic diagram of the ATR configuration for surface mode excitation. (f) Theoretically calculated SPP dispersion (blue) along with the ATR-measured reflection curve that shows SPP mode excitation at  $1.95 \mu\text{m}$ . The light lines in the vacuum and in ATR crystal are shown by the magenta and orange dotted curves respectively. The bulk plasma wavelength ( $\lambda_p$ ) is shown with the green line.

Excitation of the surface plasmon-polaritons (SPP) is demonstrated (see Fig. 3.1e) with polarization-dependent reflectivity measurement in the attenuated-total-reflection (ATR) configuration inside an FTIR-spectrometer in the Kretschmann configuration at  $45^\circ$  angle-of-incidence. Diamond is used as a high refractive index medium and to provide the additional momentum for the light coupling to the SPP modes. A clear dip in the  $p$ -/ $s$ -polarized reflection spectrum at  $\sim 1.95 \mu\text{m}$  (see Fig. 3.1f) with a full-width-at-the-half-maxima (FWHM) of  $\sim 0.27 \mu\text{m}$  demonstrate the coupling of energy from the incident radiation to the SPP mode. The SPP dispersion<sup>19</sup> is calculated (see Fig. 3.1f) taking into account the measured dielectric permittivity of ScN that show close matching of the  $\lambda_{SPP}$

(wavelength corresponding to the SPP mode frequency) with the experimentally measured dip in reflectivity curve.

While the above analysis unambiguously demonstrates SWIR plasmon excitation in ScN, spectral position of the plasmon-resonance and the SPP mode frequencies are varied by altering the carrier concentration (see Eq. 3.2) through doping control. With a decrease in the carrier concentration from  $1.6 \times 10^{21} \text{ cm}^{-3}$  (a) to  $1.4 \times 10^{21} \text{ cm}^{-3}$  (b),  $7.7 \times 10^{20} \text{ cm}^{-3}$  (c) and  $3.3 \times 10^{20} \text{ cm}^{-3}$  (d), ellipsometry measurements show that the  $\lambda_p$  shifts from 1.83  $\mu\text{m}$  to 2.08  $\mu\text{m}$ , 2.25  $\mu\text{m}$  and 2.35  $\mu\text{m}$ , respectively (see Fig. 3.2a). Such monotonic red-shift in the  $\lambda_p$  is consistent with the predictions from the Drude model (see Eq. 3.3) of dielectric permittivity, and cover a wide SWIR range. In the Fig. 3.2b,  $\epsilon_2$  of ScN with  $3.3 \times 10^{20} \text{ cm}^{-3}$  carrier densities show the lowest value, primarily due to its higher mobility of 43  $\text{cm}^2/\text{Vs}$ . Since the highest mobility and the lowest optical loss is obtained in the as-deposited ScN without any intentional doping,  $\lambda_p$  of 2.35  $\mu\text{m}$  with the lowest optical loss of 1.0 could be regarded as the baseline plasmon response in ScN. Dielectric permittivity at the longer wavelength regions (1.5- 5  $\mu\text{m}$ ) is measured further with an IR-ellipsometer (Appendix B supplementary data Fig. B2.3) which demonstrates ScN's metallic response in the SWIR-to-mid-IR spectral region. Similar to the tunable bulk plasmon frequency, tunability of the SPP mode frequencies are further demonstrated by the polarization-dependent ATR measurements, which show a dip at 2.70  $\mu\text{m}$  with a FWHM of 0.56  $\mu\text{m}$  for ScN with  $3.3 \times 10^{20} \text{ cm}^{-3}$  (d) carrier concentrations (see Fig. 3.2c).

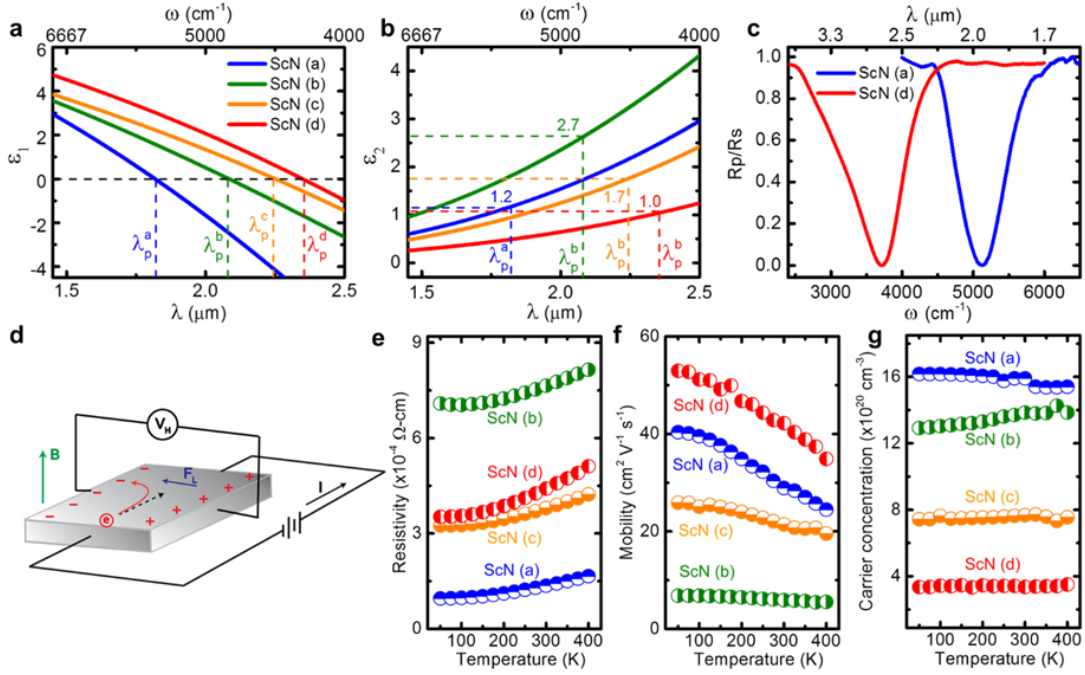


**Figure 3.2 Tunable SWIR plasmon response and electrical properties of ScN.** (a)  $\epsilon_1$  and (b)  $\epsilon_2$  of ScN films with varying carrier concentrations are presented. With the decrease in carrier concentration,  $\lambda_p$  shifts to longer wavelengths.  $\lambda_p$  of 2.35  $\mu\text{m}$  and corresponding  $\epsilon_2$  of 1.0 is obtained for as-deposited ScN film without any intentional doping which makes it a high-quality and low-loss SWIR plasmonic material. (c) Normalized reflectivity curves of ScN with  $1.6 \times 10^{21} \text{ cm}^{-3}$  (a) and  $3.3 \times 10^{20} \text{ cm}^{-3}$  (d) are presented as the ratio between  $p$ -polarized and  $s$ -polarized intensity ( $R_p/R_s$ ) obtained from the ATR measurements (d) Schematic diagram of the Hall measurement is shown. Temperature-dependent (e) resistivity; (f) mobility and (g) carrier concentration of ScN films are shown which highlights its degenerate semiconducting nature.

The plasmonic response is further characterized by temperature-dependent Hall measurements (see Fig. 3.2d). The resistivity of all ScN films increases slightly with an increase in temperature (see Fig. 3.2e) which is representative of their degenerate semiconducting or semi-metallic nature due to high carrier concentrations. On the other hand, mobility decreases with an increase in temperature as found in Fig. 3.2f. A combination of ionized impurity and dislocation scattering model is found to fit the temperature-dependence of mobility very well with a high dislocation density in the  $10^9$ - $10^{11} \text{ cm}^{-2}$  range (see Appendix B2 supplementary data Fig. B2.4), which can be seen as well in transmission electron microscopy (TEM) images. The carrier concentration of the ScN films remain nearly unchanged within the measured temperature range (see Fig. 3.2g).

Temperature-dependent dielectric permittivity is measured further to highlight the refractory plasmonic behavior of ScN. Results show that with an increase in temperature from 100 K-to-500 K,  $\lambda_p$  exhibits a redshift from 1.76  $\mu\text{m}$  to 1.83  $\mu\text{m}$  (see Fig. 3.3a), and  $\epsilon_2$  increases from 0.95 to 1.32 at the corresponding  $\lambda_p$  for the ScN film with  $1.6 \times 10^{21} \text{ cm}^{-3}$  carrier concentrations. Such an increase in  $\lambda_p$  and optical losses, especially at longer wavelengths (see Fig. 3.3b) can be directly attributed to the decrease in mobility as shown in Fig. 3.3c. However, near the  $\lambda_p$  wavelength region, the increase in  $\epsilon_2$  is rather small that highlight the suitability of ScN for high-temperature applications. Note that though the permittivity is measured till 500 K due to instrumental limitations, ScN exhibits a high melting temperature of  $\sim 2600^\circ\text{C}$ , and hence could be useful for many plasmonic applications at high-temperatures.

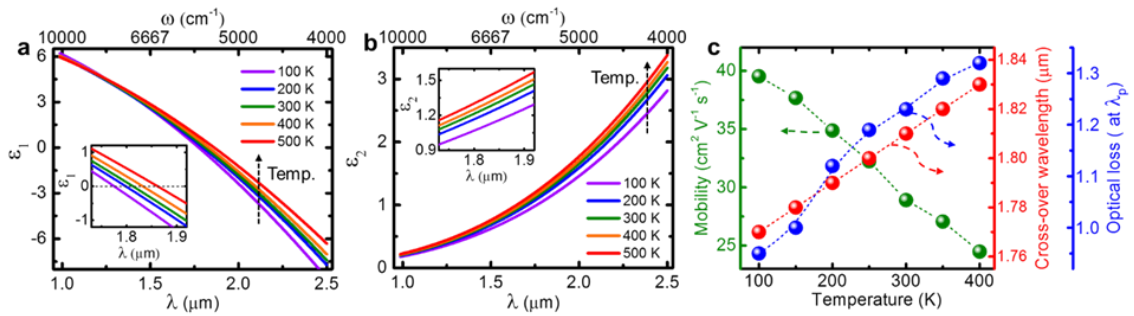


**Figure 3.3 Temperature-dependent dielectric permittivity of ScN.** Temperature-dependent (a)  $\epsilon_1$  (b)  $\epsilon_2$  of the ScN thin film with  $1.6 \times 10^{21} \text{ cm}^{-3}$  carrier concentrations are presented. With an increased temperature,  $\lambda_p$  and the optical loss increase. (c) Cross-over wavelength ( $\lambda_p$ ) and optical loss was found to increase with increasing temperature as mobility is decreasing.

With the above refractory plasmonic properties in the SWIR spectral range, ScN's suitability for various nano-photonic applications<sup>80,109</sup> such as in SPP waveguides, localized surface-plasmon-resonance (LSPR), epsilon-near-zero (ENZ), hyperbolic metamaterials (HMM), and transformation optics are determined. Each of these applications requires its own optimum operating conditions that are determined by the structure and geometry of devices, as well as material properties. Our analysis show that the plasmon-resonance and SPP in ScN should be useful for the non-resonant SWIR applications such as waveguides, ENZ, HMM<sup>80</sup> (see Appendix B supplementary data Fig. B2.5). As an example, ScN exhibits a high SPP propagation length ( $L$ ) and low electric-field confinement length ( $D$ ) that is comparable to other doped-semiconductors and CMOs

for high-performance waveguides. A ratio between the L and D, referred as the figure-of-merit ( $M_1^{2D}$ )<sup>110</sup> is high in ScN and compares well to its alternatives in the near and mid-IR spectral range. Similarly, a low  $\epsilon_2$  of 1.00 at  $\lambda_p$  should be suitable for ENZ device applications<sup>34</sup> such as photon funnels, or spatial filtering for beaming. Even for the localized SPP resonance, the figure-of-merit (FOM) of ScN is comparable to its counterparts. Nevertheless, with more advanced deposition methods such as molecular-beam-epitaxy (MBE) and hybrid vapor phase epitaxy, mobility of ScN could be increased further which should improve its performance metrics.

### 3.4 Phonon polariton in ScN

While the carrier concentration control leads to the SWIR plasmonic response in ScN, demonstration of SPhP excitation requires that the electronic resonance do not contribute to the total dielectric permittivity in the LWIR spectral range. To achieve this condition, Mg (hole)-doped ScN films with low carrier concentrations are deposited (see Table 3.1). To separate the contributions of MgO (substrate) phonon modes, a 100 nm IR reflective TiN buffer layer is deposited on (001) MgO substrates before ScN depositions (see Appendix B supplementary data Fig. B2.6). Infrared reflectivity measurement (see Fig. 3.4a) of ScN with  $5 \times 10^{18} \text{ cm}^{-3}$  carrier concentration shows well-defined Reststrahlen band (see Fig. 3.4b), a highly reflective region between the TO ( $359 \text{ cm}^{-1}$ ) and LO ( $686 \text{ cm}^{-1}$ ) phonon modes where light couples with the polar optical lattice vibrations. Calculated  $\epsilon_1$  is found to exhibit negative values within the Reststrahlen band, with an epsilon-near-pole (ENP) resonance at  $359 \text{ cm}^{-1}$  since light couples directly to the TO phonon mode (see Fig. 3.4c). Concomitantly,  $\epsilon_2$  exhibits a sharp peak at the TO phonon frequency. Both LO and TO phonon frequencies are consistent with recent inelastic X-ray scattering (IXS) phonon dispersion of ScN<sup>107</sup>. IXS measurement has also shown a phonon lifetime of 0.21 ps for the LO phonon mode at the  $\Gamma$ -point that is dominated primarily by three-body phonon-phonon interactions. Since the crystalline quality of ScN is very high, optical losses in the SPhP resonance should primarily arise from the phonon-phonon interactions.

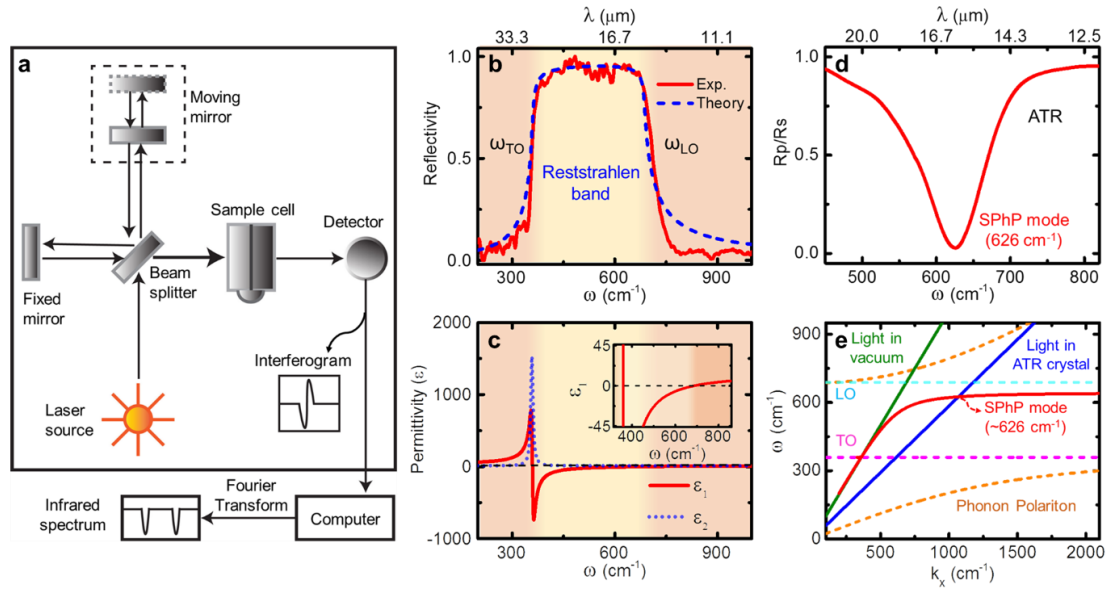


**Figure 3.4 Phonon-polariton in ScN.** (a) Schematic diagram of Fourier-transform infrared spectrometer (FTIR). (b) Normalized FTIR reflection (red) spectra of ScN film is shown and the calculated reflection spectrum is presented (in blue shade). (c) Calculated dielectric permittivity ( $\epsilon$ ) of ScN thin film showing negative  $\epsilon_1$  within the Reststrahlen band. (d) Normalized reflection spectra obtained from the ATR measurement showing excitation of the SPhP mode with  $p$ -polarized light. (e) Theoretically calculated dispersion of SPhP is presented. The light lines, in the vacuum and ATR crystal, are shown by the green and blue curve respectively. The frequency positions of  $\omega_{LO}$  and  $\omega_{TO}$  are shown by cyan and magenta dotted lines respectively. Lower and upper bulk phonon polaritons are shown by the orange dotted curve.

Further, polarization-dependent ATR measurements are performed which show a dip at  $626 \text{ cm}^{-1}$  in the  $p$ -polarized light, representing coupling of light with the SPhP mode (see Fig. 3.4d). Calculated SPhP dispersion is consistent with the experimental observations and highlight the bulk phonon-polaritons at frequencies above and below the Reststrahlen band (see Fig. 3.4e). Performance FOM of SPhP modes<sup>87</sup> is calculated and compared with other well-established polar dielectric materials such as SiC<sup>88</sup>, h-BN<sup>89</sup>, c-BN<sup>111</sup>, AlN<sup>91</sup>, and GaN<sup>112</sup>. SPhP FOM of ScN is around two times higher than its peers due to its high  $\epsilon_\infty$  of 12.8 (see Fig. 3.5 (b) and Appendix B2 supplementary data section B2.9). Further improvement in materials quality is likely to reduce the phonon damping and increase FOM in ScN.

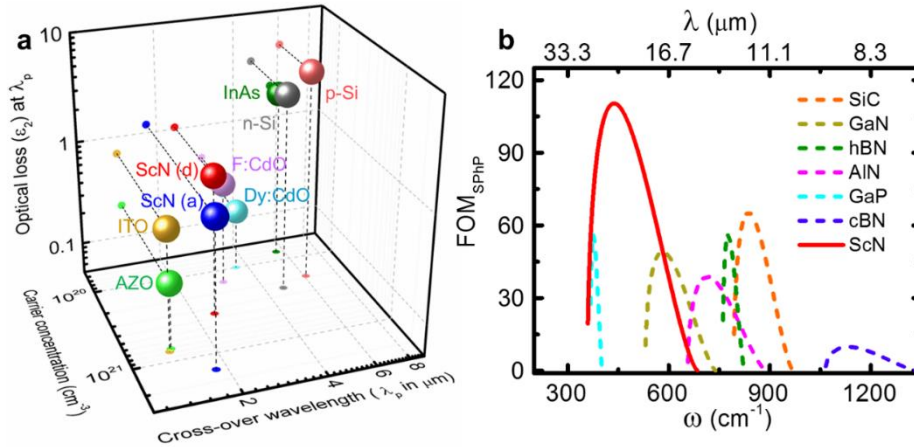


**Figure 3.5** (a) Comparison of plasmonic properties of ScN with transparent conductive oxides (ITO<sup>80</sup>, AZO<sup>80</sup>, F:CdO<sup>81</sup>, Dy:CdO<sup>82</sup>), doped silicon (*n*-Si, *p*-Si)<sup>79</sup> and InAs<sup>78</sup> their optical loss at crossover wavelength (or ENZ wavelength). (b) Comparison of FOM of SPP of ScN with other polar dielectric materials (SiC<sup>88</sup>, GaN<sup>112</sup>, hBN<sup>89</sup>, AlN<sup>91</sup>, GaP<sup>113</sup>, cBN<sup>111</sup>).

The comparison of plasmonic properties (cross-over wavelength and optical loss) shows that the ENZ wavelength of ScN covers  $\sim 1750$  nm–2500 nm spectral region that lies in between the ENZ wavelength typically exhibited by TCOs and doped-CdO.  $\epsilon_2$  of ScN is slightly higher compared to the NIR plasmonic materials such as ITO, AZO; as well as with the MIR plasmonic materials such as CdO primarily due to its lower carrier mobility (see Fig. 3.5 (a)). However, compared to the MIR plasmonic materials such as *n*-Si, *p*-Si, InAs, etc., the optical loss of ScN is smaller. Since advanced deposition methods such as hybrid vapor phase epitaxy (HVPE) and molecular beam epitaxy<sup>102</sup> (MBE) results in higher carrier mobility (with a maximum reported mobility of  $\sim 280$  cm $^2$ /Vs in ScN)<sup>114</sup>, optical losses could be reduced.

While the compelling optical properties of ScN makes it an attractive IR polaritonic material, SPP waveguides, HMM, ENZ and other device implementations require low surface roughness, a lattice-matched interfaces with the substrate and compatibility with industrially relevant materials.

### 3.5 Transmission electron microscopy of ScN

Scanning transmission electron microscopy (STEM), energy-dispersive x-ray spectroscopy (EDS) mapping and electron diffraction were applied to characterize the microstructure of the film (see Appendix supplementary data section B2.11 for detail). Both oxygen and



magnesium-doped ScN films deposited in this work on (001) MgO substrates at high-temperatures grow epitaxially with [001](001) ScN || [001](001) MgO (see Fig. 3.6a and 3.6b). The ScN/MgO interface is sharp despite the presence of a few misfit-dislocations, resulting from the 7% lattice-mismatch between ScN and MgO. Importantly, both oxygen and magnesium dopants make homogeneous solid-solutions with ScN without any precipitations or secondary phase formations (see EDS maps in Fig. 3.6 c-f) resulting in a small rms. surface roughness of  $\sim 2$  nm (see Appendix supplementary data Fig. B2.7). Electron energy loss spectroscopy (EELS) O K-edge and Mg L-edges are consistent with the bonding of O with Sc and Mg with N respectively and splitting of the peaks highlight hybridization between different orbitals (see Appendix supplementary data Fig. B2.8). While the present work utilizes (001) MgO as a substrate with the same crystal structure, it must be mentioned that ScN films are regularly deposited on industrially important  $\text{Al}_2\text{O}_3$  and Si substrates that should provide seamless chip integration. In addition, due to its near-perfect lattice-matching, (111) ScN films have been deposited on (0001) GaN with very little defects<sup>103,104</sup> that would also lead to its integration with GaN-based light-emission and power electronic applications.

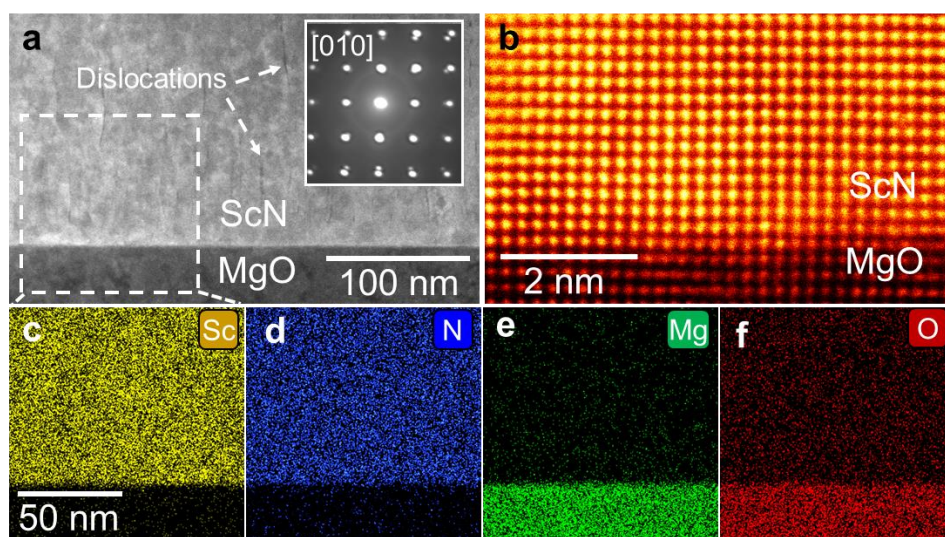


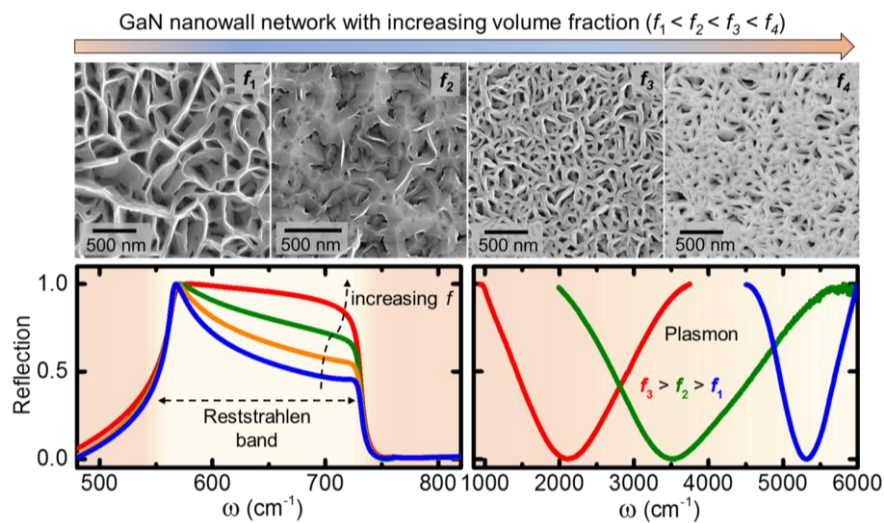
**Figure 3.6 STEM images and EDS maps of ScN deposited on (001) MgO substrate.** (a) Low-magnification STEM image showing homogeneous and uniform ScN growth with a few dislocations. The electron diffraction pattern in the inset confirms the cubic epitaxial growth. (b) Atomic resolution STEM image of the ScN/MgO demonstrating a sharp interface. STEM-EDS elemental mapping of (c) Sc, (d) N, (e) Mg and (f) O shows the homogeneous elemental distribution.

### 3.6 Conclusion

In conclusion, we present epitaxial refractory group-III scandium nitride (ScN) as a dual plasmon- and phonon-polariton material, where tunable plasmon resonance in the short-wave-infrared (SWIR) spectral range and the phonon-polariton in the long-wave-infrared (LWIR) region are obtained by carrier concentration control. Oxygen-doped ScN films with carrier concentrations between  $10^{20}$ - $10^{21}$   $\text{cm}^{-3}$  exhibit high-quality and low-loss plasmon resonance in the 1.8-2.3  $\mu\text{m}$  SWIR spectral region, where most plasmonic materials do not work satisfactorily. High figure-of-merit (FOM) surface phonon-polariton resonance is also achieved in the long-wavelength-infrared (LWIR) by reducing the carrier concentration with Mg-hole doping in ScN. Demonstration of plasmon- and phonon-polariton in one host material, ScN with doping-control makes it an attractive material for applications in waveguides, hyperbolic and epsilon-near-zero metamaterials, optical communication, solar-energy harvesting and infrared photonic applications.

## Morphology-Controlled Reststrahlen Band and Infrared Plasmon-Polariton in GaN Nanostructures

Gallium nitride (GaN) is one of the most famous semiconductors and its nanostructures such as nanorod, nanocolumns, and nanowall-networks have several benefits over thin film due to their reduced dislocation-density and large surface-to-volume ratio i.e., enhanced light-emission, sensing, catalysis etc. Coupling of infrared light with optical phonon mode resulting in the Reststrahlen band and excitation of surface phonon polariton has been demonstrated in GaN thin films. However, the impact of nanostructuring on GaN's Reststrahlen band and plasmonic properties have not been studied. In this chapter, we show that induced dipoles at the edges and asperities in GaN nanostructures lead to phonon absorption that drastically alters the shape of its Reststrahlen band. The hexagonal honeycomb-shaped GaN nanowall networks and vertically standing nanorod are fabricated by controlling the growth modes with plasma-assisted molecular beam epitaxy. Lichtenecker's effective-medium-approximation is used to model the experimental Reststrahlen band and to determine nanostructures' effective permittivity. Also, the formation energy of the N-vacancy at the surface of the nanostructures is more favorable than in bulk, resulting in high carriers and the plasmon resonance in the mid-infrared regime. Morphology-controlled tunable plasmon polariton as well as tailored Reststrahlen band, make GaN nanostructures an attractive material for infrared nanophotonics.



K. C. Maurya\*, A. Chatterjee\*, S. M. Shivaprasad, and B. Saha, *Nano Letters*, 22, 9606–9613 (2022).

## 4.1 Introduction

Ever since the demonstration of blue light emission in light-emitting diodes (LEDs),<sup>115</sup> gallium nitride (GaN) has emerged as one of the most dominating semiconducting materials over the last three decades. Numerous device technologies, such as laser diodes, transistors, high-power electronics, and optoelectronic devices based on GaN, are already commercialized.<sup>116</sup> At the same time, GaN is also actively researched for high electron mobility transistors (HEMTs), dilute magnetic semiconductors, solar cells, bio-sensors, photochemical water splitting, and space-related applications.<sup>117–119</sup> Most of these technological advances in GaN stem from its excellent material properties, including large direct bandgap, high carrier mobility, high breakdown voltage, ease in bandgap tunability, and superior structural and chemical stability at ambient and high temperatures. However, due to the refractive index mismatch between GaN and air, the light extraction efficiency of planar GaN-based LEDs is relatively low. Similarly, planar thin film geometry is also not ideally suited for applications such as photochemical reaction, bio-sensing, and others, where access to a large surface area of GaN is required.<sup>118,119</sup>

To circumvent these challenges, porous hexagonal honeycomb-shaped GaN nanowall networks (*NwN*) are developed that exhibit monochromatic and coherent luminescence from nanocavities, improved photo-collection efficiency, and lower dislocation densities.<sup>120</sup> These nanostructures (nanorod, nanocolumns, and *NwN*) exhibit sharp band-edge photoemission and almost no defect-related emission peaks often found in GaN films.<sup>120</sup> By altering the growth conditions such as the substrate temperature, nitrogen and gallium flux; single-crystalline polygonal-shaped cavities with steep-wedge-shaped nanowalls with different GaN fill fractions are also developed. Cross-sectional microscopy imaging revealed that the nanowall networks are ~ 100-200 nm wide at the bottom, ~ 5-10 nm wide at the top, and exhibit micron-sized heights that can be tuned with growth durations. Significant changes in the growth parameters also result in vertically aligned nanorod that are 100-200 nm in diameter, ~ 1  $\mu\text{m}$  in height, and are directly deposited on Si or  $\text{Al}_2\text{O}_3$  substrates.<sup>121–123</sup>

Though the visible-wavelength photoemission properties of such GaN nanostructures have been studied before, the impact of nanostructuring on GaN's infrared (IR) optical properties is not elucidated. Achieving optical resonances in the mid<sup>57,80,81,124</sup>-and-far<sup>75,125,126</sup> IR

spectral range is necessary to further the progress in GaN research and for its potential applications<sup>2,34,76,77</sup> in many emerging device technologies such as radiative cooling,<sup>127</sup> solar-thermophotovoltaics,<sup>15,128</sup> nano-laser,<sup>69</sup> sensing,<sup>129</sup> and surveillance<sup>130</sup>, etc. In general, IR light in the mid-to-long wavelength spectral range couple directly to the transverse optical (TO) phonon mode in polar semiconductors and lead to a highly reflecting region bounded by the TO and longitudinal optical (LO) phonon modes, known as the Reststrahlen band.<sup>86</sup> Inside the Reststrahlen band, the dielectric permittivity becomes negative, and the material repels the incident electric field.<sup>23</sup> The Reststrahlen effect is traditionally used to study semiconductors' vibrational properties and has also found applications in geophysics and meteorology.<sup>131</sup>

For GaN epilayers deposited with molecular beam epitaxy (MBE) or metal-organic chemical vapor deposition (MOCVD), the rectangular-shaped Reststrahlen band covering a spectral range from  $\sim 533 \text{ cm}^{-1}$  to  $744 \text{ cm}^{-1}$  has been demonstrated<sup>132,133</sup>. Surface phonon-polariton (SPhP) excitations are also shown in GaN thin films at  $\sim 693 \text{ cm}^{-1}$  within the Reststrahlen band using *p*-polarized light in the attenuated total reflection (ATR) measurement method.<sup>112,134</sup> However, in GaN nanostructures, free surfaces, pores, and cavities are expected to impact the Reststrahlen band and alter the infrared light-matter coupling. In general, such free surfaces, edges, and asperities in the cavity lead to induced dipoles that can absorb incident light.<sup>135,136</sup> Such dipole maxima appear inside the Reststrahlen band depending on the shape of the asperities and are known as the surface polaritons. Such dipolar and multipolar resonances accompany phonon absorption and can drastically impact the optical properties of materials.

In addition to the Reststrahlen effect in the far-IR spectral range, the nanostructures could also be explored as hosts for mid-IR plasmon-polariton resonance. As-deposited GaN thin films in MBE or MOCVD techniques generally possess *n*-type carriers due to nitrogen vacancies and oxygen as impurities. However, in GaN nanostructures, the carrier concentration is significantly higher and ranges from  $10^{19}$ - $10^{20} \text{ cm}^{-3}$  due to additional carrier generation from the surface vacancies and defects.<sup>121</sup> Previously, density-functional theory (DFT)-based calculations have revealed that the formation energy of the nitrogen-vacancy at the surface of the GaN nanostructures is more favorable than inside the bulk or inside the thin films.<sup>137</sup> Therefore, by controlling the morphology of the GaN

nanostructures, their carrier concentration can be tuned, and high-quality plasmon resonance can be achieved.

## 4.2 Growth of GaN nanostructures

GaN nanostructures are deposited using plasma-assisted molecular beam epitaxy (PAMBE) in an ultra-high vacuum chamber at a base pressure of  $3 \times 10^{-11}$  Torr on (0001)  $\text{Al}_2\text{O}_3$  substrates. A radio-frequency (RF) plasma source operating at a forward power of 375 W was used as the nitrogen plasma source. The substrate temperature was maintained at 630°C. With changes in the nitrogen and gallium flux, GaN nanowall networks with various volume fractions are obtained (see Appendix B3 supplementary data section B3.1 for details). In general, a high  $\text{N}_2/\text{Ga}$  flux ratio gives more open surfaces or a low volume fraction of GaN structure. Major changes in the growth conditions in terms of nitrogen-to-gallium flux ratio are utilized to deposit vertically aligned nanorods on Si substrates. For an epitaxial thin film with a smooth surface as a reference, 3  $\mu\text{m}$  thick *n*-type GaN deposited on (0001)  $\text{Al}_2\text{O}_3$  substrates are procured that exhibit a carrier concentration of  $\sim 2 \times 10^{18} \text{ cm}^{-3}$  at room temperature.

Plan-view field-emission scanning electron microscopy (FESEM) images of GaN nanostructures (see Figure 4.1 (a-e)) show the evolution of surface morphology with changes in deposition conditions. At a high substrate temperature, increased Ga adatom diffusion results in large domains of GaN that are formed both in the lateral and vertical directions (see Appendix B3 supplementary data Figure B3.1). However, with the reduction of substrate temperature, the Ga adatom mobility reduces substantially, and the growth is dominated by the Volmer-Weber growth mechanism, where nitrogen-rich (N-rich) condition results in the formation of tetrahedral islands. First principles calculations show that the adatom attachment at the edges of the tetrahedral islands is energetically favorable which leads to an anisotropic growth resulting in the formation of 'Y'-shaped structures.<sup>138</sup> With time, these structures merge and give rise to the particular NwN morphology. A further reduction in the lateral diffusion of adatoms finally leads to a nanorod morphology, as shown in Figure 4.1(e). Such a non-equilibrium growth mode<sup>139</sup> of GaN in the MBE deposition method gives rise to complex surface patterns and nanostructures (see Ref. <sup>120,138,140</sup> for detailed discussion).

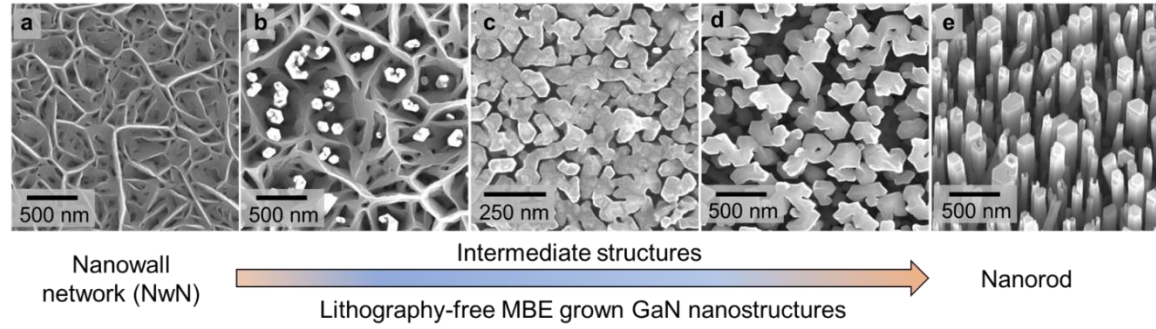


**Figure 4.1** Plan-view FESEM microstructure of MBE-deposited GaN nanostructures. (a-e) Surface topography of nanowall network to nanorod along with various intermediate complex structures. Crystal growth under non-equilibrium conditions gives rise to such complex surface morphology.

### 4.3 Reststrahlen band of GaN nanostructures

Optical characterization reveals that compared to the rectangular-shaped Reststrahlen band in GaN epitaxial layer with a smooth surface (see Figure 4.2(a)), GaN NwN exhibits a right-trapezoid-shaped Reststrahlen band (see Figure 4.2(c)). Reflectivity in NwN decreases progressively from GaN's TO phonon frequency at  $566 \text{ cm}^{-1}$  to LO phonon frequency at  $731 \text{ cm}^{-1}$ . The optical phonon frequencies of the thin film and nanostructures are measured using Raman spectroscopy and presented in supplementary data section 4. To obtain the dielectric permittivity, the measured reflection spectrum is fitted with Fresnel's equation. The frequency-dependent total dielectric permittivity ( $\epsilon_{total}(\omega)$ ) is expressed as<sup>18</sup>

$$\epsilon_{total}(\omega) = \epsilon_1 + i\epsilon_2 = \epsilon_\infty \left( 1 - \frac{\omega_p^2}{\omega^2 + i\gamma\omega} + \frac{\omega_{LO}^2 - \omega_{TO}^2}{\omega_{TO}^2 - \omega^2 - i\omega\Gamma} \right) \quad (4.1)$$

$$\omega_p = \sqrt{\frac{ne^2}{m^*\epsilon_0}} \quad (4.2)$$

$$\epsilon_{plasmon}(\omega) = -\frac{\omega_p^2}{\omega^2 + i\gamma\omega} \quad (4.3)$$

Here the second term corresponds to the plasmon or Drude component, while the third term refers to the phonon resonance.  $\omega_{LO}$  ( $\omega_{TO}$ ) are the LO (TO) phonon frequencies,  $\Gamma$  is the phonon damping constant for phonon scattering,  $\epsilon_\infty$  the background permittivity due to bound charges (5.35),  $\omega_p$ ,  $\gamma$ ,  $n$  and  $m^*$  are the high-frequency dielectric constant, plasma frequency, plasmon damping constants, carrier concentration and effective mass,

respectively. Since the GaN epitaxial layer exhibit a very low carrier concentration ( $\sim 2 \times 10^{18} \text{ cm}^{-3}$ ), the electronic contribution to the dielectric permittivity in the mid-to-long wavelength IR spectral range can be neglected. However, for the NwN, since the carrier concentration is relatively large (in the  $\sim 10^{19}$ - $10^{20} \text{ cm}^{-3}$  range), electronic contribution to the permittivity is included in modeling the Reststrahlen band spectral region.

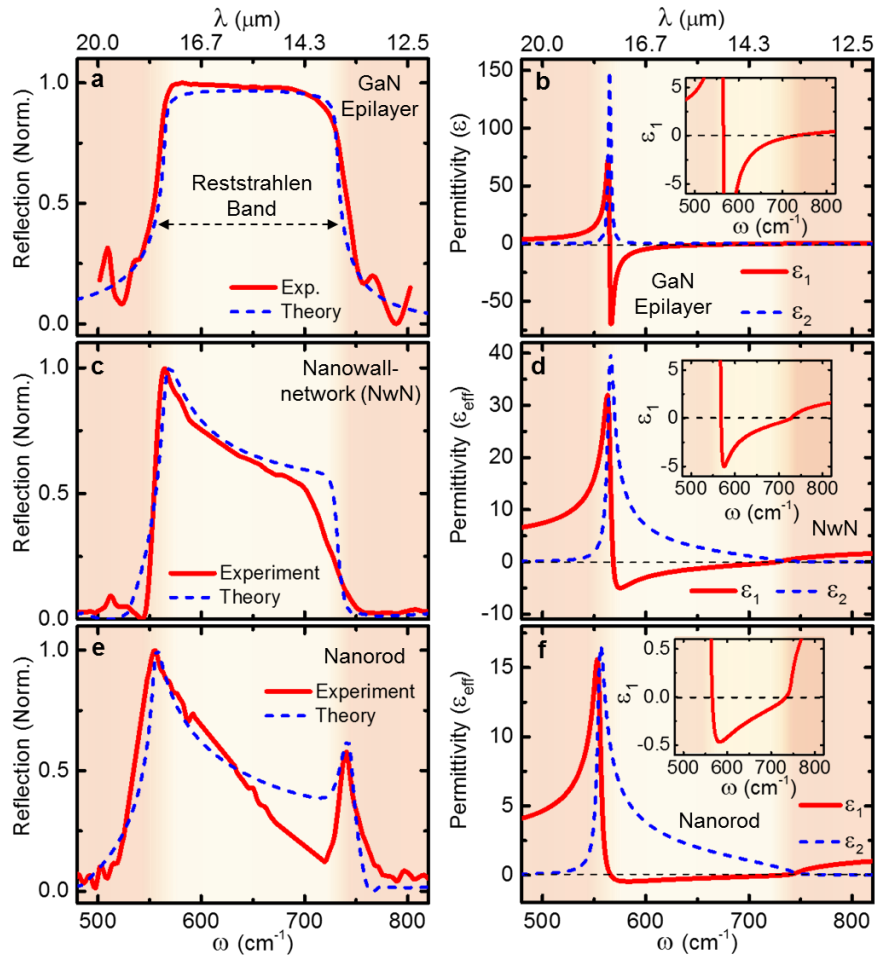


**Figure 4.2 Reststrahlen band of GaN epilayer and nanostructures.** Reflection spectrum (red curve) along with the theoretically fitted curve (blue curve) of (a) GaN epilayer; (c) GaN nano-wall network (volume fractions of  $\sim 70\%$ ); (e) GaN nanorod (volume fractions of  $\sim 55\%$ ). A highly asymmetrical right trapezoidal shaped Reststrahlen band appears in the GaN nanostructure. The calculated real ( $\epsilon_1$ ) and imaginary ( $\epsilon_2$ ) component of the effective dielectric permittivity ( $\epsilon_{eff}$ ) of (b) GaN epilayer, (d) GaN nanowall network and (f) GaN nanorod. Nanostructuring leads to asymmetry in epsilon-near-pole (ENP) resonance at the TO phonon frequency. To capture the sharp dip in the reflection spectrum of the nanorod near LO phonon, phonon confinement effect<sup>141,142</sup> is included in the modeling as presented in SI section 8.



The calculated real part of the dielectric permittivity ( $\epsilon_1$ ) for the epitaxial layer undergoes a positive-to-negative transition at the LO phonon mode frequency (see Figure 4.2(b)). The  $\epsilon_1$  remains negative within the Reststrahlen band and exhibits an epsilon-near-pole (ENP) resonance at the TO phonon frequency. As light couples directly to the TO phonon mode, the imaginary part of the dielectric permittivity, represented as the optical loss, exhibits a sharp symmetric peak located at TO phonon frequency, as shown in Figure 4.2(b).

Since the *NwN* and nanorods contain voids and asperities, effectively reducing GaN fill fraction, the infrared reflection spectrum of the nanostructures is modelled using Fresnel's equation with Lichtenecker's effective medium approximation (LEMA).<sup>143</sup> The expression for the effective permittivity ( $\epsilon_{eff} = \epsilon_1 + i \epsilon_2$ ) can be presented as

$$\text{Log } \epsilon_{eff} = f \text{Log } \epsilon_i + (1 - f) \text{Log } \epsilon_s \quad (4)$$

Where  $f$  is the volume fraction of GaN,  $\epsilon_i$  ( $\epsilon_s$ ) is the permittivity of the GaN (air). LEMA softens the dielectric constant of GaN with its fill fraction  $f$ .

Compared to the epitaxial layer, the dielectric permittivity of *NwN* exhibits (see Figure 4.2(d)) an asymmetric response due to the asymmetry in the reflection spectrum (see Fig. 4.2(c)). Starting from the ENP resonance at the TO phonon frequency, the real component of the effective dielectric permittivity ( $\text{Re}[\epsilon_{eff}]$  or  $\epsilon_1$ ) is smeared towards the LO phonon frequency (see Figure 4.2(d)). Similarly, the optical loss ( $\text{Im}[\epsilon_{eff}]$  or  $\epsilon_2$ ) also shows an asymmetric peak at the ENP. Optical losses are also found away from the TO phonon frequency due to the phonon absorptions. The magnitude of  $\text{Re}[\epsilon_{eff}]$  in *NwN* is also smaller than that of the  $\text{Re}[\epsilon]$  of GaN epitaxial layers due to the decrease in the effective volume fraction of GaN inside the *NwN*.

Compared to the *NwN*, the reflection spectrum of the nanorod structure exhibit a much more significant asymmetry (see Figure 4.2(e)), with a pronounced dip at  $\sim 720 \text{ cm}^{-1}$ . Reflectivity recovers slightly at the position of the LO phonon frequency before vanishing outside of the Reststrahlen band spectral region, thus exhibiting a peak-like feature. Extraction of the dielectric permittivity shows higher asymmetry in the real component of the dielectric permittivity with very small values of  $\text{Re}[\epsilon_{eff}]$  or  $\epsilon_1$  and minimal dispersion

as the LO phonon frequency is approached (see Figure 4.2(f)). The values of  $\text{Re}[\epsilon_{\text{eff}}]$  or  $\epsilon_1$  are also much smaller compared to the ones determined for the  $NwN$ . Notably, while the optical loss is nearly negligible in the region close to the LO phonon frequency in an epitaxial film,  $(\text{Im}[\epsilon_{\text{eff}}]$  or  $\epsilon_2)$  of the nanorod is significant in the regions close to the LO phonon frequency, highlighting a great extent of optical absorption away from the TO phonon frequency region.

The origin of the changes in the shape of the Reststrahlen band can be explained due to the dipole-induced phonon absorption at the surfaces, edges, and asperities in the nanostructures. The distribution of the size and shape of the asperities ensures multiple dipole peaks with various degrees of geometrical factors (or depolarization factor), which essentially results in a tapered decrease in the reflectivity from the TO frequency to LO frequency. Following the description of previous work<sup>135</sup>, the generation of the surface polariton is modeled by assuming the asperities as having ellipsoidal shapes with dimensions much smaller compared to the wavelength of light. The induced dipole moment ( $\mathbf{p}$ ) in the ellipsoid is calculated by equation (4.5)<sup>136</sup>

$$\mathbf{p} = v \frac{\epsilon - \epsilon_m}{\epsilon_m + L_j(\epsilon - \epsilon_m)} \epsilon_m \mathbf{E}_0 \quad (4.5)$$

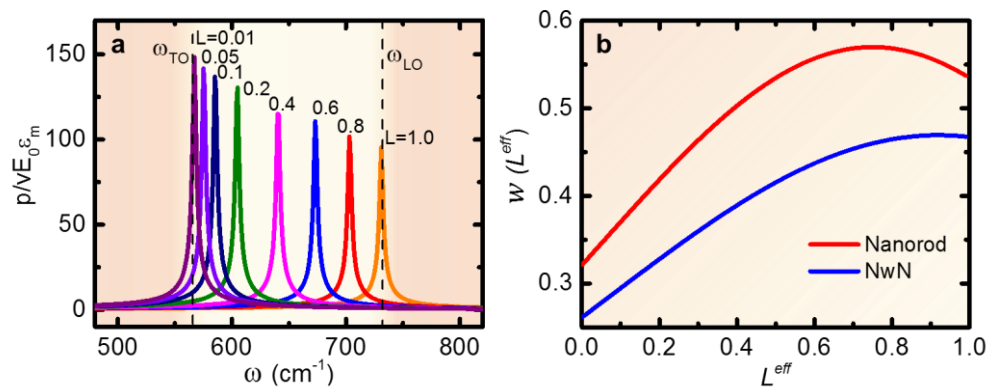
Where  $v$  is the volume of the ellipsoidal particle ( $4\pi abc/3$ );  $a$ ,  $b$  and  $c$  are the principal semi-axis of the ellipsoid.  $\epsilon$  and  $\epsilon_m$  are the dielectric permittivity of GaN and the matrix (air) respectively.  $E_0$  is the electric field of the light. Here  $L_j$  is the geometrical factor along the  $j^{\text{th}}$  principal axis of the ellipsoid with  $L_1 + L_2 + L_3 = 1$ . The geometrical factor depends on the shape of the structure.

Figure 4.3(a) shows that the induced dipole maxima (or surface polariton) appearing closer to the LO phonon frequency exhibit high depolarization factors ( $L$  close to 1). On the other hand, for  $L$  approaching zero, the induced dipole modes appear close to TO phonon frequency. However, since the dipoles interact with those from the surface and with each other, and due to the fact that the asperities are not perfectly ellipsoidal, several induced dipoles with different depolarization factors can arise inside the Reststrahlen band. To determine the dominating  $L$  values for the GaN nanostructures, Andersson and Ribbing formalism<sup>135</sup> is utilized (see Eq. 4.6), which correlates the induced dipole probability with

the effective geometrical factor ( $L^{eff}$ ) and effective permittivity ( $\epsilon_{eff}^{phonon}$ ) of the complex structures.

$$\epsilon_{eff}^{phonon} = \epsilon + f(\epsilon - \epsilon_m)\epsilon_m \int_0^1 \frac{w(L^{eff})}{L^{eff}(\epsilon - \epsilon_m)} dL^{eff} \quad (4.6)$$

Here,  $w(L^{eff})$  is the probability function for induced dipole which depends on the effective depolarization factor  $L^{eff}$  or the topography of the surfaces (see supplementary data section B3.5 ).<sup>144</sup> In general, for planar flat flakes, the probability function exhibits a large contribution for  $L^{eff}$  less than 1/3 (see supplementary data section B3.4 and B3.6 for detail). In the case of round edges or spherical surfaces, the probability function exhibit maxima for  $L^{eff} = 1/3$ . While for out-of-plane (vertically-standing) sharp asperities, the probability function contributes more near regions where the  $L^{eff}$  are close to one. In the case of the GaN NwN and nanorods, the probability function contributes more to the higher values of  $L^{eff}$  as the nanostructures exhibit niddle-like asperities. Figure 4.3(b) show that  $w(L^{eff})$  increases monotonically with  $L^{eff}$  for the NwN, which explains the continuous decrease in the reflectivity of GaN NwN from TO-to-LO mode. On the other hand,  $w(L^{eff})$  exhibits a maximum for the  $L^{eff}$  between 0.6 and 0.85 for the nanorod that leads to a dip in reflection inside the Reststrahlen band (see Figure 4.2(e)). The magnitude of  $w(L^{eff})$  for the nanorods is also higher than the NwN which explains the higher absorption in the nanorods.



**Figure 4.3 Induced dipole moment and its distribution within the Reststrahlen band.** (a) Normalized induced dipole moments of the surface polaritons as a function of wavenumber with depolarization factors  $L$  as a parameter. For  $L$  close to 1, the surface polariton maximum appears close to the LO phonon frequency. While for  $L$  close to zero, surface polariton maxima are located close to the TO phonon frequency. (b) The

probability distribution function for dipole absorption as a function of effective depolarization factor of GaN nanostructure.

To determine the effects of fill fraction on NwN's optical properties, Reststrahlen bands are measured with varying  $f$ , ranging from ~60% to ~83%. With a decrease in  $f$ , the Reststrahlen band appear more asymmetric (see Figure 4.4(e)), and reflection decreases progressively as one moves away from the TO phonon to LO phonon frequency. As the FESEM images show (see Figure 4.4(a-d)), GaN NwN with a lower volume fraction ( $f_1$ ) has more open surfaces and edges than the NwN with a high-volume fraction ( $f_4$ ). Consequently, more surface polariton absorption takes place in NwN ( $f_1$ ) resulting in more asymmetry in the Reststrahlen band. This phenomenon is further verified by calculating the dielectric permittivity using the LEMA and by determining the theoretical reflection curve, where the volume fraction ( $f$ ) is decreased from 0.9 to 0.6. A clear decrease in reflectivity can be found in Figure 4.4(f), which leads to a more right-trapezoidal-shaped Reststrahlen band with a reduction in GaN volume fraction. Apart from the decrease in the  $\epsilon_1$  of the nanostructure with decreasing GaN fill fraction, larger asymmetry is found on both  $\epsilon_1$  and  $\epsilon_2$  with respect to the ENP at the TO phonon frequency (see supplementary data figure B3.6).

Apart from the changes in the shape of the Reststrahlen band, our results also show that nanostructuring alters far-IR optical properties of GaN, such as thermal emission. The emission spectra are measured by mounting the samples on a copper hot plate, from where the radiation is collected in the FTIR spectrometer (see supplementary data figure B3.7). Thermal emission of the NwN follows the inverse of the asymmetric Reststrahlen band of the nanostructure (see supplementary data section-B3.7 for details). Since according to Kirchhoff's law, emissivity is same as the absorptivity, the measured emission spectrum is expected to follow the opposite trends of the Reststrahlen band.

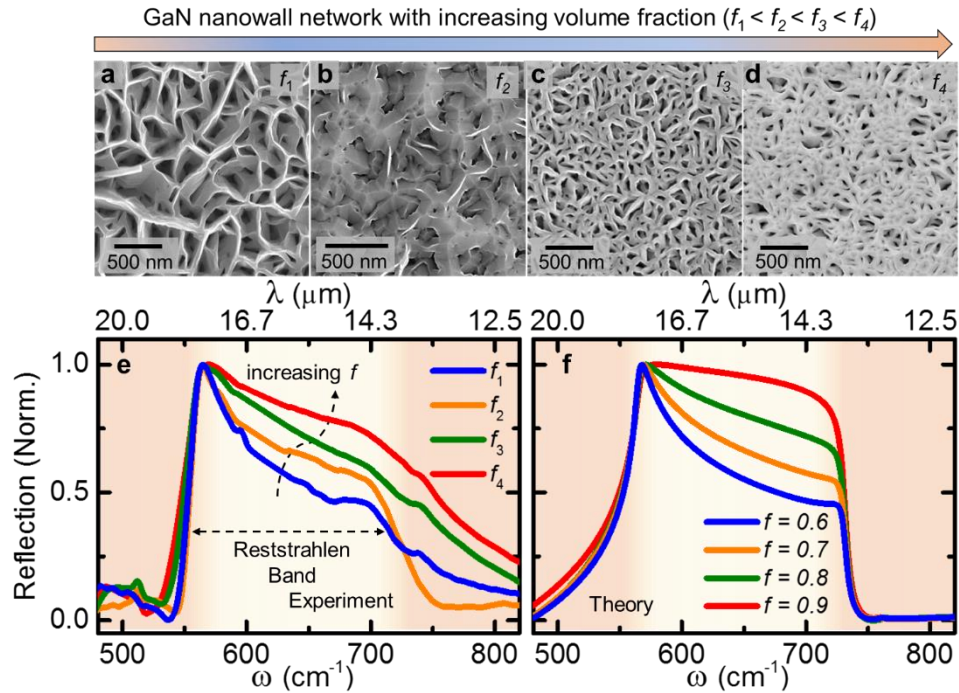


**Figure 4.4** Impact of GaN volume fraction on nanostructure's Reststrahlen band. FESEM images of GaN nanowall-networks with increasing volume fraction (a)  $f_1$  (~0.60), (b)  $f_2$  (~0.70), (c)  $f_3$  (~0.77), (d)  $f_4$  (~0.83). (e) Experimentally measured reflection curve of the NwNs. (f) Calculated reflection curve using LEMA for volume fraction of 0.6, 0.7, 0.8, 0.9. Both the experimental and the theoretical results show that a lower volume fraction of GaN leads to higher asymmetry in the Reststrahlen band.

#### 4.4 Infrared plasmon polariton in GaN nanostructures

Along with the influence on the Reststrahlen band, nanostructuring in GaN also produces plasmon resonance in the mid-IR spectral range. Since the nitrogen-vacancies are easier to form on the free surfaces, exposed surfaces of the GaN structures lead to a higher concentration of nitrogen-vacancies resulting in a large carrier concentration. Reflectivity measurements in the mid-IR spectral range show that for NwNs, the plasmon resonance appear at  $5316 \text{ cm}^{-1}$  ( $1.86 \mu\text{m}$ ),  $3532 \text{ cm}^{-1}$  ( $2.83 \mu\text{m}$ ),  $2116 \text{ cm}^{-1}$  ( $4.72 \mu\text{m}$ ) and  $1911 \text{ cm}^{-1}$  ( $5.23 \mu\text{m}$ ) for volume fraction  $f_1, f_2, f_3, f_4$  respectively (see the Figure 4.5 (a) and 4.5 (b), reflection of GaN ( $f_4$ ) is shown in supplementary data Figure B3.8). The lowest volume fraction GaN ( $f_1$ ) NwN has the highest exposed free surface, as well as the highest free carriers (see table 4.1). In the case of GaN nanorod, a minimum in the reflection spectra at  $1892 \text{ cm}^{-1}$  ( $5.28 \mu\text{m}$ ) is obtained that corresponds to the free-carrier plasmon resonances. Utilizing the Drude function (Eq. 4.3), reflection spectra are modelled using Fresnel's equation and the dielectric permittivity is obtained.

**Table 4.1.** Plasmonic and electrical properties of the GaN nanostructures.

| GaN nanostructures | Resonance Energy ( $E_p$ ) ( $\text{cm}^{-1}$ ) | FWHM ( $\Delta E$ ) (meV) | Carrier concentration ( $\text{cm}^{-3}$ ) | Mobility ( $\text{cm}^2/\text{Vs}$ ) | Optical loss ( $\epsilon_2$ ) at $E_p$ |
|--------------------|---|---------------------------|--|--------------------------------------|--|
| NwN ( $f_1$ )      | 5316  | 200                       | $3.2 \times 10^{20}$                       | 29                                   | 0.5                                    |
| NwN ( $f_2$ )      | 3530  | 240                       | $1.7 \times 10^{20}$                       | 12                                   | 1.6                                    |
| NwN ( $f_3$ )      | 2116  | 193                       | $6.1 \times 10^{19}$                       | 15                                   | 2.1                                    |
| NwN ( $f_4$ )      | 1911  | 152                       | $4.7 \times 10^{19}$                       | 19                                   | 1.9                                    |
| Nanorod            | 1892  | 220                       | $4.5 \times 10^{19}$                       | 13                                   | 2.2                                    |

The  $\epsilon_1$  of NwN ( $f_1$ ) to NwN ( $f_4$ ) and nanorod exhibit a positive-to-negative cross-over at  $5113 \text{ cm}^{-1}$ ,  $3515 \text{ cm}^{-1}$ ,  $2065 \text{ cm}^{-1}$ ,  $1820 \text{ cm}^{-1}$  and  $1808 \text{ cm}^{-1}$ , respectively, near to their plasma frequency, also known as of the epsilon-near-zero (ENZ) frequency (see Figure 4.5c). Note that plasma frequency and ENZ frequency coincide with each other only in the case of a lossless medium. In the present samples, GaN NwN ( $f_1$ ) has the lowest optical loss ( $\epsilon_2$ ) at the plasmon resonance frequency (see Figure 4.5d), which is lower than the  $\epsilon_2$  of visible plasmonic materials such as Au,<sup>25</sup> refractory transition metals,<sup>145</sup> metal nitrides TiN<sup>57,80</sup> and IR plasmonic materials such as ScN,<sup>98,126</sup> transparent conducting oxides<sup>80</sup> etc.

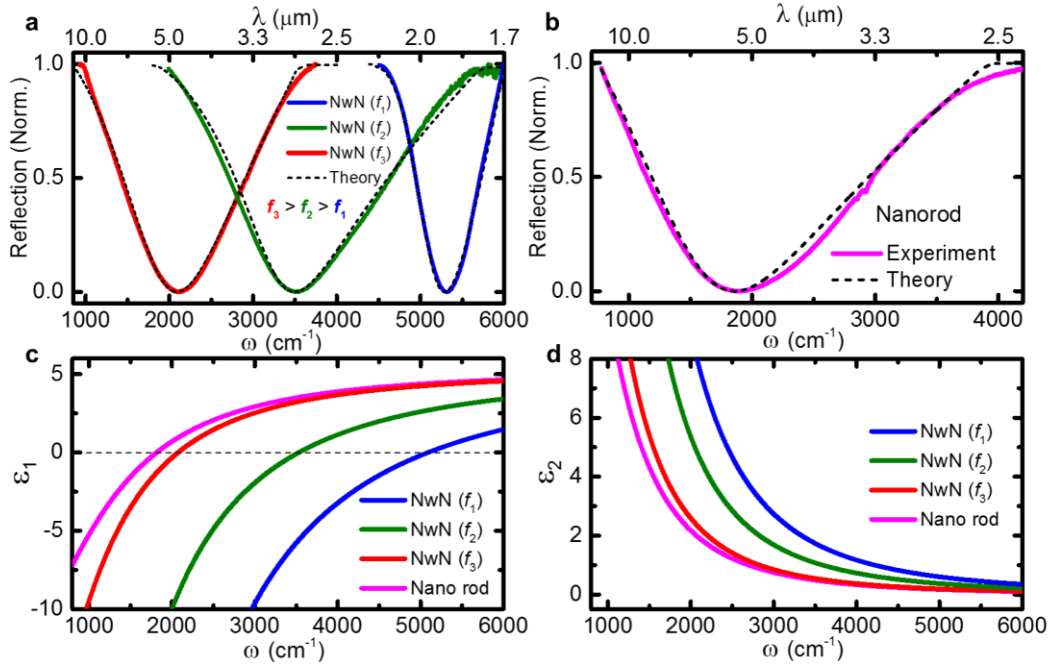


**Figure 4.5 Plasmon-polariton in GaN nanostructures.** (a) Plasmon response in GaN NwNs with volume fraction  $f_1$  (blue curve),  $f_2$  (green curve) and  $f_3$  (red curve) where  $f_3 > f_2 > f_1$ . (b) Plasmon response in GaN nanorods. GaN NwN exhibit more open surfaces compared to nanorods, consequently, more carriers are present in NwNs. The (c) real ( $\epsilon_1$ ) and (d) imaginary ( $\epsilon_2$ ) component of the dielectric permittivity of GaN NwNs of volume fraction  $f_1$  (blue curve),  $f_2$  (green curve),  $f_3$  (red curve) and nanorod (magenta curve).

In this work, we show that surface polariton excitations at the edges and asperities in GaN nanostructure significantly alter the shape of its far-IR Reststrahlen band. Located close to the LO phonon frequencies, the induced dipoles absorb optical phonons reducing the reflectance and modifying the Reststrahlen band. In addition, surface defects lead to carriers' generation, resulting in tunable plasmon resonances in the nanostructures. Excitation of the surface-polaritons in the far-IR and generation of high-quality low-loss plasmon-polaritons in mid-IR make GaN an attractive IR nanophotonic material.

#### 4.5 Plasmonic response of various mid-IR nanostructured plasmonic material

A comparison of the plasma frequency, damping factor and the plasmon resonance quality factor of GaN NwN with other well-established IR plasmonic materials show (see Figure 4.6) that depending on the fill fraction, the NwN and nanorods exhibit plasma frequency spanning a significant spectral range. The quality factor of the NwN's plasma resonance is also comparable to, or higher than other mid-infrared plasmonic nanostructures such as InN,<sup>146</sup> Al/ZnO,<sup>147</sup> Cu<sub>2-x</sub>S,<sup>148</sup> Sn/In<sub>2</sub>O<sub>3</sub>,<sup>149</sup> Ce/In<sub>2</sub>O<sub>3</sub><sup>150</sup> due to its low optical losses.

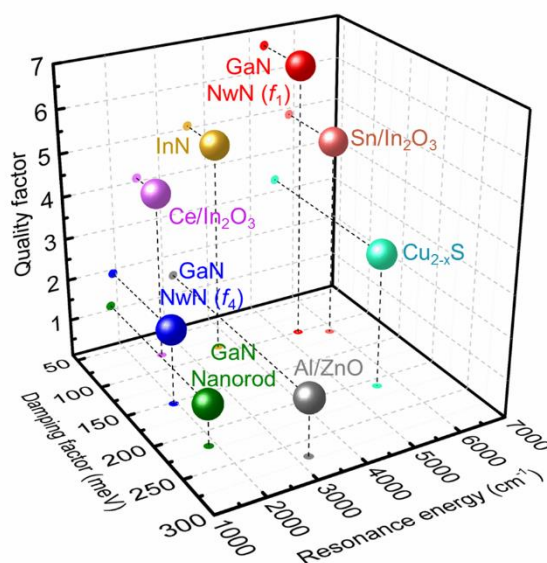


**Figure 4.6** Comparison of the plasmonic response of GaN nanostructures with other mid-IR nanostructured plasmonic material. GaN NwN ( $f_1$ ) exhibits a high-quality factor value of 6.6 which is higher than the previously reported quality factor for several nanostructured plasmonic materials such as InN, Al/ZnO, Cu<sub>2-x</sub>S, Sn/In<sub>2</sub>O<sub>3</sub>, Ce/In<sub>2</sub>O<sub>3</sub>. Low optical loss in the GaN nanostructure is the reason for the high-quality factor.

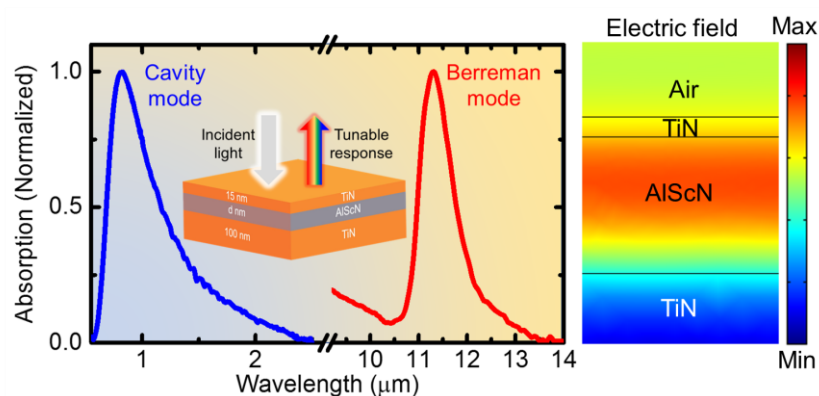
#### 4.6 Conclusion

In conclusion, optical resonance in GaN is extended from visible to far-and-mid infrared spectral regions by the excitation of surface-polariton and plasmon-polaritons modes in nanostructures, respectively. Single-crystalline hexagonal honeycomb-shaped GaN nanowall network and vertically standing nanorods are developed with a plasma-assisted molecular beam epitaxy (PAMBE). Surface polaritons resulting from the dipole-induced phonon absorption at surfaces, edges, and asperities in nanostructures are found to control the shape of the Reststrahlen band. Most surface polaritons occur close to the LO mode frequency due to the geometry of the sharp needle-like asperities standing out of the surface. The Reststrahlen band shape changed to right-trapezoidal with increased asperities and pore volume fraction from a rectangular shape in the planar epitaxial thin film. Free surfaces of the nanostructure also generate carriers with high concentrations, resulting in mid-infrared plasmon resonance with high-quality factors. Demonstration of morphology-controlled infrared resonances in GaN will further its progress in thermophotovoltaics, IR sensors, emitters, and other emerging device technologies.



## TiN/Al<sub>0.72</sub>Sc<sub>0.28</sub>N Metal/Dielectric Multilayers-based Bi-functional Optical Cavity

Traditionally, light-matter interactions in the visible spectral range utilize tailored plasmonic nanostructure in metals that often require advanced nanofabrication techniques. Concomitantly, polar lattice vibrations in dielectrics are used to achieve mid-to-long wavelength infrared (IR) light-matter coupling. Achieving optical resonances simultaneously in the visible and mid-to-long wavelength IR spectral range in one host medium has been challenging due to mutually conflicting material and optical property requirements. In this chapter, we show simultaneous light-matter coupling and development of super absorbers in the visible and mid-IR spectral ranges with a lithography-free planar wide-angle metal-(polar)-dielectric-metal (MDM) Fabry-Pérot cavity composed of ultrathin refractory metallic TiN as the top layer and polar dielectric Al<sub>0.72</sub>Sc<sub>0.28</sub>N as the spacer layer. Lattice-matched TiN/Al<sub>0.72</sub>Sc<sub>0.28</sub>N/TiN MDM cavities exhibit super absorption resonance with maximum absorptivity of ~ 99%. The absorption maxima spectral position is tuned with changes in spacer layer thickness and by utilizing multiple cavity interactions. Al<sub>0.72</sub>Sc<sub>0.28</sub>N inside the MDM is also used for light coupling to the transverse optical phonon mode and to the Berreman mode near the longitudinal phonon frequency with strong selective absorption. Demonstration of refractory epitaxial TiN/Al<sub>0.72</sub>Sc<sub>0.28</sub>N/TiN MDM metamaterials mark significant progress towards developing compact optical meta-structures with on-demand optical resonances at different spectral ranges.



## 5.1 Introduction

Artificially structured metamaterials provide unprecedented opportunities to control light-matter interactions at the nanoscale and lead to a plethora of device applications. Light-matter interactions in the visible and near-IR spectral ranges are utilized for various device technologies such as photovoltaics,<sup>151,152</sup> photodetectors,<sup>153</sup> photocatalysis,<sup>13</sup> phototransistors,<sup>154</sup> light emitting diodes (LEDs),<sup>155</sup> and electro-optic modulator<sup>156,157</sup>. At the same time, in recent years infrared light-matter coupling is becoming increasingly important for many other emerging device applications such as radiative cooling,<sup>127,158</sup> thermophotovoltaics,<sup>15,128,159</sup> telecommunication,<sup>160</sup> sensing,<sup>129</sup> and surveillance<sup>1302</sup>. Therefore, materials and structures that demonstrate simultaneous light-matter interactions and optical resonances in the visible and in mid-to-long wavelength IR spectral ranges would usher in a new era of compact multifunctional device technologies.<sup>77</sup>

Traditionally, light-matter interactions in the visible and near IR spectral range utilize plasmon resonance on metals and surface-plasmon-polaritons at metal/dielectric interfaces.<sup>19,80,145</sup> Various self-assembled and patterned nanostructures have been also employed for nanophotonic applications.<sup>161–163</sup> Plasmonic nanostructures have been used to achieve sub-wavelength light confinement, field localization, refractive index control, phase and amplitude control and others.<sup>164,165</sup> Many device functionalities such as perfect absorbers over a broad spectral range, or wavelength-selective perfect emitters, were also demonstrated.<sup>166–168</sup> Also, the planar multilayer structures have attracted significant interest for high absorptions using Tamm plasmon resonances (TP)<sup>169,170</sup>, coherent perfect absorption (CPA)<sup>171,172</sup> etc. The Tamm resonances can be achieved at the surface between a periodic dielectric structure (Bragg mirror) and a metallic layer, while the CPA can be achieved in MDM structure by optimizing the thickness and permittivity of the metal-dielectric layers. However, tailored optical resonances in most of these devices are usually achieved with nanostructures that often require advanced lithography and nanofabrication methods.<sup>166–168,173</sup> Moreover, spectral selectivity and device performance are strongly dependent on the periodicity, size and shape of these nanostructures, which limits their application space.

Similarly, optical resonance in the mid-to-long wavelength IR spectral range utilizes polar dielectrics, where the electromagnetic wave can couple to the polar lattice vibrations.<sup>22,87,125</sup>

Owing to the transverse nature of the electromagnetic wave, light couples directly to the transverse optical (TO) phonon modes in polar dielectrics such as AlN<sup>91</sup>, SiC<sup>88</sup>, GaN<sup>112</sup>, ScN<sup>98,126</sup>, and leads to the phonon-polaritons (a hybrid quasiparticle made of photons and phonons) formations. As a result of such coupling, polar dielectrics exhibit negative dielectric permittivity within a frequency range, known as the Reststrahlen band that is encompassed by the transverse optical (TO) and longitudinal optic (LO) phonon modes.<sup>23</sup> Due to the negative permittivity, polar dielectrics behave like conventional metals and reflect incident radiation strongly within the Reststrahlen band. Along with the direct coupling and optical absorption with the TO phonon modes, electromagnetic modes can also couple to the leaky polaritonic Berreman modes<sup>174,175</sup> near the LO phonon frequency in planar polar dielectric films deposited on metal surfaces. Coupling of light with such Berreman mode also leads to optical absorptions and is proposed for selective emitter design in the mid-IR spectral ranges.

Therefore, (meta)-materials or (meta)-structures that can utilize the light-matter interactions over the visible to long-wavelength IR spectral range could lead to many hybrid device functionalities that no individual materials can provide.<sup>77</sup> Yet, despite the apparent benefits very little progress has been in this pursuit primarily due to the materials incompatibility and nanofabrication challenges. For example, noble metals such as Ag and Au are used for the plasmon resonance in the near-UV-to-visible spectral ranges. However, as noble metals do not possess optical phonon modes, they do not lead to optical resonances in the mid-to-long wavelength IR spectral ranges. Similarly, though polar dielectrics exhibit the light-matter coupling in the mid-to-long wavelength IR spectral ranges, they do not show plasmonic response due to the absence of carriers. Noble metals are also soft and unstable at high temperatures, which compounds this fundamental material incompatibility challenge.<sup>80</sup> Due to their high surface energies, noble metals cannot be deposited in thin-film and ultrathin film with low roughness. At the same time, noble metals are not compatible with complementary-metal-oxide-semiconducting (CMOS) technologies and are not suitable for epitaxial heterostructure development without atomic intermixing at the interfaces.<sup>176</sup>

With the emergence of transition metal nitrides (TMNs) as alternative plasmonic materials,<sup>59,80,126,177</sup> the situation has improved substantially. TMNs such as TiN are mechanically hard, corrosion-resistant, exhibit a high melting temperature, and can be

deposited in ultrathin films with low surface roughness.<sup>61,63</sup> Planar epitaxial TiN/Al<sub>0.72</sub>Sc<sub>0.28</sub>N metal/dielectric superlattices with nanoscale period thicknesses have been developed that exhibit hyperbolic photonic dispersion and a significantly enhanced photonic density of states, as well as tunable plasmonic resonances.<sup>178,179</sup> Such superlattice metamaterials are also found to be stable at high-temperatures for an extended period of time.<sup>180,181</sup> While TiN in TiN/Al<sub>0.72</sub>Sc<sub>0.28</sub>N metamaterials act as the metallic component, it is also important to note that Al<sub>0.72</sub>Sc<sub>0.28</sub>N is a polar dielectric that can support optical resonances in the mid-to-long wavelength IR spectral range. AlN, which is the parent material of Al<sub>x</sub>Sc<sub>1-x</sub>N, is a well-known polar dielectric with the TO and LO phonon mode frequencies at 673 cm<sup>-1</sup> and 890 cm<sup>-1</sup>, respectively. Though the inclusion of scandium inside AlN is necessary for stabilizing Al<sub>x</sub>Sc<sub>1-x</sub>N in the rocksalt phase,<sup>182</sup> and for the lattice-matching with TiN, it does not change AlN's polar semiconducting nature considerably.

In this work, motivated by the idea of creating simultaneous optical resonances in the visible and mid-to-long wavelength IR spectral ranges, we demonstrate epitaxial TiN/Al<sub>0.72</sub>Sc<sub>0.28</sub>N/TiN MDM Fabry-Pérot cavity that not only results in tunable super absorption in the 500-1200 nm spectral range but also exhibit narrow-band selective absorption/emission corresponding to Al<sub>0.72</sub>Sc<sub>0.28</sub>N's TO phonon mode and Berreman mode frequencies. Importantly, we achieve three different types of resonances, namely Fabry-Pérot cavity resonance,<sup>169</sup> light coupling to the polar TO phonon modes and to the Berreman modes<sup>183</sup> in one planar, lithography-free large-area CMOS compatible MDM structure deposited on insulating substrates that can be seamlessly integrated with devices.

## 5.2 Growth of TiN/Al<sub>0.72</sub>Sc<sub>0.28</sub>N/TiN MDM structures

TiN/Al<sub>0.72</sub>Sc<sub>0.28</sub>N/TiN MDM Fabry-Pérot cavity heterostructures are fabricated on (001) MgO substrates with dc-magnetron sputtering inside an ultrahigh vacuum chamber at a base pressure of  $2 \times 10^{-9}$  Torr. All growths are performed at 10 mTorr deposition pressure at a substrate temperature of 800°C. Details about the growth method are presented in Appendix B4 supplementary data (SD) section B4.1. Structural properties of the heterostructure metamaterials determined with high-resolution (scanning) transmission electron microscopy (HR(S)/TEM) imaging (see Fig. 5.1 for a representative double cavity structure) show that the TiN and Al<sub>0.72</sub>Sc<sub>0.28</sub>N layers grow with cubic epitaxy on (001) MgO surfaces. The 100 nm thick bottom TiN layer serves as the back mirror for light reflection and grows with lattice-matched epitaxy. The Al<sub>0.72</sub>Sc<sub>0.28</sub>N layers are homogeneous,

uniform and exhibit very little interface roughness with TiN (see Fig. 5.1(b)). The atomic resolution STEM image in Fig. 5.1(c) shows coherent growth of Al<sub>0.72</sub>Sc<sub>0.28</sub>N layers on TiN with [001] (001) Al<sub>0.72</sub>Sc<sub>0.28</sub>N || [001] (001) TiN epitaxial relationship. The STEM energy dispersive x-ray spectroscopy (EDS) analysis show Ti, Al, and Sc have not been diffusing between the layers during growth. Due to the x-ray emission peak overlap between Sc and N, the N map shows slight inhomogeneities.

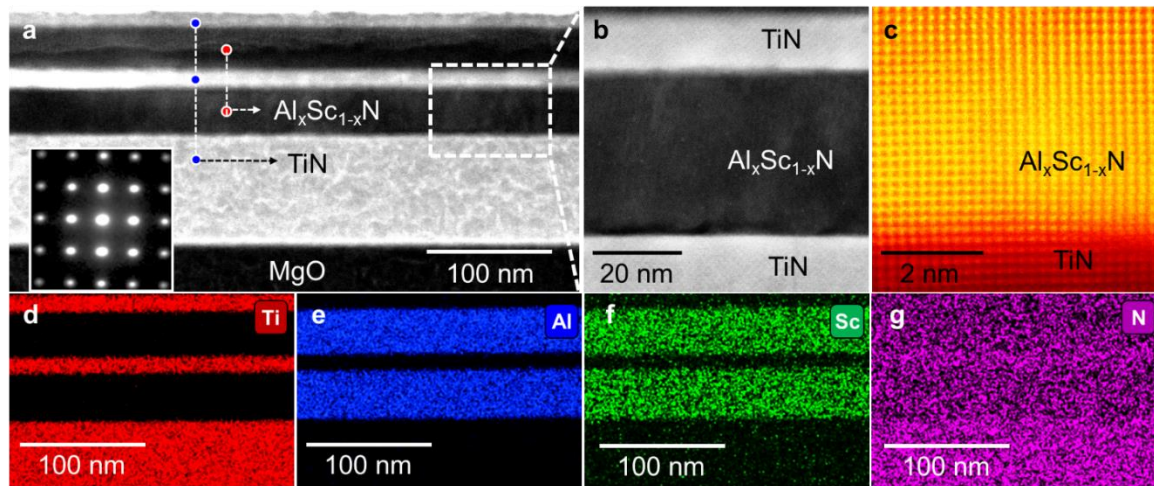


**Figure 5.1** a) STEM micrograph of TiN/Al<sub>0.72</sub>Sc<sub>0.28</sub>N multilayer stack deposited on (001) MgO is presented. Coherent epitaxial interfaces between different layers are visible in the images. The electron diffraction pattern in the inset confirms the lattice-matched cubic epitaxial growth. b) High-magnification STEM image highlight the TiN/Al<sub>0.72</sub>Sc<sub>0.28</sub>N interfaces. c) Atomic resolution STEM image of the TiN/Al<sub>0.72</sub>Sc<sub>0.28</sub>N interface is presented demonstrating a sharp interface. STEM-EDS elemental mapping of d) Ti, e) Al, f) Sc, and g) N demonstrates well-separated layers without diffusion of atoms into adjacent layers.

### 5.3 Optical characterization of TiN/Al<sub>0.72</sub>Sc<sub>0.28</sub>N/TiN MDM structures

MDM cavities are fabricated with a 100 nm TiN as the bottom layer for super absorber design in the visible spectral range. The top TiN layer thickness is kept constant at 15 nm, while the Al<sub>0.72</sub>Sc<sub>0.28</sub>N spacer layer thickness is varied from 50 nm to 100 nm and 150 nm (see Fig. 5.2(a)). As the bottom TiN layer is optically opaque with zero transmission, the absorptivity ( $A$ ) of the structures is calculated from the reflectivity spectrum with  $A=1-R$  ( $T=0$ ) relationship. Absorption spectra show that all the three cavity structures exhibit very high absorption maxima at 99%, 97%, and 97% respectively (see Fig. 5.2(b)). It is also important to note that the absorption maxima in the three structures cover a large portion

of the visible-to-near-IR spectral range (580 nm- 1200 nm). A higher-order absorption peak starts to appear at ~ 480 nm for the MDM cavity with a spacer layer thickness of 150 nm.

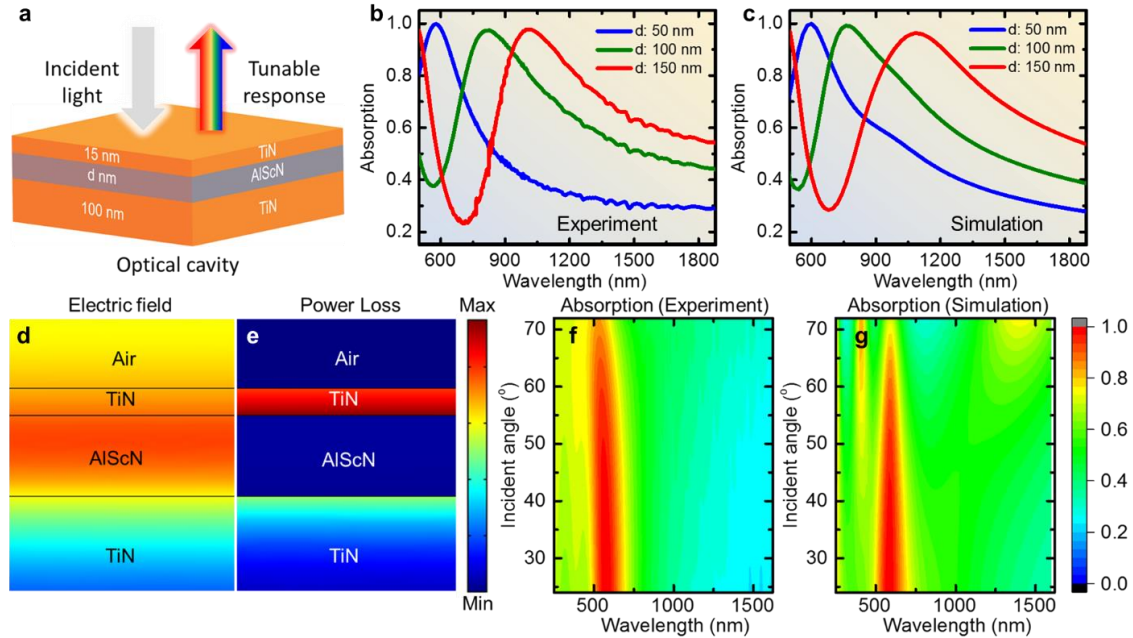


**Figure 5.2** a) Schematic diagram of the unit cell of metal-dielectric-metal (MDM) optical cavity. b) Experimental and c) simulated absorption spectra of the MDM structures with varying dielectric Al<sub>0.72</sub>Sc<sub>0.28</sub>N layer thickness (50 nm (blue), 100 nm (green), 150 nm (red)). d) Magnitude of electric field profile and (e) electromagnetic power-loss density distribution for the MDM structure (50 nm of Al<sub>0.72</sub>Sc<sub>0.28</sub>N thickness) at the maximum absorption peak wavelength of 580 nm. f) Experimental and g) simulated angle-dependent absorption curve of MDM structure (of 50 nm thick Al<sub>0.72</sub>Sc<sub>0.28</sub>N).

The MDM cavities' absorption spectra are simulated with the finite element method (FEM). The complex dielectric constants of the bottom 100 nm and top 15 nm TiN, and Al<sub>0.72</sub>Sc<sub>0.28</sub>N spacer layers are obtained with spectroscopic ellipsometry measurements (see Appendix B4 supplementary data (SD) section B4.4 for details). The real component of the dielectric permittivity ( $\epsilon_1$ ) of TiN shows a positive-to-negative transition at ~ 480 nm that corresponds to the wavelength associated with TiN's plasma frequency. The optical losses, represented by the imaginary component of the dielectric permittivity ( $\epsilon_2$ ) of TiN, increase with an increase in the wavelength due to free-electron Drude scattering. The wavelength corresponding to the plasma frequency and dielectric permittivity of TiN is comparable to previous reports.<sup>59,80,177</sup> Al<sub>0.72</sub>Sc<sub>0.28</sub>N spacer layers, on the other hand,

exhibit nearly constant permittivity above 500 nm that is consistent with its dielectric nature. Due to the direct bandgap of Al<sub>0.72</sub>Sc<sub>0.28</sub>N of ~ 3.4 eV, Lorentz peaks are observed in both spectrums (see supplementary data (SD) Fig. B4.1 (b)). Notably, the optical losses of Al<sub>0.72</sub>Sc<sub>0.28</sub>N are negligible above 500 nm spectral range. As shown in Fig. 5.2(c), the calculated absorption spectra of MDM structures match the experimental results. The peak positions, peak-width, and peak-shape are nearly identical between the experiment and simulated results.

Unlike the spectrally selective absorbers that use the plasmon resonances, the super absorbers developed in this work utilize light interference inside the MDM cavity. The Fabry-Pérot cavity with a nearly lossless dielectric spacer layer bounded by the optically thick bottom metallic TiN and thin top TiN layer supports the coherent perfect absorption (CPA). The behavior of the cavity resonance can be described qualitatively by the resonance condition,<sup>169</sup>

$$2 \left( \frac{2\pi}{\lambda_{res}} \right) n_d t_d + \varphi_{Bottom-TiN} + \varphi_{Top-TiN} = 2m\pi \quad (1)$$

The first term on the left side of the equation represents the round-trip propagation phase shift within the cavity. Where  $n_d$  and  $t_d$  are the refractive index and thickness on the dielectric Al<sub>0.72</sub>Sc<sub>0.28</sub>N layer.  $\lambda_{res}$  is the resonance wavelength and  $m$  is an integer number determining the order of cavity mode.  $\varphi_{Bottom-TiN}$  and  $\varphi_{Top-TiN}$  are the phase shifts upon reflection at the bottom and top metal-dielectric interfaces, respectively. The FEM simulation-derived electric field distributions show the underlying mechanism more clearly. Fig. 5.2 (d) shows that the electric field is highly confined inside the Al<sub>0.72</sub>Sc<sub>0.28</sub>N spacer layer due to the formation of standing waves. Constructive interference between the incoming and reflected light leads to such effects with the field maxima located at the center of the spacer layer. Since the electric field is maximum at the middle of the spacer layer, most energy is absorbed in the top metal layer and at the bottom spacer/metal interfaces, as shown in Fig. 5.2(e).

Further, the origin of the optical resonance of the MDM structures is explained using a quantum mechanical description of the MDM cavity as a double barrier quantum well and the classical harmonic oscillator model (as presented in detail in the reference<sup>184,185</sup>). TiN

is found to satisfy the Hermiticity limit to obtain the resonances by resonant tunnelling through the metal (see Appendix B4 supplementary data figure B4.4). On the other hand, using the effective dielectric permittivity obtained from the classical harmonic oscillator, we show that the cavity resonance corresponds to the epsilon-near-zero (ENZ) mode of the MDM structures (see the supplementary data section-B4.7 and section-B4.8 for the detailed analysis). Both the classical oscillator and the quantum mechanical approaches exhibit very good agreement with the experimental results.

Angle-dependent absorption is further measured (see Fig. 5.2(f)), and its numerical simulation results are presented in Fig. 5.2(g). The super absorption peak is visible at all angles of incidence (24°-72°). However, the super absorption intensity decreases with an increase in the angles of incidence. From the measured absorption spectra (Fig. 5.2(b)), a resonance full-width-half-maxima (FWHM) of 175 nm, 324 nm, and 367 nm is calculated that lead to a quality factor ( $Q$ -factor) of 3.3, 2.5, and 2.7 for the three MDM structures with 50 nm, 100 nm, and 150 nm spacer layer thicknesses. Though the  $Q$ -factors ( $\lambda/\Delta\lambda$ ) are rather low, it is a manifestation of the higher optical loss of TiN compared to noble metals such as Ag and Au.<sup>186</sup> While a narrowband absorber is generally useful for sensing, imaging and color filter applications,<sup>186-188</sup> the slightly broadband TiN-based absorber can be useful for thermal photovoltaics, radiative cooling, photodetectors, etc.<sup>189,190</sup> Since the dielectric properties of TiN can also be tuned with growth conditions, a narrowband absorber can be achieved by reducing the optical loss of the metallic TiN. Also, it is known that the cavity mode can be tailored by ultrafast optical pumping, which increases the local permittivity and results in a redshift in the resonance mode.<sup>191</sup> This approach can be useful for the TiN/Al<sub>0.72</sub>Sc<sub>0.28</sub>N/TiN MDM multilayer structure as well, which will further the progress in ultrafast manipulation of optical nonlinearities, such as high harmonic generation and other ultrafast light-driven technologies.

#### 5.4 Optical characterization of TiN/Al<sub>0.72</sub>Sc<sub>0.28</sub>N based double cavity

Besides demonstrating tunable absorption in the visible spectral range, optical resonance engineering is performed through multi-cavity interactions. An additional 50 nm Al<sub>0.72</sub>Sc<sub>0.28</sub>N spacer layer and 15 nm thick TiN layer are deposited on the existing MDM structure with 50 nm Al<sub>0.72</sub>Sc<sub>0.28</sub>N spacer layer (see Fig. 5.3(a)). The first-order mode at 580 nm splits into two at ~ 440 nm ( $\lambda_1$ ) and ~ 690 nm ( $\lambda_2$ ) (see Fig. 5.3(c)). Such splitting



of the modes due to multi-cavity interactions<sup>185,192</sup> is an effective way to achieve tailored absorptions in the desired spectral ranges and is well-supported by the simulation results (see Fig. 5.3(d)). Simulation results show that corresponding to the first split peak at ~ 440 nm, the electric field is highly confined in cavity 2 (or the bottom cavity spacer layer). Whereas the electric field is found to be maximum at the Al<sub>0.72</sub>Sc<sub>0.28</sub>N spacer layer inside cavity 1 for the second peak located at ~ 690 nm (see Fig. 5.3(e) and 5.3(f)). Similarly, most of the energy is absorbed in the top and middle TiN layers as well as at the TiN/Al<sub>0.72</sub>Sc<sub>0.28</sub>N interfaces as Fig. 5.3(g) and 5.3(h) show. Higher-order cavity mode splitting experiments and simulations are further performed, and the results are presented in the supplementary data section-B4.6. This splitting of optical modes due to the interactions among multiple cavities is analogous to the formation of bonding and antibonding orbitals in the molecular orbital theory.<sup>193,194</sup>

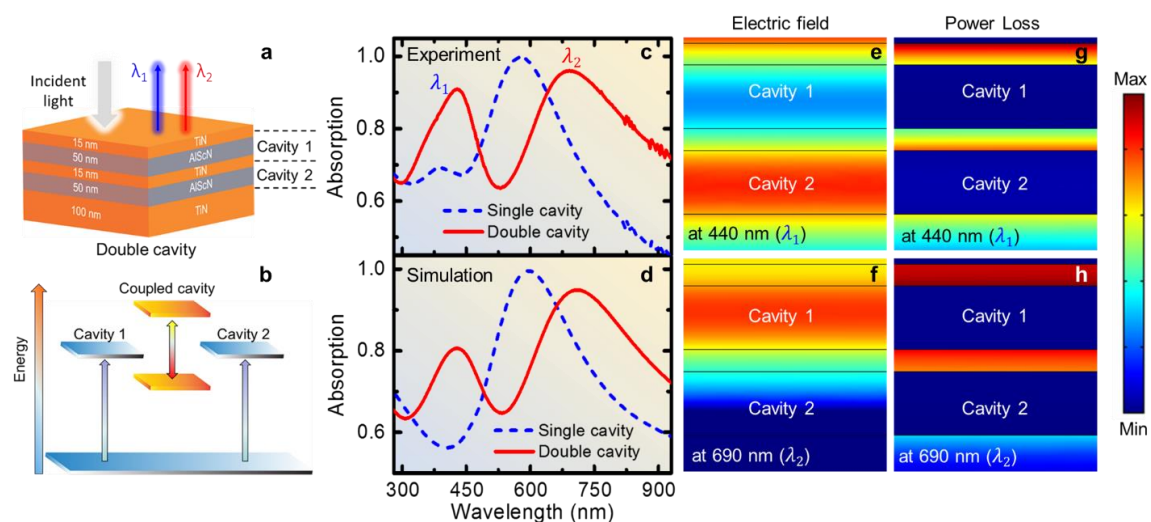


**Figure 5.3** a) Schematic diagram of TiN/Al<sub>0.72</sub>Sc<sub>0.28</sub>N based double cavity structure. b) Schematic diagram that shows the splitting of energy states due to the coupling between double cavities. c) Experimental and d) simulated absorption spectra of double cavity mode (red line) along with the single cavity mode (blue dash line). The splitting of the curve corresponds to the direct coupling of the two cavities. (e, f) Magnitude of electric field profile and (g, h) electromagnetic power-loss density distribution for the double cavity (50 nm of Al<sub>0.72</sub>Sc<sub>0.28</sub>N thickness) at the maximum absorption peak wavelength of 440 nm and 690 nm.

## 5.5 Optical phonon modes in MDM structures

Having demonstrated super absorbers in the visible spectral range with MDM Fabry-Pérot cavities, we focus on achieving selective absorption at the mid-IR frequencies. The absorption spectrum of the cavity structures in the mid-to-long wavelength IR is measured with a Fourier Transform Infrared spectrometer (FTIR). Since the bottom 100 nm TiN is optically opaque for light transmission in the entire mid-to-long wavelength IR, reflectivity (R) measurements and subsequent utilization of the  $A=1-R$  relationship are used to obtain the absorption. MDM cavity with 100 nm  $\text{Al}_{0.72}\text{Sc}_{0.28}\text{N}$  spacer layer exhibits an absorption peak at  $891\text{ cm}^{-1}$  (see Fig. 5.4(a)) corresponding to the Berreman mode excitation near the  $\text{Al}_{0.72}\text{Sc}_{0.28}\text{N}$ 's LO phonon frequency (discussed in detail subsequently). The FWHM of the absorption peak is  $62\text{ cm}^{-1}$ , which results in a measured  $Q$ -factor of 14. Similarly, cavities with 50 nm and 150 nm  $\text{Al}_{0.72}\text{Sc}_{0.28}\text{N}$  spacer layers exhibit selective absorption due to the Berreman mode excitations (see supplementary data Fig. B4.8). It is important to note that the Berreman mode mid-IR absorption is visible in these MDM metamaterials despite the presence of a 15 nm TiN on top of the  $\text{Al}_{0.72}\text{Sc}_{0.28}\text{N}$  spacer layer. Removal of the top TiN layer increases the absorption coefficient slightly (as shown in Fig. 5.4(a)). These results, therefore, show that the MDM Fabry-Pérot cavities exhibit simultaneous visible and mid-IR light absorption (as shown in Fig. 5.4(b)).

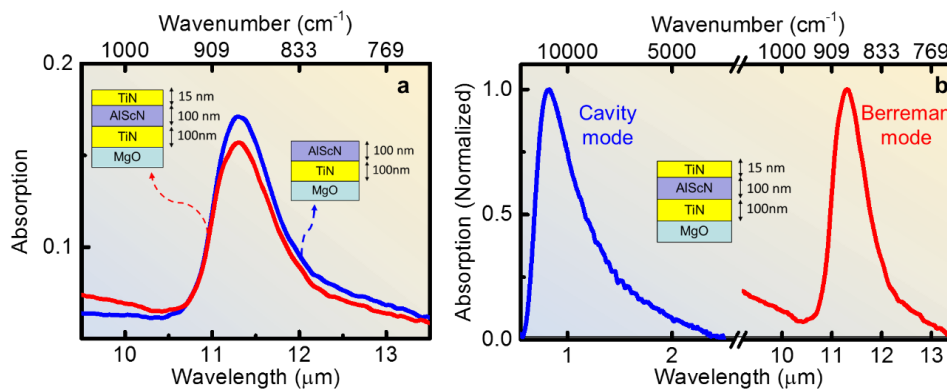


**Figure 5.4** Effect of TiN top-layer on  $\text{Al}_{0.72}\text{Sc}_{0.28}\text{N}/\text{TiN}/\text{MgO}$  sample in IR and visible range. a) FTIR reflection of  $\text{Al}_{0.72}\text{Sc}_{0.28}\text{N}/\text{TiN}/\text{MgO}$  and  $\text{TiN}/\text{Al}_{0.72}\text{Sc}_{0.28}\text{N}/\text{TiN}/\text{MgO}$  samples. Thin TiN (15 nm) top layer film does not affect the optical phonon much, while strong absorption in the visible range appeared due to the cavity resonance. (b) Simultaneous optical resonances, cavity mode and Berreman mode can be achieved in MDM structures.

Detailed experiments and modeling are performed to determine the absorption mechanism. Reflectivity measurement ( $R$ ) of (001) MgO substrates show a clear and well-defined Reststrahlen band with more than 90 % of the incident light reflected within the band. From the fitting of the reflectivity spectrum with the Fresnel equation, TO and LO phonon frequencies of 395  $\text{cm}^{-1}$  and 795  $\text{cm}^{-1}$  are determined for MgO (see Fig. 5.5a) which is consistent with literature reports.<sup>195</sup> Similarly, when a thick 200 nm AlN (parent polar dielectric Al<sub>0.72</sub>Sc<sub>0.28</sub>N) layer is deposited on (001) MgO substrate, two distinct Reststrahlen bands are observed in the reflectivity spectrum. One of the Reststrahlen bands corresponds to MgO, while the other results from light reflection from the AlN Reststrahlen band. Fitting the spectrum with the Fresnel equation further shows that an LO and TO phonon frequency of 673  $\text{cm}^{-1}$  and 896  $\text{cm}^{-1}$  for AlN is consistent with previous reports.<sup>196</sup> With the demonstration of the Reststrahlen bands, 200 nm AlN layer is deposited on a 100 nm TiN base-layer on (001) MgO substrate. Such metal/polar-dielectric structures are known to support leaky modes known as Berreman modes. Though these optical modes were initially attributed to the excitation of LO phonon modes,<sup>183</sup> later research showed that these modes correspond to phonon-polariton in polar-dielectrics that fall within the light cone and a surface mode beyond the light cones that are characterized with a real wave vector and complex frequency.<sup>174</sup>

The reflectivity ( $R$ ) spectrum of the 200 nm AlN deposited on 100 nm TiN, indeed, shows the coupling of incident light with the Berreman modes with a sharp dip in the reflection at 891  $\text{cm}^{-1}$  that is very close to AlN's LO phonon frequency (see Fig. 5.5b). The FWHM of the absorption peak corresponding to the Berreman peak is 32  $\text{cm}^{-1}$ , resulting in a  $Q$ -factor of 28. The reflectivity ( $R$ ) spectrum also shows a dip at 673  $\text{cm}^{-1}$  that is close to the TO phonon frequency of AlN and represents the direct light coupling to the TO mode of AlN. The Fresnel equation is modified to model the reflectivity spectrum, and a Berreman term<sup>183</sup> is included. The total reflection coefficient is obtained by using the equation (2)

$$R = R_{Fresnel} \times R_{Berreman} = \left| \frac{r_{12} + r_{23} e^{2ik_z d}}{1 + r_{12} r_{23} e^{2ik_z d}} \right|^2 \left[ 1 - 4\delta \left( \frac{\text{Im}(\epsilon_{PD})}{\text{Re}(\epsilon_{PD})^2 + \text{Im}(\epsilon_{PD})^2} \right) \right] \quad (2)$$

Where the first term ( $R_{Fresnel}$ ) represents reflectivity for the three-layer system by utilizing the Maxwell's equation,  $r_{ij}$  is the complex reflection coefficient between layers  $i$  and  $j$  (with layers 1, 2, and 3 referring to air, AlN, and TiN, respectively), and  $k_{zi}$  is the

wavevector component of light in the  $i^{\text{th}}$  layer. The second term ( $R_{\text{Berreman}}$ ) is Berreman's term to explain light absorption near to the LO mode of AlN, and  $\epsilon_{PD}$  is the permittivity of AlN

$$\epsilon_{PD} = \epsilon_{\infty} \left( 1 + \frac{\omega_{LO}^2 - \omega_{TO}^2}{\omega_{TO}^2 - \omega^2 - i\omega\Gamma} \right) \quad (3)$$

Here the  $\omega_{LO}$  ( $\omega_{TO}$ ) is the LO (TO) phonon frequencies of AlN respectively,  $\Gamma$  is the damping of the phonons, and  $\delta/2\pi$  is the thickness of the dielectric film, measured in vacuum wavelengths of the incident radiation. Fig. 5.5(b) show that the modeled reflectivity spectrum matches well with the experimental results.

Further,  $\text{Al}_{0.72}\text{Sc}_{0.28}\text{N}$  layers with thicknesses of 100 nm and 1000 nm (1  $\mu\text{m}$ ) are deposited on 100 nm TiN, respectively and their reflection spectra are measured. For both  $\text{Al}_{0.72}\text{Sc}_{0.28}\text{N}$  films, light coupling to the Berreman modes is observed at  $\sim 895 \text{ cm}^{-1}$  (see Fig. 5.5c), which is close to AlN's LO phonon frequency. As mentioned previously, the inclusion of scandium inside AlN does not impact the high-frequency LO modes due to the higher atomic mass of scandium atoms. The absorption measurements, therefore, confirm it. Reflection spectra of 1  $\mu\text{m}$   $\text{Al}_{0.72}\text{Sc}_{0.28}\text{N}$  film also show the light coupling to the TO optical phonon mode at  $565 \text{ cm}^{-1}$  at a slightly smaller frequency than AlN. Optical phonon modes in  $\text{Al}_x\text{S}_{1-x}\text{cN}$  have been studied in detail and similar consequence has been seen in the previous reports.<sup>197</sup> The broadening and shift of the mode frequencies can unambiguously be attributed to an elongation of Al (Sc)-N bonds because of Sc doping. Contrary to that, 100 nm  $\text{Al}_{0.72}\text{Sc}_{0.28}\text{N}$  film show almost no reflection dip at the TO phonon frequency. This behavior was also observed previously for thin AlN layers deposited on metallic Mo layers<sup>198</sup> due to the small optical path length for the light to couple with the sample's TO phonon. It is important to note that though the absorption peaks in AlN and  $\text{Al}_{0.72}\text{Sc}_{0.28}\text{N}$  are located near to one another, the FWHM of the  $\text{Al}_{0.72}\text{Sc}_{0.28}\text{N}$  peaks is much broader than that of AlN's absorption peak. Compared to the AlN absorption peak FWHM of  $14 \text{ cm}^{-1}$  (for TO) and  $32 \text{ cm}^{-1}$  (for LO),  $\text{Al}_{0.72}\text{Sc}_{0.28}\text{N}$  exhibits a much larger FWHM of  $103 \text{ cm}^{-1}$  (for TO) and  $102 \text{ cm}^{-1}$  (for LO). Such higher FWHM results from higher damping constant of  $\text{Al}_{0.72}\text{Sc}_{0.28}\text{N}$  with respect to AlN, leading to  $\text{Al}_{0.72}\text{Sc}_{0.28}\text{N}$ 's smaller resonance  $Q$ -factor. Since the inclusion of scandium inside AlN is necessary to achieve

rocksalt-Al<sub>0.72</sub>Sc<sub>0.28</sub>N with lattice-matched interfaces, there seems to be a tread-off between the structural requirements for stable epitaxial film and high-quality optical resonance.

The spectral response of the Berreman modes can be further calculated<sup>198</sup> in the limit of optically thin Al<sub>0.72</sub>Sc<sub>0.28</sub>N layers.

$$\varepsilon_{PD}k_{z1} + idk_{z2}^2 = 0 \quad (4)$$

The dispersion spectrum (see Fig. 5.5d) shows that the thin 100 nm Al<sub>0.72</sub>Sc<sub>0.28</sub>N layer exhibits close to angle independent Berreman mode frequencies. Whereas 1  $\mu\text{m}$ . Al<sub>0.72</sub>Sc<sub>0.28</sub>N exhibits a much dispersive Berreman mode spectral response. Though the experiments are performed for a fixed angle of incident, the Berreman mode frequencies in the experiment and in the dispersion spectrum match with each other.

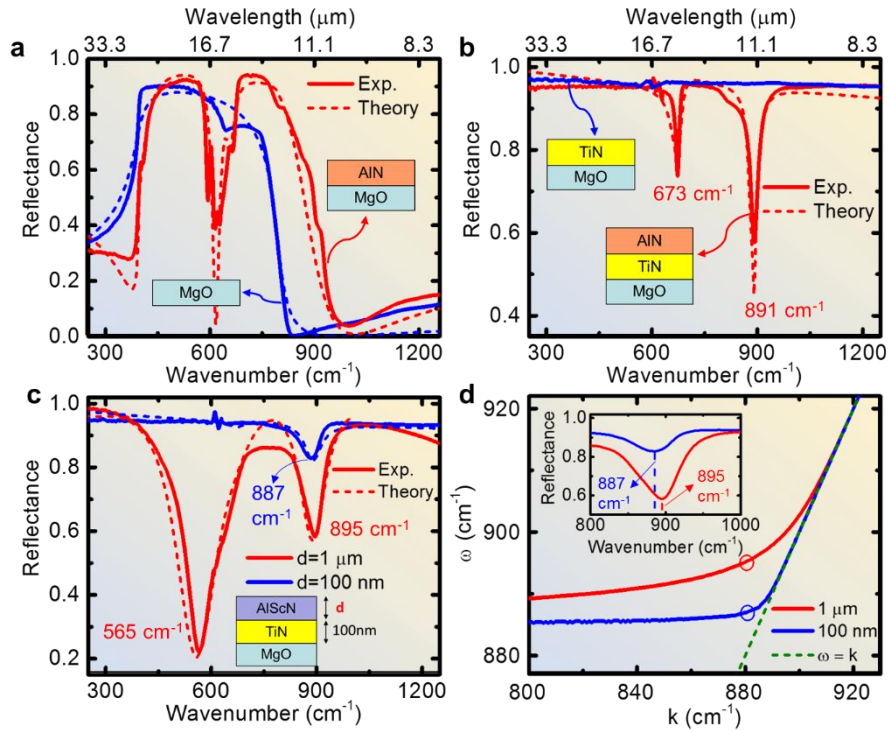


**Figure 5.5** FTIR Reflection spectra are collected from a) AlN/MgO (red) along with MgO substrate (blue). For MgO substrate, a clear Reststrahlen band spread over 395  $\text{cm}^{-1}$  to 767  $\text{cm}^{-1}$ . For the sample AlN/MgO, two Reststrahlen bands appeared from AlN and MgO. b) Reflection spectra of TiN/MgO and AlN/TiN/MgO. Metal TiN reflectivity is around 95% in the whole FTIR spectral range. For the sample AlN/TiN/MgO, two dips in the reflection spectra correspond to the absorption of TO and LO phonon of AlN. c) IR-reflection of Al<sub>0.72</sub>Sc<sub>0.28</sub>N/TiN/MgO samples of two different thicknesses of Al<sub>0.72</sub>Sc<sub>0.28</sub>N 100 nm and 1000nm is compared. Two dips in the reflection spectra correspond to the TO and LO modes appearing in the thicker Al<sub>0.72</sub>Sc<sub>0.28</sub>N while the optical modes are barely visible in the thinner film. d) Berreman mode dispersion

---

relationship for 100 nm (blue) and 1  $\mu\text{m}$  (red) thick  $\text{Al}_{0.72}\text{Sc}_{0.28}\text{N}/\text{TiN}$  samples calculated using Eq. 3. The light line is shown as a dotted green line. The inset shows the Berreman mode of  $\text{Al}_{0.72}\text{Sc}_{0.28}\text{N}$  films.

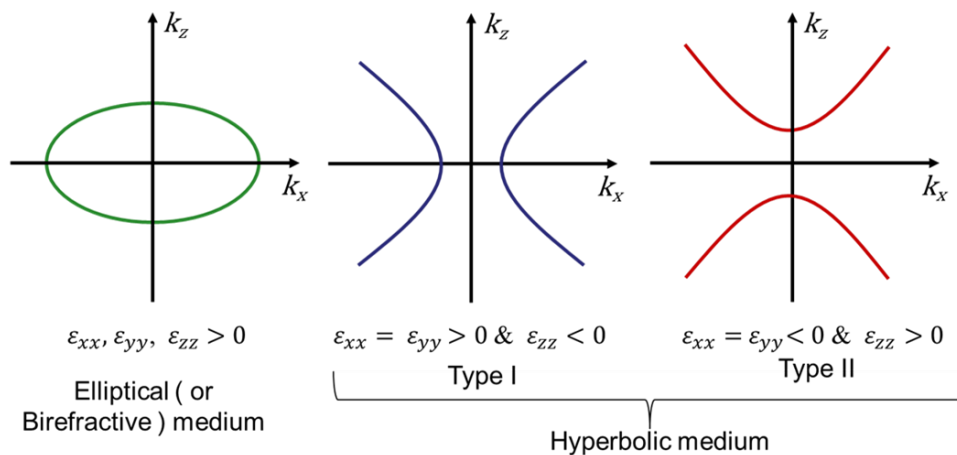
Therefore, this study demonstrates that the metal-polar dielectric-metal multilayer structures can provide dual optical resonances at two different spectral regimes. The cavity resonance governs the optical absorption in the visible-to-NIR spectral range, while excitation of the TO phonon and the Berreman modes leads to light absorption in the mid-to-long wavelength infrared regime. In addition, we achieve both of these resonances utilizing refractory epitaxial and CMOS-compatible TiN as the plasmonic and  $\text{Al}_{0.72}\text{Sc}_{0.28}\text{N}$  as the polar-dielectric layer that overcomes many of the material challenges that noble metal-based optical structures encounter. Through the present work exhibit, optical resonances in the 580 nm - 1200 nm for the visible-to-NIR and 10.5  $\mu\text{m}$  - 13  $\mu\text{m}$  in the mid-to-long wavelength IR spectral ranges, the structures could be further optimized to achieve the resonances at specific wavelengths necessary for radiative cooling and thermophotovoltaic applications.

## 5.6 Conclusion

In conclusion, we show simultaneous light-matter interaction and optical resonance in the visible and mid-IR spectral range with a lithography-free planar wide-angle  $\text{TiN}/\text{Al}_{0.72}\text{Sc}_{0.28}\text{N}/\text{TiN}$  metal-(polar)-dielectric-metal (MDM) Fabry-Pérot cavity. Tunable super absorption with absorptivity exceeding 99 % is achieved in the 580 nm - 1200 nm spectral range by varying the dielectric layer thickness inside the MDM cavity. Splitting of the cavity modes through interactions between multiple cavities is also demonstrated as a method to tailor the optical absorption in the visible-to-near-IR spectral region. The MDM metamaterials are shown to exhibit mid-to-long IR light absorption due to the direct light coupling not only to the transverse optical (TO) phonon modes but also to the leaky polaritonic Berreman modes. Detailed analysis of the Reststrahlen bands in AlN and  $\text{Al}_{0.72}\text{Sc}_{0.28}\text{N}$  along with the spectral response of the Berreman mode is further demonstrated. Demonstration of optical absorption and simultaneous light-matter coupling in the visible and in the mid-to-long wavelength IR spectral range with a single metamaterial mark important progress in the quest to design functional optical materials that can be used for energy conversion, sensing, healthcare, security and other applications.

## TiN/Al<sub>0.72</sub>Sc<sub>0.28</sub>N Superlattice-based Anisotropic Optical Medium for Spin Photonics

The hyperbolic optical medium is an artificially structured material with extreme dielectric anisotropy (+ve (dielectric) in one direction & -ve (metal) in another direction) for potential applications in subwavelength imaging, coherent thermal emission, optical spin Hall effect (OSHE) etc. Generally, metal-dielectric based metamaterial structures are used for designing such type of anisotropic medium. To make high-quality refractory photonic structure, titanium nitride (TiN) is used as a refractory metal along with a dielectric aluminum scandium nitride (Al<sub>0.72</sub>Sc<sub>0.28</sub>N). TiN/Al<sub>0.72</sub>Sc<sub>0.28</sub>N superlattices are grown which shows the hyperbolic dispersion in a certain wavelength range. In Magnus effect, a spinning ball experiences a force due to pressure gradient and its path gets deviated from the expected trajectory. Similarly, photon spin is associated with the circularly polarized light (helicity = +/- 1), enters an extreme anisotropic optical medium (or hyperbolic medium), and experiences a force due to a refractive index gradient. Thus, a photon of the opposite spin travel in the opposite direction, also known as the photonic spin Hall effect. In this chapter, theoretical demonstration of the spin hall effect in TiN/Al<sub>0.72</sub>Sc<sub>0.28</sub>N superlattice-based hyperbolic medium is presented.



## 6.1 Introduction

Metal-dielectric nanostructures are the building block of the nanophotonic and optoelectronic devices, enabling precise manipulation of electromagnetic waves by leveraging diverse light–matter interaction mechanisms at subwavelength dimensions.<sup>199</sup> Metamaterials enable several optical mediums such as hyperbolic and epsilon-near-zero (ENZ), which allow propagation of large wavevector light, such as surface wave or evanescent wave, applicable for subwavelength imaging, enhanced Purcell effect, nano-laser, etc. Apart from that, anisotropic optical medium is a good platform for spin photonics. As photon has spin, the right- and left-handed circularly polarized light (or helicity  $\sigma = \pm 1$ ) is regarded as two quantum states.<sup>200–203</sup> It is also well known that when circular-polarized light enters an inhomogeneous (or anisotropic) medium, light experiences a force which depends on the refractive index gradient.<sup>203</sup> Consequently, photons of opposite spin propagate in the opposite directions, also known as the optical spin Hall effect.

One can make extreme anisotropic optical medium (or hyperbolic medium) by using metal-dielectric composite superlattices or nanorods.<sup>204</sup> Recently hyperbolic dispersion is shown in twisted double-layers of MoO<sub>3</sub> flakes by changing the moiré angle as well.<sup>205</sup> In this chapter, TiN/Al<sub>0.72</sub>Sc<sub>0.28</sub>N based superlattice is grown to make hyperbolic medium. Titanium Nitride (TiN) is a well-known alternative refractory plasmonic material. TiN is hard (hardness of  $\sim 30$  GPa), exhibits a very high melting temperature of 2930°C and stable against creep deformation to high temperatures. The surface energy of TiN is 24–39 mJ/m<sup>2</sup> which is significantly smaller than the surface energies of noble metals ( $\sim 1$ –2 J/m<sup>2</sup>) that allows uniform TiN ultrathin film depositions with smooth surfaces. TiN is also compatible with Si-technology, it already has been used for as a buffer layer in integrated circuit (IC) fabrication. So, TiN is a good plasmonic material that play the role for the metallic component, but it is also very crucial to choose a suitable dielectric medium for making the epitaxial superlattice. In the previous study, aluminum scandium nitride (Al<sub>x</sub>Sc<sub>1-x</sub>N) alloy exhibit tunable lattice constant that depends on the ScN and AlN concentration. Al<sub>0.72</sub>Sc<sub>0.28</sub>N lattice constant (4.24 Å) and crystal structure (Rocksalt) was found similar to the TiN. Planar epitaxial TiN/Al<sub>0.72</sub>Sc<sub>0.28</sub>N metal/dielectric superlattices with nanoscale period thicknesses have been developed that exhibit hyperbolic photonic dispersion and a significantly enhanced photonic density of states, as well as tunable plasmonic



resonances.<sup>178,179</sup> Such superlattices are also found to be stable at high-temperatures for an extended period of time.<sup>180,181</sup>

## 6.2 Growth of TiN/Al<sub>0.72</sub>Sc<sub>0.28</sub>N Superlattice

Superlattices consisting of TiN and Al<sub>0.72</sub>Sc<sub>0.28</sub>N alternating layers of equal thickness were grown on (001) MgO substrates by dc-magnetron sputtering inside an ultrahigh vacuum chamber at a base pressure of  $2\text{-}3 \times 10^{-9}$  Torr. All growths are performed at 10 mTorr deposition pressure at a substrate temperature of 800°C. Structural properties of the superlattice are determined with high-resolution (scanning) transmission electron microscopy (HR(S)/TEM) imaging that show the TiN and Al<sub>0.72</sub>Sc<sub>0.28</sub>N layers grow with cubic epitaxy on (001) MgO surfaces. The Al<sub>0.72</sub>Sc<sub>0.28</sub>N layers are homogeneous, uniform and exhibit very little interface roughness with TiN (see Fig. 6.1(a)). The high-resolution STEM image in Fig. 6.1(b) shows coherent growth of Al<sub>0.72</sub>Sc<sub>0.28</sub>N layers on TiN with [001] (001) Al<sub>0.72</sub>Sc<sub>0.28</sub>N || [001] (001) TiN epitaxial relationship.

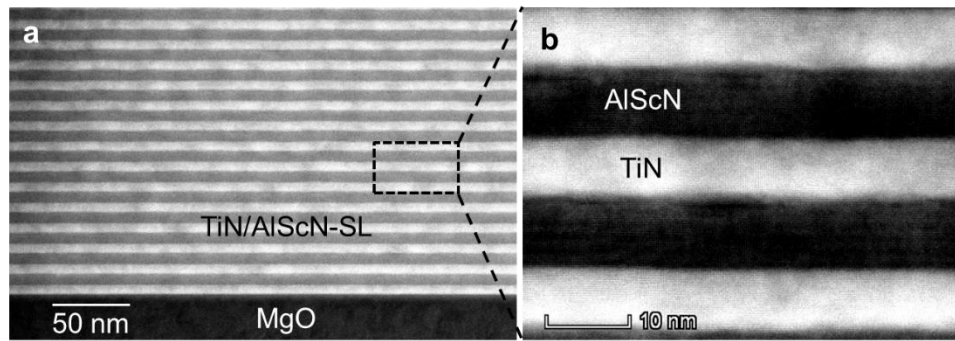


**Figure 6.1** (a) STEM micrograph of TiN/Al<sub>0.72</sub>Sc<sub>0.28</sub>N (metal/dielectric) superlattice deposited on the MgO substrate. (b) High-magnification STEM image highlight the TiN and Al<sub>0.72</sub>Sc<sub>0.28</sub>N are separated by clean and abrupt interfaces.

## 6.3 Optical characterization

The dielectric permittivity of the superlattice (SL) consisting of 20-nm thick layers of TiN and Al<sub>0.72</sub>Sc<sub>0.28</sub>N of 8 periods is characterized by a variable angle spectroscopic ellipsometer (RC-2 J.A. Woollam Co.) from 210 nm-2500 nm range. Fig. 6.2 (a) and (b) show the dielectric permittivity of TiN and Al<sub>0.72</sub>Sc<sub>0.28</sub>N respectively that constitute the superlattice. TiN is metallic (real part of the dielectric permittivity  $\epsilon_1 < 0$ ) for wavelengths longer than 480 nm and Al<sub>0.72</sub>Sc<sub>0.28</sub>N is dielectric throughout the UV to near-infrared (NIR) ranges. The effective dielectric permittivity of the superlattice in the direction normal to the plane of the layers ( $\epsilon^\perp$ ) and parallel to the plane of the layers ( $\epsilon^\parallel$ ) is evaluated by

utilizing the ellipsometer data and effective medium theory. The real parts of the dielectric permittivity (Fig. 6.2 (c)) exhibit opposite signs for wavelength  $486 \text{ nm} < \lambda < 580 \text{ nm}$  (i.e.,  $\epsilon_1^\perp < 0$ ,  $\epsilon_1^\parallel > 0$ ) which produces a type-I hyperbolic dispersion and for  $\lambda > 580 \text{ nm}$  (i.e.,  $\epsilon_1^\perp > 0$ ,  $\epsilon_1^\parallel < 0$ ) which produces a type-II hyperbolic dispersion. The perpendicular permittivity  $\epsilon^\perp$  has a Lorentz-like response with a resonance pole at 609 nm. While the parallel dielectric constant act as Drude-like dispersion, and the presence of the weakly dispersive dielectric layers effectively adds a positive background dielectric constant. As a result, the dielectric layers serve to dilute the metal and redshift in the crossover wavelength (or plasma frequency) of the multilayer superlattice.

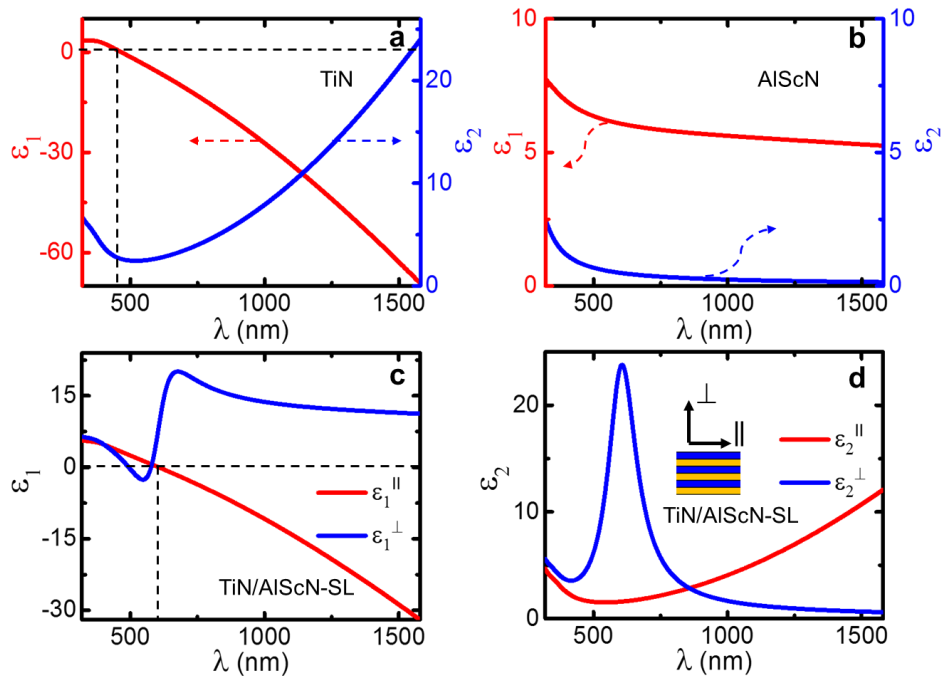


**Figure 6.2** Dielectric functions (measured using spectroscopic ellipsometry) of (a) TiN and (b) AlScN that constitute the superlattice (20 nm/20 nm of 8 periods) together with (c) the real and (d) imaginary parts of the dielectric functions of the effective medium that approximates the superlattice. The perpendicular permittivity has a Lorentz-like response while parallel permittivity has a Drude-like response.

The red shift of the crossover wavelength, from the 471 nm to 608 nm, in the effective permittivity of the superlattice can be also seen in the reflection spectrum of the superlattice. In figure 6.3 (a), angle-dependent reflection (R) measurement of the superlattices and theoretical calculations (see Figure 6.3 (b)) further justify the hyperbolic nature of the superlattices. At longer wavelengths ( $> 603 \text{ nm}$ ), since the superlattices act as type-II HMM, high reflectivity is observed in both experiment as well as in the modeling.

However, a dip in the reflection spectra at  $\sim 603$  nm is observed that corresponds to the crossover wavelength of the effective permittivity of the superlattice.

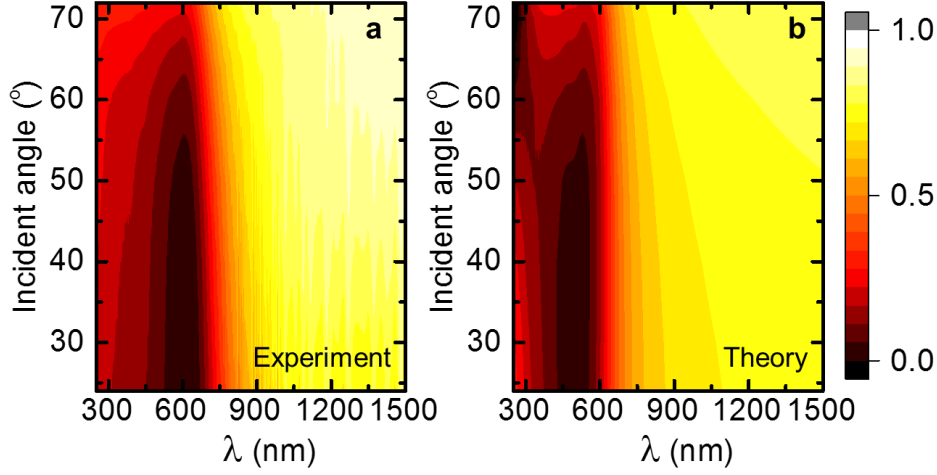


**Figure 6.3** (a) The experimental reflection spectrum of 20 nm/20 nm TiN/AlScN superlattice presented as a function of incident angle (measured using spectroscopic ellipsometry). (b) Theoretically calculated reflection spectra of the same superlattice (using COMSOL Multiphysics Software) that indicates a clear match up with experimentally measured spectrum.

#### 6.4 Hyperbolic photonic dispersion in uniaxial medium:

The dielectric permittivity of diagonal permittivity tensor with degenerate values in the  $ab$ -plane (or  $xy$  plane) and one along the  $c$ -axis ( $z$ -direction) are represented by  $\epsilon_{xx}$  and  $\epsilon_{zz}$  respectively. So, the dielectric permittivity of a uniaxial anisotropic material can be described by a tensor as follow

$$\epsilon = \begin{pmatrix} \epsilon_{xx} & 0 & 0 \\ 0 & \epsilon_{xx} & 0 \\ 0 & 0 & \epsilon_{zz} \end{pmatrix} \quad (6.1)$$

Propagation of the electromagnetic wave through such material is determined by the dispersion relation

$$\frac{k_x^2 + k_y^2}{\epsilon_{zz}} + \frac{k_z^2}{\epsilon_{xx}} = \frac{\omega^2}{c^2} \quad (6.2)$$

The relative signs of  $\epsilon_{xx}$  and  $\epsilon_{zz}$  determine the type of dispersion medium such as an elliptical or a hyperbolic medium. Materials with anisotropy as  $\epsilon_{xx} \neq \epsilon_{zz} > 0$  shows elliptical dispersion (see Fig. 6.4 (a)) also known as birefringent crystal such as calcite. If the permittivity has opposite sign in opposite direction ( $\epsilon_{xx} \epsilon_{zz} < 0$ ), then the material shows hyperbolic dispersion and known as hyperbolic material. There are two types of hyperbolic nature exhibit in uniaxial material, first  $\epsilon_{zz} < 0$  and  $\epsilon_{xx} > 0$  known as type-I [see Fig. 6.4 (b)] and second  $\epsilon_{zz} > 0$  and  $\epsilon_{xx} < 0$  known as type-II [see Fig. 6.4 (c)].

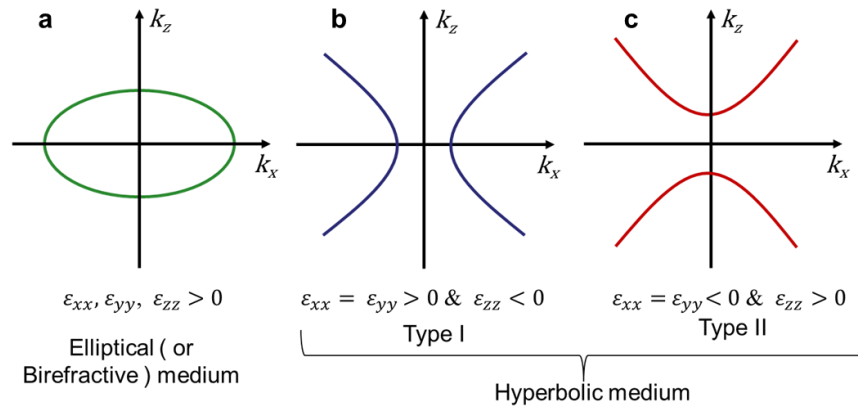


**Figure 6.4** Schematic diagram of isofrequency surfaces in momentum space for elliptical (a), hyperbolic type-I (b) and type-II (c) medium.

## 6.5 Photon spin Hall effect

It is well known that when light passes through one medium to another medium, its direction of propagation and momentum change during refraction or reflection. However, the trajectory of light, in the isotropic medium, is independent of its polarization. In the case of anisotropic medium, propagation of light depends on the gradient-index medium with refractive index  $n(\mathbf{R})$  described by the following equations of motion.<sup>203</sup>

$$\dot{\mathbf{P}} = \nabla n(\mathbf{R}) \quad (6.3)$$

$$\dot{\mathbf{R}} = \frac{\mathbf{P}}{P} - \frac{\sigma}{k_0} \frac{\mathbf{P} \times \dot{\mathbf{P}}}{P^3} \quad (6.4)$$

The equation-6.4 describes the spin-dependent trajectory of light, in other words, the spin-Hall effect of light. The theoretical demonstration for the light spin-Hall effect in TiN/Al<sub>0.72</sub>Sc<sub>0.28</sub>N superlattice is obtained by solving Maxwell's equations for incident circular polarized light using the finite element method (FEM). In FEM, geometry is divided into the subdomain and expresses the differential equation of electromagnetic field

in terms of charges and currents distributed along with the associated boundary conditions. The boundary conditions for the electromagnetic field provide a set of linear integral equations that are solved computationally using the COMSOL Multiphysics software. The dielectric permittivity of the superlattice is obtained by ellipsometer and used as the input optical parameter in the software.

In figure 6.5, the photonic spin-Hall effect in TiN/Al<sub>0.72</sub>Sc<sub>0.28</sub>N superlattice-based hyperbolic medium is demonstrated where the light of opposite spin (helicity  $\sigma = \pm 1$ ) propagates in opposite direction. The experimental demonstration of this phenomenon will be the future avenue of our research.

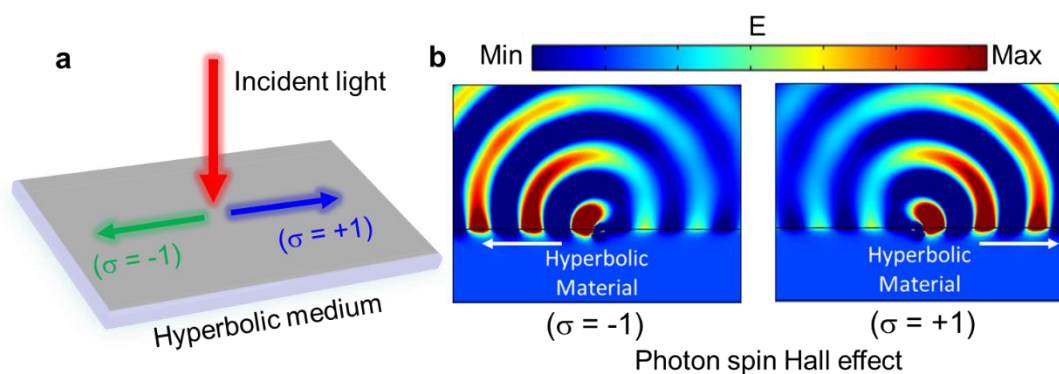


**Figure 6.5 Photonic spin Hall effect in TiN/Al<sub>0.72</sub>Sc<sub>0.28</sub>N superlattice-based hyperbolic medium.** (a) Schematic of photon dynamics of opposite spin in the hyperbolic medium. (b) Simulated electric field distribution (which represents the light propagation) in the hyperbolic medium. Light of helicity ( $\sigma$ ) = -1 propagates in the left direction and vice versa.

## 6.6 Conclusion

We have presented a detailed analysis of the optical response of periodic epitaxial, CMOS- and biocompatible, thermally stable TiN/Al<sub>0.72</sub>Sc<sub>0.28</sub>N metal/dielectric superlattice-based hyperbolic medium. The optical parameters are obtained by ellipsometry and utilized for electromagnetic simulation to observe the photon spin Hall effect. Anisotropic optical media affect the trajectory of the photon of a different spin. The spin-Hall effect of light will be an important part of modern quantum photonics research. Therefore, TiN/Al<sub>0.72</sub>Sc<sub>0.28</sub>N based hyperbolic medium can be promising for spin-photonics based integrated chip.

## Conclusion and Outlook

The thesis focuses on the interaction of light with collective excitations, specifically plasmons and phonon polaritons, in refractory metals and nitrides. These materials are known for their chemical stability, compatibility with complementary metal-oxide-semiconductor (CMOS) technology, and suitability for optoelectronic and nanophotonic applications across the visible to infrared spectrum. The research in this thesis encompasses both fundamental understanding and practical applications of this area of research.

On the fundamental side, the thesis deals with the underlying physics of plasmons and phonon polaritons in refractory metals and nitrides. It includes theoretical and experimental investigations such as their dispersion, damping, coupling with electromagnetic fields and how they collectively affect the optical response of the materials. On the application side, the thesis investigates and discusses the potential practical applications of plasmons and phonon polaritons in refractory metals and nitrides. These include plasmonic waveguides, optical cavities, hyperbolic metamaterials, sensors, detectors, modulators and optical filters operating in the visible to infrared spectral range. The work also explores how the properties of refractory metals and nitrides can be tailored and optimized to achieve desired functionalities in optoelectronic and nanophotonic applications.

Plasmonic materials such as TiN, HfN, ZrN, Ta, W, and Mo have been designed to cover the UV-visible spectral range, enabling enhanced light-matter interactions for applications such as surface-enhanced Raman spectroscopy, sensing, and photocatalysis. Notably, plasmon polaritons have been observed in doped ScN and GaN nanostructures for the first time, covering the near-to-mid infrared region. This breakthrough opens possibilities for designing plasmonic devices and sensors in the mid to long infrared, with applications in imaging, sensing, and communication. In addition, dielectric materials such as (Al,Sc)N have been utilized as spacers in the design of metal-dielectric artificial structures or metamaterials. These dielectric materials play a crucial role in tailoring the plasmonic and phononic properties of the overall structure, leading to enhanced performance in various applications.

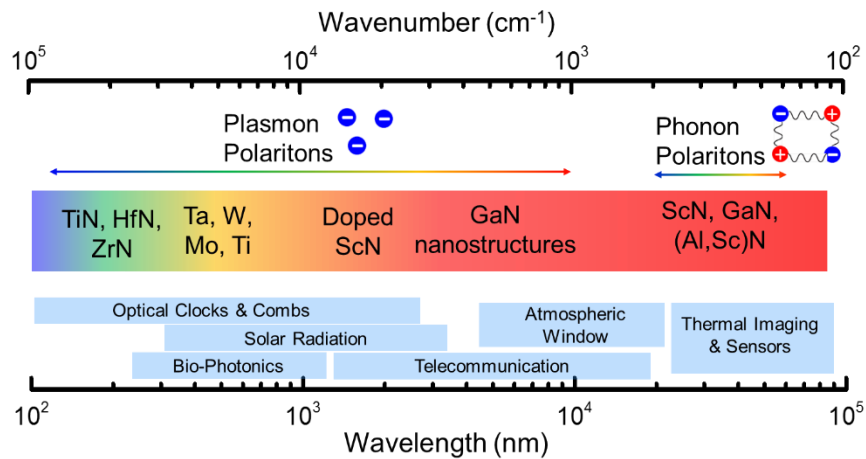


**Figure 7.1 Refractory nitride materials platform for the nanophotonic application.** Plasmon and phonon polariton in refractory transition-metal-nitrides covering a wide range of the electromagnetic spectrum, from visible to infrared range. Plasmon resonances of refractory metals, such as TiN, ZrN, W, Ta, etc., can be utilized for visible to near-infrared regimes. The plasmon resonances in doped ScN and GaN nanostructures can be utilized for the near-infrared to the mid-infrared range. For mid-to-long infrared, phonon polariton of ScN, GaN, and AlScN can be utilized.

Advances in refractory metal and nitride based plasmonic and phononic materials have significant implications for solar energy harvesting, where plasmonic materials can enhance light absorption and improve the efficiency of solar cells. In optical telecommunications, these materials can enable novel devices for information processing and communication in the infrared. In bio-photonics, plasmonic and phononic materials can be used for sensitive detection and manipulation of biological molecules and cells. In thermal imaging and sensing, these materials can enable high-performance thermal detectors and sensors for surveillance, defense, and industrial monitoring applications.

Table 7.1: The following table summarizes the important properties such as melting point, resistivity, carrier concentration, epsilon near zero wavelength of refractory metals and nitrides along with Ag and Au.

| Materials                | Bulk melting temperature (C°) | $\lambda_{ENZ}$ ( $\mu\text{m}$ ) | Optical loss ( $\epsilon_2$ ) at $\lambda_{ENZ}$ | Carrier concentration ( $\text{cm}^{-3}$ ) | Resistivity ( $\Omega \text{ cm}$ ) | $\lambda_{LO}(\lambda_{TO})$ ( $\mu\text{m}$ ) |
|--------------------------|-------------------------------|-----------------------------------|--|--|-------------------------------------|--|
| <b>Ag</b> <sup>206</sup> | 962                           | 0.31                              | 0.5  | $5.86 \times 10^{22}$                      | $1.16 \times 10^{-6}$               | -  |
| <b>Au</b> <sup>206</sup> | 1064                          | 0.51                              | 1.2  | $5.90 \times 10^{22}$                      | $1.32 \times 10^{-6}$               | -  |

|  |      |                |                |  |  |                  |
|--|------|----------------|----------------|--|--|------------------|
| <b>HT-Ta<br/>(RT-Ta)</b>                   | 3017 | 0.52<br>(1.41) | 12.5<br>(9.9)  | $1.15 \times 10^{22}$<br>( $5.61 \times 10^{21}$ ) | $8.85 \times 10^{-5}$<br>( $5.34 \times 10^{-4}$ ) | -                |
| <b>HT-W<br/>(RT-W)</b>                     | 3422 | 0.86<br>(0.88) | 24.0<br>(12.7) | $9.8 \times 10^{21}$<br>( $7.23 \times 10^{21}$ )  | $1.02 \times 10^{-5}$<br>( $1.84 \times 10^{-4}$ ) | -                |
| <b>HT-Mo<br/>(RT-Mo)</b>                   | 2633 | 0.72<br>(1.20) | 24.5<br>(9.48) | $1.09 \times 10^{22}$<br>( $7.45 \times 10^{21}$ ) | $1.17 \times 10^{-5}$<br>( $2.59 \times 10^{-4}$ ) | -                |
| <b>TiN</b>                                 | 2947 | 0.46           | 2.0            | $1.45 \times 10^{22}$                              | $9.45 \times 10^{-5}$                              | -                |
| <b>ZrN</b>                                 | 2980 | 0.35           | 1.6            | $6.6 \times 10^{22}$                               | $2.7 \times 10^{-5}$                               | -                |
| <b>HfN</b>                                 | 3310 | 0.38           | 1.7            | $6.7 \times 10^{22}$                               | $1.8 \times 10^{-5}$                               | -                |
| <b>doped-ScN</b>                           | 2600 | 1.8-<br>2.4    | 1.0-2.7        | $10^{18} - 10^{21}$                                | $10^{-1} - 10^{-4}$                                | 14.58<br>(27.80) |
| <b>GaN-<br/>nanostructure</b>              | 2500 | 1.9-<br>5.3    | 0.5-2.2        | $10^{19} - 10^{20}$                                | $10^{-2} - 10^{-4}$                                | 13.51<br>(18.87) |
| <b>Al<sub>0.72</sub>Sc<sub>0.28</sub>N</b> | 2200 | -              | -              | $5 \times 10^{14}$                                 | $2 \times 10^4$                                    | 11.17<br>(17.70) |

More specifically, in Chapter 2 the plasmonic response of highly crystalline transition metals (Ta, W and Mo) and nitrides (TiN, HfN and ZrN) is demonstrated. Transition metals exhibit higher optical losses compared to noble metals. Traditionally, metals with very low optical losses ( $\epsilon_2$ ) are regarded as excellent plasmonic materials. But recently, plasmonic materials with high optical loss have been utilized for the confinement and impedance effects<sup>34</sup>, such as loss-induced heating<sup>35</sup>, plasmon-induced hot carrier<sup>7</sup>, thermo-plasmonic nanotweezer<sup>8</sup>, etc. Apart from that, plasmonic materials with low optical loss are required for optical nano-circuits<sup>48</sup>, photon tunneling<sup>49,50</sup>, super-coupling<sup>51</sup>, extreme nonlinear interactions<sup>52</sup>, ultrafast switching<sup>53</sup>, etc. Metals from the transition metal nitrides family such as TiN, HfN, and ZrN emerged as promising alternatives to noble metals. Here, we have reported the plasmonic response of TiN film with very low optical loss compared to the previously reported MBE or sputter-deposited TiN films. Also, our present TiN film's optical loss is lower than the Au in a wide spectral range.



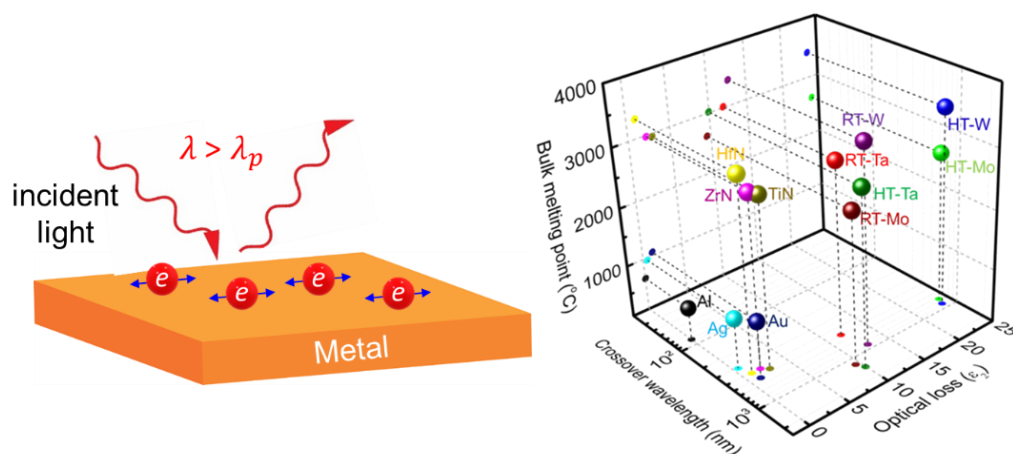


**Figure 7.2 Plasmon polariton in transition metals and nitrides.** Comparison of metals with their optical loss at crossover wavelength and their bulk melting point.

Traditionally, doped-semiconductors are used to achieve plasmon-polaritons in the near-to-mid infrared (IR), while polar dielectrics are utilized for realizing phonon-polaritons in the long-wavelength IR (LWIR) spectral regions. Demonstrating plasmon- and phonon-polariton in one host material with low-loss is challenging due to the mutually conflicting physical property requirements. In chapter 3, we have shown high-quality tunable short-wavelength IR (SWIR) plasmon-polariton (from 1.8  $\mu\text{m}$  to 2.3  $\mu\text{m}$ ) and LWIR phonon-polariton (from 15  $\mu\text{m}$  to 27  $\mu\text{m}$ ) in complementary metal-oxide-semiconductor (CMOS) compatible group III-V polar semiconducting scandium nitride (ScN) thin films. Oxygen and magnesium doping in ScN is utilized to modulate the carrier from  $5 \times 10^{18}$  to  $1.6 \times 10^{21}$   $\text{cm}^{-3}$  to achieve these optical resonances.

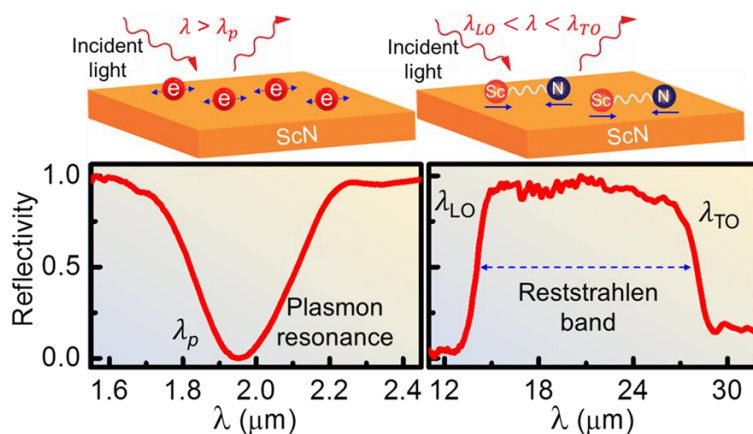


**Figure 7.3** Polar semiconducting ScN can host both types of plasmon and phonon polariton.

The optical resonances can be tuned not only by the external dopant but also by controlling the morphology of the material. In chapter 4, morphology-controlled Reststrahlen band and plasmon polariton are shown in gallium nitride (GaN). Gallium nitride is one of the most famous semiconductors and its nanostructures such as nanowires, nanocolumns, and nanowall-networks have several benefits over thin film due to their reduced dislocation-density and large surface-to-volume ratio. The GaN nanostructures (as shown in figure 7.4) are grown by using molecular beam epitaxy (MBE) by changing the  $N_2$  & Ga flux ratio, without any lithography. Here we have shown that GaN nanowall networks and vertically standing nanorods exhibit morphology-dependent Reststrahlen band (the region between LO and TO phonon). Also, in GaN nanostructures, native defects such as N-vacancy is responsible for high carrier concentration. Therefore, by controlling the morphology of the GaN nanostructures, their carrier concentration can be tuned, consequently, tunable plasmon resonance can be achieved. Lichtenecker's effective-medium-approximation is used to model the experimental reflection curve to obtain the nanostructures' dielectric-permittivity and explain the phenomena. This methodology is not only applicable to GaN nanostructures but also can be used for other polar dielectric (i.e., SiC, AlN, GaAs) nanostructures.

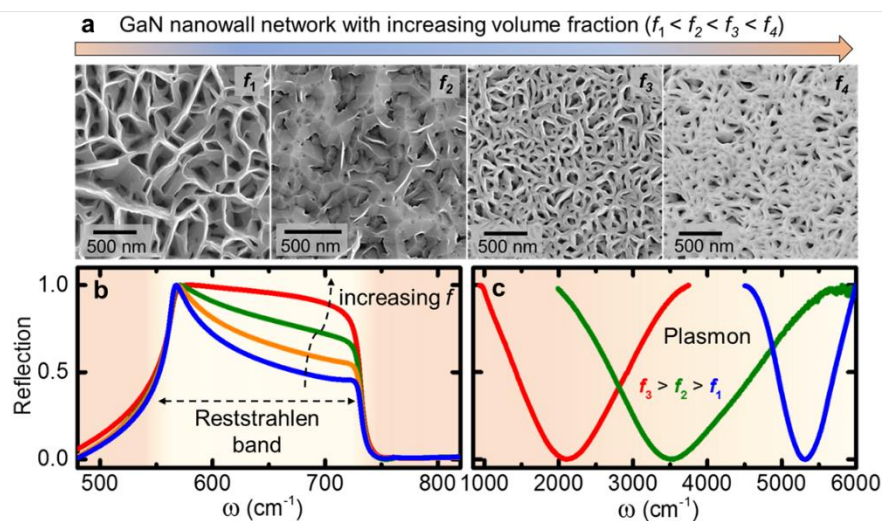


**Figure 7.4 Reststrahlen band and plasmon polariton in GaN nanostructures** (a) Lithography free MBE grown GaN nanostructures of various volume fractions ( $f$ ). Morphology controlled (b) tailored Reststrahlen band, and (c) tunable plasmon polariton.

In chapter 5, the combined effect of TiN (metal) and AlScN (dielectric) based photonic structure is utilized for bi-functional optical cavity. Bi-functional photonic structures are

essential for several applications such as solar-thermo-photo-voltaics (STPV), radiative cooling, etc. Metal-dielectric-metal (MDM) structures are used in designing optical cavities and achieving the Fabry-Perot resonances, which depend on the distance between the top and bottom metals. We have shown that along with the cavity mode, one can achieve optical phonon modes in the infrared by choosing the dielectric material wisely.

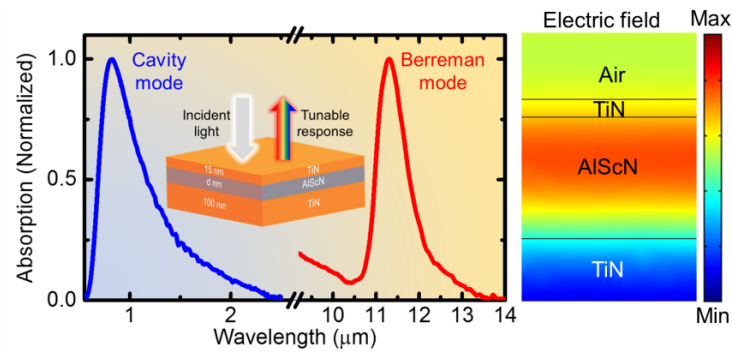


**Figure 7.5** TiN-AlScN based MDM structure: to achieve the optical cavity mode along with optical phonon mode (Berreman mode). The right-side figure shows the light confinement in the MDM cavity at the resonance frequency.

Finally, we have discussed metal-dielectric superlattice-based extreme anisotropic optical medium, called hyperbolic optical medium. The hyperbolic medium is an artificially structured material with extreme dielectric anisotropy (+ve (dielectric) in one direction & -ve (metal) in another direction) for potential applications in subwavelength imaging, coherent thermal emission, optical spin Hall effect (OSHE), etc.<sup>204</sup> Generally, metal-dielectric based composite structures are used for designing such type of anisotropic medium. In Magnus effect, a spinning ball experiences a force due to pressure gradient and its path gets deviated from the expected trajectory. Similarly, photon spin is associated with the circularly polarized light (helicity ( $\sigma$ ) =  $\pm 1$ ), enters an inhomogeneous optical medium, and experiences a force due to a refractive index gradient. Consequently, a photon of opposite spin propagates in the opposite direction, also known as the optical spin Hall effect. Here, we have demonstrated the hyperbolic dispersion in TiN/AlScN superlattice which can be utilized for spin-photonics.

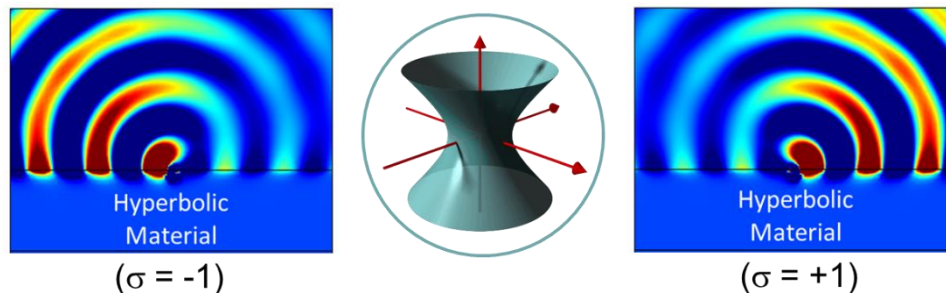


**Figure 7.6** Signature of optical spin Hall effect in TiN-AlScN superlattice-based hyperbolic medium. Light of opposite helicity (i.e.,  $\sigma = -1$  or  $\sigma = +1$ ) propagates in opposite directions.

## 7.1 Future perspective:

Polaritons in refractory nitrides can be the platform for the development of various fields, including optical computing<sup>207,208</sup>, biophotonics<sup>209,210</sup>, and agriculture<sup>211,212</sup>. Here are some specific advantages of polaritons in these fields:

**Optical computing:** One of the most promising areas of photonics is the development of optical computing, which uses light instead of electrons to perform computations. Polaritons can be used to create highly efficient optical modulators and it also enables strong optical nonlinearities. Nonlinear optical phenomena are essential for implementing logic gates in optical computing, where signals are processed by manipulating the intensity, phase, or polarization of light. Polaritons have the potential to revolutionize optical computing with their strong coupling with light, allowing for efficient and fast computing tasks such as logic gates, signal processing, and data storage, surpassing conventional computing technologies in speed, energy efficiency, and scalability.

**Biophotonics:** Polaritons can find applications in sensing, imaging, therapy, and optogenetics in biophotonics. They can enable sensitive detection of biological molecules, imaging of biological structures with high resolution, and controlled manipulation of biological processes using light. Polariton-based therapies can be explored for targeted treatment of diseases, and optogenetics, which involves using light to control biological processes, can benefit from the unique properties of polaritons for precise and efficient control of cellular activities.

**Agriculture:** Polaritons have the potential to revolutionize plant health monitoring by enabling non-invasive and real-time sensing of physiological processes, while enhancing

photosynthesis by modifying light-matter interactions. For example, nanophotonic coatings applied to greenhouse materials can selectively transmit or reflect specific wavelengths of light, creating optimal lighting conditions that promote faster growth, earlier flowering and higher yields in plants. In addition, polaritons can be explored as environmentally friendly alternatives to conventional pesticides, as they can selectively target and control pests without harming beneficial organisms, providing environmentally sustainable pest management solutions.

As our understanding of polariton physics continues to advance, we are likely to discover new and innovative ways to use them to improve agriculture, computing, biophotonics, and other fields. The unique properties of polaritons make them a promising platform for the development of cutting-edge technologies with wide-ranging applications.

## **7.2 Conclusion:**

In conclusion, advances in refractory metal and nitride based plasmonics and phononics have significant implications for next generation technologies. One potential application is in the field of optical communications, where plasmonic and phononic structures can be integrated into photonic circuits for ultra-compact and high-speed communication devices. In addition, the ability to control and manipulate light at the nanoscale using plasmons and phonon polaritons opens up opportunities for high-resolution imaging, sensing and spectroscopy applications. In addition, the development of CMOS-compatible material platforms for optoelectronic and nanophotonic applications holds promise for the integration of plasmonic and phononic devices with existing semiconductor technologies, enabling new functionalities and improved performance in areas such as computing, imaging and energy harvesting. Furthermore, the potential to exploit quantum effects in plasmonic and phononic systems could lead to advances in quantum information processing and quantum communication technologies. Overall, advances in refractory metal and nitride based plasmonics and phononics offer promising prospects for next generation technologies in a wide range of applications.

## Appendix A- Experimental Techniques

### A1 Magnetron Sputtering

Magnetron sputtering is a type of physical vapor deposition technique. It is used for the deposition of thin films using plasma. The gaseous plasma is developed and confined near the target material to be deposited. The high-energy ions strike the surface of the target, ejecting (sputtering) the atoms from the surface which then get deposited on the substrate forming a thin film.

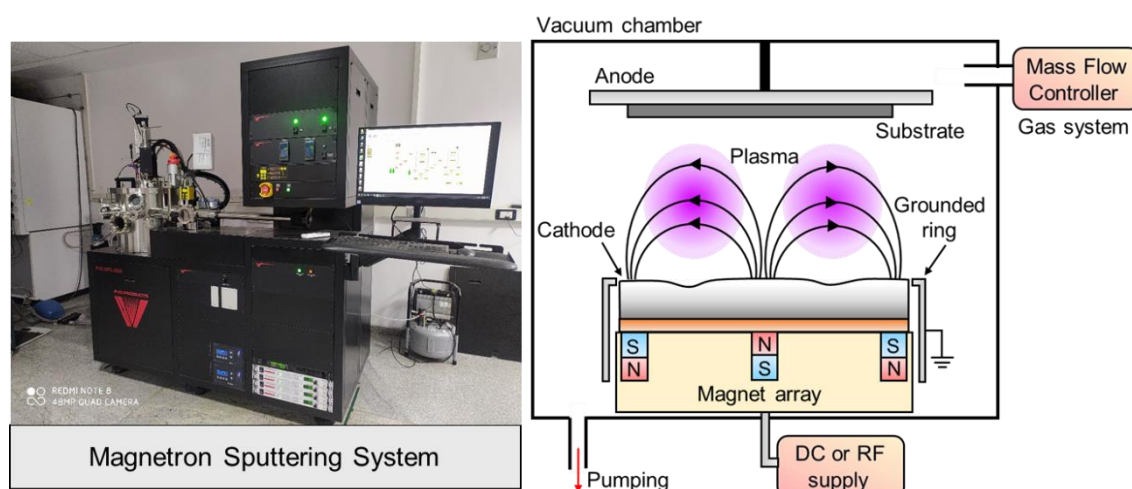


Figure A.1 Ultra-high vacuum magnetron sputtering system.

To avoid potential contamination and to reduce the partial pressure of background gases, the deposition process is done in an ultra-high vacuum chamber. Usually, the base pressure of  $10^{-7} - 10^{-9}$  Torr is maintained before deposition. When the chamber is filled with the sputtering gas which makes up the plasma, the total pressure is controlled and adjusted in the milli-Torr range.

Plasma generation is initiated with the help of very high voltage applied between the cathode (located directly behind the target) and the anode (usually attached to the chamber as electrical ground). Often a high molecular weight gas like argon is used as sputtering gas to produce plasma, in order to permit as many high-energy collisions as possible, which will result in an enhanced deposition rate. Also, extremely powerful magnets are used to constrict electrons in plasma near the target which gives higher-density plasma and faster deposition rates.

The reactive sputtering process can be used to deposit nitrides or oxides, in which nitrogen or oxygen are added into the chamber during the deposition. The proper selection of a power supply system (DC, RF, pulsed DC) is necessary for a successful deposition. Conductive materials can be easily deposited by using a DC power source however, an RF power source is required for depositing insulating targets. While a pulsed DC source is preferred for reactive sputtering when the oxide or nitride to be deposited is insulating, as it increases the possibility of arcing.

Since the target material does not need to be melted or evaporated, magnetic sputtering has a significant advantage over other deposition techniques. The adhesivity of films deposited by sputtering is better compared with evaporated films and the composition of films deposited is also retained to a composition that is close to that of the target material. Magnetron sputtering is a versatile technique and can be used for wide applications, such as optical coating, microelectronics, solar cells, and thin film research.

## A2 Spectroscopic ellipsometry measurements

Ellipsometry is a widely used experimental technique for determining the optical properties of thin films, superlattices and other complicated nanostructures. The term "ellipsometry" comes because elliptically polarized light is used as a probe to determine the optical properties of the materials. Ellipsometry measures the change of polarization after the reflection or transmission from the samples in the quantity called psi ( $\psi$ ) and delta ( $\Delta$ ). The psi is the ratio of the amplitudes of the electric fields in the plane of incidence to the out of the plane of incidence, while the delta is the phase shift of light in those directions as shown in the following equation.

$$\rho = \frac{r_p}{r_s} = \frac{\tilde{E}_p^{out} / \tilde{E}_p^{in}}{\tilde{E}_s^{out} / \tilde{E}_s^{in}} = \frac{|E_p^{out}| / |E_p^{in}|}{|E_s^{out}| / |E_s^{in}|} e^{i(\delta_p - \delta_s)} = \tan(\Psi) e^{i\Delta}$$

This change in polarization depends on the quantities of interest such as thickness and optical parameters such as dielectric permittivity or refractive index. One can determine these parameters by using the appropriate physical model to best fit the measured ellipsometry values. All the optical measurements from 210nm to 2500nm for this thesis are performed by RC-2 Ellipsometer provided by J. A. Woollam Co. The Xenon arc lamp

is used for the light source while Silicon detector from 210nm-to 1000nm and InGaAs detector are used from 1000nm to 2500nm.

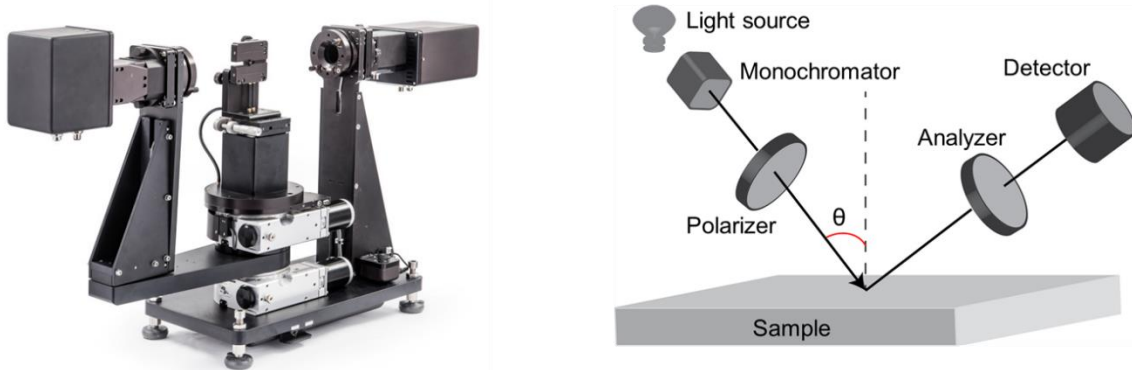


**Figure A.2 Spectroscopic ellipsometer**

Spectroscopic ellipsometer measurements were performed in the reflection mode at three different angles ( $55^\circ$ ,  $65^\circ$  and  $75^\circ$ ) of incidences. The experimental ( $\Psi$  ( $\psi$ ),  $\Delta$ ) data were fitted to a physical model containing fixed parameters obtained from independent measurements or known values from the literature. For example, the sample thickness was known from SEM or TEM measurements, the carrier density and mobility were known from electrical measurements (e.g., Hall effect), and were fixed in the ellipsometry fitting to improve the accuracy of the determination of other parameters.

Once the permittivity data was obtained from ellipsometry measurements, it was used to calculate the reflection using appropriate optical modeling techniques, such as Fresnel equations, finite elements methods, or other numerical methods. The calculated reflection curve was compared with the experimental reflection curve to assess the accuracy of the permittivity data. A good agreement between the calculated reflection curve using the obtained permittivity data and the experimental reflection curve indicate that the ellipsometry results are consistent with the experimental data, and the obtained permittivity values are reliable.

The temperature-dependent optical properties were measured with a cryostat from 100 K-700 K temperature range at  $70^\circ$  angle of incidence. The cryostat chamber was attached with a turbo-molecular pump leading to a chamber pressure of  $10^{-7}$  Torr that reduces possibilities for oxidation.



### A3 Fourier-transform infrared spectroscopy (FTIR)

Infrared reflection (for  $200\text{ cm}^{-1}$  to  $6000\text{ cm}^{-1}$ ) was performed with Bruker V70v Fourier Transform Infrared vacuum spectrometer using pyroelectric deuterated triglycine sulfate (DTGS) detector with  $4\text{ cm}^{-1}$  resolutions for 120 scans. FTIR is fundamentally based on Michelson interferometer. It has five major components.

- (a) **Light source:** A broadband infrared light source, silicon carbide (SiC) element, electrically heated to about  $1,200\text{ K}$  ( $930\text{ }^{\circ}\text{C}$ ), is used for light source in FTIR. It is also known as Globar light source whose output is like a blackbody.
- (b) **Detector:** An infrared detector acts as a transducer, turning one form of energy (light) into another form of energy (electrical impulses). Pyroelectric deuterated triglycine sulfate (DTGS) and liquid nitrogen cooled mercury cadmium telluride (MCT) detector are used for the measurements.
- (c) **Michelson interferometer:** The interferometer splits (using beam splitter) the single light beam into two light beams. One of the two beam paths is reflected off by a fixed mirror, while the second beam path is directed toward a moving mirror. The moving mirror changes the path length difference between the two optical beams. The change of the phase difference leads to constructive and destructive of the two optical paths. After the two light beams have traveled their different paths, they are recombined into one beam, and then the light beam leaves the interferometer and focused on the sample under investigation. A plot of light intensity (or detector signal) versus optical path difference, is called an interferogram. To measure an interferogram using a Michelson interferometer the mirror is moved back and forth once. This is called a scan.
- (d) **Laser:** This laser light is not the infrared source. Virtually every FTIR contains a laser whose light follows the infrared beam through the interferometer. A helium-neon (He-Ne) laser light source is used to align accessories and monitor the mirror position.
- (e) **Fourier transform:** Interferogram is the superposition of the interferences of the beams of several frequency of the light source. In other word, by passing the light through the interferometer the spectrum of the infrared beam is optically transformed into the interference pattern (the interferogram). The phase-dependent interferogram is related to the frequency-dependent spectrum. The infrared detector measures this interference pattern, and the Fourier transform turns it back into a

spectrum. Additional information about FTIR spectroscopy can be found in the references [213,214].

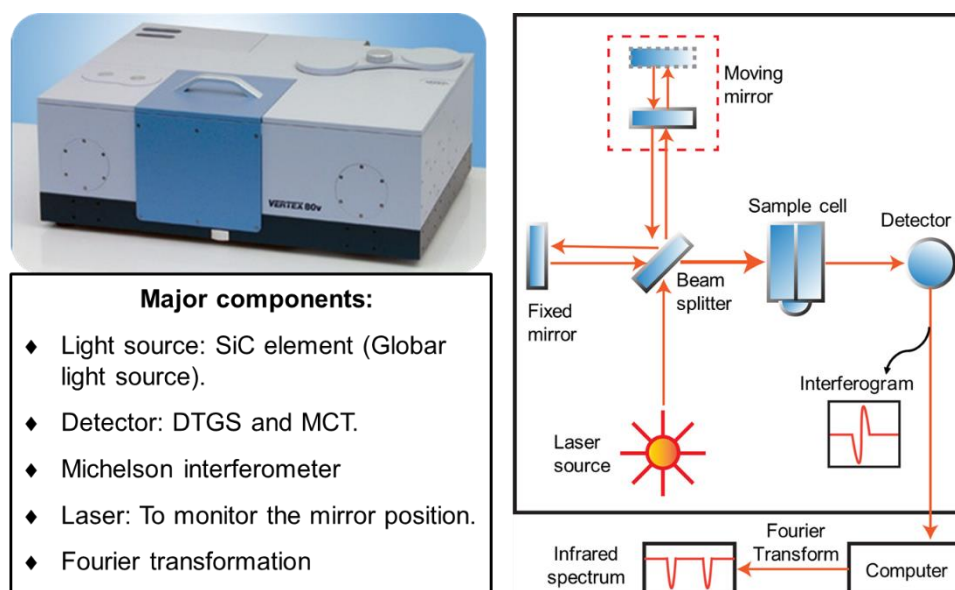


**Figure A.3 Fourier-transform infrared spectroscopy (FTIR)**

Polarized attenuated-total-reflection (ATR) was performed by Bruker V70v Fourier Transform Infrared (FTIR) vacuum spectrometer using a room temperature pyroelectric deuterated triglycine sulfate (DTGS) detector with  $4\text{ cm}^{-1}$  resolutions for 120 scans to detect the surface plasmon and phonon modes.

## **Appendix B - Supplementary data**

### **B1 Supplementary data of chapter 2**

#### **B1.1 Sample preparation**

##### **(i) Transition metals (Ta, W and Mo)**

RTM (Ta, W, and Mo) thin films were deposited on (001) MgO and (0001) Al<sub>2</sub>O<sub>3</sub> substrates with reactive rf-magnetron sputtering (PVD Products Inc.) inside an ultrahigh vacuum chamber with a base pressure of  $3 \times 10^{-9}$  Torr. The growth chamber had the capability to accommodate five targets and was equipped with four dc and one rf power supplies. Substrates were cleaned with wet-chemical (acetone and methanol) methods before transferring to the load lock that operated at a pressure of  $5 \times 10^{-8}$  Torr. Ta (purity of 99.95%), W (purity of 99.95%) and Mo (purity of 99.95%) targets had a dimension of 2 inch in diameter and 0.25 inch in thickness and were sputtered with 100 W rf-power. All depositions were performed in Ar (10 sccm.) atmosphere at a deposition pressure of 10 mTorr. Two sets of samples with substrate held at (a) room temperature (30°C) denoted as RT and (b) 700°C denoted as HT were deposited.

##### **(ii) MBE grown TiN**

TiN thin films were deposited with UHV-PAMBE on (001) MgO and (0001) Al<sub>2</sub>O<sub>3</sub> substrates at a base-pressure of  $1 \times 10^{-10}$  Torr and growth temperature of 600°C. The MBE system was enabled with a load-lock and a sample preparation chamber that operated at a base-pressure of  $1 \times 10^{-9}$  Torr for substrates cleaning. Prior to the deposition and after the cleaning of the substrates with wet-chemicals (acetone and methanol), the substrates were thermally cleaned inside the prep-chamber at 600°C for 1 hour. Substrates were then transferred to the growth chamber and were further thermally cleaned at 800°C for 2 hours before the growth temperature was lowered to 600°C. Ti metal (with a purity of 99.999%) was evaporated from a TiC-coated graphite effusion cell at 1500°C that resulted in a beam-equivalent pressure of  $5 \times 10^{-8}$  Torr and plasma-activated nitrogen source (purity of 99.99999%) was used with 375 W rf-power and 1.5 sccm of nitrogen gas flow.

#### **B1.2 Spectroscopic ellipsometry measurements**

Spectroscopic ellipsometer measurements have been performed in the reflection mode at three different angles ( $55^0$ ,  $65^0$  and  $75^0$ ) of incidences. The experimental (Psi ( $\psi$ ), Delta ( $\Delta$ )) spectrum of refractory metals Ta, W and Mo films was modeled by Drude-Lorentz terms (eq. (B1.1)), in CompleteEASE software provided by J. A. Woollam Co. Where Drude term presents the contribution from the conduction electrons, while the Lorentz terms correspond to the interband transitions

$$\varepsilon(\omega) = \varepsilon_1 + i\varepsilon_2 = \varepsilon_\infty - \frac{\omega_p^2}{\omega^2 + i\Gamma_D\omega} + \sum_{j=1}^n \frac{\omega_{L,j}^2}{\omega_{0,j}^2 - \omega^2 - i\gamma_j\omega} \quad (\text{B1.1})$$

Where  $\varepsilon_\infty$  is the high-frequency dielectric constant,  $\omega_p$  and  $\Gamma_D$  are the plasma frequency and Drude damping constant respectively,  $f_j$ ,  $\omega_{0,j}$  and  $\gamma_j$  are the Lorentz oscillator strength, resonant energy and the damping factor respectively with a relation  $\omega_{L,j}^2 = f_j\omega_{0,j}\gamma_j$  and  $n$  is the number of oscillator. The real part of permittivity ( $\varepsilon_1$ ) signifies the optical response of the material and the imaginary part of permittivity ( $\varepsilon_2$ ) is the optical losses.

**Table B1.1:** Optical (Drude and Lorentz) parameters of RTMs obtained from ellipsometer data fitting.

| Parameters           | RT-Ta | HT-Ta | RT-W | HT-W  | RT-Mo | HT-Mo |
|----------------------|-------|-------|------|-------|-------|-------|
| $\varepsilon_\infty$ | 1.48  | 1.22  | 1.68 | 2.60  | 1.00  | 1.61  |
| $\omega_p$ (eV)      | 3.41  | 6.85  | 3.93 | 4.30  | 4.14  | 4.76  |
| $\Gamma_D$ (eV)      | 0.67  | 0.27  | 0.74 | 0.17  | 1.36  | 0.23  |
| $f_1$                | 4.61  | 6.81  | 2.69 | 21.80 | 3.21  | 18.41 |
| $\gamma_1$ (eV)      | 4.49  | 2.64  | 0.63 | 0.66  | 1.61  | 2.09  |
| $\omega_{0,1}$ (eV)  | 3.17  | 3.14  | 0.98 | 0.97  | 2.25  | 2.14  |
| $f_2$                | 3.12  | 4.69  | 7.09 | 11.99 | 0.74  | 8.55  |
| $\gamma_2$ (eV)      | 3.32  | 2.34  | 2.61 | 1.26  | 3.77  | 2.12  |
| $\omega_{0,2}$ (eV)  | 5.59  | 5.35  | 2.00 | 1.90  | 6.17  | 4.01  |
| $f_3$                | 0.63  | 3.89  | 1.79 | 14.90 | 2.77  | 1.72  |

|                     |      |      |      |       |      |       |
|---------------------|------|------|------|-------|------|-------|
| $\gamma_3$ (eV)     | 0.97 | 19.0 | 1.93 | 3.55  | 4.19 | 83.74 |
| $\omega_{0,3}$ (eV) | 2.21 | 2.45 | 3.27 | 3.56  | 4.11 | 2.93  |
| $f_4$               | N.A. | N.A. | 3.30 | 10.33 | N.A. | N.A.  |
| $\gamma_4$ (eV)     | N.A. | N.A. | 4.61 | 1.53  | N.A. | N.A.  |
| $\omega_{0,4}$ (eV) | N.A. | N.A. | 5.60 | 5.36  | N.A. | N.A.  |
| MSE                 | 3    | 3    | 3    | 5     | 6    | 6     |

Note: MSE is the mean square error between the fitted model and acquired experimental data.

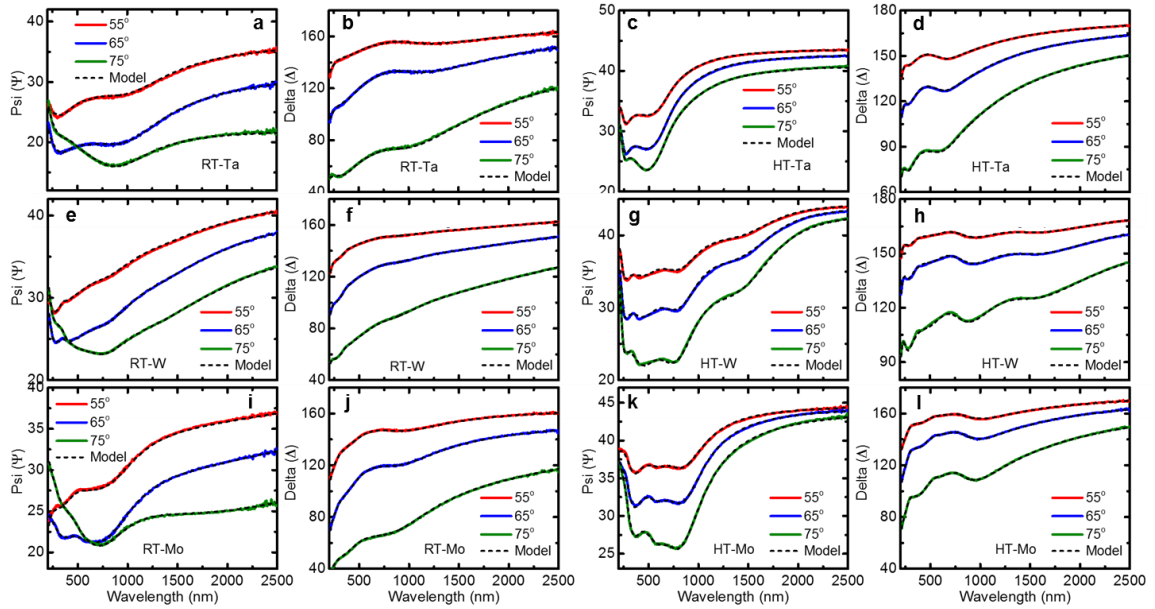


**Figure B1.1: Variable angle spectroscopic ellipsometry data.** Experimental and fitted Psi and Delta of (a, b) RT-Ta, (c, d) RT-W, (e, f) RT-Mo, (g, h) HT-Ta, (i, j) HT-W, (k, l) HT-Mo thin films.

**Table B1.2: Optical (Drude and Lorentz) parameters of MBE deposited TiN/MgO film** obtained from ellipsometer data fitting.

|                   |                 |                     |                 |                 |                     |       |                 |                     |
|-------------------|-----------------|---------------------|-----------------|-----------------|---------------------|-------|-----------------|---------------------|
| $\epsilon_\infty$ | $\omega_p$ (eV) |                     | $\Gamma_D$ (eV) |                 |                     |       |                 |                     |
| 1.913             | 5.26            |                     | 0.52            |                 |                     |       |                 |                     |
| $f_1$             | $\gamma_1$ (eV) | $\omega_{0,1}$ (eV) | $f_2$           | $\gamma_2$ (eV) | $\omega_{0,2}$ (eV) | $f_3$ | $\gamma_3$ (eV) | $\omega_{0,3}$ (eV) |
| 7.97              | 2.52            | 5.58                | 1.98            | 1.02            | 3.69                | 0.58  | 0.59            | 2.15                |

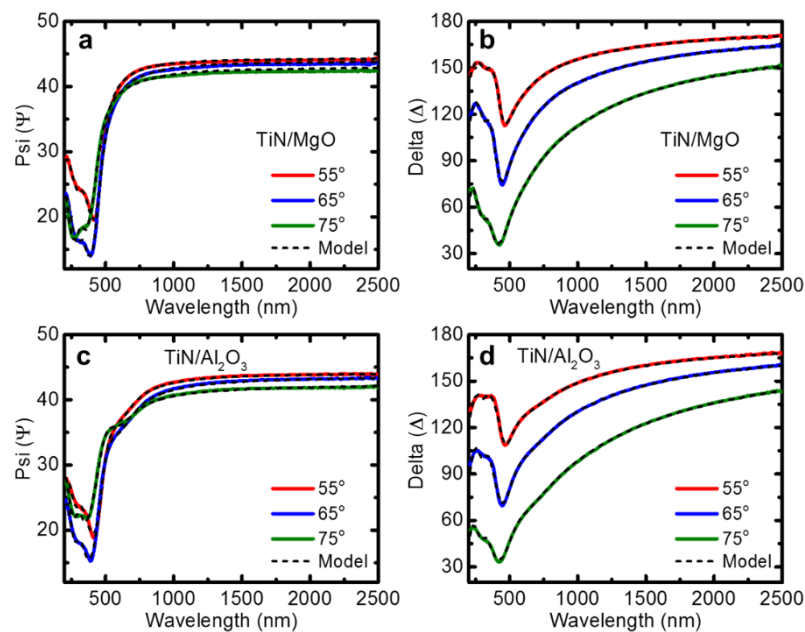
**Table B1.3:** Optical (Drude and Lorentz) parameters of MBE deposited TiN/ Al<sub>2</sub>O<sub>3</sub> film obtained from ellipsometer data fitting.

| $\epsilon_{\infty}$ |  |  | $\omega_p$ (eV) |  |  | $\Gamma_D$ (eV) |  |  |
|---------------------|--|--|-----------------|--|--|-----------------|--|--|
| 1.647               |  |  | 4.58            |  |  | 0.278           |  |  |

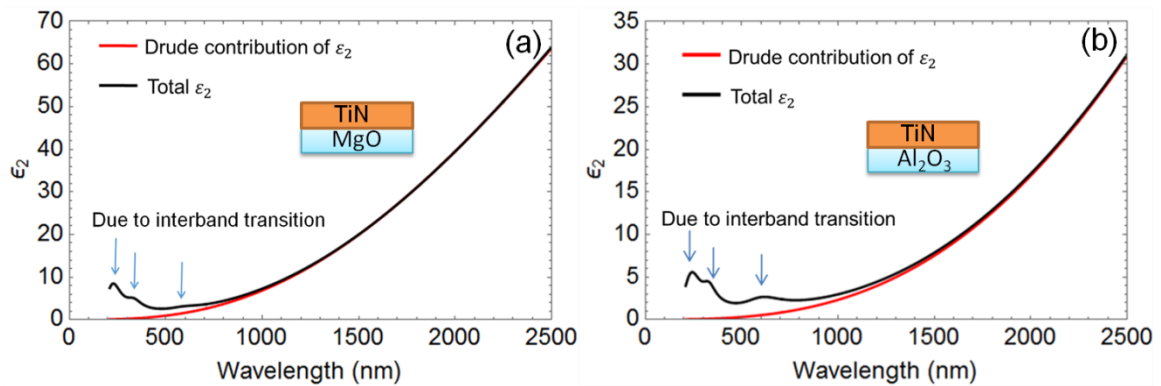
  

| $f_1$ | $\gamma_1$ (eV) | $\omega_{0,1}$ (eV) | $f_2$ | $\gamma_2$ (eV) | $\omega_{0,2}$ (eV) | $f_3$ | $\gamma_3$ (eV) | $\omega_{0,3}$ (eV) |
|-------|-----------------|---------------------|-------|-----------------|---------------------|-------|-----------------|---------------------|
| 5.13  | 2.63            | 5.31                | 1.89  | 0.98            | 3.76                | 1.22  | 0.75            | 2.13                |

**Note:**  $\omega_{0,j}$  represent the peak position of interband transition. There are three Lorentz oscillators that have been used with Drude function for best fitting.



**Figure B1.2:** Variable angle spectroscopic ellipsometry data. Experimental and fitted Psi and delta of (a,b) TiN film grown on MgO substrate, (c,d) TiN film grown on Al<sub>2</sub>O<sub>3</sub> substrate.



**Figure B1.3** Optical loss ( $\epsilon_2$ ) in 100nm (a) TiN/MgO, (b) TiN/ Al<sub>2</sub>O<sub>3</sub> films (Black). Drude model (red) explains the intraband transition very well. There are three peaks which correspond to interband transition.

The Drude model (red) explains the intraband transition as we can see in figure B1.3. The three peaks appeared in the TiN films due to interband transitions between 200nm-1000nm. As we can see that Drude's dielectric function doesn't explain these peaks. This interband process is intrinsically a quantum mechanical process. It occurs from an occupied state below the Fermi level to an unoccupied state above the Fermi level. Lorentz's model has been used to explain this process.

### B1.3 X-ray diffraction spectrum of Ta

The XRD peak intensity is significantly smaller and peak width is much larger for RT-Ta than HT-Ta that represents its poorer crystal quality. Therefore, the superior optical properties of HT-Ta are not only due to its better crystal quality but also due from its different crystal structure and crystal phase. XRD data of the HT-Ta showed two sharp peaks (peak 1 and peak 2) at  $38.26^\circ$  and  $54.68^\circ$  representing its (110) and (200) oriented growth respectively on (002) MgO substrates. From the HRXRD analysis, it appears that HT-Ta crystallizes in body-centered cubic  $\alpha$ -Ta phase with a space group  $Im\bar{3}m$  (229) and a lattice constant of  $3.35\text{\AA}$ . XRD analysis on the RT-Ta exhibit only one peak (peak 1') at  $37.2^\circ$  that correspond to the (111) oriented growth of  $\beta$ -Ta phase and represents a lattice constant of  $3.41\text{\AA}$ .

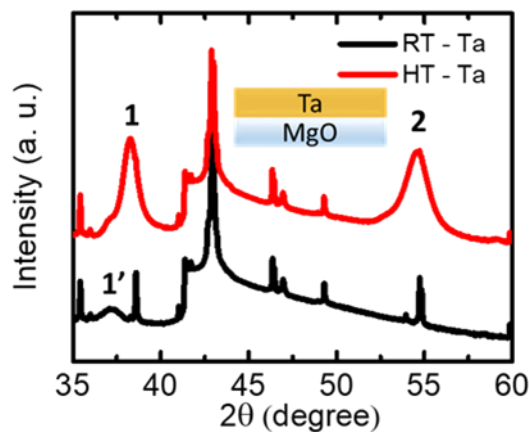


**Figure B1.4** XRD spectra of sputtered deposited HT-Ta/MgO film (red) and RT-Ta/MgO (black).

## B2 Supplementary data of chapter 3

### B2.1 Scandium Nitride (ScN) sample preparation

Sputter-deposited ScN thin films without any intentional doping contain  $1.6 \pm 1$  atomic % of oxygen that arises primarily from target contaminations. In order to increase the oxygen concentration, and thereby to increase the *n*-type carrier concentration inside ScN, three separate Sc targets with different amount of oxygen impurity concentrations are utilized.

Mg-doped ScN films were deposited with co-sputtering from both Sc and Mg targets. Mg-target power was varied from 6W-to-16W, while the Sc target power was fixed at 100W that leads to higher concentration of Mg inside ScN and an associated decrease in the ScN's carrier concentration.

### B2.2 Electronic structure, effective mass and carrier relaxation time in ScN.

Electronic band structure (adapted from the author's previous work (Ref. 99) and presented in Fig. B2.1) shows that ScN exhibit an indirect  $\Gamma - X$  bandgap of  $\sim 0.9$  eV and the direct  $\Gamma - \Gamma$  gap of  $\sim 2.2$  eV.<sup>100</sup> Note that the direct bandgap of ScN is overestimated slightly in the modeling compared to the experimental results ( $\sim 2.2$  eV) due to the limitations of density functional theory exchange-correlation functional. Since as-deposited (and oxygen-doped) ScN thin films exhibit *n*-type carriers, effective mass of carriers has been determined at the *X*-point (conduction band minima) of the Brillouin zone. Results show that ScN exhibit an *n*-type density of states effective mass of  $0.33 \pm 0.02m_o$  and transport effective mass of  $0.40 \pm 0.02m_o$  (where,  $m_o$  is the mass of a free electron). Utilizing the band structure, we have also calculated the hole effective mass at the  $\Gamma$ -point (valance band maxima). Results show that ScN exhibit a heavy hole effective mass of  $1.18m_o$  and light hole effective mass of  $0.22m_o$ .

From the ellipsometry data fitting, an electron effective mass of  $0.39m_o$  is extracted, which is consistent with the previous reports. Ellipsometry data fitting also shows an average electron scattering time of 9 fs. for ScN that is consistent with the scattering time calculated in a recent first-principles calculation. The scattering time for ScN is slightly smaller than the ones reported for other plasmonics materials such as F-doped CdO, Ag or Au. Nevertheless, the relatively low effective mass and high average scattering time of ScN



help it achieve high electrical conductivity and mobility and, therefore, an overall low optical loss.

Even though ScN exhibit an indirect bandgap of  $\sim 0.9$  eV, Fermi level in as-deposited ScN resides  $\sim 100$ - $150$  meV inside the conduction band edge, due to its high carrier concentrations ( $3.3 \times 10^{20} \text{ cm}^{-3}$ ). Further doping of ScN with oxygen increases the carrier concentrations (as shown in Table 3.1) and moves the Fermi level further inside the conduction band (as shown in Fig. B2.1 (b)). On the other hand, Mg-hole doping compensates for the high  $n$ -type carrier concentration, and the Fermi level shifts to the bandgap. At higher hole-doping, ScN undergoes an  $n$ -type to  $p$ -type carrier transition and the Fermi level shifts close to the valence band. Therefore, though both the oxygen and magnesium doping does not alter the band structure and the effective mass (due to the dilute doping level), the position of the Fermi level changes substantially due to doping. From the ellipsometry data fitting, the average carrier scattering time is determined as a function of the doping. At higher doping concentrations ( $1.6 \times 10^{21} \text{ cm}^{-3}$ ), the average carrier scattering time becomes smaller (6 fs) as expected.

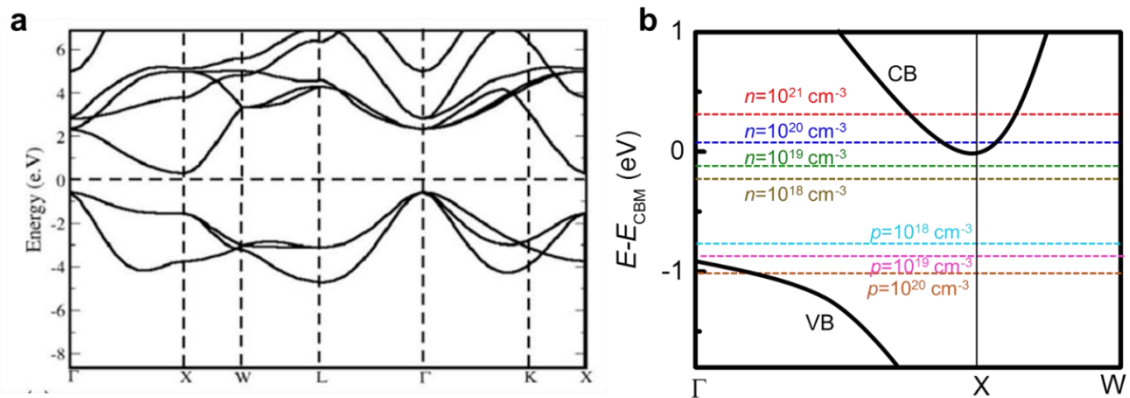


**Figure B2.1:** (a) Electronic structure of ScN showing  $\Gamma$ -X indirect bandgap of  $\sim 0.9$  eV and  $\Gamma$ - $\Gamma$  direct bandgap (adapted from our previous work (Ref. 40)). (b) Position of the Fermi level in ScN as a function of the carrier concentration and carrier type.

Table B2.1: Free carrier mean scattering time ( $\tau$ ) of ScN films.

| ScN films | $\tau$ (fs) |
|-----------|-------------|
| ScN (a)   | 6           |

|         |   |
|---------|---|
| ScN (b) | 2 |
| ScN (c) | 5 |
| ScN (d) | 9 |

### B2.3 Spectroscopic ellipsometry measurements

Spectroscopic ellipsometer measurements were performed in the reflection mode at three different angles ( $55^\circ$ ,  $65^\circ$  and  $75^\circ$ ) of incidences. The experimental (Psi ( $\psi$ ), Delta ( $\Delta$ )) spectrum of ScN films was modeled with Drude & general oscillators (Gaussian and Tauc lorentz) in Complete EASE, J. A. Woollam Co software. Since ScN turned plasmonic in the infrared region, the Drude model takes into account the free-electron response primarily in the IR range, Gaussian and Tauc-Lorentz oscillators were used to fit the interband transitions in the visible spectrum region. While plasmonic property of ScN films can be described with Drude model.

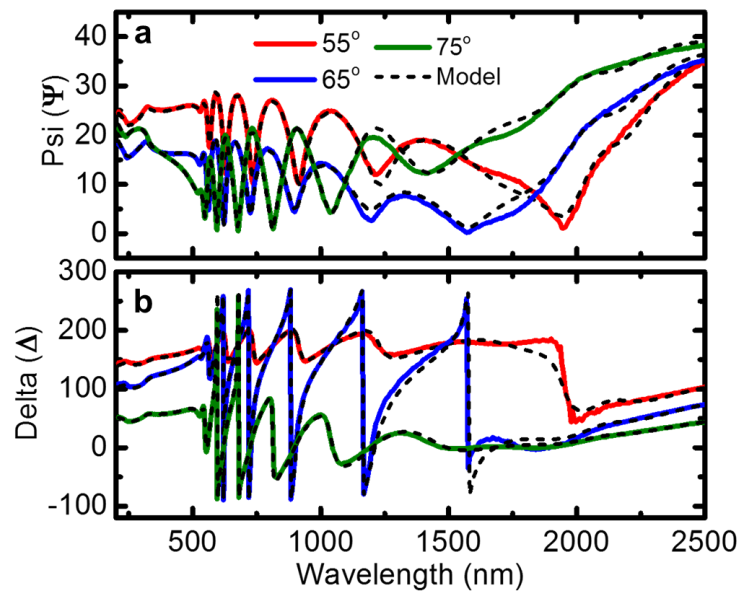


**Figure B2.2: Variable angle spectroscopic ellipsometry data.** Experimental and fitted (a) Psi and (b) delta of ScN (d) film grown on MgO substrate.

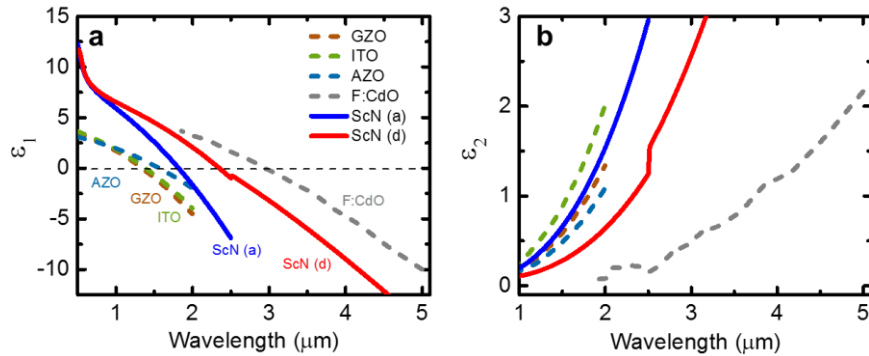
In the following table carrier concentration and mobility obtained by the ellipsometry data-fitting is compared with the hall measurement data. The values are consistent with both the methods. Room-temperature transport data were measured with the Van-der-Pauw technique using an Ecopia HMS-3000 Hall measurement system.

Table S2: Comparison of carrier concentration and mobility obtained by Ellipsometry and Hall measurement.

| Sample  | ENZ Wavelength<br>$\lambda_p$ ( $\mu\text{m}$ ) | Carrier concentration<br>( $\text{cm}^{-3}$ ) | Mobility<br>( $\text{cm}^2\text{V}^{-1}\text{s}^{-1}$ ) | Carrier concentration<br>( $\text{cm}^{-3}$ ) | Mobility<br>( $\text{cm}^2\text{V}^{-1}\text{s}^{-1}$ ) |
|---------|---|---|---|---|---|
|         |   | Hall measurement                              |   | Ellipsometry                                  |   |
| ScN (a) | 1.83  | $1.59 \times 10^{21}$                         | 29  | $1.56 \times 10^{21}$                         | 29  |
| ScN (b) | 2.08  | $1.38 \times 10^{21}$                         | 6   | $1.23 \times 10^{21}$                         | 6   |
| ScN (c) | 2.25  | $7.68 \times 10^{20}$                         | 21  | $7.67 \times 10^{20}$                         | 22  |
| ScN (d) | 2.35  | $3.35 \times 10^{20}$                         | 42  | $3.34 \times 10^{20}$                         | 42  |

### B2.4 Comparison of Plasmonic Properties of ScN with other IR Plasmonic Materials

A comparison of ScN (ScN (a) ( $n = 1.59 \times 10^{21} \text{ cm}^{-3}$ ) and ScN (d) ( $n = 3.35 \times 10^{20} \text{ cm}^{-3}$ )) with other infrared plasmonic materials discussed in this article such as ITO, GZO, AZO, F: CdO. For ScN(d), IR-VASE ellipsometer is used beyond 2.5  $\mu\text{m}$  spectral range.



**Figure B2.3.** (a) The real ( $\epsilon_1$ ) and (b) imaginary ( $\epsilon_2$ ) component of the dielectric permittivity sputter deposited ScN thin films are compared with the optical parameters of AZO, GZO, ITO, F: CdO. Apparent discontinuity in the red curve (ScN(d)) appear due to the measurement with two different ellipsometer systems.

## B2.5 Interband Transitions in ScN

In ultraviolet (UV)-to-visible range, the imaginary part of the dielectric function ( $\varepsilon_2$ ) was extracted by using the general oscillators (Gaussian and Tauc-Lorentz (T-L)) and Kramers-Kronig relations gives the real part of permittivity ( $\varepsilon_1$ ). The peak in the  $\varepsilon_2$  curve describes the interband transitions.

$$\varepsilon_2^{Gaussian} = Amp \cdot \left( \exp \left[ - \left( \frac{E-E0_n}{\sigma_n} \right)^2 \right] - \exp \left[ - \left( \frac{E+E0_n}{\sigma_n} \right)^2 \right] \right) \quad (B2.1)$$

$$\text{where } \sigma_n = \frac{Br_n}{2\sqrt{\ln(2)}}$$

$$\varepsilon_2^{T-L} = Amp \cdot \exp \left[ - \left( \frac{E-Eg}{E} \right)^2 \right] \quad (B2.2)$$

Where,  $\varepsilon_\infty$  is the high-frequency dielectric constant,  $Amp$  is the amplitude,  $E0$  is the resonance energy,  $n$ = number of oscillators,  $Br$  is the broadening,  $Eg$  is the bandgap.

Finally, the total dielectric permittivity function can be written as

$$\varepsilon^{Total}(\omega) = \varepsilon^{Gaussian} + \varepsilon^{T-L}$$

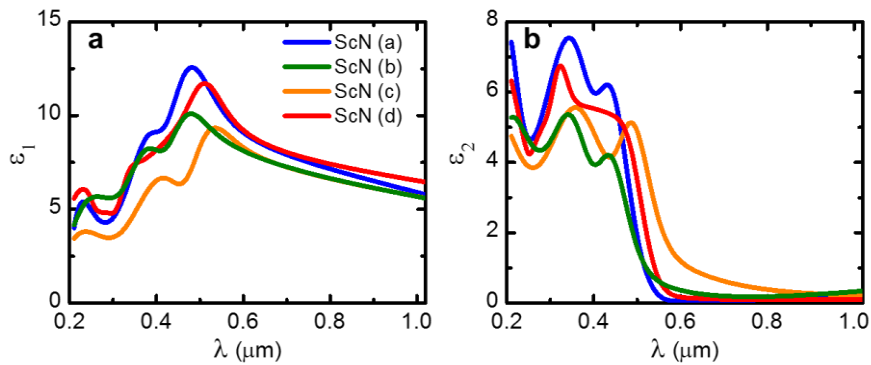


**Figure B2.4.** (a) The real ( $\varepsilon_1$ ) and imaginary ( $\varepsilon_2$ ) component of the dielectric permittivity sputter deposited ScN thin films.

## B2.6 Modeling of Temperature-dependent Mobility

To understand the details of the carrier scattering mechanism, the temperature-dependent mobility was modeled with a combination of ionized impurities ( $\mu_{ionized\ impurity}$ ) as well as dislocation scattering ( $\mu_{dislocation}$ ) of electrons, expressed in the following equation<sup>102</sup>

$$\frac{1}{\mu_{Total}} = \frac{1}{\mu_{ionized\ impurity}} + \frac{1}{\mu_{dislocation}}$$

The electron mobility increases at low temperatures due to ionized impurity scattering with a functional relationship,

$$\mu_{ionized\ impurity} = A T^{1.5}$$

where T is the absolute temperature and A is a constant.

Dislocation scattering can be expressed as

$$\mu_{dislocation} = \left( \frac{3q}{8N_d R} \right) \frac{1}{(3m^* k_B T)^{0.5}}$$

where  $N_d$  and  $R$  are the dislocation density and dislocation core radius, respectively,  $m^*$  is the electron effective mass, and  $q$  and  $k_B$  are the charge of an electron and the Boltzmann constant, respectively. An effective mass of  $0.39m_o$  ( $m_t = 0.28$ ,  $m_l = 2.06$ )<sup>108</sup> is used for ScN.

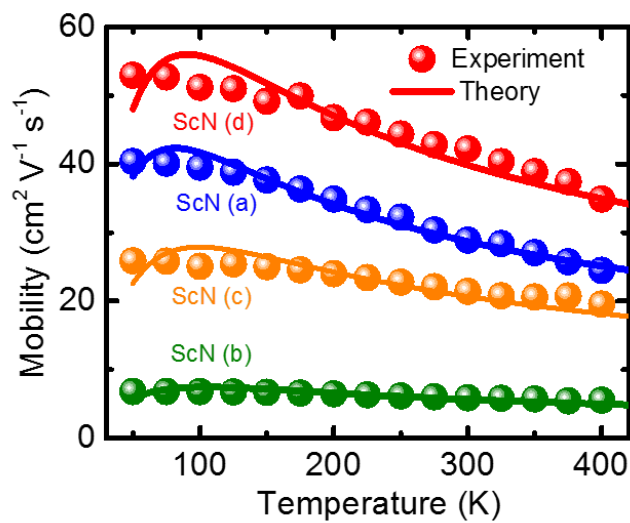


**Figure B2.5.** Temperature dependent mobility of ScN thin films.

Table S4: Scattering parameters

|         | <b>A</b> | <b>N<sub>d</sub></b> ( $\times 10^{10} \text{ cm}^{-2}$ ) | <b>R</b> (nm) |
|---------|----------|---|---------------|
| ScN (a) | 0.23     | 0.7   | 0.34          |
| ScN (b) | 0.028    | 19.5  | 0.07          |
| ScN (c) | 0.11     | 5.1   | 0.07          |
| ScN (d) | 0.25     | 1.7   | 0.11          |

### B2.7 Surface plasmon polaritons (SPPs) dispersion

Beyond the cross over wavelength ScN behave like a metal. The SPP propagation length ( $L$ ) at metal (ScN)-air interfaces and plasmon-decay length ( $\delta$ ) in the metal (or penetration depth) are calculated from the experimental dielectric permittivity. The SPP propagation constant in the direction of propagation can be written as<sup>19</sup>

$$k_x = \frac{2\pi}{\lambda} \sqrt{\frac{\epsilon_{\text{ScN}}\epsilon_{\text{D}}}{\epsilon_{\text{ScN}} + \epsilon_{\text{D}}}},$$

where,  $\epsilon_{\text{ScN}} = \epsilon_1 + i\epsilon_2$  is the dielectric function of ScN,  $\epsilon_{\text{D}}$  is the dielectric function of dielectric medium (air in this case). The propagation length ( $L$ ) is defined as the distance for the SPP intensity to decay by a factor of  $1/e$ .

$$L = \frac{1}{2 \text{Im}(k_x)}$$

The confinement width ( $D$ ) is calculated as<sup>110</sup>

$$D = \frac{1}{\frac{2\pi}{\lambda} \sqrt{\frac{-1}{\epsilon_1 + 1}}} + \frac{(1 - \text{Ln}|\epsilon_1|)}{\frac{2\pi}{\lambda} \sqrt{\frac{-\epsilon_1^2}{\epsilon_1 + 1}}}$$

the figure of merit for SPP  $M_1^{1D}$  is defined as<sup>110</sup>

$$M_1^{1D} = \frac{L}{D}$$

The FOM for and for localized SPP resonance is defined as<sup>215</sup>

$$FOM_{LSP} = -\frac{\varepsilon_1}{\varepsilon_2}$$

Plasmonic response of ScN is compared with the other IR plasmonic materials.

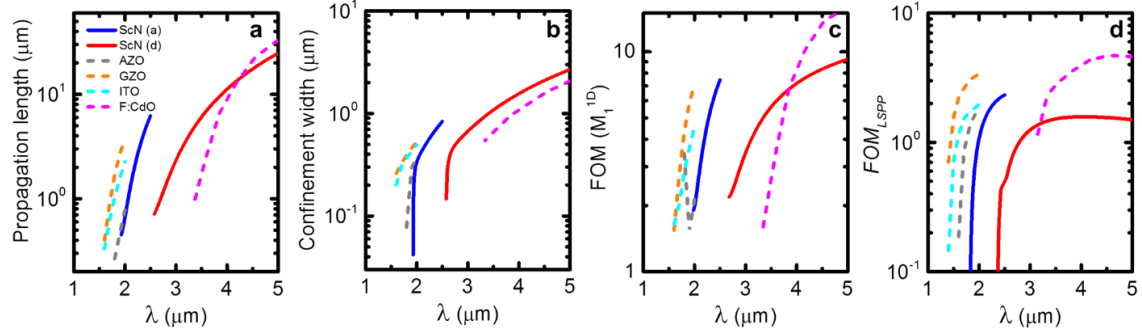


**Figure B2.6** (a) SPP propagation length (L); (b) confinement width (D); (c) FOM of surface plasmon polariton (SPP) and (d) FOM of localized SPP resonance of ScN thin films are compared with the optical parameters of AZO, GZO, ITO, F:CdO.

## B2.8 Reststrahlen band of ScN on different substrates

Since MgO optical phonon energies are very close to that of ScN. So, TiN buffer layer was deposited to avoid the signal from MgO substrate in FTIR-spectrum. Also, ScN film was grown on W/Al<sub>2</sub>O<sub>3</sub> substrate, Reststrahlen band region was found to be the same for both the substrate. Further, we also observed that the contribution of MgO substrate was negligible in thicker ScN film (~1 μm).

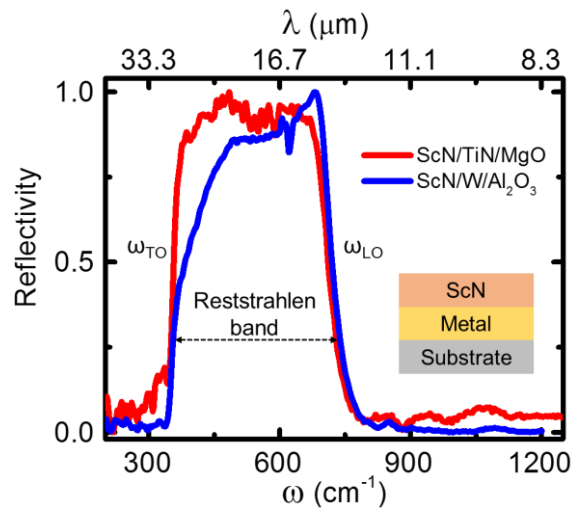


**Figure B2.7.** FTIR Reflection spectra collected from ScN film grown on two different substrates (TiN/MgO and W/Al<sub>2</sub>O<sub>3</sub>).

Infrared reflection was performed with Bruker V70v Fourier Transform Infrared (FTIR) vacuum spectrometer using pyroelectric deuterated triglycine sulfate (DTGS) detector with 4 cm<sup>-1</sup> resolutions for 120 scans.

### B2.9 Surface Phonon Polaritons (SPhPs) dispersion

Like SPP mode, SPhP mode can be excited within the Reststrahlen band. The SPhP dispersion curve can be expressed as<sup>23</sup>

$$k_{SPhP} = \frac{2\pi}{\lambda} \sqrt{\frac{\epsilon_{ScN}\epsilon_a}{\epsilon_{ScN} + \epsilon_a}}$$

Here,  $\epsilon_{ScN}$  and  $\epsilon_a$  are the complex permittivity of the ScN and the ambient medium, respectively.

The FOM for SPhP modes can be described by the following expression<sup>87</sup>:

$$FOM_{SPhP} = \frac{\sqrt{\epsilon_\infty} (\omega_{LO}^2 - \omega^2)(\omega^2 - \omega_{TO}^2)}{\Gamma\omega(\omega_{LO}^2 - \omega_{TO}^2)}$$

### B2.10 Surface morphology of ScN

The plan-view field-emission scanning electron microscopy (FESEM) and atomic force microscopy (AFM) imaging were performed with FEI Inspect F50 and Bruker Innova respectively. The film showed square-shaped structure that arises from the formation of kinetically driven mound structures formations. Such mounds are related to an Ehrlich-Schwoebel surface diffusion barrier that inhibits adatom migration down steps promoting nucleation on the terraces. The measured surface rms. roughness is 2 nm for the ScN film (of carrier concentration  $3.35 \times 10^{20}$  cm<sup>-3</sup>).



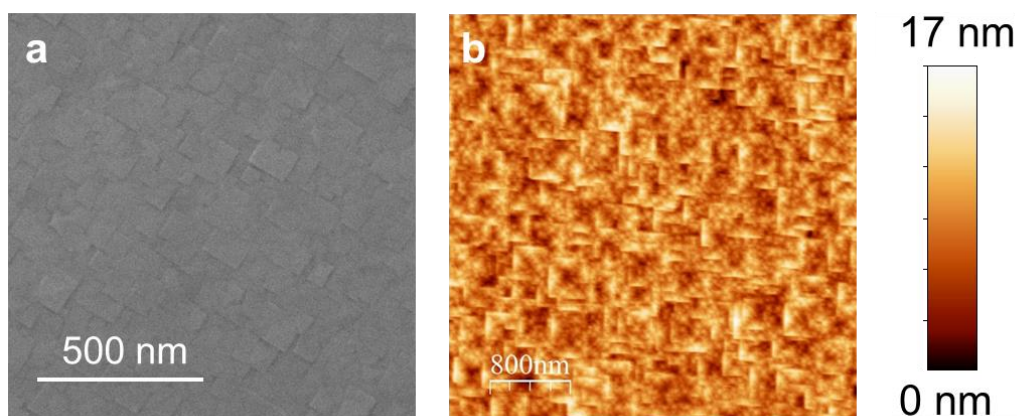


**Figure B2.8** (a) Plan-view FESEM image and (b) AFM image of the ScN film is presented that exhibit the rms. surface roughness of 2 nm.

### B2.11 Transmission electron microscopy

TEM sample preparation was done via Focused Ion beam (FIB). A 100 nm Pt protective cap was deposited at the target location with 5 kV electron beam followed by a 1  $\mu\text{m}$  Pt+C protective cap with a 12 kV Xe beam in Thermo Fisher Scientific Helios Hydra PFIB. Trenching and lift out were done with a 30 kV Xe beam at 60, 15, 4 and 1 nA. The TEM sample was welded to Mo grid using a 30 kV Xe beam Pt weld. Thinning was done with tilt angles of  $\pm 1.5^\circ$  with currents of 300, 100 and 30 pA, checking for electron transparency using a 5 kV electron beam with a secondary electron detector. When the ROI was thin enough it was polished with 5 kV Xe beam with tilt angles of  $\pm 3.5^\circ$ . Final cleaning was performed with 2 kV Xe beam with tilt angles of  $\pm 5.5^\circ$ .

Cross-section STEM and EDS mapping were recorded with a monochromated and image- and probe corrected FEI Themis-Z transmission electron microscope at 300 kV. EDS maps were recorded with count rates of well above 1 million per map and background correction was performed by k-factor methods and absorption correction.

### B2.12 Electron Energy Loss Spectroscopy (EELS) Analysis

EELS was recorded with the same instrument utilizing a GATAN quantum GIF Dual EELS system. High resolution electron energy-loss spectroscopy (EELS) analysis was performed

to observe O K-edge and Mg L-edges in ScN. Spectra were recorded with a monochromated and aberration-corrected FEI Themis-Z in probe mode at 300 kV. The electronic configurations of scandium, nitrogen, magnesium, and oxygen are  $3d^1 4s^2$ ,  $2s^2 2p^3$ ,  $2p^6 3s^2$ , and  $2s^2 2p^4$  respectively. At the O K-edge, peak splitting ( $e_g$  and  $t_{2g}$ ) near 535 eV arises due to the hybridization of O- $2p$  orbitals with the  $d$  orbitals of Sc, and a peak near 543 eV arises due to the hybridization of O- $2p$  states with Sc- $4p$  states see figure B2.8(a). In figure B2.8 (b),  $L_2$  and  $L_3$  edges of Mg are shown. The  $L_2$  and  $L_3$ -edges arise due to the hybridization from Mg  $2p_{1/2}$  and  $2p_{3/2}$  to Sc- $3d$  orbital respectively. In general, these peaks split into  $t_{2g}$  and  $e_g$  orbitals due to the octahedral symmetry in the crystal structure. This analysis, therefore, confirms that both oxygen and magnesium dopants make homogeneous solid solutions in ScN without any precipitations or secondary phase formations. Deconvolution to the spectra was applied to account for multiple scattering and background subtraction.

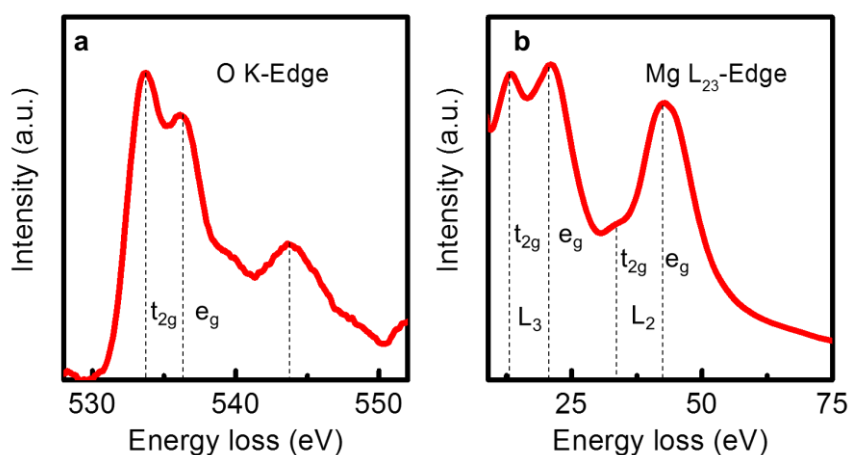


**Figure B2.9.** Electron energy loss spectroscopy (EELS) measurement of **a**, O-K edge and **b**, Mg-L edge are presented.

## B3 Supplementary data of chapter 4

### B3.1 Sample preparation

GaN nanostructures are deposited on the *c*-sapphire substrate with plasma-assisted molecular beam epitaxy (PEMBE). Prior to the deposition, the substrates were cleaned in organic solvents such as acetone and propanol, rinsed in de-ionized water and blow dried. Later they were inserted inside the MBE chamber and thermally degassed for 60 minutes at 600°C in the preparation chamber, and then for 30 minutes at 800°C in the growth chamber.

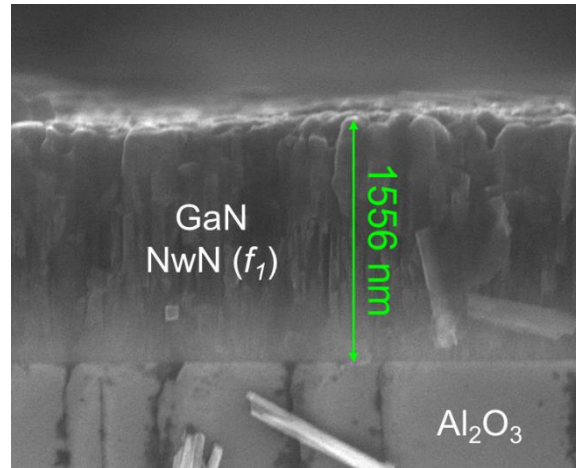
The beam equivalent pressure (BEP) of the source fluxes used for growth, along with the growth temperature and duration are presented in the following table.

Table B3.1: Growth parameters of GaN nanostructures

| GaN Nanostructure | Ga flux BEP ( $\times 10^{-7}$ Torr) | N <sub>2</sub> flux BEP ( $\times 10^{-5}$ Torr) | N <sub>2</sub> /Ga Ratio | Substrate temperature (°C) |
|-------------------|--------------------------------------|--|--------------------------|----------------------------|
| Nano rod          | 2.0                                  | 2.25   | 112.50                   | 630                        |
| NwN ( $f_1$ )     | 3.3                                  | 2.5  | 75.76                    | 630                        |
| NwN ( $f_2$ )     | 2.4                                  | 1.5  | 62.50                    | 630                        |
| NwN ( $f_3$ )     | 5.2                                  | 1.45   | 27.88                    | 630                        |
| NwN ( $f_4$ )     | 5.5                                  | 1.45   | 26.36                    | 630                        |

Given that the nanowall network (NwN) and the nanorod samples are deposited on Al<sub>2</sub>O<sub>3</sub> and Si substrates, respectively, the N<sub>2</sub>/Ga ratio between the two types of films should not be compared.

**B3.2 Cross-section & atomic force microscopy (AFM) images:** The FESEM cross-section images show that the height of the nanostructures is ~ 1600 nm.



**Figure B3.1.** FESEM cross-section image of GaN (a) NwN ( $f_1$ ).

3-dimensional topographic atomic force microscopy (AFM) image of the vertically standing nanowall network (NwN) is presented. The nanowalls are clearly visible in the image.

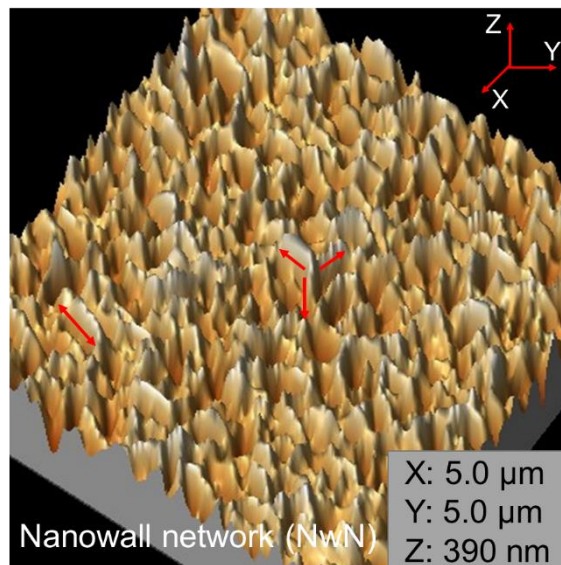


**Figure B3.2:** AFM images ( $5 \mu\text{m} \times 5 \mu\text{m}$ ) of GaN nanowall network

### B3.3 Raman Spectrum: Optical Phonon

Raman spectroscopy of epitaxial GaN layers on sapphire was performed in backscattering geometry with a Horiba Raman spectrometer at room temperature with incident photon energies, 2.3 eV ( $\lambda=540 \text{ nm}$ ). In the Raman spectrum, two peaks appeared at  $566 \text{ cm}^{-1}$  and

$731\text{ cm}^{-1}$  which corresponds to TO and LO phonons respectively. These values are consistent with literature reports.

Raman spectra of the GaN nanostructures are measured as well. Compared to the TO phonon peak at  $566\text{ cm}^{-1}$  in epitaxial film, all GaN nanostructures exhibit a TO phonon peak at  $561\text{ cm}^{-1}$ . Such a slight shift in the TO phonon frequency could be related to the difference in growth methods, strains in the film, and other effects. GaN epitaxial layer is deposited with the CVD method in an industrial setup, while the GaN nanostructures are deposited with PEMBE. The linewidth of the TO phonon modes in GaN nanostructures is slightly higher than the linewidth in the epitaxial layer (FWHM of the TO phonon mode of the epitaxial layer and nanostructures are  $\sim 5\text{ cm}^{-1}$  and  $\sim 10\text{ cm}^{-1}$ , respectively). Such slight broadening of the linewidth is due to the nanostructuring effects. However, compared to the sharp LO phonon mode in GaN epitaxial layer, GaN nanostructures exhibit very faint LO phonon modes. Interestingly, compared to the GaN thin film, no prominent (clear) Raman modes appear between the TO and LO phonon frequencies. It is important to note that though the surface modes are not Raman active, such surface phonons can still interact with light and lead to infrared light absorptions. Surface polariton modes that we have described in the manuscript originate from the interaction of light with the surface phonon modes.

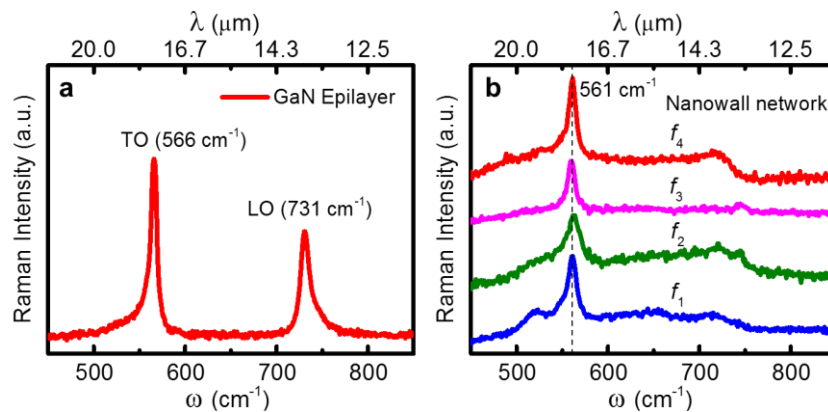


**Figure B3.3.** Raman spectroscopy of (a) GaN epilayer and (b) GaN nanowall network of volume fraction  $f_1, f_2, f_3, f_4$ .

### B3.4 Effect of geometry on the Reststrahlen band of GaN nanostructures: Geometrical factor and Depolarization factor

The spectral features of induced dipoles in GaN nanostructures depends on the shape and geometry of the asperities. The relation of the geometrical factor (and/or depolarization factor) with an induced dipole is presented in the equation 4.5 of the main manuscript. Here we discuss these parameters in detail.

Electric field ( $E_j$ ) and polarization ( $P_j$ ) induced in a particle by the applied field  $E_0$  (assumed in the  $z$ -direction) is given by the following equation<sup>136</sup>

$$E_j = E_0 j - \check{L}_j P_j$$

Where  $\check{L}_j$  is the depolarization factor and related to the geometrical factor ( $L_j$ ) by the following equation

$$\check{L}_j = \frac{\varepsilon - \varepsilon_m L_j}{\varepsilon - \varepsilon_0 \varepsilon_m}$$

The  $\check{L}$  and  $L$  are related by  $\check{L} = L/\varepsilon_0$  for a particle is in free space.  $\check{L}_j$  is the geometrical factor along the  $j^{\text{th}}$  principal axis of the ellipsoid with  $L_1 + L_2 + L_3 = 1$ .

For example, a sphere is a special ellipsoid with  $a=b=c$ , therefore

$$L_1 = L_2 = L_3 = 1/3$$

In the case of a prolate spheroid,  $a = b < c$ , therefore

$$L_1 = \frac{1 - e^2}{e^2} \left( -1 + \frac{1}{2e} \ln \frac{1 + e}{1 - e} \right)$$

$$\text{Here, } e^2 = 1 - \frac{a^2}{c^2}$$

$$L_1 = L_2, L_3 = 1 - 2L_1$$

In the case of an oblate spheroid,  $a > b = c$ , therefore

$$\check{L}_1 = \frac{g(e)}{2e^2} \left( \frac{\pi}{2} - \tan^{-1} g(e) \right) - \frac{g^2(e)}{2}$$

$$g(e) = \left( \frac{1 - e^2}{e^2} \right)^{1/2}, \quad e^2 = 1 - \frac{b^2}{a^2}$$

$$L_2 = L_3 = (1 - L_1)/2$$

The shape of the prolate ranges from a needle ( $e = 1$ ) to a sphere ( $e = 0$ ). The shape of the oblate ranges from a disk ( $e = 1$ ) to a sphere ( $e = 0$ ).

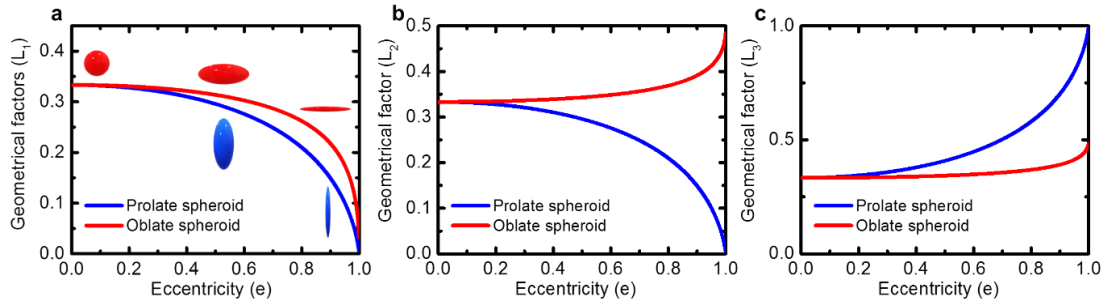


**Figure B3.4** Geometrical factor (a)  $L_1$  (b)  $L_2$  and (c)  $L_3$  as a function of eccentricity ( $e$ )

GaN NwN and nanorods are vertical structures, and the shapes of the asperities can be considered as the prolate type. So, the dipole induced by  $L_3$  is more dominating. As a result, more induced-dipole (or related phonon absorption) occurs for higher  $L$  value (or near LO phonon, as shown in Figure 4.3(a) of the main manuscript).

Since induced dipoles with different  $L$  shapes impact the Reststrahlen band, the ellipsoid model gives us the freedom to combine several structures, starting from needles-to-spheres. In figure B3.5, illustrations of various particle shapes are drawn for visual perception of the particle's geometry as a function of the depolarization factor (or geometrical factor). In the case of the GaN nanostructures, combined effect of the depolarization factor of various shapes is considered in the form of  $L^{eff}$  (effective depolarization factor). We found that for both the NwN and the nanorod,  $L^{eff}$  is close to the 0.6 to 0.8 range (shown in Fig. 4.3), which is akin to prolate types of asperities, resembling needle-like asperities coming out of the surface.

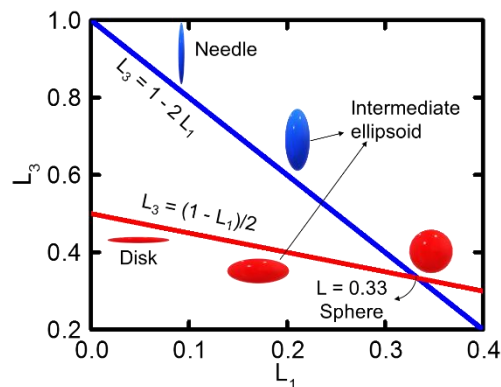


**Figure B3.5** Ellipsoidal particle shape of various geometry as a function of depolarization factor (or geometrical factor).

### B3.5 Probability of the dipole absorption

To find out the probability of the dipole absorption for different shapes of the GaN structures of various effective geometrical factor ( $L^{eff}$ ),  $\omega(L^{eff})$  is replaced by the following normal distribution function<sup>144</sup> in the equation (4.6) of main manuscript.

$$w(L^{eff}) = \frac{1}{\sigma\sqrt{2\pi}} \exp \left[ -\frac{1}{2} \left( \frac{L^{eff} - m}{\sigma} \right)^2 \right]$$

where  $\sigma$  and  $m$  are the standard deviation and the mean value of  $L^{eff}$  respectively. After solving equation 6, the value of  $\sigma$  and  $m$  for NwN (volume fraction 0.7) and nanorod (volume fraction 0.55) are presented in the following table.

Table B3.2:  $m$  and  $\sigma$  are the mean value and the standard deviation for NwN and nanorod

| Sample                          | $m$  | $\sigma$ |
|---------------------------------|------|----------|
| Nanowall network ( $f = 0.70$ ) | 0.92 | 0.85     |
| Nanorod ( $f = 0.55$ )          | 0.75 | 0.70     |

### B3.6 Effective medium approximation

In the case of GaN nanostructures, Lichtenecker's effective medium approximation (LEMA) is used to fit the experimental reflection curve and to obtain the effective response of the material. Lichtenecker's logarithmic mixture formula has been derived from Maxwell's equations assuming a random distribution of shapes and orientations for each component enabling the charge density at any position to be replaced by the mean charge density of the mixture. This allows the charge fraction of each component (GaN and air in this case) to be replaced by its volume fraction ( $f$ ). We found that Lichtenecker's mixture formula works best for the GaN nanostructures such as nanowall-networks and nanorod. Lichtenecker's formula has been applied to obtain the permittivity of a wide range of



mixtures including human blood, dry rocks and minerals, polymer/ceramic composite materials etc.

The effective permittivity for GaN nanostructures is obtained by fitting the experimental reflection curve utilizing the LEMA in Fresnel's equation. The effective permittivity for GaN *NwN* and nanorod is presented in Fig. 4.2 (c) and Fig. 4.2 (d) with volume fractions of ~70% and ~55% respectively. Further, the effect of volume fraction on the Reststrahlen band (see figure 4.3 (f)) and effective permittivity (see figure B3.6) is shown. With the increment of volume fraction, the asymmetric Reststrahlen band and permittivity lead to GaN epilayer.

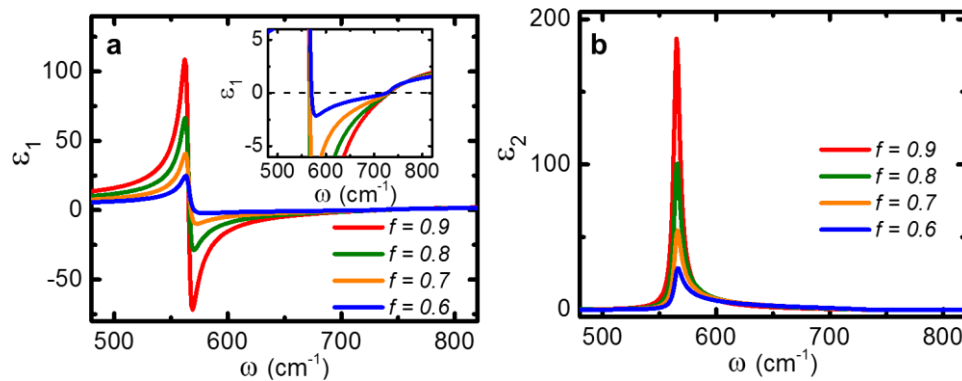


**Figure B3.6.** Calculated (a) real and (b) imaginary parts of the effective dielectric permittivity for GaN nanostructures for volume fraction from 0.6 to 0.9.

### B3.7 Thermal Emission of GaN Nanostructures:

Thermal emission is a ubiquitous process by which every object at non-zero temperatures radiates electromagnetic energy that is governed by Planck's law. Engineering of thermal emission in materials is necessary for solid-state lighting, thermoregulation, energy harvesting, tagging, and imaging. Beyond reflection, the strong absorptive nature of polaritonic resonances provides an alternative method for probing their response through thermal emission. According to Kirchhoff's law, thermal emission is equivalent to absorption at the same temperature,  $\epsilon(\lambda) = \alpha(\lambda) = 1 - R(\lambda) - T(\lambda)$ , here  $\alpha$  is absorptivity,  $\epsilon$  the emissivity,  $R$  is reflectance and  $T$  is transmittance. Since in the Reststrahlen band, the reflectivity is very high, as a result absorptivity and emissivity will be very low within the band. The thermal emission phenomenon is strongly influenced by the coupling of phonons

and long-range electromagnetic fields at infrared frequencies. Recently, it has been found theoretically that at mesoscopic scales, where phonon polaritons can be strongly influenced by the objects' finite sizes, shapes, and nonlocal or many-body response to electromagnetic fluctuations.

Here, we experimentally demonstrated the effect of nanostructuring on GaN's thermal emission properties. Thermal emission spectra are measured by mounting the samples on a copper hot plate, from where the radiation is collected in the FTIR spectrometer. The thermal radiation of the samples, blackbody and the ambient background is measured at 400°C. Thermal emissivity of the sample can be calculated by the following equation:

$$\epsilon(\omega) = \frac{S_s(\omega) - S_a(\omega)}{S_b(\omega) - S_a(\omega)}$$

Where  $S_s$ ,  $S_b$  and  $S_a$  are the sample spectrum, the blackbody spectrum, and the ambient background spectrum.

Emission spectra follow the opposite trends as the IR reflection for example, in the case of the thin film low emissivity is exhibited in the Reststrahlen band (563  $\text{cm}^{-1}$  to 739  $\text{cm}^{-1}$ ). Similarly, for the nanowall, emission showed a dip near TO phonon frequency and triangular spectra opposite to the reflection spectrum.

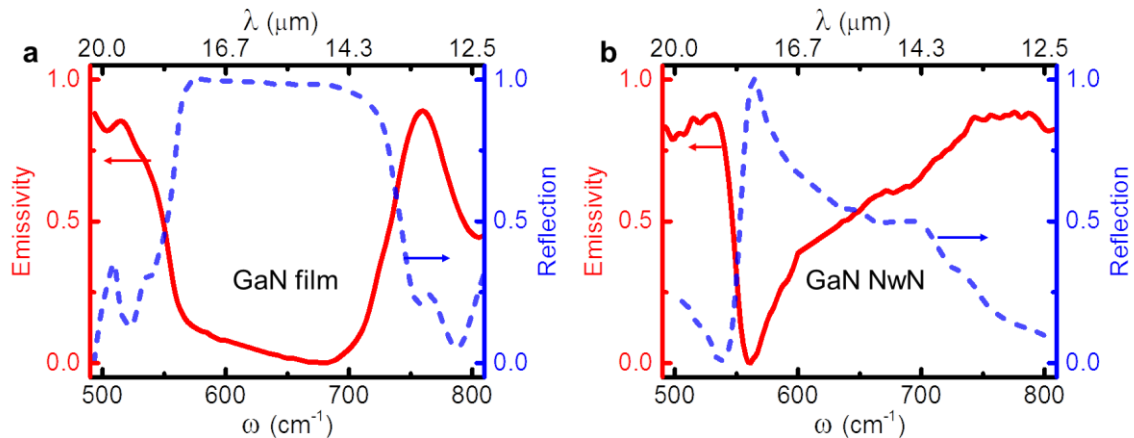


**Figure B3.7.** Thermal emissivity of GaN along with the reflection for (a) thin film and (b) nano-wall network is presented.

**B3.8 Plasmon-polariton in GaN NwN ( $f_4$ ):** Plasmon response of GaN nanostructures is shown in Fig. 4 of the main manuscript. To avoid the overlap and for clarity, plasmon response of GaN NwN ( $f_4$ ) is shown here.

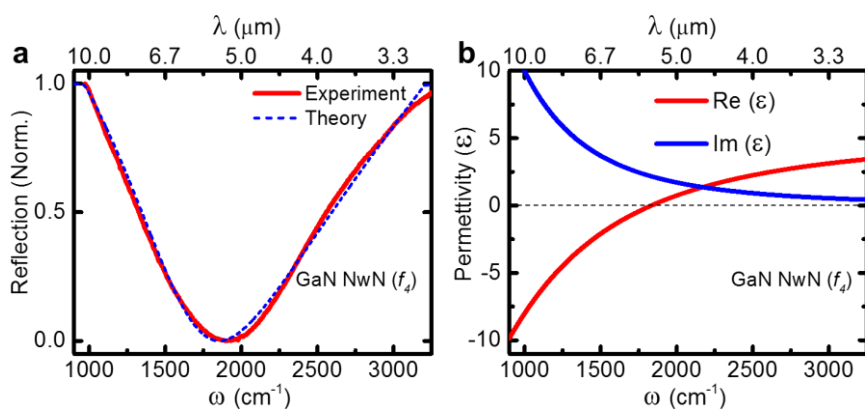


**Figure B3.8.** (a) Plasmonic response and (b) calculated permittivity of GaN NwN ( $f_4$ ).

## **B4 Supplementary data of chapter 5**

### **B4.1 Sample preparation**

TiN/Al<sub>0.72</sub>Sc<sub>0.28</sub>N planner metamaterials are deposited on (001) MgO substrates with dc-magnetron sputtering (PVD Products Inc.) inside an ultrahigh vacuum chamber with a base pressure of (2-4) ×10<sup>-9</sup> Torr. Substrates were cleaned with wet-chemical (acetone and methanol) methods before transferring to the load lock that operated at a pressure of 5 ×10<sup>-8</sup> Torr. Ti (purity of 99.95%), Al (purity of 99.95%), Sc (purity of 99.95%), targets had a dimension of 2-inch in diameter and 0.25 inch in thickness and was sputtered with DC-power of 100 W, 90W and 50W respectively. Deposition pressure of 10 mTorr inside the chamber was maintained with a 9 sccm : 2sccm Ar:N<sub>2</sub> mixture. The substrates temperatures were fixed at 750°C, and the growth rate of TiN and Al<sub>0.72</sub>Sc<sub>0.28</sub>N was 1.2 nm/min. and 2.4 nm/min respectively.

### **B4.2 STEM imaging and EDS mapping**

STEM imaging and EDS mapping were performed with a monochromated image- and probe-corrected FEI Themis Z microscope equipped with high-brightness XFEG with ChemiSTEM EDS detector system for ultra-high-count rates, operated at 300 kV.

### **B4.3 TEM sample preparation**

TEM sample preparation was done with a Thermo Fisher Scientific Helios Hydra Plasma FIB. Samples were coated with 5 nm of Au to prevent charging prior to FIB. A 200 nm Pt protective cap was deposited at the target location with 5 kV electron beam followed by a 1.5 μm Pt+C protective cap with a 12 kV Xe beam in PFIB. Trenching and lift out were done with a 30 kV Xe beam at 15, 4 and 1 nA. The TEM sample was welded to Mo grid using a 30 kV Xe beam Pt weld. Thinning was done with tilt angles of ±1.5° with currents of 300, 100 and 30 pA, checking for electron transparency using a 5 kV electron beam with a secondary electron detector. When the ROI was thin enough it was polished with 5 kV Xe beam with tilt angles of ±3.5°. Final cleaning was performed with 2 kV Xe beam with tilt angles of ±5.5°.

#### B4.4 Spectroscopic ellipsometry measurements

Spectroscopic ellipsometer measurements were performed in the reflection mode at three different angles ( $55^\circ$ ,  $65^\circ$  and  $75^\circ$ ) of incidences from 210 nm to 2500 nm spectral range. The experimental (Psi ( $\psi$ ), Delta ( $\Delta$ )) spectrum of TiN- $\text{Al}_{0.72}\text{Sc}_{0.28}\text{N}$  based planner structures were modeled with Drude & general oscillators (Lorentz and Tauc Lorentz) in Complete EASE, J. A. Woollam Co software. Since TiN become metallic after 480nm, the Drude model takes into account the free-electron response, while Lorentz oscillator takes care of interband transitions in TiN. Since  $\text{Al}_{0.72}\text{Sc}_{0.28}\text{N}$  is a dielectric, Lorentz and Tauc-Lorentz oscillators were used to fit the interband transitions in the visible spectrum region.

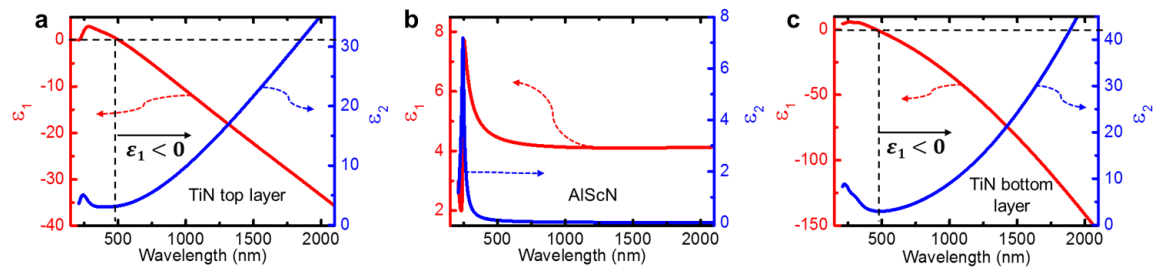


**Figure B4.1** The complex dielectric permittivity ( $\epsilon_1 + i\epsilon_2$ ) of TiN-  $\text{Al}_{0.72}\text{Sc}_{0.28}\text{N}$  -TiN (MDM) structure. a) TiN top layer, b)  $\text{Al}_{0.72}\text{Sc}_{0.28}\text{N}$  and c) TiN bottom layer.

#### B4.5 Effect of top and bottom TiN layer on the optical cavity modes

FEM simulation is performed to optimize the TiN/ $\text{Al}_{0.72}\text{Sc}_{0.28}\text{N}$ /TiN planner structures for optical cavity mode. Top TiN film plays a crucial role in absorption. In the figure, the absorption is highest for 10 nm to 20 nm top TiN film. As a result, all experimental samples are deposited with a 15 nm TiN top layer. In all the samples, we intentionally chose the bottom TiN layer thickness (100 nm) more than the skin depth ( $\sim 40$  nm)<sup>59</sup> so that light cannot pass through the sample (Transmission=0) for the maximum absorption. However, the FEM simulation is performed to check the effect of the bottom layer thickness, we could not find any appreciable change in sharpness of the cavity mode in the 60-140 nm range that lies well beyond the skin depth.

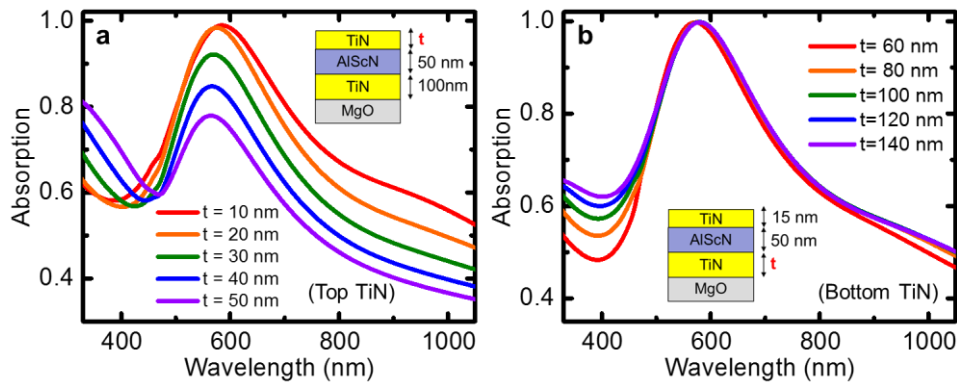


**Figure B4.2.** Effect of (a) top and (b) bottom TiN layer on the optical cavity mode.

### B4.6: Multi-splitting in triple-cavity

The absorption peak of MDM structures (single cavity) splits into two peaks for MDMDM structures (double cavity) as shown in the manuscript. Further, higher-order splitting can also be observed with increasing the number of metal and dielectric layers. Three absorption peaks are visible for the MDMDMDM structure (triple cavity).

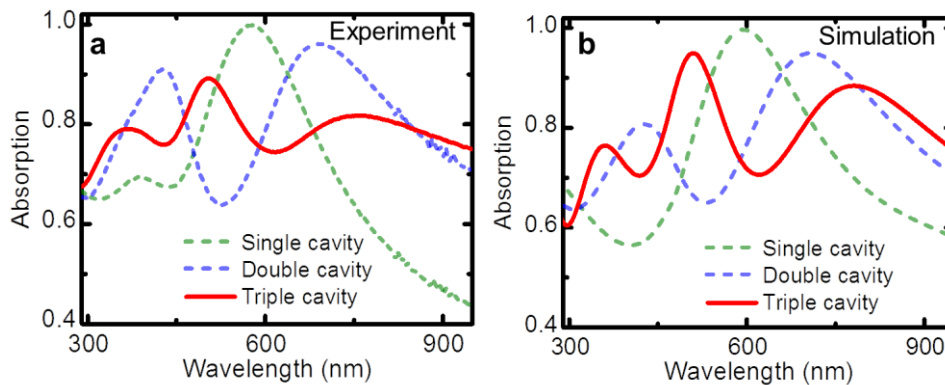


**Figure B4.3** (a) Experimental and (b) Simulated absorption curve of a triple cavity (red) along with single (green) and double (blue) cavity.

### B4.7: The quantum mechanical description of MDM structure

Previously, the MDM multilayers have been studied as the quantum mechanical analogy where the photon tunnel through the potential barrier.<sup>184</sup> The square of the refractive index

$(\tilde{n}_j = n_j - i\kappa_j)$  is taken as the optical equivalent of the potential that defines the barrier height. The equation for the photon propagation in the material is expressed as

$$\frac{d^2}{dx^2}\psi(x) + [k_0(n_j - i\kappa_j)]^2\psi(x) = 0 \quad (\text{B4.1})$$

To obtain the optical resonances such as cavity modes (or ENZ modes) the Hamiltonian should be Hermitian. To satisfy the Hermitian condition, the real or imaginary part of the refractive index should be negligible. Considering the metal-dielectric system, the dielectric's imaginary part of the refractive index is almost negligible, while the metal's imaginary part exhibits high value. It is shown that to satisfy the Hermitian condition and excite the cavity modes the ratio of  $n/\kappa$  should be less than 0.2 in the desired spectral range.<sup>184</sup> On the other hand, the non-Hermitian range is related to the interband transition of the metals. In the case of the Ag, the  $n/\kappa$  is lower than the 0.2 in the visible to IR range. In the case of Au and TiN, the ratio  $n/\kappa$  is high in the interband transition range (<550 nm) and becomes Hermitian after that. While for the transition metals such as Ta and W, the ratio  $n/\kappa$  is higher than 0.2 in the whole visible to NIR range. The optical parameters of Ta and W are taken from the reference<sup>145</sup>.

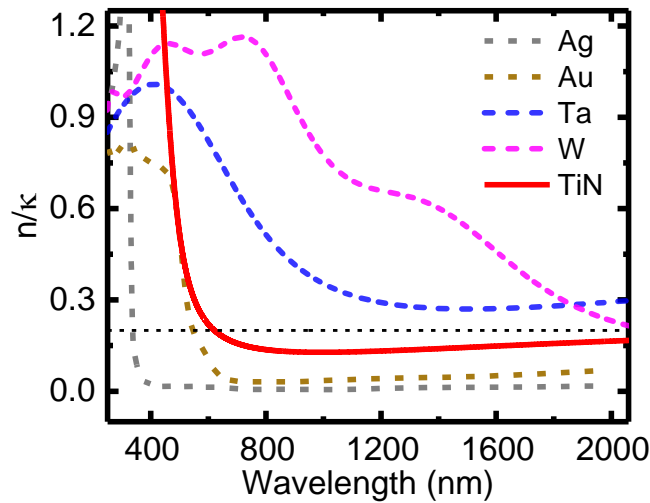


**Figure B4.4.** The Ratio  $n/\kappa$  for the metals (Ag, Au, Ta, W and TiN) defining the Hermitian limit (<0.2), in which the cavity mode can be sustained for MDM structures.

By solving the equation B4.1, the analytical dispersion of the cavity mode can be found as

$$\tan\left(k_0 n_d \frac{t_d}{2} + e^{-2k_0 \kappa_m t_m}\right) = \frac{\kappa_m}{n_d} \quad (\text{B4.2})$$

$$-\cot\left(k_0 n_d \frac{t_d}{2} + e^{-2k_0 \kappa_m t_m}\right) = \frac{\kappa_m}{n_d} \quad (\text{B4.3})$$

The detailed derivation of the equations is presented in the reference <sup>184</sup>. The cavity resonance mode red shifts with the dielectric layer thickness increment (as shown in figure 5.2b in the main manuscript). The calculated dispersion is compared with the experimental absorption mode maxima of the MDM cavity which show good agreement.

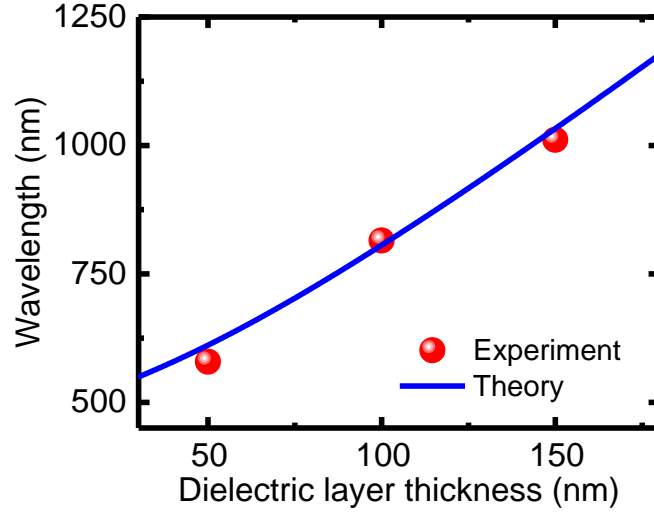


**Figure B4.5** The dispersion of the cavity modes vs thickness of the dielectric layer demonstrates the good agreement between experiment and theory.

#### B4.8: The classical harmonic oscillator description of MDM structure

Previously, the optical response of the MDM structure has been described as a harmonic oscillator and the effective permittivity can be expressed as

$$\varepsilon(\omega) = \varepsilon_1 + i\varepsilon_2 = \varepsilon_\infty - \frac{\omega_p^2}{(\omega^2 + i\gamma\omega)} - \frac{\omega_{MDM}^2}{(\omega^2 - \omega_{0,MDM}^2 + i\omega\Gamma_{MDM})} \quad (\text{B4.4})$$

The derivation of the equations can be found in the reference <sup>184</sup>. Where  $\varepsilon_\infty$  is the permittivity at high frequency (2.5), the  $\omega_p$  is the plasma frequency of the TiN (4.1 eV) and  $\gamma$  is the damping factor (0.65 eV) of the TiN. The parameters  $\omega_{MDM} = 2.58$  eV,  $\Gamma_{MDM} = 0.112$  eV and  $\omega_{0,MDM} = 2.7$  eV, 1.8 eV and 1.4 eV for MDM cavity (as shown in figure 5.2a) of dielectric layer thickness 50nm, 100nm and 150 nm respectively, are obtained from fitting the experimental absorption curve. The real part of the effective permittivity exhibits



cross-over wavelength (positive-to-negative permittivity), also known as epsilon-near-zero (ENZ) wavelength, at 660nm, 890nm and 1060nm near the cavity resonance mode of 50nm, 100nm and 150nm (dielectric layer thickness) MDM cavities respectively. The ENZ wavelength coincides with the optical resonances in the case of a lossless medium.

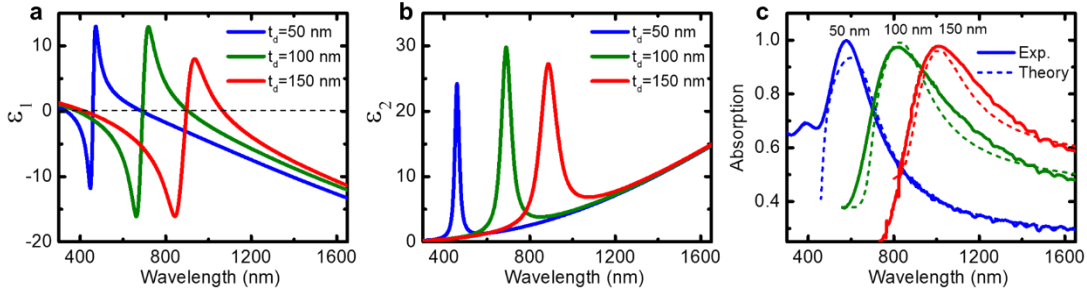


**Figure B4.6.** The real (a) and imaginary (b) part of the effective permittivity of the MDM structures with the dielectric layer thickness of 50nm, 100nm and 150nm. (c) The calculated absorption curve by utilizing the effective permittivity in Fresnel's equation along with the experimental absorption curve.

Further, the effective dielectric permittivity of the MDMDM structure, utilizing the harmonic oscillator model can be expressed as<sup>185</sup>

$$\epsilon(\omega) = \epsilon_1 + i\epsilon_2 = \epsilon_\infty - \frac{\omega_p^2}{(\omega^2 + i\gamma\omega)} - \frac{\omega_{MDM}^2}{(\omega^2 - \omega_{0,MDM1}^2 + i\omega\Gamma_{MDM1})} - \frac{\omega_{MDM}^2}{(\omega^2 - \omega_{0,MDM2}^2 + i\omega\Gamma_{MDM2})} \quad (\text{B4.5})$$

The parameters  $\omega_{MDM} = 3.0$  eV,  $\omega_{0,MDM1} = 2.2$  eV,  $\omega_{0,MDM2} = 3.4$  eV,  $\Gamma_{MDM1} = 0.5$  eV and  $\Gamma_{MDM2} = 0.7$  eV are obtained by fitting the experimental absorption curve of MDMDM (double cavity) structure (as shown in Figure 5.3a of main manuscript). The real part of the permittivity exhibits two ENZ modes corresponding to the cavity resonance modes (absorption maxima) of the double cavity.

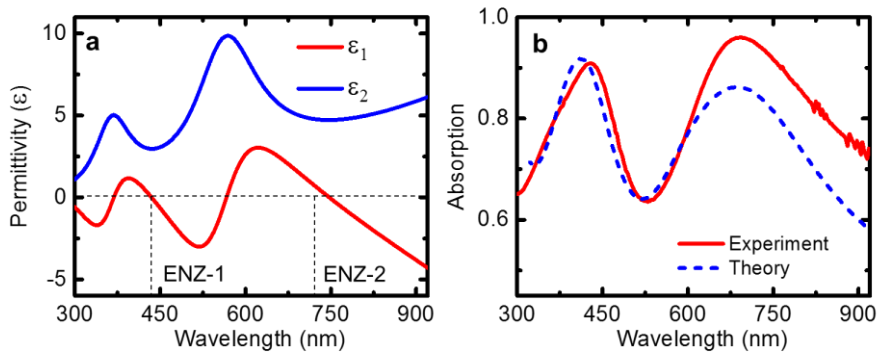


**Figure B4.7.** (a) The effective permittivity of the MDMD (double cavity) structure with a dielectric layer thickness of 50nm. (b) The calculated absorption curve by utilizing the effective permittivity in Fresnel's equation along with the experimental absorption curve.

#### B4.9: Berreman mode in MDM structures

The MDM structures are not only useful for the visible spectral range optical absorption but the optical phonons of the polar-dielectric layer can also be utilized. FTIR spectra of MDM metamaterials with  $\text{Al}_{0.72}\text{Sc}_{0.28}\text{N}$  spacer layer thickness of 50 nm, 100 nm and 150 nm are shown. The absorption peak near the LO phonon frequency is observed in all cases, which is also known as the Berreman mode. Though the Berreman mode frequencies of all the three films should appear at the same frequency, slight variations in the composition of the polar dielectric ( $\text{Al}_{0.72}\text{Sc}_{0.28}\text{N}$ ) layer and growth variations have caused a small shift in the mode frequency.

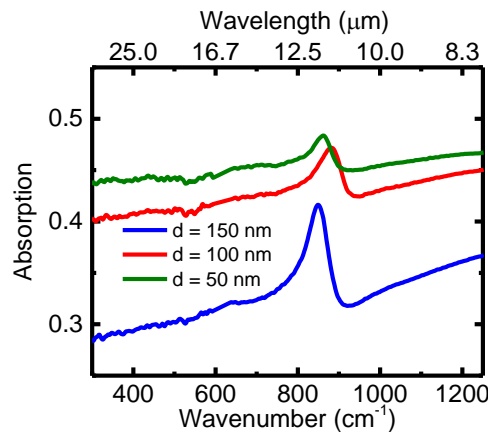


**Figure B4.8.** Berreman mode in MDM structures

#### B4.9: Angle dependent reflection of MDM structures:

Using an ellipsometer, the angle-dependent absorption spectrum of MDM (metal-dielectric-metal) structures was measured. The absorption peak corresponding to the first order Fabry-Perot mode was observed for cavity thicknesses (i.e., thickness of  $\text{AlScN}$ ,  $d$ ) of 100 nm and 150 nm. Interestingly, it was observed that the absorption peak remained relatively unchanged regardless of the angle of incidence.

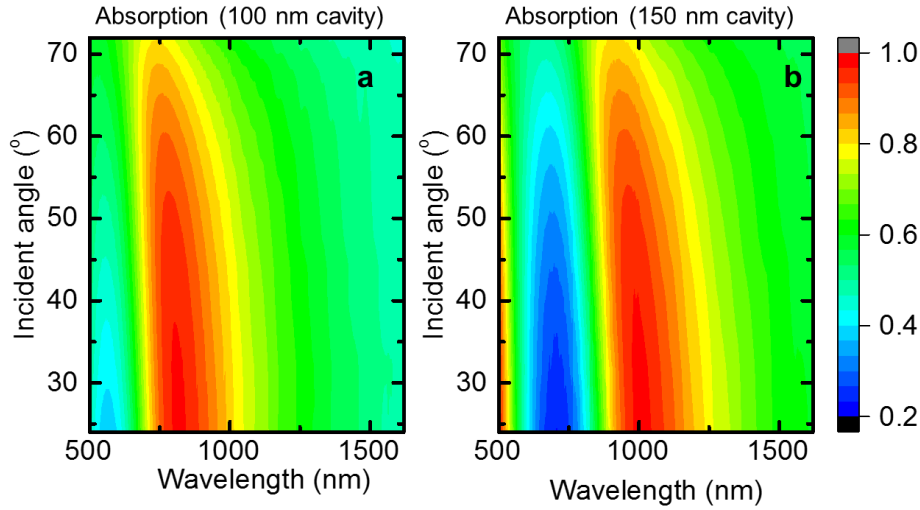


**Figure B4.9.** Angle dependent absorption curve of MDM structures of (a) 100 nm and (b) 150 thick  $\text{Al}_{0.72}\text{Sc}_{0.28}\text{N}$ .

In the case of TiN/AlScN/TiN structure, interference occurs between the waves reflected from the top and bottom layer of AlScN. For constructive interference

$$2dn_2 \cos\theta_r = \left(m - \frac{1}{2}\right) \lambda$$

Where  $m$  is an integer. Since,

$$n_1 \sin\theta_i = n_2 \sin\theta_r$$

$$\cos\theta_r = \sqrt{1 - \left(\frac{n_1}{n_2}\right)^2 \sin^2\theta_i}$$

For 1<sup>st</sup> order,

$$\lambda_{res} = 2dn_2 \sqrt{1 - \left(\frac{n_1}{n_2}\right)^2 \sin^2\theta_i}$$

In general, refractive index of metals ( $n_{metal}$ ) have much lower values in comparison to dielectrics ( $n_{dielectric}$ ),  $n_{metal} < n_{dielectric}$ .

In case of MDM structure ( $n_1 = n_{metal}$ ,  $n_2 = n_{dielectric}$ ),  $\left(\frac{n_1}{n_2}\right)^2 \sin^2\theta_i \ll 1$ .

Consequently,  $\lambda_{res} \approx 2dn_2$ , the resonance wavelength in a TiN-AlScN-based metal-dielectric-metal (MDM) structure is not significantly affected by changes in angle of incidence.

## List of Figures

**Figure 1.1 Schematic diagram of the evolution of industry along with the materials.** New materials enable the new scientific concept and further into next-generation technology and industrial revolution. Conventionally, industry revolution can be divided into four major leaps. The first industrial revolution: steam. The second industrial revolution: electricity. The third industrial revolution: digital / computing. The fourth industrial revolution: connectivity / artificial intelligence. ....6

**Figure 1.2 Types of polaritons.** In material several type of electronic oscillator or dipole can interact with light to form polaritons. For example- plasmon of metal, phonon of dielectric, exciton of semiconductor, cooper pair of superconductors, magnon of magnetic materials and more (there are 70 types of polaritons are discussed in ‘Polariton Panorama’<sup>3</sup>), can interact with light to form various types of polaritons. ....8

**Figure 1.3 Energy scale of various types of polaritons.** In general, exciton and plasmon polaritons lie in the ultraviolet to the near-infrared electromagnetic spectrum, depending on the materials. Phonon polaritons lie in the mid-to-long infrared region while spin-wave-polaritons lie in the far infrared. Cooper-pair-polariton lies in the terahertz range. One can choose the material for various polariton according to the requirement. ....8

**Figure 1.4 Ancient Roman Lycurgus cup.** It appears green in reflected light while red in transmitted light. These glasses are mixed with gold nanoparticles (typically 10–100 nm in size).<sup>16</sup> .....9

**Figure 1.5 Fresnel coefficients for s and p polarized light.** Schematic representation of the incident, reflected and transmitted light at the boundary between two materials with permittivity  $\epsilon_a$  and  $\epsilon_b$  for both the s and p polarizations, in terms of their corresponding Fresnel coefficients. .... 11

**Figure 1.6. Interaction of light with a metal.** (a) Schematics for interaction of light with free electrons in metal (bulk plasmon). (b) Reflection curve of silver along with its real part of dielectric permittivity. Beyond 330 nm, Ag is highly reflective, and the real part of permittivity turns from positive-to-negative, this crossover wavelength is known as plasma wavelength ( $\lambda_p$ ) and corresponding frequency as plasma frequency..... 12

**Figure 1.7 Schematics for the two types of surface-plasmon-resonances.** (a) propagating surface plasmon polaritons along the dielectric-metal interface; (b) localized surface plasmons on the surface of a metal nanoparticles. .... 13

**Figure 1.8 Dispersion relation of surface plasmon-polaritons in an air-silver interface.** We represent the real and imaginary parts of the dispersion relation of surface plasmons in an air-silver interface, given by equation 1.8. We use the Drude model to describe the metal, with parameters  $\epsilon_\infty = 1.5$ ,  $\omega_P = 9.0$  eV and  $\gamma = 70$  meV..... 15

**Figure 1.9 Interaction of light with a polar dielectric.** (a) Schematics for interaction of light with ionic lattice of polar dielectric material. (b) Reflection curve of a polar dielectric material along with its real part of the dielectric permittivity. Polar dielectric material shows high reflectivity between the longitudinal optical (LO) and transverse optical (TO) phonon frequency, which is referred to as the Reststrahlen band..... 16

**Figure 1.10** The elements which form stable nitrides are shown in the periodic table. Color codes indicate the physical properties or use of elements in the nitride family. This figure is adapted from Jena et.al.<sup>21</sup> ..... 18

**Figure 2.1** (a) The real ( $\epsilon_1$ ) and imaginary ( $\epsilon_2$ ) component of the dielectric permittivity sputter-deposited Ta, W and Mo thin film are compared with the optical parameters of noble metals (such as Au<sup>17</sup> and Ag<sup>17</sup>). Reproduced with permission from Maurya et al., Appl. Phys. Lett. 118, 041902 (2021).<sup>22</sup> ..... 27

**Figure 2.2** Symmetric  $2\theta - \omega$  X-ray diffractogram of Ta thin film on MgO substrate along with their rocking curve ( $\omega$ -scan) in the inset. Ta was found to grow with (110) orientations on (002) MgO substrate. The FWHM of the rocking curve was found  $2.4^\circ$  in the Ta/MgO film (b) Reflectivity of Ta film exhibit a sharp dip close to ENZ regions. (c) Atomic force micrographs (AFM) of exhibit rms. surface roughness of 0.5 nm in Ta film. Reproduced with permission from Maurya et al., Appl. Phys. Lett. 118, 041902 (2021).<sup>22</sup> ..... **Error! Bookmark not defined.**

**Figure 2.3** (a) The real ( $\epsilon_1$ ) and (b) imaginary ( $\epsilon_2$ ) part of the dielectric permittivity of MBE-deposited TiN thin film on MgO and Al<sub>2</sub>O<sub>3</sub> substrates are presented. Reproduced with permission from Maurya et al., Optical Materials Express 2679, (2020).<sup>45</sup> ..... 30

**Figure 2.4** XRD spectrum of TiN/MgO (a) and TiN/Al<sub>2</sub>O<sub>3</sub> (b) thin films along with their rocking curve ( $\omega$ -scan) in the inset. Atomic force micrographs of TiN/MgO (c) and TiN/Al<sub>2</sub>O<sub>3</sub> (d). Reproduced with permission from Maurya et al., Optical Materials Express 2679, (2020).<sup>45</sup> ..... 31

**Figure 2.5** (a) Transmission and (b) reflection spectrum of TiN/Al<sub>2</sub>O<sub>3</sub> are presented as a function of wavelength and the angle of incidence. Reproduced with permission from Maurya et al., Optical Materials Express 2679, (2020).<sup>45</sup> ..... 31

**Figure 2.6** Comparison of metals with their optical loss at crossover wavelength and their bulk melting point. Reproduced with permission from Maurya et al., Appl. Phys. Lett. 118, 041902 (2021).<sup>22</sup> ..... 33

**Figure 3. 1 Plasmon-polariton in ScN.** (a) Schematic diagram of a spectroscopic ellipsometer. (b) The real ( $\epsilon_1$ ) and imaginary ( $\epsilon_2$ ) component of the dielectric permittivity of ScN film with the highest carrier concentration of  $1.6 \times 10^{21} \text{ cm}^{-3}$  is presented. ScN becomes plasmonic after  $1.83 \mu\text{m}$ . ( $\epsilon_1 < 0$ ) with the optical loss of 1.2 at

the wavelength ( $\lambda_p$ ) corresponding to its plasma frequency. Experimentally measured normalized reflectivity of ScN film is plotted as the ratio between the  $p$ -polarized to  $s$ -polarized light intensity which shows a dip near the  $\lambda_p$ . (c) Angle-dependent reflectivity curve of ScN film is presented. Brewster's angle is visible in the reflectivity curve. (d) Fresnel's equation-based theoretically calculated reflection curve matches well with the experimentally measured reflection curve. (e) A schematic diagram of the ATR configuration for surface mode excitation. (f) Theoretically calculated SPP dispersion (blue) along with the ATR-measured reflection curve that shows SPP mode excitation at 1.95  $\mu\text{m}$ . The light lines in the vacuum and in ATR crystal are shown by the magenta and orange dotted curves respectively. The bulk plasma wavelength ( $\lambda_p$ ) is shown with the green line.....40

**Figure 3.2 Tunable SWIR plasmon response and electrical properties of ScN.** (a)  $\epsilon_1$  and (b)  $\epsilon_2$  of ScN films with varying carrier concentrations are presented. With the decrease in carrier concentration,  $\lambda_p$  shifts to longer wavelengths.  $\lambda_p$  of 2.35  $\mu\text{m}$  and corresponding  $\epsilon_2$  of 1.0 is obtained for as-deposited ScN film without any intentional doping which makes it a high-quality and low-loss SWIR plasmonic material. (c) Normalized reflectivity curves of ScN with  $1.6 \times 10^{21} \text{ cm}^{-3}$  (a) and  $3.3 \times 10^{20} \text{ cm}^{-3}$  (d)) are presented as the ratio between  $p$ -polarized and  $s$ -polarized intensity ( $R_p/R_s$ ) obtained from the ATR measurements (d) Schematic diagram of the Hall measurement is shown. Temperature-dependent (e) resistivity; (f) mobility and (g) carrier concentration of ScN films are shown which highlights its degenerate semiconducting nature.....42

**Figure 3.3 Temperature-dependent dielectric permittivity of ScN.** Temperature-dependent (a)  $\epsilon_1$  (b)  $\epsilon_2$  of the ScN thin film with  $1.6 \times 10^{21} \text{ cm}^{-3}$  carrier concentrations are presented. With an increased temperature,  $\lambda_p$  and the optical loss increase. (c) Cross-over wavelength ( $\lambda_p$ ) and optical loss was found to increase with increasing temperature as mobility is decreasing.....43

**Figure 3.4 Phonon-polariton in ScN.** (a) Schematic diagram of Fourier-transform infrared spectrometer (FTIR). (b) Normalized FTIR reflection (red) spectra of ScN film is shown and the calculated reflection spectrum is presented (in blue shade). (c) Calculated dielectric permittivity ( $\epsilon$ ) of ScN thin film showing negative  $\epsilon_1$  within the Reststrahlen band. (d) Normalized reflection spectra obtained from the ATR measurement showing excitation of the SPhP mode with  $p$ -polarized light. (e) Theoretically calculated dispersion of SPhP is presented. The light lines, in the vacuum and ATR crystal, are

shown by the green and blue curve respectively. The frequency positions of  $\omega LO$  and  $\omega TO$  are shown by cyan and magenta dotted lines respectively. Lower and upper bulk phonon polaritons are shown by the orange dotted curve.....45

**Figure 3.5** (a) Comparison of plasmonic properties of ScN with transparent conductive oxides (ITO<sup>67</sup>, AZO<sup>67</sup>, F:CdO<sup>68</sup>, Dy:CdO<sup>69</sup>), doped silicon (n-Si, p-Si)<sup>66</sup> and InAs<sup>65</sup> their optical loss at crossover wavelength (or ENZ wavelength). (b) Comparison of FOM of SPhP of ScN with other polar dielectric materials (SiC<sup>76</sup>, GaN<sup>100</sup>, hBN<sup>77</sup>, AlN<sup>79</sup>, GaP<sup>101</sup>, cBN<sup>99</sup>). .....46

**Figure 3.6 STEM images and EDS maps of ScN deposited on (001) MgO substrate.**

(a) Low-magnification STEM image showing homogeneous and uniform ScN growth with a few dislocations. The electron diffraction pattern in the inset confirms the cubic epitaxial growth. (b) Atomic resolution STEM image of the ScN/MgO demonstrating a sharp interface. STEM-EDS elemental mapping of (c) Sc, (d) N, (e) Mg and (f) O shows the homogeneous elemental distribution. ....47

**Figure 4.1 Plan-view FESEM microstructure of MBE-deposited GaN**

**nanostructures.** (a-e) Surface topography of nanowall network to nanorod along with various intermediate complex structures. Crystal growth under non-equilibrium conditions gives rise to such complex surface morphology. ....53

**Figure 4.2 Reststrahlen band of GaN epilayer and nanostructures.** Reflection spectrum (red curve) along with the theoretically fitted curve (blue curve) of (a) GaN epilayer; (c) GaN nano-wall network (volume fractions of ~70%); (e) GaN nanorod (volume fractions of ~55%). A highly asymmetrical right trapezoidal shaped Reststrahlen band appears in the GaN nanostructure. The calculated real ( $\epsilon_1$ ) and imaginary ( $\epsilon_2$ ) component of the effective dielectric permittivity ( $\epsilon_{eff}$ ) of (b) GaN epilayer, (d) GaN nanowall network and (f) GaN nanorod. Nanostructuring leads to asymmetry in epsilon-near-pole (ENP) resonance at the TO phonon frequency. To capture the sharp dip in the reflection spectrum of the nanorod near LO phonon, phonon confinement effect<sup>41,42</sup> is included in the modeling as presented in SI section 8. ....54

**Figure 4.3 Induced dipole moment and its distribution within the Reststrahlen band.**

(a) Normalized induced dipole moments of the surface polaritons as a function of wavenumber with depolarization factors  $L$  as a parameter. For  $L$  close to 1, the surface polariton maximum appears close to the LO phonon frequency. While for  $L$  close to zero,

surface polariton maxima are located close to the TO phonon frequency. (b) The probability distribution function for dipole absorption as a function of effective depolarization factor of GaN nanostructure.....57

**Figure 4.4 Impact of GaN volume fraction on nanostructure's Reststrahlen band.**

FESEM images of GaN nanowall-networks with increasing volume fraction (a)  $f_1$  (~0.60), (b)  $f_2$  (~0.70), (c)  $f_3$  (~0.77), (d)  $f_4$  (~0.83). (e) Experimentally measured reflection curve of the NwNs. (f) Calculated reflection curve using LEMA for volume fraction of 0.6, 0.7, 0.8, 0.9. Both the experimental and the theoretical results show that a lower volume fraction of GaN leads to higher asymmetry in the Reststrahlen band. ....59

**Figure 4.5 Plasmon-polariton in GaN nanostructures.** (a) Plasmon response in GaN NwNs with volume fraction  $f_1$  (blue curve),  $f_2$  (green curve) and  $f_3$  (red curve) where  $f_3 > f_2 > f_1$ . (b) Plasmon response in GaN nanorods. GaN NwN exhibit more open surfaces compared to nanorods, consequently, more carriers are present in NwNs. The (c) real ( $\epsilon_1$ ) and (d) imaginary ( $\epsilon_2$ ) component of the dielectric permittivity of GaN NwNs of volume fraction  $f_1$  (blue curve),  $f_2$  (green curve),  $f_3$  (red curve) and nanorod (magenta curve). ...61

**Figure 4.6 Comparison of the plasmonic response of GaN nanostructures with other mid-IR nanostructured plasmonic material.** GaN NwN ( $f_1$ ) exhibits a high-quality factor value of 6.6 which is higher than the previously reported quality factor for several nanostructured plasmonic materials such as InN, Al/ZnO,  $\text{Cu}_{2-x}\text{S}$ , Sn/ $\text{In}_2\text{O}_3$ , Ce/ $\text{In}_2\text{O}_3$ . Low optical loss in the GaN nanostructure is the reason for the high-quality factor. ....62

**Figure 5.1** a) STEM micrograph of TiN/ $\text{Al}_{0.72}\text{Sc}_{0.28}\text{N}$  multilayer stack deposited on (001) MgO is presented. Coherent epitaxial interfaces between different layers are visible in the images. The electron diffraction pattern in the inset confirms the lattice-matched cubic epitaxial growth. b) High-magnification STEM image highlight the TiN/ $\text{Al}_{0.72}\text{Sc}_{0.28}\text{N}$  interfaces. c) Atomic resolution STEM image of the TiN/ $\text{Al}_{0.72}\text{Sc}_{0.28}\text{N}$  interface is presented demonstrating a sharp interface. STEM-EDS elemental mapping of d) Ti, e) Al, f) Sc, and g) N demonstrates well-separated layers without diffusion of atoms into adjacent layers.....67

**Figure 5.2** a) Schematic diagram of the unit cell of metal-dielectric-metal (MDM) optical cavity. b) Experimental and c) simulated absorption spectra of the MDM structures with varying dielectric  $\text{Al}_{0.72}\text{Sc}_{0.28}\text{N}$  layer thickness (50 nm (blue), 100 nm (green), 150 nm (red)). d) Magnitude of electric field profile and (e) electromagnetic power-loss density



distribution for the MDM structure (50 nm of  $\text{Al}_{0.72}\text{Sc}_{0.28}\text{N}$  thickness) at the maximum absorption peak wavelength of 580 nm. f) Experimental and g) simulated angle-dependent absorption curve of MDM structure (of 50 nm thick  $\text{Al}_{0.72}\text{Sc}_{0.28}\text{N}$ )..... 68

**Figure 5.3** a) Schematic diagram of  $\text{TiN}/\text{Al}_{0.72}\text{Sc}_{0.28}\text{N}$  based double cavity structure. b) Schematic diagram that shows the splitting of energy states due to the coupling between double cavities. c) Experimental and d) simulated absorption spectra of double cavity mode (red line) along with the single cavity mode (blue dash line). The splitting of the curve corresponds to the direct coupling of the two cavities. (e, f) Magnitude of electric field profile and (g, h) electromagnetic power-loss density distribution for the double cavity (50 nm of  $\text{Al}_{0.72}\text{Sc}_{0.28}\text{N}$  thickness) at the maximum absorption peak wavelength of 440 nm and 690nm..... 71

**Figure 5.4** Effect of TiN top-layer on  $\text{Al}_{0.72}\text{Sc}_{0.28}\text{N}/\text{TiN}/\text{MgO}$  sample in IR and visible range. a) FTIR reflection of  $\text{Al}_{0.72}\text{Sc}_{0.28}\text{N}/\text{TiN}/\text{MgO}$  and  $\text{TiN}/\text{Al}_{0.72}\text{Sc}_{0.28}\text{N}/\text{TiN}/\text{MgO}$  samples. Thin TiN (15 nm) top layer film does not affect the optical phonon much, while strong absorption in the visible range appeared due to the cavity resonance. (b) Simultaneous optical resonances, cavity mode and Berreman mode can be achieved in MDM structures..... 72

**Figure 5.5** FTIR Reflection spectra are collected from a)  $\text{AlN}/\text{MgO}$  (red) along with MgO substrate (blue). For MgO substrate, a clear Reststrahlen band spread over  $395\text{ cm}^{-1}$  to  $767\text{ cm}^{-1}$ . For the sample  $\text{AlN}/\text{MgO}$ , two Reststrahlen bands appeared from AlN and MgO. b) Reflection spectra of  $\text{TiN}/\text{MgO}$  and  $\text{AlN}/\text{TiN}/\text{MgO}$ . Metal TiN reflectivity is around 95% in the whole FTIR spectral range. For the sample  $\text{AlN}/\text{TiN}/\text{MgO}$ , two dips in the reflection spectra correspond to the absorption of TO and LO phonon of AlN. c) IR-reflection of  $\text{Al}_{0.72}\text{Sc}_{0.28}\text{N}/\text{TiN}/\text{MgO}$  samples of two different thicknesses of  $\text{Al}_{0.72}\text{Sc}_{0.28}\text{N}$  100 nm and 1000nm is compared. Two dips in the reflection spectra correspond to the TO and LO modes appearing in the thicker  $\text{Al}_{0.72}\text{Sc}_{0.28}\text{N}$  while the optical modes are barely visible in the thinner film. d) Berreman mode dispersion relationship for 100 nm (blue) and  $1\text{ }\mu\text{m}$  (red) thick  $\text{Al}_{0.72}\text{Sc}_{0.28}\text{N}/\text{TiN}$  samples calculated using Eq. 3. The light line is shown as a dotted green line. The inset shows the Berreman mode of  $\text{Al}_{0.72}\text{Sc}_{0.28}\text{N}$  films. .... 75

**Figure 6.1** (a) STEM micrograph of  $\text{TiN}/\text{Al}_{0.72}\text{Sc}_{0.28}\text{N}$  (metal/dielectric) superlattice deposited on the on the MgO substrate. (b) High-magnification STEM image highlight the TiN and  $\text{Al}_{0.72}\text{Sc}_{0.28}\text{N}$  are separated by clean and abrupt interfaces. .... 79

- Figure 6.2** Dielectric functions (measured using spectroscopic ellipsometry) of (a) TiN and (b) (Al,Sc)N that constitute the superlattice (20 nm/20 nm of 8 period) together with (c) the real and (d) imaginary parts of the dielectric functions of the effective medium that approximates the superlattice. The perpendicular permittivity has a Lorentz-like response while parallel permittivity has Drude like response. ....80
- Figure 6.3** (a) Experimental reflection spectrum of 20 nm/20 nm TiN/(Al,Sc)N superlattice presented as a function of incident angle (measured using spectroscopic ellipsometry). (b) Theoretically calculated reflection spectra of the same superlattice (using COMSOL Multiphysics Software) that indicates a clear match up with experimentally measured spectrum.....81
- Figure 6.4** Schematic diagram of isofrequency surfaces in momentum space for elliptical (a), hyperbolic type-I (b) and type-II (c) medium.....82
- Figure 6.5** Photonic spin Hall effect in TiN/Al<sub>0.72</sub>Sc<sub>0.28</sub>N superlattice-based hyperbolic medium. (a) Schematic of photon dynamics of opposite spin in the hyperbolic medium. (b) Simulated electric field distribution (which represents the light propagation) in the hyperbolic medium. Light of helicity ( $\sigma$ ) = -1 propagates in the left direction and vice versa. ....83
- Figure 7.1 Refractory materials platform for nanophotonic application.** Plasmon and phonon polariton in refractory transition-metal-nitrides covering wide range of electromagnetic spectrum, from visible to infrared range. Plasmon resonances of refractory metals, such as TiN, ZrN, W, Ta etc., can be utilized for visible to near-infrared regime. The plasmon resonances in doped ScN and GaN nanostructures can be utilized for near-infrared to mid-infrared range. For mid-to-long infrared, phonon polariton of ScN, GaN and AlScN can be utilized. ....85
- Figure 7.2 Plasmon polariton in transition metals and nitrides.** Comparison of metals with their optical loss at crossover wavelength and their bulk melting point.....87
- Figure 7.3** Polar semiconducting ScN can host both types of plasmon and phonon polariton. ....87
- Figure 7.4 Reststrahlen band and plasmon polariton in GaN nanostructures** (a) Lithography free MBE grown GaN nanostructures of various volume fractions (*f*). Morphology controlled (b) tailored Reststrahlen band and (c) tunable plasmon polariton. ....88
- Figure 7.5** TiN-AlScN based MDM structure: to achieve the optical cavity mode along with optical phonon mode (Berreman mode). The right-side figure shows the light confinement in the MDM cavity at the resonance frequency. ....89
- Figure 7.6** Signature of optical spin Hall effect in TiN-AlScN superlattice based hyperbolic medium. Light of opposite helicity (i.e.,  $\sigma = -1$  or  $\sigma = +1$ ) propagates in the opposite directions. ....90

## References

---

- (1) Moore, G. E. Cramming More Components onto Integrated Circuits. *Proc. IEEE* **1998**, *86* (1), 82–85. <https://doi.org/10.1109/JPROC.1998.658762>.
- (2) Sanvitto, D.; Kéna-Cohen, S. The Road towards Polaritonic Devices. *Nat. Mater.* **2016**, *15* (10), 1061–1073. <https://doi.org/10.1038/nmat4668>.
- (3) Basov, D. N.; Asenjo-Garcia, A.; Schuck, P. J.; Zhu, X.; Rubio, A. Polariton Panorama. *Nanophotonics* **2020**, *10* (1), 549–577. <https://doi.org/10.1515/nanoph-2020-0449>.
- (4) Fleischmann, M.; Hendra, P. J.; McQuillan, A. J. Raman Spectra of Pyridine Adsorbed at a Silver Electrode. *Chem. Phys. Lett.* **1974**, *26* (2), 163–166. [https://doi.org/10.1016/0009-2614\(74\)85388-1](https://doi.org/10.1016/0009-2614(74)85388-1).
- (5) Ndukaife, J. C.; Shalaev, V. M.; Boltasseva, A. Plasmonics--Turning Loss into Gain. *Science* (80-. ). **2016**, *351* (6271), 334–335. <https://doi.org/10.1126/science.aad9864>.
- (6) Boriskina, S. V.; Cooper, T. A.; Zeng, L.; Ni, G.; Tong, J. K.; Tsurimaki, Y.; Huang, Y.; Meroueh, L.; Mahan, G.; Chen, G. Losses in Plasmonics: From Mitigating Energy Dissipation to Embracing Loss-Enabled Functionalities. *Adv. Opt. Photonics* **2017**, *9* (4), 775. <https://doi.org/10.1364/aop.9.000775>.
- (7) Brongersma, M. L.; Halas, N. J.; Nordlander, P. Plasmon-Induced Hot Carrier Science and Technology. *Nature Nanotechnology*. 2015, pp 25–34. <https://doi.org/10.1038/nnano.2014.311>.
- (8) Ndukaife, J. C.; Kildishev, A. V.; Nnanna, A. G. A.; Shalaev, V. M.; Wereley, S. T.; Boltasseva, A. Long-Range and Rapid Transport of Individual Nano-Objects by a Hybrid Electrothermoplasmonic Nanotweezer. *Nat. Nanotechnol.* **2016**, *11* (1), 53–59. <https://doi.org/10.1038/nnano.2015.248>.
- (9) Yoon, J.; Zhou, M.; Badsha, M. A.; Kim, T. Y.; Jun, Y. C.; Hwangbo, C. K. Broadband Epsilon-Near-Zero Perfect Absorption in the Near-Infrared. *Sci. Rep.* **2015**, *5*, 1–8. <https://doi.org/10.1038/srep12788>.
- (10) Tian, Y.; García de Arquer, F. P.; Dinh, C. T.; Favraud, G.; Bonifazi, M.; Li, J.;

- Liu, M.; Zhang, X.; Zheng, X.; Kibria, M. G.; Hoogland, S.; Sinton, D.; Sargent, E. H.; Fratalocchi, A. Enhanced Solar-to-Hydrogen Generation with Broadband Epsilon-Near-Zero Nanostructured Photocatalysts. *Adv. Mater.* **2017**.  
<https://doi.org/10.1002/adma.201701165>.
- (11) Juan, M. L.; Righini, M.; Quidant, R. Plasmon Nano-Optical Tweezers. *Nat. Photonics* **2011**, *5* (6), 349–356. <https://doi.org/10.1038/nphoton.2011.56>.
- (12) Juan, M. L.; Gordon, R.; Pang, Y.; Eftekhari, F.; Quidant, R. Self-Induced Back-Action Optical Trapping of Dielectric Nanoparticles. *Nat. Phys.* **2009**, *5* (12), 915–919. <https://doi.org/10.1038/nphys1422>.
- (13) Hou, B.; Shen, L.; Shi, H.; Kapadia, R.; Cronin, S. B. Hot Electron-Driven Photocatalytic Water Splitting. *Phys. Chem. Chem. Phys.* **2017**, *19* (4), 2877–2881. <https://doi.org/10.1039/c6cp07542h>.
- (14) Dyachenko, P. N.; Molesky, S.; Petrov, A. Y.; Störmer, M.; Krekeler, T.; Lang, S.; Ritter, M.; Jacob, Z.; Eich, M. Controlling Thermal Emission with Refractory Epsilon-near-Zero Metamaterials via Topological Transitions. *Nat. Commun.* **2016**, *7* (May). <https://doi.org/10.1038/ncomms11809>.
- (15) Chang, C. C.; Kort-Kamp, W. J. M.; Nogan, J.; Luk, T. S.; Azad, A. K.; Taylor, A. J.; Dalvit, D. A. R.; Sykora, M.; Chen, H. T. High-Temperature Refractory Metasurfaces for Solar Thermophotovoltaic Energy Harvesting. *Nano Lett.* **2018**, *18* (12), 7665–7673. <https://doi.org/10.1021/acs.nanolett.8b03322>.
- (16) Leonhardt, U. Optical Metamaterials: Invisibility Cup. *Nat. Photonics* **2007**, *1* (4), 207–208. <https://doi.org/10.1038/nphoton.2007.38>.
- (17) Griffiths, D. J. *Introduction to Electrodynamics*; Cambridge University Press, 2017. <https://doi.org/10.1017/9781108333511>.
- (18) Folland, T. G.; Nordin, L.; Wasserman, D.; Caldwell, J. D. Probing Polaritons in the Mid- to Far-Infrared. *J. Appl. Phys.* **2019**, *125* (19), 191102. <https://doi.org/10.1063/1.5090777>.
- (19) Maier, S. A. Excitation of Surface Plasmon Polaritons at Planar Interfaces. In *Plasmonics: Fundamentals and Applications*; Springer US: New York, NY, 2007;

- pp 39–52. [https://doi.org/10.1007/0-387-37825-1\\_3](https://doi.org/10.1007/0-387-37825-1_3).
- (20) Kravets, V. G.; Kurioz, P. Y.; Poperenko, L. V. Spectral Dependence of the Magnetic Modulation of Surface Plasmon Polaritons in Permalloy/Noble Metal Films. *J. Opt. Soc. Am. B* **2014**, *31* (8), 1836. <https://doi.org/10.1364/josab.31.001836>.
- (21) Stockman, M. I. Nanoplasmonics: Past, Present, and Glimpse into Future. *Opt. Express* **2011**, *19* (22), 22029. <https://doi.org/10.1364/OE.19.022029>.
- (22) Hu, G.; Shen, J.; Qiu, C. W.; Alù, A.; Dai, S. Phonon Polaritons and Hyperbolic Response in van Der Waals Materials. *Adv. Opt. Mater.* **2020**, *8* (5), 1–19. <https://doi.org/10.1002/adom.201901393>.
- (23) Strocio, M. A.; Dutta, M. Phonons in Bulk Würtzite Crystal. In *Phonons in Nanostructures*; Cambridge University Press, 2001; pp 16–25. <https://doi.org/10.1017/CBO9780511534898.004>.
- (24) Jena, D.; Page, R.; Casamento, J.; Dang, P.; Singhal, J.; Zhang, Z.; Wright, J.; Khalsa, G.; Cho, Y.; Xing, H. G. The New Nitrides: Layered, Ferroelectric, Magnetic, Metallic and Superconducting Nitrides to Boost the GaN Photonics and Electronics Eco-System. *Jpn. J. Appl. Phys.* **2019**, *58* (SC). <https://doi.org/10.7567/1347-4065/ab147b>.
- (25) P. B. Johnson and R. W. Christy. Optical Constant of the Nobel Metals. *Phys. Rev. B* **1972**, *6* (12), 4370–4379.
- (26) Li, W.; Guler, U.; Kinsey, N.; Naik, G. V.; Boltasseva, A.; Guan, J.; Shalaev, V. M.; Kildishev, A. V. Refractory Plasmonics with Titanium Nitride: Broadband Metamaterial Absorber. *Adv. Mater.* **2014**, *26*, 7959–7965. <https://doi.org/10.1002/adma.201401874>.
- (27) Logeeswaran, V. J.; Kobayashi, N. P.; Islam, M. S.; Wu, W.; Chaturvedi, P.; Fang, N. X.; Wang, S. Y.; Williams, R. S. Ultrasoother Silver Thin Films Deposited with a Germanium Nucleation Layer. *Nano Lett.* **2009**, *9* (1), 178–182. <https://doi.org/10.1021/nl8027476>.
- (28) Chen, W.; Thoreson, M. D.; Ishii, S.; Kildishev, A. V.; Shalaev, V. M. Ultra-Thin

- Ultra-Smooth and Low-Loss Silver Films on a Germanium Wetting Layer. *Opt. Express* **2010**, *18* (5), 5124. <https://doi.org/10.1364/oe.18.005124>.
- (29) Kalpakjian, S.; Schmid, S. R. *Manufacturing Engineering and Technology*, 6th ed.; Stark, H., Opaluch, W., Eds.; Prentice Hall, 2010.
- (30) Kolawa, E.; Chen, J. S.; Reid, J. S.; Pokela, P. J.; Nicolet, M. Tantalum-Based in Si / Cu VLSI Metallizations. *J. Appl. Phys.* **1991**, *1369* (70), 1369–1373.
- (31) Hasan, D.; Pitchappa, P.; Wang, J.; Wang, T.; Yang, B.; Ho, C. P.; Lee, C. Novel CMOS-Compatible Mo – AlN – Mo Platform for Metamaterial- Based Mid-IR Absorber. **2017**. <https://doi.org/10.1021/acsphotonics.6b00672>.
- (32) Park, J. H.; Han, S. E.; Nagpal, P.; Norris, D. J. Observation of Thermal Beaming from Tungsten and Molybdenum Bull ’ s Eyes. **2016**. <https://doi.org/10.1021/acsphotonics.6b00022>.
- (33) Arpin, K. A.; Losego, M. D.; Braun, P. V. Electrodeposited 3D Tungsten Photonic Crystals with Enhanced Thermal Stability. **2011**, 4783–4788. <https://doi.org/10.1021/cm2019789>.
- (34) Kinsey, N.; DeVault, C.; Boltasseva, A.; Shalaev, V. M. Near-Zero-Index Materials for Photonics. *Nat. Rev. Mater.* **2019**, *4*, 742–760. <https://doi.org/10.1038/s41578-019-0133-0>.
- (35) Baffou, G.; Quidant, R. Thermo-Plasmonics: Using Metallic Nanostructures as Nano-Sources of Heat. *Laser and Photonics Reviews*. 2013. <https://doi.org/10.1002/lpor.201200003>.
- (36) Javani, M. H.; Stockman, M. I. Real and Imaginary Properties of Epsilon-Near-Zero Materials. *Phys. Rev. Lett.* **2016**, *117* (10), 1–6. <https://doi.org/10.1103/PhysRevLett.117.107404>.
- (37) Enoch, S.; Tayeb, G.; Sabouroux, P.; Guérin, N.; Vincent, P. A Metamaterial for Directive Emission. *Phys. Rev. Lett.* **2002**, *89* (21), 1–4. <https://doi.org/10.1103/PhysRevLett.89.213902>.
- (38) Ziolkowski, R. W. Propagation in and Scattering from a Matched Metamaterial Having a Zero Index of Refraction. *Phys. Rev. E* **2004**, *70* (4), 046608.

- <https://doi.org/10.1103/PhysRevE.70.046608>.
- (39) Alù, A.; Silveirinha, M. G.; Salandrino, A.; Engheta, N. Epsilon-near-Zero Metamaterials and Electromagnetic Sources: Tailoring the Radiation Phase Pattern. *Phys. Rev. B - Condens. Matter Mater. Phys.* **2007**, *75* (15), 1–13. <https://doi.org/10.1103/PhysRevB.75.155410>.
- (40) Juenker, D. W.; LeBlanc, L. J.; Martin, C. R. Optical Properties of Some Transition Metals. *J. Opt. Soc. Am.* **1968**, *58* (2).
- (41) Wells, M. P.; Bower, R.; Kilmurray, R.; Zou, B.; Mihai, A. P.; Gobalakrishnan, G.; Alford, N. M.; Oulton, R. F. M.; Cohen, L. F.; Maier, S. A.; Zayats, A. V.; Petrov, P. K. Temperature Stability of Thin Film Refractory Plasmonic Materials. *Opt. Express* **2018**, *26* (12), 15726. <https://doi.org/10.1364/oe.26.015726>.
- (42) Gnanarajan, S.; Lam, S. K. H.; Bendavid, A. Coexistence of Epitaxial Ta(111) and Ta(110) Oriented Magnetron Sputtered Thin Film on c-Cut Sapphire. *J. Vac. Sci. Technol. A Vacuum, Surfaces, Film.* **2010**, *28* (2), 175–181. <https://doi.org/10.1116/1.3276801>.
- (43) Zheng, P.; Ozsdolay, B. D.; Gall, D. Epitaxial Growth of Tungsten Layers on MgO(001). *J. Vac. Sci. Technol. A Vacuum, Surfaces, Film.* **2015**, *33* (6), 061505. <https://doi.org/10.1116/1.4928409>.
- (44) Mertler, G.; Rey, M.; Reichelt, K. Hetero-Epitaxial Growth of Mo Single Crystal Films on MgO-Crystals and of W, Nb, and Ta on Mo Thin Film Substrates. *Nucl. Instruments Methods* **1982**, *192* (2–3), 535–538. [https://doi.org/10.1016/0029-554X\(82\)90869-2](https://doi.org/10.1016/0029-554X(82)90869-2).
- (45) Ehrlich, G.; Hudda, F. G. Atomic View of Surface Self-Diffusion: Tungsten on Tungsten. *J. Chem. Phys.* **1966**. <https://doi.org/10.1063/1.1726787>.
- (46) Schwoebel, R. L.; Shipsey, E. J. Step Motion on Crystal Surfaces. *J. Appl. Phys.* **1966**. <https://doi.org/10.1063/1.1707904>.
- (47) Lee, S. L.; Doxbeck, M.; Mueller, J.; Cipollo, M.; Cote, P. Texture, Structure and Phase Transformation in Sputter Beta Tantalum Coating. **2004**, *178*, 44–51. <https://doi.org/10.1016/j.surfcoat.2003.06.008>.

- (48) Engheta, N. Circuits with Light at Nanoscales: Optical Nanocircuits Inspired by Metamaterials. *Science* (80-. ). **2007**, *317* (5845), 1698–1702. <https://doi.org/10.1126/science.1133268>.
- (49) Silveirinha, M.; Engheta, N. Tunneling of Electromagnetic Energy through Subwavelength Channels and Bends Using  $\epsilon$ -near-Zero Materials. *Phys. Rev. Lett.* **2006**, *97*, 157403. <https://doi.org/10.1103/PhysRevLett.97.157403>.
- (50) Adams, D. C.; Inampudi, S.; Ribaldo, T.; Slocum, D.; Vangala, S.; Kuhta, N. A.; Goodhue, W. D.; Podolskiy, V. A.; Wasserman, D. Funneling Light through a Subwavelength Aperture with Epsilon-near-Zero Materials. *Phys. Rev. Lett.* **2011**, *107* (13), 133901. <https://doi.org/10.1103/PhysRevLett.107.133901>.
- (51) Campione, S.; Wendt, J. R.; Keeler, G. A.; Luk, T. S. Near-Infrared Strong Coupling between Metamaterials and Epsilon-near-Zero Modes in Degenerately Doped Semiconductor Nanolayers. *ACS Photonics* **2016**, *3* (2), 293–297. <https://doi.org/10.1021/acsp Photonics.5b00663>.
- (52) Reshef, O.; De Leon, I.; Alam, M. Z.; Boyd, R. W. Nonlinear Optical Effects in Epsilon-near-Zero Media. *Nat. Rev. Mater.* **2019**, *4* (8), 535–551. <https://doi.org/10.1038/s41578-019-0120-5>.
- (53) Kinsey, N.; DeVault, C.; Kim, J.; Ferrera, M.; Shalaev, V. M.; Boltasseva, A. Epsilon-near-Zero Al-Doped ZnO for Ultrafast Switching at Telecom Wavelengths. *Optica* **2015**, *2* (7), 616. <https://doi.org/10.1364/optica.2.000616>.
- (54) Yu, I.-S.; Cheng, H.-E.; Chang, C.-C.; Lin, Y.-W.; Chen, H.-T.; Wang, Y.-C.; Yang, Z.-P. Substrate-Insensitive Atomic Layer Deposition of Plasmonic Titanium Nitride Films. *Opt. Mater. Express* **2017**, *7* (3), 777. <https://doi.org/10.1364/ome.7.000777>.
- (55) Naik, G. V.; Kim, J.; Boltasseva, A. Oxides and Nitrides as Alternative Plasmonic Materials in the Optical Range [Invited]. *Opt. Mater. Express* **2011**, *1* (6), 1090–1099. <https://doi.org/10.1103/PhysRevLett.107.133901>.
- (56) Patsalas, P.; Kalfagiannis, N.; Kassavetis, S.; Abadias, G.; Bellas, D. V.; Lekka, C.; Lidorikis, E. Conductive Nitrides: Growth Principles, Optical and Electronic Properties, and Their Perspectives in Photonics and Plasmonics. *Mater. Sci. Eng. R*



- Reports* **2018**, *123*, 1–55. <https://doi.org/10.1016/j.mser.2017.11.001>.
- (57) Maurya, K. C.; Shalaev, V. M.; Boltasseva, A.; Saha, B. Reduced Optical Losses in Refractory Plasmonic Titanium Nitride Thin Films Deposited with Molecular Beam Epitaxy. *Opt. Mater. Express* **2020**, *10* (10), 2679. <https://doi.org/10.1364/ome.405259>.
- (58) Das, P.; Maurya, K. C.; Schroeder, J. L.; Garbrecht, M.; Saha, B. Near-UV-to-Near-IR Hyperbolic Photonic Dispersion in Epitaxial (Hf,Zr)N/ScN Metal/Dielectric Superlattices. *ACS Appl. Energy Mater.* **2022**, *5* (4), 3898–3904. <https://doi.org/10.1021/acsaem.1c03467>.
- (59) Maurya, K. C.; Shalaev, V. M.; Boltasseva, A.; Saha, B. Reduced Optical Losses in Refractory Plasmonic Titanium Nitride Thin Films Deposited with Molecular Beam Epitaxy. *Opt. Mater. Express* **2020**, *10* (10), 2679. <https://doi.org/10.1364/ome.405259>.
- (60) Das, P.; Biswas, B.; Maurya, K. C.; Garbrecht, M.; Saha, B. Refractory Plasmonic Hafnium Nitride and Zirconium Nitride Thin Films as Alternatives to Silver for Solar Mirror Applications. *ACS Appl. Mater. Interfaces* **2022**. <https://doi.org/10.1021/acsaem.2c09852>.
- (61) Babinova, R. V.; Smirnov, V. V.; Useenov, A. S.; Kravchuk, K. S.; Gladkikh, E. V.; Shapovalov, V. I.; Mylnikov, I. L. Mechanical Properties of Titanium Nitride Films Obtained by Reactively Sputtering with Hot Target. *J. Phys. Conf. Ser.* **2017**, *872*, 012035.
- (62) Datta, S.; Das, M.; Balla, V. K.; Bodhak, S.; Murugesan, V. K. Mechanical, Wear, Corrosion and Biological Properties of Arc Deposited Titanium Nitride Coatings. *Surf. Coat. Technol.* **2018**, *344*, 214–222. <https://doi.org/10.1016/j.surfcoat.2018.03.019>.
- (63) Pang, X.; Zhang, L.; Yang, H.; Gao, K.; Volinsky, A. A. Residual Stress and Surface Energy of Sputtered TiN Films. *J. Mater. Eng. Perform.* **2015**, *24*, 1185–1191. <https://doi.org/10.1007/s11665-015-1393-5>.
- (64) Tyson, W. R. Surface Free Energies of Solid Metals Estimation from Liquid Surface Tension Measurements. *Surf. Sci.* **1977**, *62*, 267–276.

- (65) Venema, L.; Verberck, B.; Georgescu, I.; Prando, G.; Couderc, E.; Milana, S.; Maragkou, M.; Persechini, L.; Pacchioni, G.; Fleet, L. The Quasiparticle Zoo. *Nat. Phys.* **2016**, *12* (12), 1085–1089. <https://doi.org/10.1038/nphys3977>.
- (66) Basov, D. N.; Fogler, M. M.; García De Abajo, F. J. Polaritons in van Der Waals Materials. *Science (80-. )*. **2016**, *354* (6309). <https://doi.org/10.1126/science.aag1992>.
- (67) Low, T.; Chaves, A.; Caldwell, J. D.; Kumar, A.; Fang, N. X.; Avouris, P.; Heinz, T. F.; Guinea, F.; Martin-Moreno, L.; Koppens, F. Polaritons in Layered Two-Dimensional Materials. *Nat. Mater.* **2017**, *16* (2), 182–194. <https://doi.org/10.1038/nmat4792>.
- (68) Schneider, C.; Rahimi-Iman, A.; Kim, N. Y.; Fischer, J.; Savenko, I. G.; Amthor, M.; Lermer, M.; Wolf, A.; Worschech, L.; Kulakovskii, V. D.; Shelykh, I. A.; Kamp, M.; Reitzenstein, S.; Forchel, A.; Yamamoto, Y.; Höfling, S. An Electrically Pumped Polariton Laser. *Nature* **2013**, *497* (7449), 348–352. <https://doi.org/10.1038/nature12036>.
- (69) Azzam, S. I.; Kildishev, A. V.; Ma, R. M.; Ning, C. Z.; Oulton, R.; Shalaev, V. M.; Stockman, M. I.; Xu, J. L.; Zhang, X. Ten Years of Spasers and Plasmonic Nanolasers. *Light Sci. Appl.* **2020**, *9* (1). <https://doi.org/10.1038/s41377-020-0319-7>.
- (70) Caspani, L.; Kaipurath, R. P. M.; Clerici, M.; Ferrera, M.; Roger, T.; Kim, J.; Kinsey, N.; Pietrzyk, M.; Di Falco, A.; Shalaev, V. M.; Boltasseva, A.; Faccio, D. Enhanced Nonlinear Refractive Index in  $\epsilon$ -Near-Zero Materials. *Phys. Rev. Lett.* **2016**, *116* (23), 233901. <https://doi.org/10.1103/PhysRevLett.116.233901>.
- (71) Ai, Q.; Sterl, F.; Zhang, H.; Wang, J.; Giessen, H. Giant Second Harmonic Generation Enhancement in a High- Q Doubly Resonant Hybrid Plasmon-Fiber Cavity System. *ACS Nano* **2021**, *15* (12), 19409–19417. <https://doi.org/10.1021/acsnano.1c05970>.
- (72) Lu, G.; Nolen, J. R.; Folland, T. G.; Tadjer, M. J.; Walker, D. G.; Caldwell, J. D. Narrowband Polaritonic Thermal Emitters Driven by Waste Heat. *ACS Omega* **2020**, *5* (19), 10900–10908. <https://doi.org/10.1021/acsomega.0c00600>.

- (73) Starko-Bowes, R.; Wang, X.; Xu, Z.; Pramanik, S.; Lu, N.; Li, T.; Jacob, Z. High-Temperature Polaritons in Ceramic Nanotube Antennas. *Nano Lett.* **2019**, *19* (12), 8565–8571. <https://doi.org/10.1021/acs.nanolett.9b03059>.
- (74) Wang, T.; Li, P.; Chigrin, D. N.; Giles, A. J.; Bezares, F. J.; Glembocki, O. J.; Caldwell, J. D.; Taubner, T. Phonon-Polaritonic Bowtie Nanoantennas: Controlling Infrared Thermal Radiation at the Nanoscale. *ACS Photonics* **2017**, *4* (7), 1753–1760. <https://doi.org/10.1021/acsp Photonics.7b00321>.
- (75) Caldwell, J. D.; Glembocki, O. J.; Francescato, Y.; Sharac, N.; Giannini, V.; Bezares, F. J.; Long, J. P.; Owrutsky, J. C.; Vurgaftman, I.; Tischler, J. G.; Wheeler, V. D.; Bassim, N. D.; Shirey, L. M.; Kasica, R.; Maier, S. A. Low-Loss, Extreme Subdiffraction Photon Confinement via Silicon Carbide Localized Surface Phonon Polariton Resonators. *Nano Lett.* **2013**, *13* (8), 3690–3697. <https://doi.org/10.1021/nl401590g>.
- (76) Jahani, S.; Jacob, Z. All-Dielectric Metamaterials. *Nat. Nanotechnol.* **2016**, *11* (1), 23–36. <https://doi.org/10.1038/nnano.2015.304>.
- (77) Caldwell, J. D.; Vurgaftman, I.; Tischler, J. G.; Glembocki, O. J.; Owrutsky, J. C.; Reinecke, T. L. Atomic-Scale Photonic Hybrids for Mid-Infrared and Terahertz Nanophotonics. *Nat. Nanotechnol.* **2016**, *11* (1), 9–15. <https://doi.org/10.1038/nnano.2015.305>.
- (78) Law, S.; Yu, L.; Wasserman, D. Epitaxial Growth of Engineered Metals for Mid-Infrared Plasmonics. *J. Vac. Sci. Technol. B, Nanotechnol. Microelectron. Mater. Process. Meas. Phenom.* **2013**, *31* (3), 03C121. <https://doi.org/10.1116/1.4797487>.
- (79) Ginn, J. C.; Jarecki, R. L.; Shaner, E. A.; Davids, P. S. Infrared Plasmons on Heavily-Doped Silicon. *J. Appl. Phys.* **2011**, *110* (4), 043110. <https://doi.org/10.1063/1.3626050>.
- (80) Naik, G. V.; Shalaev, V. M.; Boltasseva, A. Alternative Plasmonic Materials: Beyond Gold and Silver. *Adv. Mater.* **2013**, *25* (24), 3264–3294. <https://doi.org/10.1002/adma.201205076>.
- (81) Runnerstrom, E. L.; Kelley, K. P.; Sachet, E.; Shelton, C. T.; Maria, J. P. Epsilon-near-Zero Modes and Surface Plasmon Resonance in Fluorine-Doped Cadmium

- Oxide Thin Films. *ACS Photonics* **2017**, *4* (8), 1885–1892.  
<https://doi.org/10.1021/acsp Photonics.7b00429>.
- (82) Sachet, E.; Shelton, C. T.; Harris, J. S.; Gaddy, B. E.; Irving, D. L.; Curtarolo, S.; Donovan, B. F.; Hopkins, P. E.; Sharma, P. A.; Sharma, A. L.; Ihlefeld, J.; Franzen, S.; Maria, J. P. Dysprosium-Doped Cadmium Oxide as a Gateway Material for Mid-Infrared Plasmonics. *Nat. Mater.* **2015**, *14* (4), 414–420.  
<https://doi.org/10.1038/nmat4203>.
- (83) Yan, H.; Low, T.; Zhu, W.; Wu, Y.; Freitag, M.; Li, X.; Guinea, F.; Avouris, P.; Xia, F. Damping Pathways of Mid-Infrared Plasmons in Graphene Nanostructures. *Nat. Photonics* **2013**, *7* (5), 394–399. <https://doi.org/10.1038/nphoton.2013.57>.
- (84) Brar, V. W.; Jang, M. S.; Sherrott, M.; Lopez, J. J.; Atwater, H. A. Highly Confined Tunable Mid-Infrared Plasmonics in Graphene Nanoresonators. *Nano Lett.* **2013**, *13* (6), 2541–2547. <https://doi.org/10.1021/nl400601c>.
- (85) Taliercio, T.; Biagioni, P. Semiconductor Infrared Plasmonics. *Nanophotonics* **2019**, *8* (6), 949–990. <https://doi.org/10.1515/nanoph-2019-0077>.
- (86) Adachi, S. The Reststrahlen Region. In *Optical Properties of Crystalline and Amorphous Semiconductors*; Springer US: Boston, MA, 1999; Vol. 5, pp 33–62.  
[https://doi.org/10.1007/978-1-4615-5241-3\\_2](https://doi.org/10.1007/978-1-4615-5241-3_2).
- (87) Caldwell, J. D.; Lindsay, L.; Giannini, V.; Vurgaftman, I.; Reinecke, T. L.; Maier, S. A.; Glembocki, O. J. Low-Loss, Infrared and Terahertz Nanophotonics Using Surface Phonon Polaritons. *Nanophotonics* **2015**, *4* (1), 44–68.  
<https://doi.org/10.1515/nanoph-2014-0003>.
- (88) Hillenbrand, R.; Taubner, T.; Keilmann, F. Phonon-Enhanced Light-Matter Interaction at the Nanometre Scale. *Nature* **2002**, *418* (6894), 159–162.  
<https://doi.org/10.1038/nature00899>.
- (89) Caldwell, J. D.; Kretinin, A. V.; Chen, Y.; Giannini, V.; Fogler, M. M.; Francescato, Y.; Ellis, C. T.; Tischler, J. G.; Woods, C. R.; Giles, A. J.; Hong, M.; Watanabe, K.; Taniguchi, T.; Maier, S. A.; Novoselov, K. S. Sub-Diffractive Volume-Confined Polaritons in the Natural Hyperbolic Material Hexagonal Boron Nitride. *Nat. Commun.* **2014**, *5* (1), 5221. <https://doi.org/10.1038/ncomms6221>.

- (90) Dai, S.; Fei, Z.; Ma, Q.; Rodin, A. S.; Wagner, M.; McLeod, A. S.; Liu, M. K.; Gannett, W.; Regan, W.; Watanabe, K.; Taniguchi, T.; Thiemens, M.; Dominguez, G.; Castro Neto, A. H.; Zettl, A.; Keilmann, F.; Jarillo-Herrero, P.; Fogler, M. M.; Basov, D. N. Tunable Phonon Polaritons in Atomically Thin van Der Waals Crystals of Boron Nitride. *Science* (80-. ). **2014**, *343* (6175), 1125–1129. <https://doi.org/10.1126/science.1246833>.
- (91) Ng, S. S.; Hassan, Z.; Abu Hassan, H. Experimental and Theoretical Studies of Surface Phonon Polariton of AlN Thin Film. *Appl. Phys. Lett.* **2007**, *90* (8), 2005–2008. <https://doi.org/10.1063/1.2645970>.
- (92) Spann, B. T.; Compton, R.; Ratchford, D.; Long, J. P.; Dunkelberger, A. D.; Klein, P. B.; Giles, A. J.; Caldwell, J. D.; Owrutsky, J. C. Photoinduced Tunability of the Reststrahlen Band in 4H-SiC. *Phys. Rev. B* **2016**, *93* (8), 085205. <https://doi.org/10.1103/PhysRevB.93.085205>.
- (93) Dunkelberger, A. D.; Ellis, C. T.; Ratchford, D. C.; Giles, A. J.; Kim, M.; Kim, C. S.; Spann, B. T.; Vurgaftman, I.; Tischler, J. G.; Long, J. P.; Glembocki, O. J.; Owrutsky, J. C.; Caldwell, J. D. Active Tuning of Surface Phonon Polariton Resonances via Carrier Photoinjection. *Nat. Photonics* **2018**, *12* (1), 50–56. <https://doi.org/10.1038/s41566-017-0069-0>.
- (94) Biswas, B.; Saha, B. Development of Semiconducting ScN. *Phys. Rev. Mater.* **2019**, *3* (2), 020301. <https://doi.org/10.1103/PhysRevMaterials.3.020301>.
- (95) Eklund, P.; Kerdsonpanya, S.; Alling, B. Transition-Metal-Nitride-Based Thin Films as Novel Energy Harvesting Materials. *J. Mater. Chem. C* **2016**, *4* (18), 3905–3914. <https://doi.org/10.1039/c5tc03891j>.
- (96) Gall, D.; Städele, M.; Järrendahl, K.; Petrov, I.; Desjardins, P.; Haasch, R. T.; Lee, T. Y.; Greene, J. E. Electronic Structure of ScN Determined Using Optical Spectroscopy, Photoemission, and Ab Initio Calculations. *Phys. Rev. B - Condens. Matter Mater. Phys.* **2001**, *63* (12), 1251191–1251199. <https://doi.org/10.1103/physrevb.63.125119>.
- (97) Gall, D.; Petrov, I.; Hellgren, N.; Hultman, L.; Sundgren, J. E.; Greene, J. E. Growth of Poly- and Single-Crystal ScN on MgO(001): Role of Low-Energy N+2

- Irradiation in Determining Texture, Microstructure Evolution, and Mechanical Properties. *J. Appl. Phys.* **1998**, *84* (11), 6034–6041.  
<https://doi.org/10.1063/1.368913>.
- (98) Maurya, K. C.; Biswas, B.; Garbrecht, M.; Saha, B. Wave-Vector-Dependent Raman Scattering from Coupled Plasmon–Longitudinal Optical Phonon Modes and Fano Resonance in n -type Scandium Nitride. *Phys. status solidi – Rapid Res. Lett.* **2019**, *13* (9), 1900196. <https://doi.org/10.1002/pssr.201900196>.
- (99) Stampfl, C.; Mannstadt, W.; Asahi, R.; Freeman, A. J. Electronic Structure and Physical Properties of Early Transition Metal Mononitrides: Density-Functional Theory LDA, GGA, and Screened-Exchange LDA FLAPW Calculations. *Phys. Rev. B - Condens. Matter Mater. Phys.* **2001**, *63* (15), 1–11.  
<https://doi.org/10.1103/PhysRevB.63.155106>.
- (100) Saha, B.; Acharya, J.; Sands, T. D.; Waghmare, U. V. Electronic Structure, Phonons, and Thermal Properties of ScN, ZrN, and HfN: A First-Principles Study. *J. Appl. Phys.* **2010**, *107* (3), 033715. <https://doi.org/10.1063/1.3291117>.
- (101) Mu, S.; Rowberg, A. J. E.; Leveillee, J.; Giustino, F.; Van de Walle, C. G. First-Principles Study of Electron Transport in ScN. *Phys. Rev. B* **2021**, *104* (7), 075118. <https://doi.org/10.1103/PhysRevB.104.075118>.
- (102) Rao, D.; Biswas, B.; Flores, E.; Chatterjee, A.; Garbrecht, M.; Koh, Y. R.; Bhatia, V.; Pillai, A. I. K.; Hopkins, P. E.; Martin-Gonzalez, M.; Saha, B. High Mobility and High Thermoelectric Power Factor in Epitaxial ScN Thin Films Deposited with Plasma-Assisted Molecular Beam Epitaxy. *Appl. Phys. Lett.* **2020**, *116* (15), 152103. <https://doi.org/10.1063/5.0004761>.
- (103) Moram, M. A.; Zhang, Y.; Kappers, M. J.; Barber, Z. H.; Humphreys, C. J. Dislocation Reduction in Gallium Nitride Films Using Scandium Nitride Interlayers. *Appl. Phys. Lett.* **2007**, *91* (15), 152101.  
<https://doi.org/10.1063/1.2794009>.
- (104) Acharya, S.; Chatterjee, A.; Bhatia, V.; Pillai, A. I. K.; Garbrecht, M.; Saha, B. Twinned Growth of ScN Thin Films on Lattice-Matched GaN Substrates. *Mater. Res. Bull.* **2021**, *143*, 111443. <https://doi.org/10.1016/j.materresbull.2021.111443>.

- (105) Saha, B.; Garbrecht, M.; Perez-Taborda, J. A.; Fawey, M. H.; Koh, Y. R.; Shakouri, A.; Martin-Gonzalez, M.; Hultman, L.; Sands, T. D. Compensation of Native Donor Doping in ScN: Carrier Concentration Control and p-Type ScN. *Appl. Phys. Lett.* **2017**, *110* (25), 252104. <https://doi.org/10.1063/1.4989530>.
- (106) Nayak, S.; Baral, M.; Gupta, M.; Singh, J.; Garbrecht, M.; Ganguli, T.; Shivaprasad, S. M.; Saha, B. Rigid-Band Electronic Structure of Scandium Nitride across the n-Type to p-Type Carrier Transition Regime. *Phys. Rev. B* **2019**, *99* (16), 161117. <https://doi.org/10.1103/PhysRevB.99.161117>.
- (107) Uchiyama, H.; Oshima, Y.; Patterson, R.; Iwamoto, S.; Shiomi, J.; Shimamura, K. Phonon Lifetime Observation in Epitaxial ScN Film with Inelastic X-Ray Scattering Spectroscopy. *Phys. Rev. Lett.* **2018**, *120* (23), 235901. <https://doi.org/10.1103/PhysRevLett.120.235901>.
- (108) Saha, B.; Perez-Taborda, J. A.; Bahk, J.-H.; Koh, Y. R.; Shakouri, A.; Martin-Gonzalez, M.; Sands, T. D. Temperature-Dependent Thermal and Thermoelectric Properties of n-Type and p-Type Sc<sub>1-x</sub>Mg<sub>x</sub>N. *Phys. Rev. B* **2018**, *97* (8), 085301. <https://doi.org/10.1103/PhysRevB.97.085301>.
- (109) Wang, Z.; Chen, C.; Wu, K.; Chong, H.; Ye, H. Transparent Conductive Oxides and Their Applications in Near Infrared Plasmonics. *Phys. Status Solidi Appl. Mater. Sci.* **2019**, *216* (5), 1–12. <https://doi.org/10.1002/pssa.201700794>.
- (110) Berini, P. Figures of Merit for Surface Plasmon Waveguides. *Opt. Express* **2006**, *14* (26), 13030–13042.
- (111) Gielisse, P. J.; Mitra, S. S.; Plendl, J. N.; Griffis, R. D.; Mansur, L. C.; Marshall, R.; Pascoe, E. A. Lattice Infrared Spectra of Boron Nitride and Boron Monophosphide. *Phys. Rev.* **1967**, *155* (3), 1039–1046. <https://doi.org/10.1103/PhysRev.155.1039>.
- (112) Torii, K.; Koga, T.; Sota, T.; Azuhata, T.; Chichibu, S. F.; Nakamura, S. An Attenuated-Total-Reflection Study on the Surface Phonon-Polariton in GaN. *J. Phys. Condens. Matter* **2000**, *12* (31), 7041–7044. <https://doi.org/10.1088/0953-8984/12/31/305>.
- (113) Marschall, N.; Fischer, B. Dispersion of Surface Polaritons in GaP. *Phys. Rev. Lett.*

- 1972**, 28 (13), 811–813. <https://doi.org/10.1103/PhysRevLett.28.811>.
- (114) Oshima, Y.; Vllora, E. G.; Shimamura, K. Hydride Vapor Phase Epitaxy and Characterization of High-Quality ScN Epilayers. *J. Appl. Phys.* **2014**, *115* (15), 153508. <https://doi.org/10.1063/1.4871656>.
- (115) Nakamura, S.; Krames, M. R. History of Gallium-Nitride-Based Light-Emitting Diodes for Illumination. *Proc. IEEE* **2013**, *101* (10), 2211–2220. <https://doi.org/10.1109/JPROC.2013.2274929>.
- (116) Pearton, S. J.; Abernathy, C. R.; Overberg, M. E.; Thaler, G. T.; Onstine, A. H.; Gila, B. P.; Ren, F.; Lou, B.; Kim, J. New Applications for Gallium Nitride. *Mater. Today* **2002**, *5* (6), 24–31. [https://doi.org/10.1016/S1369-7021\(02\)00636-3](https://doi.org/10.1016/S1369-7021(02)00636-3).
- (117) Liu, C.; Yun, F.; Morkoç, H. Ferromagnetism of ZnO and GaN: A Review. *J. Mater. Sci. Mater. Electron.* **2005**, *16* (9), 555–597. <https://doi.org/10.1007/s10854-005-3232-1>.
- (118) Xiao, Y.; Vanka, S.; Pham, T. A.; Dong, W. J.; Sun, Y.; Liu, X.; Navid, I. A.; Varley, J. B.; Hajibabaei, H.; Hamann, T. W.; Ogitsu, T.; Mi, Z. Crystallographic Effects of GaN Nanostructures in Photoelectrochemical Reaction. *Nano Lett.* **2022**, *22* (6), 2236–2243. <https://doi.org/10.1021/acs.nanolett.1c04220>.
- (119) Han, S.; Noh, S.; Yu, Y. T.; Lee, C. R.; Lee, S. K.; Kim, J. S. Highly Efficient Photoelectrochemical Water Splitting Using GaN-Nanowire Photoanode with Tungsten Sulfides. *ACS Appl. Mater. Interfaces* **2020**, *12* (52), 58028–58037. <https://doi.org/10.1021/acsami.0c17811>.
- (120) Chatterjee, A.; Acharya, S.; Shivaprasad, S. M. Morphology-Related Functionality in Nanoarchitected GaN. *Annu. Rev. Mater. Res.* **2020**, *50* (July), 179–206. <https://doi.org/10.1146/annurev-matsci-081919-014810>.
- (121) Zhong, A.; Fan, P.; Zhong, Y.; Zhang, D.; Li, F.; Luo, J.; Xie, Y.; Hane, K. Structure Shift of GaN Among Nanowall Network, Nanocolumn, and Compact Film Grown on Si (111) by MBE. *Nanoscale Res. Lett.* **2018**, *13*, 1–7. <https://doi.org/10.1186/s11671-018-2461-1>.
- (122) Consonni, V. Self-Induced Growth of GaN Nanowires by Molecular Beam



- Epitaxy: A Critical Review of the Formation Mechanisms. *Phys. Status Solidi - Rapid Res. Lett.* **2013**, 7 (10), 699–712. <https://doi.org/10.1002/pssr.201307237>.
- (123) Avit, G.; Lekhal, K.; André, Y.; Bougerol, C.; Réveret, F.; Leymarie, J.; Gil, E.; Monier, G.; Castelluci, D.; Trassoudaine, A. Ultralong and Defect-Free GaN Nanowires Grown by the HVPE Process. *Nano Lett.* **2014**, 14 (2), 559–562. <https://doi.org/10.1021/nl403687h>.
- (124) Metaxa, C.; Kassavetis, S.; Pierson, J. F.; Gall, D.; Patsalas, P. Infrared Plasmonics with Conductive Ternary Nitrides. *ACS Appl. Mater. Interfaces* **2017**, 9 (12), 10825–10834. <https://doi.org/10.1021/acsami.6b16343>.
- (125) Foteinopoulou, S.; Devarapu, G. C. R.; Subramania, G. S.; Krishna, S.; Wasserman, D. Phonon-Polaritons: Enabling Powerful Capabilities for Infrared Photonics. *Nanophotonics* **2019**, 8 (12), 2129–2175. <https://doi.org/10.1515/nanoph-2019-0232>.
- (126) Maurya, K. C.; Rao, D.; Acharya, S.; Rao, P.; Pillai, A. I. K.; Selvaraja, S. K.; Garbrecht, M.; Saha, B. Polar Semiconducting Scandium Nitride as an Infrared Plasmon and Phonon–Polaritonic Material. *Nano Lett.* **2022**, 22 (13), 5182–5190. <https://doi.org/10.1021/acs.nanolett.2c00912>.
- (127) Hossain, M. M.; Jia, B.; Gu, M. A Metamaterial Emitter for Highly Efficient Radiative Cooling. *Adv. Opt. Mater.* **2015**, 3 (8), 1047–1051. <https://doi.org/10.1002/adom.201500119>.
- (128) Chirumamilla, M.; Chirumamilla, A.; Yang, Y.; Roberts, A. S.; Kristensen, P. K.; Chaudhuri, K.; Boltasseva, A.; Sutherland, D. S.; Bozhevolnyi, S. I.; Pedersen, K. Large-Area Ultrabroadband Absorber for Solar Thermophotovoltaics Based on 3D Titanium Nitride Nanopillars. *Adv. Opt. Mater.* **2017**, 5 (22). <https://doi.org/10.1002/adom.201700552>.
- (129) Lewis, R. A. A Review of Terahertz Detectors. *J. Phys. D: Appl. Phys.* **2019**, 52 (43), 433001. <https://doi.org/10.1088/1361-6463/ab31d5>.
- (130) Corsi, C. Infrared: A Key Technology for Security Systems. *Adv. Opt. Technol.* **2012**, 2012 (2). <https://doi.org/10.1155/2012/838752>.

- (131) Shirley, K. A.; Glotch, T. D. Particle Size Effects on Mid-Infrared Spectra of Lunar Analog Minerals in a Simulated Lunar Environment. *J. Geophys. Res. Planets* **2019**, *124* (4), 970–988. <https://doi.org/10.1029/2018JE005533>.
- (132) Barker, A. S.; Ilegems, M. Infrared Lattice Vibrations and Free-Electron Dispersion in GaN. *Phys. Rev. B* **1973**, *7* (2), 743–750. <https://doi.org/10.1103/PhysRevB.7.743>.
- (133) Azuhata, T.; Matsunaga, T.; Shimada, K.; Yoshida, K.; Sota, T.; Suzuki, K.; Nakamura, S. Optical Phonons in GaN. *Phys. B Condens. Matter* **1996**, *219–220* (1–4), 493–495. [https://doi.org/10.1016/0921-4526\(95\)00789-X](https://doi.org/10.1016/0921-4526(95)00789-X).
- (134) Ng, S. S.; Hassan, Z.; Abu Hassan, H. Surface Phonon Polariton of Wurtzite GaN Thin Film Grown on C-Plane Sapphire Substrate. *Solid State Commun.* **2008**, *145* (11–12), 535–538. <https://doi.org/10.1016/j.ssc.2008.01.006>.
- (135) Andersson, S. K.; Ribbing, C. G. Light Extinction by Bulk Voids and Surface Irregularities in Ceramic Materials. *Phys. Rev. B* **1994**, *49* (16), 11336–11343. <https://doi.org/10.1103/PhysRevB.49.11336>.
- (136) Bohren, C. F. Particles Small Compared with the Wavelength. In *Absorption and Scattering of Light by Small Particles*; Wiley-VCH Verlag GmbH: Weinheim, Germany, 2007; pp 130–157. <https://doi.org/10.1002/9783527618156.ch5>.
- (137) Nayak, S.; Naik, M. H.; Jain, M.; Waghmare, U. V.; Shivaprasad, S. M. First-Principles Theoretical Analysis and Electron Energy Loss Spectroscopy of Vacancy Defects in Bulk and Nonpolar (101 $\bar{0}$ ) Surface of GaN. *J. Vac. Sci. Technol. A* **2020**, *38* (6), 063205. <https://doi.org/10.1116/6.0000402>.
- (138) Nayak, S.; Kumar, R.; Shivaprasad, S. M. Edge Enhanced Growth Induced Shape Transition in the Formation of GaN Nanowall Network. *J. Appl. Phys.* **2018**, *123* (1). <https://doi.org/10.1063/1.5004496>.
- (139) Ben-Jacob, E.; Garik, P. The Formation of Patterns in Non-Equilibrium Growth. *Nature* **1990**, *343* (6258), 523–530. <https://doi.org/10.1038/343523a0>.
- (140) Kesaria, M.; Shetty, S.; Shivaprasad, S. M. Evidence for Dislocation Induced Spontaneous Formation of GaN Nanowalls and Nanocolumns on Bare C-Plane

- Sapphire. *Cryst. Growth Des.* **2011**, *11* (11), 4900–4903.  
<https://doi.org/10.1021/cg200749w>.
- (141) Arora, A. K.; Rajalakshmi, M.; Ravindran, T. R.; Sivasubramanian, V. Raman Spectroscopy of Optical Phonon Confinement in Nanostructured Materials. *J. Raman Spectrosc.* **2007**, *38* (6), 604–617. <https://doi.org/10.1002/jrs.1684>.
- (142) Kushvaha, S. S.; Kumar, M. S.; Shukla, A. K.; Yadav, B. S.; Singh, D. K.; Jewariya, M.; Ragam, S. R.; Maurya, K. K. Structural, Optical and Electronic Properties of Homoepitaxial GaN Nanowalls Grown on GaN Template by Laser Molecular Beam Epitaxy. *RSC Adv.* **2015**, *5* (107), 87818–87830.  
<https://doi.org/10.1039/c5ra11361j>.
- (143) Sihvola, A. Generalised Mixing Rules. In *Electromagnetic Mixing Formulas and Applications*; Institution of Engineering and Technology, 1999; pp 161–176.  
[https://doi.org/10.1049/PBEW047E\\_ch9](https://doi.org/10.1049/PBEW047E_ch9).
- (144) Tazawa, M.; Fujii, A.; Tanemura, S. The Surface Substructural Effects on Reststrahlen Bands in Reflectance of Alumina Ceramics with Different Sized Grains. *Netsu Bussei* **1995**, *9* (3), 157–162. <https://doi.org/10.2963/jjtp.9.157>.
- (145) Maurya, K. C.; Biswas, B.; Rao, D.; Saha, B. Giant Enhancement of Plasmonic Response and Epsilon-near-Zero Signature in Refractory Transition Metals (Ta, W, and Mo) Deposited at High-Temperature. *Appl. Phys. Lett.* **2021**, *118* (4), 041902.  
<https://doi.org/10.1063/5.0027497>.
- (146) Askari, S.; Mariotti, D.; Stehr, J. E.; Benedikt, J.; Keraudy, J.; Helmersson, U. Low-Loss and Tunable Localized Mid-Infrared Plasmons in Nanocrystals of Highly Degenerate InN. *Nano Lett.* **2018**, *18* (9), 5681–5687.  
<https://doi.org/10.1021/acs.nanolett.8b02260>.
- (147) Greenberg, B. L.; Ganguly, S.; Held, J. T.; Kramer, N. J.; Mkhoyan, K. A.; Aydil, E. S.; Kortshagen, U. R. Nonequilibrium-Plasma-Synthesized ZnO Nanocrystals with Plasmon Resonance Tunable via Al Doping and Quantum Confinement. *Nano Lett.* **2015**, *15* (12), 8162–8169. <https://doi.org/10.1021/acs.nanolett.5b03600>.
- (148) Luther, J. M.; Jain, P. K.; Ewers, T.; Alivisatos, A. P. Localized Surface Plasmon Resonances Arising from Free Carriers in Doped Quantum Dots. *Nat. Mater.* **2011**,

- 10 (5), 361–366. <https://doi.org/10.1038/nmat3004>.
- (149) Lounis, S. D.; Runnerstrom, E. L.; Bergerud, A.; Nordlund, D.; Milliron, D. J. Influence of Dopant Distribution on the Plasmonic Properties of Indium Tin Oxide Nanocrystals. *J. Am. Chem. Soc.* **2014**, *136* (19), 7110–7116. <https://doi.org/10.1021/ja502541z>.
- (150) Runnerstrom, E. L.; Bergerud, A.; Agrawal, A.; Johns, R. W.; Dahlman, C. J.; Singh, A.; Selbach, S. M.; Milliron, D. J. Defect Engineering in Plasmonic Metal Oxide Nanocrystals. *Nano Lett.* **2016**, *16* (5), 3390–3398. <https://doi.org/10.1021/acs.nanolett.6b01171>.
- (151) Atwater, H. A.; Polman, A. Plasmonics for Improved Photovoltaic Devices. *Nat. Mater.* **2010**, *9* (3), 205–213. <https://doi.org/10.1038/nmat2629>.
- (152) Nikolis, V. C.; Mischok, A.; Siegmund, B.; Kublitski, J.; Jia, X.; Benduhn, J.; Hörmann, U.; Neher, D.; Gather, M. C.; Spoltore, D.; Vandewal, K. Strong Light-Matter Coupling for Reduced Photon Energy Losses in Organic Photovoltaics. *Nat. Commun.* **2019**, *10* (1), 1–8. <https://doi.org/10.1038/s41467-019-11717-5>.
- (153) An, S.; Liao, Y.; Kim, M. Flexible Titanium Nitride/Germanium-Tin Photodetectors Based on Sub-Bandgap Absorption. *ACS Appl. Mater. Interfaces* **2021**, *13* (51), 61396–61403. <https://doi.org/10.1021/acsami.1c15181>.
- (154) Li, F.; Tao, R.; Cao, B.; Yang, L.; Wang, Z. Manipulating the Light-Matter Interaction of PtS/MoS<sub>2</sub> p–n Junctions for High Performance Broadband Photodetection. *Adv. Funct. Mater.* **2021**, *31* (36), 2104367. <https://doi.org/10.1002/adfm.202104367>.
- (155) Kwon, M. K.; Kim, J. Y.; Kim, B. H.; Park, I. K.; Cho, C. Y.; Byeon, C. C.; Park, S. J. Surface-Plasmon-Enhanced Light-Emitting Diodes. *Adv. Mater.* **2008**, *20* (7), 1253–1257. <https://doi.org/10.1002/adma.200701130>.
- (156) Vinnakota, R. K.; Dong, Z.; Briggs, A. F.; Bank, S. R.; Wasserman, D.; Genov, D. A. Plasmonic Electro-Optic Modulator Based on Degenerate Semiconductor Interfaces. *Nanophotonics* **2020**, *9* (5), 1105–1113. <https://doi.org/10.1515/nanoph-2019-0518>.

- (157) Haffner, C.; Chelladurai, D.; Fedoryshyn, Y.; Josten, A.; Baeuerle, B.; Heni, W.; Watanabe, T.; Cui, T.; Cheng, B.; Saha, S.; Elder, D. L.; Dalton, L. R.; Boltasseva, A.; Shalaev, V. M.; Kinsey, N.; Leuthold, J. Low-Loss Plasmon-Assisted Electro-Optic Modulator. *Nature* **2018**, *556* (7702), 483–486.  
<https://doi.org/10.1038/s41586-018-0031-4>.
- (158) Zhai, Y.; Ma, Y.; David, S. N.; Zhao, D.; Lou, R.; Tan, G.; Yang, R.; Yin, X. Scalable-Manufactured Randomized Glass-Polymer Hybrid Metamaterial for Daytime Radiative Cooling. *Science* (80-. ). **2017**, *355* (6329), 1062–1066.  
<https://doi.org/10.1126/science.aai7899>.
- (159) Molesky, S.; Dewalt, C. J.; Jacob, Z. High Temperature Epsilon-near-Zero and Epsilon-near-Pole Metamaterial Emitters for Thermophotovoltaics. *Opt. Express* **2013**, *21* (January), 549–554. [https://doi.org/10.1364/cleo\\_qels.2013.qtu1a.6](https://doi.org/10.1364/cleo_qels.2013.qtu1a.6).
- (160) Nikolajsen, T.; Leosson, K.; Bozhevolnyi, S. I. Surface Plasmon Polariton Based Modulators and Switches Operating at Telecom Wavelengths. *Appl. Phys. Lett.* **2004**, *85* (24), 5833–5835. <https://doi.org/10.1063/1.1835997>.
- (161) Aydin, K.; Ferry, V. E.; Briggs, R. M.; Atwater, H. A. Broadband Polarization-Independent Resonant Light Absorption Using Ultrathin Plasmonic Super Absorbers. *Nat. Commun.* **2011**, *2* (1), 1–7. <https://doi.org/10.1038/ncomms1528>.
- (162) Chen, X.; Gong, H.; Dai, S.; Zhao, D.; Yang, Y.; Li, Q.; Qiu, M. Near-Infrared Broadband Absorber with Film-Coupled Multilayer Nanorods. *Opt. Lett.* **2013**, *38* (13), 2247. <https://doi.org/10.1364/ol.38.002247>.
- (163) Zhou, L.; Tan, Y.; Ji, D.; Zhu, B.; Zhang, P.; Xu, J.; Gan, Q.; Yu, Z.; Zhu, J. Self-Assembly of Highly Efficient, Broadband Plasmonic Absorbers for Solar Steam Generation. *Sci. Adv.* **2016**, *2* (4), 1–8. <https://doi.org/10.1126/sciadv.1501227>.
- (164) Fei Guo, C.; Sun, T.; Cao, F.; Liu, Q.; Ren, Z. Metallic Nanostructures for Light Trapping in Energy-Harvesting Devices. *Light Sci. Appl.* **2014**, *3* (4), e161–e161. <https://doi.org/10.1038/lsa.2014.42>.
- (165) Lin, K.-T.; Lin, H.; Jia, B. Plasmonic Nanostructures in Photodetection, Energy Conversion and Beyond. *Nanophotonics* **2020**, *9* (10), 3135–3163.  
<https://doi.org/10.1515/nanoph-2020-0104>.

- (166) Dao, T. D.; Chen, K.; Ishii, S.; Ohi, A.; Nabatame, T.; Kitajima, M.; Nagao, T. Infrared Perfect Absorbers Fabricated by Colloidal Mask Etching of Al-Al<sub>2</sub>O<sub>3</sub>-Al Trilayers. *ACS Photonics*. 2015, pp 964–970.  
<https://doi.org/10.1021/acsp Photonics.5b00195>.
- (167) Tittl, A.; Michel, A. K. U.; Schäferling, M.; Yin, X.; Gholipour, B.; Cui, L.; Wuttig, M.; Taubner, T.; Neubrech, F.; Giessen, H. A Switchable Mid-Infrared Plasmonic Perfect Absorber with Multispectral Thermal Imaging Capability. *Advanced Materials*. 2015, pp 4597–4603.  
<https://doi.org/10.1002/adma.201502023>.
- (168) Landy, N. I.; Sajuyigbe, S.; Mock, J. J.; Smith, D. R.; Padilla, W. J. Perfect Metamaterial Absorber. *Phys. Rev. Lett.* **2008**, *100* (20), 207402.  
<https://doi.org/10.1103/PhysRevLett.100.207402>.
- (169) Kavokin, A.; Baumberg, J. J.; Malpuech, G.; Laussy, F. P. *Microcavities*, 2nd ed.; oxford university press, 2008.  
<https://doi.org/10.1093/acprof:oso/9780199228942.001.0001>.
- (170) Wang, Z.; Clark, J. K.; Ho, Y. L.; Vilquin, B.; Daiguji, H.; Delaunay, J. J. Narrowband Thermal Emission Realized through the Coupling of Cavity and Tamm Plasmon Resonances. *ACS Photonics* **2018**, *5* (6), 2446–2452.  
<https://doi.org/10.1021/acsp Photonics.8b00236>.
- (171) Baranov, D. G.; Krasnok, A.; Shegai, T.; Alù, A.; Chong, Y. Coherent Perfect Absorbers: Linear Control of Light with Light. *Nat. Rev. Mater.* **2017**, *2* (12), 17064. <https://doi.org/10.1038/natrevmats.2017.64>.
- (172) Wang, Y.; Zhou, L.; Zhang, Y.; Yu, J.; Huang, B.; Wang, Y.; Lai, Y.; Zhu, S.; Zhu, J. Hybrid Solar Absorber–Emitter by Coherence-Enhanced Absorption for Improved Solar Thermophotovoltaic Conversion. *Adv. Opt. Mater.* **2018**, *6* (24), 1–7. <https://doi.org/10.1002/adom.201800813>.
- (173) Hentschel, M.; Karst, J.; Giessen, H. Tailored Optical Functionality by Combining Electron-Beam and Focused Gold-Ion Beam Lithography for Solid and Inverse Coupled Plasmonic Nanostructures. *Adv. Opt. Mater.* **2020**, *8*, 2000879.  
<https://doi.org/https://doi.org/10.1002/adom.202000879>.

- (174) Vassant, S.; Hugonin, J.-P.; Marquier, F.; Greffet, J.-J. Berreman Mode and Epsilon near Zero Mode. *Opt. Express* **2012**, *20* (21), 23971. <https://doi.org/10.1364/oe.20.023971>.
- (175) Khan, I.; Fang, Z.; Palei, M.; Lu, J.; Nordin, L.; Simmons, E. L.; Dominguez, O.; Islam, S. M.; Xing, H. G.; Jena, D.; Podolskiy, V. A.; Wasserman, D.; Hoffman, A. J. Engineering the Berreman Mode in Mid-Infrared Polar Materials. *Opt. Express* **2020**, *28* (19), 28590. <https://doi.org/10.1364/oe.401733>.
- (176) Yau, L. D.; Sah, C. T. Measurement of Trapped-Minority-Carrier Thermal Emission Rates from Au, Ag, and Co Traps in Silicon. *Appl. Phys. Lett.* **1972**, *21* (4), 157–158. <https://doi.org/10.1063/1.1654324>.
- (177) Gadalla, M. N.; Chaudhary, K.; Zgrabik, C. M.; Capasso, F.; Hu, E. L. Imaging of Surface Plasmon Polaritons in Low-Loss Highly Metallic Titanium Nitride Thin Films in Visible and Infrared Regimes. *Opt. Express* **2020**, *28* (10), 14536. <https://doi.org/10.1364/oe.391482>.
- (178) Saha, B.; Naik, G. V.; Saber, S.; Akatay, C.; Stach, E. A.; Shalaev, V. M.; Boltasseva, A.; Sands, T. D. TiN/(Al,Sc)N Metal/Dielectric Superlattices and Multilayers as Hyperbolic Metamaterials in the Visible Spectral Range. *Phys. Rev. B* **2014**, *90*, 125420. <https://doi.org/10.1103/PhysRevB.90.125420>.
- (179) Garbrecht, M.; Hultman, L.; Fawey, M. H.; Sands, T. D.; Saha, B. Tailoring of Surface Plasmon Resonances in TiN/(Al<sub>0.72</sub>Sc<sub>0.28</sub>)N Multilayers by Dielectric Layer Thickness Variation. *J. Mater. Sci.* **2018**, *53* (6), 4001–4009. <https://doi.org/10.1007/s10853-017-1837-4>.
- (180) Schroeder, J. L.; Saha, B.; Garbrecht, M.; Schell, N.; Sands, T. D.; Birch, J. Thermal Stability of Epitaxial Cubic-TiN/(Al,Sc)N Metal/ Semiconductor Superlattices. *J. Mater. Sci.* **2015**, *50* (8), 3200–3206.
- (181) Garbrecht, M.; Hultman, L.; Fawey, M. H.; Sands, T. D.; Saha, B. Void-Mediated Coherency-Strain Relaxation and Impediment of Cubic-to-Hexagonal Transformation in Epitaxial Metastable Metal/Semiconductor TiN/Al<sub>0.72</sub>Sc<sub>0.28</sub>N Multilayer. *Phys. Rev. Mater.* **2017**, *1* (3), 033402. <https://doi.org/10.1103/PhysRevMaterials.1.033402>.

- (182) Saha, B.; Saber, S.; Stach, E. A.; Kvam, E. P.; Sands, T. D. Understanding the Rocksalt-to-Wurtzite Phase Transformation through Microstructural Analysis of ( Al , Sc ) N Epitaxial Thin Films. *Appl. Phys. Lett.* **2016**, *109*, 172102. <https://doi.org/10.1063/1.4966278>.
- (183) Berreman, D. W. Infrared Absorption at Longitudinal Optic Frequency in Cubic Crystal Films. *Phys. Rev.* **1963**, *130* (6), 2193–2198. <https://doi.org/10.1103/PhysRev.130.2193>.
- (184) Caligiuri, V.; Palei, M.; Biffi, G.; Artyukhin, S.; Krahn, R. A Semi-Classical View on Epsilon-Near-Zero Resonant Tunneling Modes in Metal/Insulator/Metal Nanocavities. *Nano Lett.* **2019**, *19* (5), 3151–3160. <https://doi.org/10.1021/acs.nanolett.9b00564>.
- (185) Caligiuri, V.; Palei, M.; Biffi, G.; Krahn, R. Hybridization of Epsilon-near-Zero Modes via Resonant Tunneling in Layered Metal-Insulator Double Nanocavities. *Nanophotonics* **2019**, *8* (9), 1505–1512. <https://doi.org/10.1515/nanoph-2019-0054>.
- (186) Li, Z.; Butun, S.; Aydin, K. Large-Area, Lithography-Free Super Absorbers and Color Filters at Visible Frequencies Using Ultrathin Metallic Films. *ACS Photonics* **2015**, *2* (2), 183–188. <https://doi.org/10.1021/ph500410u>.
- (187) Kim, J.; Oh, H.; Seo, M.; Lee, M. Generation of Reflection Colors from Metal-Insulator-Metal Cavity Structure Enabled by Thickness-Dependent Refractive Indices of Metal Thin Film. *ACS Photonics*. 2019, pp 2342–2349. <https://doi.org/10.1021/acsp Photonics.9b00894>.
- (188) Ghobadi, A.; Hajian, H.; Butun, B.; Ozbay, E. Strong Light-Matter Interaction in Lithography-Free Planar Metamaterial Perfect Absorbers. *ACS Photonics* **2018**, *5* (11), 4203–4221. <https://doi.org/10.1021/acsp Photonics.8b00872>.
- (189) Roberts, A. S.; Chirumamilla, M.; Wang, D.; An, L.; Pedersen, K.; Mortensen, N. A.; Bozhevolnyi, S. I. Ultra-Thin Titanium Nitride Films for Refractory Spectral Selectivity [Invited]. *Opt. Mater. Express* **2018**, *8* (12), 3717. <https://doi.org/10.1364/ome.8.003717>.
- (190) Aalizadeh, M.; Khavasi, A.; Butun, B.; Ozbay, E. Large-Area, Cost-Effective,



- Ultra-Broadband Perfect Absorber Utilizing Manganese in Metal-Insulator-Metal Structure. *Sci. Rep.* **2018**, *8* (1), 1–13. <https://doi.org/10.1038/s41598-018-27397-y>.
- (191) Kuttruff, J.; Garoli, D.; Allerbeck, J.; Krahn, R.; De Luca, A.; Brida, D.; Caligiuri, V.; Maccaferri, N. Ultrafast All-Optical Switching Enabled by Epsilon-near-Zero-Tailored Absorption in Metal-Insulator Nanocavities. *Commun. Phys.* **2020**, *3* (1), 1–7. <https://doi.org/10.1038/s42005-020-0379-2>.
- (192) Li, Q.; Wang, T.; Su, Y.; Yan, M.; Qiu, M. Coupled Mode Theory Analysis of Mode-Splitting in Coupled Cavity System. *Opt. Express* **2010**, *18* (8), 8367. <https://doi.org/10.1364/oe.18.008367>.
- (193) Bayer, M.; Gutbrod, T.; Reithmaier, J. P.; Forchel, A.; Reinecke, T. L.; Knipp, P. A.; Dremin, A. A.; Kulakovskii, V. D. Optical Modes in Photonic Molecules. *Phys. Rev. Lett.* **1998**, *81* (12), 2582–2585. <https://doi.org/10.1103/PhysRevLett.81.2582>.
- (194) Liao, K.; Hu, X.; Gan, T.; Liu, Q.; Wu, Z.; Fan, C.; Feng, X.; Lu, C.; Liu, Y.; Gong, Q. Photonic Molecule Quantum Optics. *Adv. Opt. Photonics* **2020**, *12* (1), 60. <https://doi.org/10.1364/aop.376739>.
- (195) Turner, A. F.; Chang, L.; Martin, T. P. Enhanced Reflectance of Reststrahlen Reflection Filters. *Appl. Opt.* **1965**, *4* (8), 927. <https://doi.org/10.1364/AO.4.000927>.
- (196) Davydov, V. Y.; Kitaev, Y. E.; Goncharuk, I.; Smirnov, A.; Graul, J.; Semchinova, O.; Uffmann, D. Phonon Dispersion and Raman Scattering in Hexagonal GaN and AlN. *Phys. Rev. B - Condens. Matter Mater. Phys.* **1998**, *58* (19), 12899–12907. <https://doi.org/10.1103/PhysRevB.58.12899>.
- (197) Deng, R.; Jiang, K.; Gall, D. Optical Phonon Modes in Al<sub>1-x</sub>Sc<sub>x</sub>N. *J. Appl. Phys.* **2014**, *115* (1), 013506. <https://doi.org/10.1063/1.4861034>.
- (198) Nordin, L.; Dominguez, O.; Roberts, C. M.; Streyer, W.; Feng, K.; Fang, Z.; Podolskiy, V. A.; Hoffman, A. J.; Wasserman, D. Mid-Infrared Epsilon-near-Zero Modes in Ultra-Thin Phononic Films. *Appl. Phys. Lett.* **2017**, *111* (9), 091105. <https://doi.org/10.1063/1.4996213>.

- (199) Zhao, D.; Lin, Z.; Zhu, W.; Lezec, H. J.; Xu, T.; Agrawal, A.; Zhang, C.; Huang, K. Recent Advances in Ultraviolet Nanophotonics: From Plasmonics and Metamaterials to Metasurfaces. *Nanophotonics* **2021**, *10* (9), 2283–2308. <https://doi.org/10.1515/nanoph-2021-0083>.
- (200) Poynting, J. H. The Wave Motion of a Revolving Shaft, and a Suggestion as to the Angular Momentum in a Beam of Circularly Polarised Light. *Proc. R. Soc. London. Ser. A, Contain. Pap. a Math. Phys. Character* **1909**, *82* (557), 560–567. <https://doi.org/10.1098/rspa.1909.0060>.
- (201) RAMAN, C. V.; BHAGAVANTAM, S. Experimental Proof of the Spin of the Photon. *Nature* **1932**, *129* (3244), 22–23. <https://doi.org/10.1038/129022a0>.
- (202) Shi, P.; Du, L.; Yuan, X. Spin Photonics: From Transverse Spin to Photonic Skyrmions. *Nanophotonics* **2021**, *10* (16), 3927–3943. <https://doi.org/10.1515/nanoph-2021-0046>.
- (203) Bliokh, K. Y.; Rodríguez-Fortuño, F. J.; Nori, F.; Zayats, A. V. Spin-Orbit Interactions of Light. *Nat. Photonics* **2015**, *9* (12), 796–808. <https://doi.org/10.1038/nphoton.2015.201>.
- (204) Guo, Z.; Jiang, H.; Chen, H. Hyperbolic Metamaterials: From Dispersion Manipulation to Applications. *J. Appl. Phys.* **2020**, *127* (7), 071101. <https://doi.org/10.1063/1.5128679>.
- (205) Hu, G.; Ou, Q.; Si, G.; Wu, Y.; Wu, J.; Dai, Z.; Krasnok, A.; Mazor, Y.; Zhang, Q.; Bao, Q.; Qiu, C. W.; Alù, A. Topological Polaritons and Photonic Magic Angles in Twisted  $\alpha$ -MoO<sub>3</sub> Bilayers. *Nature* **2020**, *582* (7811), 209–213. <https://doi.org/10.1038/s41586-020-2359-9>.
- (206) Beach, R. T.; Christy, R. W. Electron-Electron Scattering in the Intraband Optical Conductivity of Cu, Ag, and Au. *Phys. Rev. B* **1977**, *16* (12), 5277–5284. <https://doi.org/10.1103/PhysRevB.16.5277>.
- (207) Minzioni, P.; Lacava, C.; Tanabe, T.; Dong, J.; Hu, X.; Csaba, G.; Porod, W.; Singh, G.; Willner, A. E.; Almaiman, A.; Torres-Company, V.; Schröder, J.; Peacock, A. C.; Strain, M. J.; Parmigiani, F.; Contestabile, G.; Marpaung, D.; Liu, Z.; Bowers, J. E.; Chang, L.; Fabbri, S.; Ramos Vázquez, M.; Bharadwaj, V.;

- Eaton, S. M.; Lodahl, P.; Zhang, X.; Eggleton, B. J.; Munro, W. J.; Nemoto, K.; Morin, O.; Laurat, J.; Nunn, J. Roadmap on All-Optical Processing. *J. Opt.* **2019**, *21* (6), 063001. <https://doi.org/10.1088/2040-8986/ab0e66>.
- (208) Kazanskiy, N. L.; Butt, M. A.; Khonina, S. N. Optical Computing: Status and Perspectives. *Nanomaterials* **2022**, *12* (13). <https://doi.org/10.3390/nano12132171>.
- (209) Homola, J. Surface Plasmon Resonance Sensors for Detection of Chemical and Biological Species. *Chem. Rev.* **2008**, *108* (2), 462–493. <https://doi.org/10.1021/cr068107d>.
- (210) Bellassai, N.; D’Agata, R.; Jungbluth, V.; Spoto, G. Surface Plasmon Resonance for Biomarker Detection: Advances in Non-Invasive Cancer Diagnosis. *Front. Chem.* **2019**, *7* (August), 1–16. <https://doi.org/10.3389/fchem.2019.00570>.
- (211) Yeong, T. J.; Jern, K. P.; Yao, L. K.; Hannan, M. A.; Hoon, S. T. G. Applications of Photonics in Agriculture Sector: A Review. *Molecules* **2019**, *24* (10), 1–39. <https://doi.org/10.3390/molecules24102025>.
- (212) Mittal, D.; Kaur, G.; Singh, P.; Yadav, K.; Ali, S. A. Nanoparticle-Based Sustainable Agriculture and Food Science: Recent Advances and Future Outlook. *Front. Nanotechnol.* **2020**, *2* (December). <https://doi.org/10.3389/fnano.2020.579954>.
- (213) Smith, B. C. *Fundamentals of Fourier Transform Infrared Spectroscopy*; CRC Press, 2011. <https://doi.org/10.1201/b10777>.
- (214) Edition, S. Theoretical Background. In *Fourier Transform Infrared Spectrometry*; John Wiley & Sons, Inc.: Hoboken, NJ, USA, 2006; Vol. 42, pp 19–55. <https://doi.org/10.1002/9780470106310.ch2>.
- (215) Blaber, M. G.; Arnold, M. D.; Ford, M. J. A Review of the Optical Properties of Alloys and Intermetallics for Plasmonics. *J. Phys. Condens. Matter* **2010**, *22* (14), 143201. <https://doi.org/10.1088/0953-8984/22/14/143201>.